Onset of sliding of elastomer interfaces : fundamental insights from model sphere/plane contact experiments

Mariana de Souza

N° d'ordre NNT : 2021LYSEC31

THESE DE DOCTORAT DE L'UNIVERSITE DE LYON

opérée au sein de

L'ECOLE CENTRALE DE LYON

École Doctorale ED162

Mécanique, Énergétique, Génie civil, Acoustique

Spécialité de doctorat : Mécanique

Soutenance publiquement le 22 Juillet 2021, par :

Mariana DE SOUZA

Onset of sliding of elastomer interfaces: fundamental insights from model sphere/plane contact experiments

---

Devant le jury composé de :

VIDAL Valérie	Directrice de Recherche CNRS, PHYSICS	Présidente (Examinatrice)
BARTHEL Etienne	Directeur de recherche CNRS, ESPCI	Rapporteur
POULARD Christophe	Maître de conférence HDR, LPS	Rapporteur
DALMAS Davy	Chargé de recherche CNRS, LTDS	Directeur de thèse
SCHEIBERT Julien	Chargé de recherche CNRS, LTDS	Co-directeur de thèse

ACKNOWLEDGEMENTS

Many people have contributed throughout this work to whom I am greatly in debt.

First and foremost I would like to express my most sincere gratitude to my supervisor, Dr. Davy Dalmas, for their tremendous support, patience, and guidance in this thesis. Thank you for always having three minutes available, and by minutes I mean hours, even days in a row.

Furthermore, I must thank my co-supervisor, Dr. Julien Scheibert, for his help and mentoring. His enthusiasm for science kept me motivated, and his honesty in presenting and treating data set a great example for me.

I would also want to express my gratitude to CNRS for providing financial assistance for this thesis through the project PréGliss (Ingénierie@Lyon).

I also thank the members of the thesis' committee, Dr. Valérie Vidal for agreeing to chair the thesis' defense, Dr. Etienne Barthel and Dr. Christophe Poulard for reporting this work. Thank you for your kindness to this one and your constructive suggestions.

In addition, I would like to express my gratitude to all staff of the LTDS, ECL and MEGA for their helpful support. Especially, Mathieu, Thibault D., and Didier for all technical support. Hélène for her always efficient administrative assistance. Emilie for bringing her expertise and sympathy to the PDMS team; I wish you were here from the beginning. And Nasario for all his help and support along the way, as well as for always sharing a good time.

Many thanks to my lab friends for the moments we spent together, Adrien, Ane, Andi, Antoine N., Karl, Maysa, Nasrya, Quing, Tadashi, Takeshi, Valentin, Vilayvone, Victor, Pushkar, Yun, Youness... To the ones that along this period I had a pleasure of sharing an office, Amal, Camille, Gabrielle, Nicolas, Thibault S., Paul, and Vito. And a special mention must be made for Antoine A. (and Marie, of course) and Cristobal; you are one-of-a-kind people, and I am grateful to have you as close friends.

My thanks also go to all of my Brazilian friends who were present, even from afar. Special thanks to Bruna and Julia for always making me feel welcome in their homes and for making my trips to Brazil so special. To Gabriela, for being my emergency contact and making me feel comfortable knowing that I have someone special around. And to Yuri, who has been there for me since the beginning, whether it is by editing

my motivation letters, teaching me MATLAB, or sending a message to see how things were going.

Finally, I would like to say thanks to my family, for whom I will be eternally grateful; this journey would not have been possible without them. Maria and José Paulo for raising me in a home where education has always been a priority. Sandro, Flora and Joana for always being there for me in all of my life decisions. Eu amo muito vocês!

Contents

To my parents.

"Por serem exatamente o que são. Por me criarem exatamente como me criaram. Por me darem toda estrutura, tanta estrutura. Por fazerem com que eu possa sentir de tudo, tentar caminhos, voar para longe, sabendo que tenho, sempre tive e sempre terei suporte. Por me darem a chance rara, o quase luxo, de apenas viver. Porque todo o resto eles fizeram por mim."

(Ruth Manus em Um dia ainda vamos rir de tudo isso)

Chapter 1

Introduction

1.1 General context

When two bodies are put in contact and slide against each other, a resistance to the motion is generated. This resistance is called friction and is one of the most important problems in tribology, which is the science and technology of interacting surfaces in relative motion - the science of friction, wear, and lubrication [1, 2]. Friction between two solid bodies can be defined as dry if there is direct contact between the two objects, and as lubricated if a substance (called lubricant) is introduced at the interface to reduce friction [1].

Solid friction has been an important subject of study in a large number of fields, as it is present in both simple daily life situations up to engineering fields. It is either desired, *e.g.* the resistance between our feet and the ground allowing walking, or undesired, *e.g.* when producing heat in mechanical systems causes an unwanted energy dissipation [3], or when it triggers damage and wear in the materials. It is even more complex than that, in the sense that the production of heat and wear can also be desired, *e.g.*, in friction welding [4] and polishing [5], respectively.

Friction, which results from the interaction at the microscopic scale of two solids in contact, is in fact a very complex phenomenon that couples many time and length scales. At larger scales, classical friction laws are necessary and are often based on average approaches. Since the Amontons-Coulomb laws in 1699 and also in most of the derived macroscopic friction laws, the response of an interface, subjected to external tangential forces, is expressed in terms of two main parameters of friction, *e.g.* the

static and kinetic friction coefficients. These laws, which are based mainly on the proportionality between friction and normal forces, only very rarely include a link to the microscopic origin of the phenomenon.

Therefore, an in-depth understanding of the sliding contact behavior of bodies, whose fundamental origins have been studied for centuries but remain contentious [6, 7], is of crucial importance. The transition between the two friction states, *i.e.* the problem of the transition from static to kinetic friction, remains insufficiently understood. It is even more crucial in the case of elastomeric interfaces as they involves materials with complex behaviors. Indeed, elastomers exhibit a unique combination of material properties, each of which being considered as challenging both from the experimental and modelling standpoints, those include: strong adhesion, strong friction, non-linear elasticity and non-linear visco-elasticity.

1.2 Scientific context

From a scientific perspective, much progress has been made in the last decades in the fundamental understanding of friction [8, 9]. However, despite centuries of investigation, the laws of friction remain essentially empirical laws.

1.2.1 Friction laws

The first two laws of friction were established from the experiments described by Leonardo da Vinci (1452-1519) [10], which were formulated later by Guillaume Amontons (1663–1705), often known as Amontons' laws, and are briefly summarized as follows:

(1) the friction force Q_s is proportional to the normal load P (first Amontons' law, 1699);

$$Q_s = \mu P \tag{1.1}$$

being μ the friction coefficient.

(2) the friction force is independent of the apparent contact area for a constant normal load (second Amontons' law, 1699);

A third law of friction was added later by Coulomb [11]:

(3) the kinetic friction coefficient μ_k (defined from the force required to maintain relative motion at a constant sliding velocity) is lower than the static friction coefficient μ_s (defined from the force required to start motion between two bodies) and is independent of the sliding speed (Coulomb's law, 1785).

1.2.2 Origin of the friction laws

Since the pioneering work of Bowden and Tabor [12], it is well known that the independence of friction from the apparent contact area arises from the fact that the real contact area A_R (see Figure 1.1b) between two surfaces is much smaller than the apparent contact area A_A (see Figure 1.1a) and that the total friction force has two main contributions: adhesion and deformation. The former is associated with short-range attractive interactions between the two solids, localized within the real contact area; the latter with the force needed to plough the asperities in contact.

In this context, one of the main challenges for the understanding of friction concerns the evaluation of the real contact area between two surfaces (because that is the region where practically all the tribological interactions occur) and its evolution both with normal and tangential forces. Note here that, in the case of visco-elastic materials, the temporal variations of the strain may also contribute to the friction.

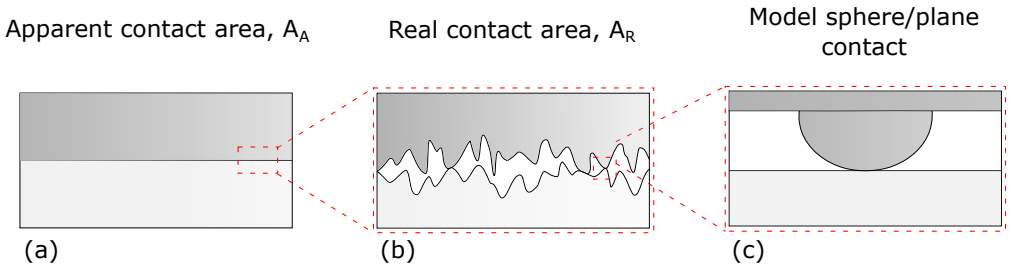

Figure 1.1: Illustration of a single-asperity approach. (a) Apparent contact area A_A between two bodies in contact, (b) zoom-in showing the multi-asperity contact forming the real contact area A_R, and (c) a single-asperity contact shown as a model sphere/plane.

Real contact area

In general, contact between both natural and engineered surfaces is discontinuous, exhibiting surface roughness on different length scales, constituting a multi-asperity contact and making friction phenomena occur at a myriad of small contacts between

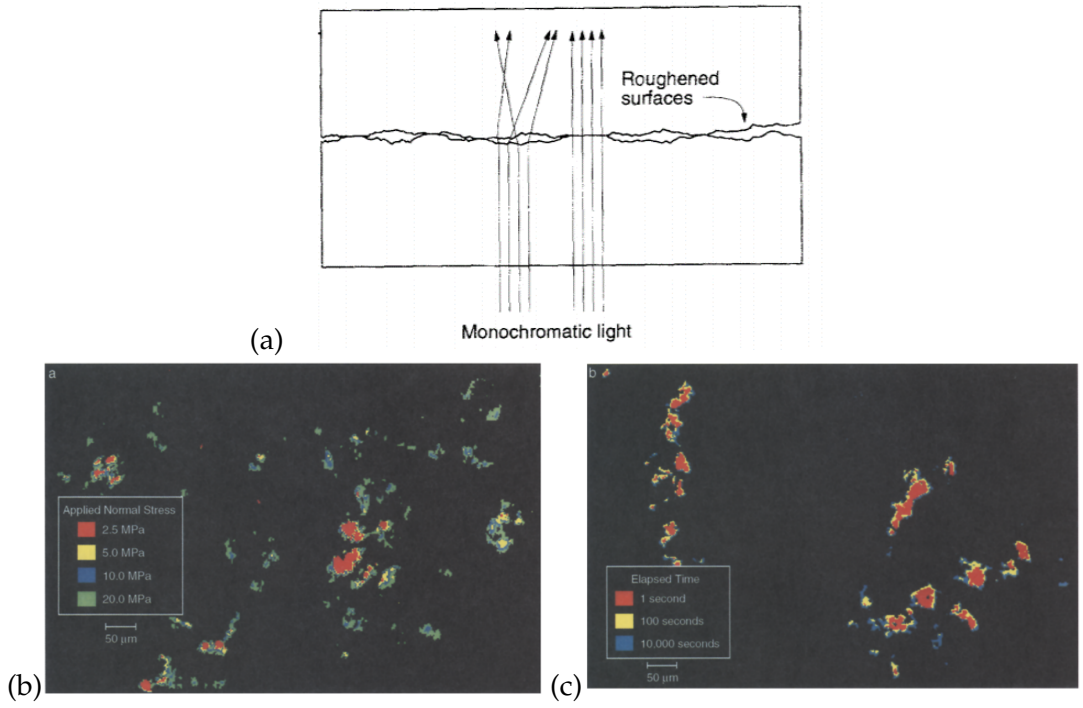

Figure 1.2: (a) Schematic representation of a rough contact interface where a monochromatic light transmitted through two blocks is scattered, except at the contact spots. Visualization of the interface between two rough PMMA blocks with (b) increasing the normal load and (c) time of stationary contact. The real contact area for low normal load or low contact time between the two solids is shown in red. The contact area increases with the load or the time spent in contact, from red to green for the load and from red to blue for the contact time. The black rectangle corresponds to the apparent contact area. Figures from [13].

the individual asperities of both surfaces. Such micro-contacts are not only difficult to characterize, both because of their small size and because of the opacity of the materials, but they are also constantly being formed or destroyed during sliding, thus also causing local normal load variations.

In particular, direct measurements on transparent interfaces, as shown in Figure 1.2(a), have shown that the real contact area A_R is a dynamic quantity, that depends on different parameters, some of them well identified in the literature, such as:

- the normal load P: the real contact area A_R of a rough interface is proportional to P [14–16], as illustrated in Figure 1.2(b), which presents the real contact area between two rough PMMA blocks for various normal loads [13]:

$$P \sim A_R; \tag{1.2}$$

- the aging time: under static conditions, the real contact area increases slowly

and generally logarithmically with time spent in contact [14, 17]. Figure 1.2(c) illustrates the aging of micro-asperities, again at the interface between two rough PMMA blocks, as the time of stationary contact increases. Depending on the material in contact, this phenomenon can be due to plastic [18] or viscoelastic [19] relaxation of the micro-contacts;

- the shearing, *i.e.* the friction force: a direct proportionality between the static friction force Q_s and the real contact area A_R is observed in shearing experiments, both for single- [17, 20–22] and multi-contact interfaces [15–17, 23]. This proportionality allows one to define the interface shear strength, σ, as the coefficient of proportionality between Q_s and A_R (see Figure 1.3):

$$Q_s = \sigma A_R \tag{1.3}$$

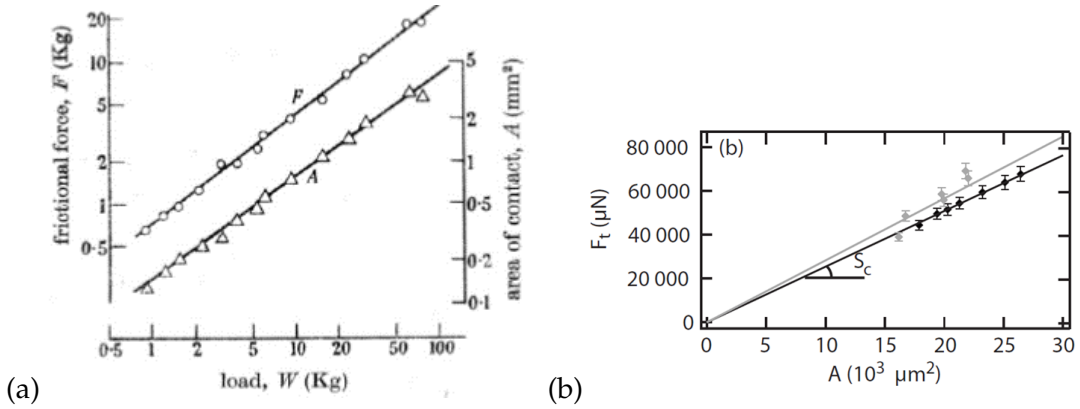

Figure 1.3: The friction force (noted F in (a) and F_t in (b)) and the real contact area (noted A) are proportional to the normal load (noted W), so they are proportional to each other. Figures from [20] and [23].

Origin of the proportionality between the real contact area and the normal load

Many different mechanical models have been proposed to describe the contact between nominally planar surfaces that contain roughness. One class of such models is the so-called asperity models, which are inspired by the pioneer work of Greenwood and Williamson [24] and Bowden and Tabor [25] which, even if based on totally antagonist assumptions, result in the same final observation, *i.e.* the proportionality between the contact area and the normal force.

On the one hand, in the Greenwood and Williamson approach in 1966 [24], the contact between a smooth rigid plane and a nominally flat rough surface is considered purely elastic. They choose to model the roughness by a collection of spherical asperities, with the same radius and a random distribution of height $\Phi(z)$ (see Figure 1.4), which deformation is described by Hertz model (see Section 1.2.3, Adhesionless normal contact). By calculating the number of contacts spots N and thus the real contact area A_R, they show that, under those elastic assumptions and for an exponential distribution of heights, the real contact area is proportional to the normal load.

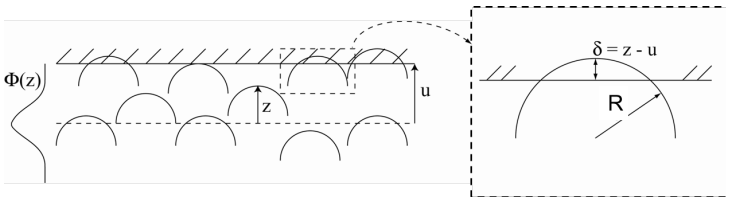

Figure 1.4: Schematic view of Greenwood and Williamson [24] model for the contact between rough surfaces. The interface is modeled by the contact between a smooth rigid plane and a collection of spherical asperities, with the same radius R and a random distribution of height $\Phi(z)$, which deformation is described by Hertz model.

On the other hand, in the Bowden and Tabor approach in 1942 [25], the contact between two rough surfaces is considered as purely plastic. By assuming that the real contact area A_R is far lower than the apparent contact area A_A, they considered that the local pressure p_0 in each micro-contact, which is highly loaded, is equal to the yield strength of the material: $p_0 = \sigma_Y$. As by definition $p_0 = P/A_R$, it results again that the real contact area is proportional to the normal load ($P = \sigma_Y A_R$).

Back to the friction laws

As we have just seen, both experimental measurements and models predict, for rough interfaces, the proportionality of P and A_R (Equation1.2). In addition, due to the rupture of the interface under shear at the transition between static and sliding contacts, the static friction force Q_s is also proportional to A_R. It thus becomes obvious that these observations can be considered as the origin of the linearity of the relationship between the static friction force Q_s and the applied normal load P. The friction coefficient, introduced by the first Amontons' law (see Equation 1.1), is just the mathematical translation of this proportionality.

1.2.3 Contact mechanics: single-asperity

Due to its small size, studying the friction behavior of a single micro-contact on a rough interface is extremely difficult, both experimentally and numerically. Thus, many studies in the literature are based on a simple approach, which consists of investigating friction in a model sphere/plane contact as a proxy for an individual micro-contact (see Figure 1.1(c)). This approach is not unreasonable because, locally, the contact between two antagonist asperities can be approximated by that of two elliptic paraboloids, which is exactly the case of Hertz's theory [26]. Then, the asperity/asperity contact can be reduced to a sphere/plane contact by using the equivalent radius and equivalent reduced modulus, as given below in Section 1.2.3 (Adhesionless normal contact) and Equation 1.4.

Note that, during the approximation of a real micro-contact by a smooth sphere/plane contact, much information may be lost, e.g. the complex multi-scale character of the roughness of the initial surfaces, the shear force induced by the non-coincidence of the apexes of the two contacting asperities, the proportionality between normal and friction forces, or the effect of the elastic interactions with neighbouring micro-contacts. Thus, going back to the initial problem is not always straightforward.

Nevertheless, there is a breadth of research into the field of contact mechanics on single-asperities under normal loading, starting from Hertz [26], where the frictionless non-adhering surfaces of linearly elastic spheres were considered, to theories that include adhesion, friction, and plasticity [27–29].

Adhesionless normal contact

The pioneer study in this area was presented by Hertz [26] where the frictionless normal contact of two elastic bodies of quadratic profile was considered (see Figure 1.5). Hertz determined the contact radius a of two spheres pressed in contact under load P as [30]:

$$a = \left(\frac{3RP}{4E^*}\right)^{1/3} \tag{1.4}$$

where $\frac{1}{R} = \frac{1}{R_1} + \frac{1}{R_2}$ and $\frac{1}{E^*} = \frac{1-\nu_1^2}{E_1} + \frac{1-\nu_2^2}{E_2}$, being R_1, R_2 the radii of curvature, E_1, E_2 the elastic moduli, and v_1, v_2 the Poisson's ratios associated with each body. This

analysis is in particular applicable to the contact of an elastic hemisphere and a rigid plane ($E_2 >> E_1$ and $R_2 >> R_1$).

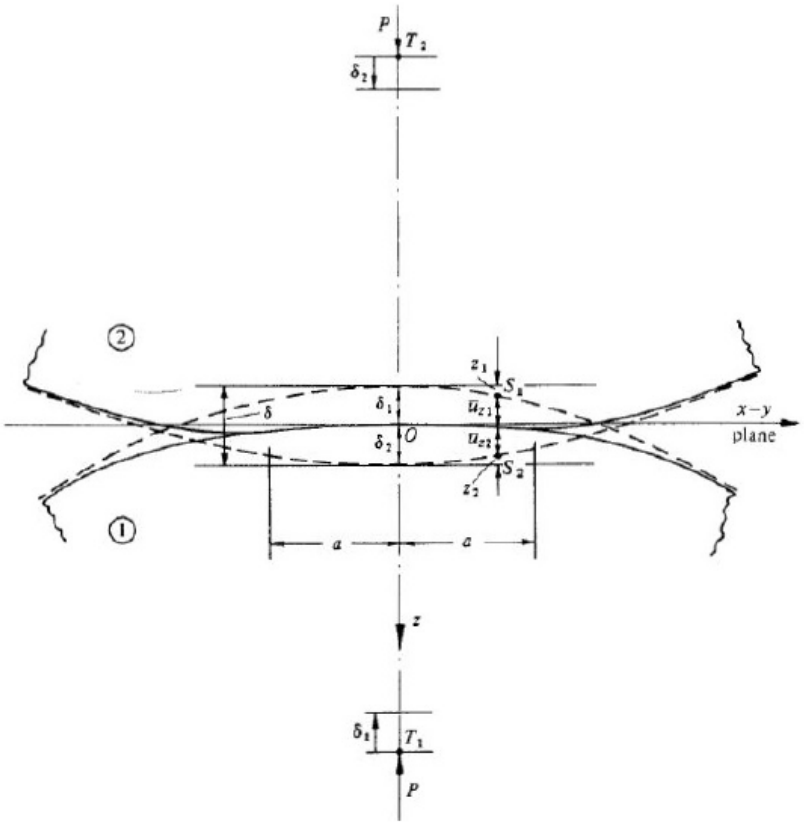

Figure 1.5: Sketch of the system considered in Hertz's theory (from [30]). Two initially circular solids with smooth surfaces are brought in unilateral contact by a normal load P. The remote displacements δ_1 and δ_2 induce surface displacements u_{z1} and u_{z2} such that a circular contact of radius a is formed.

Adhesive contact

A major improvement to Hertz's contact theory for elastic materials, proposed in two different models by Johnson, Kendall, and Roberts (JKR theory) [27] and by Derjaguin, Muller and Toporov (DMT theory) [28], was the consideration of attractive interactions (adhesion) that arise mainly from Van der Waals forces acting between two contacting surfaces [31].

JKR's theory assumes perfectly smooth surfaces, linearly elastic materials and attractive interactions acting only at very small gaps, *i.e.* within the real contact region. In this model (see Barthel [32] for a complete review), the attractive interactions introduce tensile stress near the contact edges while it is compressive at the centre. There is

a finite contact area at zero normal load P as well as a greater contact area compared to the Hertzian prediction under a given P. The JKR contact radius a expression is given by,

$$a = \frac{3R}{4E^*}\left(P + 3\omega_0\pi R + \sqrt{6\omega_0\pi RP + (3\omega_0\pi R)^2}\right)^{1/3} \tag{1.5}$$

where ω_0 is called the work of adhesion, that represents the work done to separate a unit area of the interface from contact to infinity.

The JKR theory also predicts a pull-off force, that is, a negative load needed to separate two surfaces from contact. That negative load has to overcome the action of adhesive forces between the surfaces in order to separate them, and it is related to the work of adhesion ω_0 by (for a pull-off procedure under imposed normal force):

$$P_{pull-off} = -\frac{3}{2}\omega_0\pi R \tag{1.6}$$

In contrast, DMT's theory assumes that the deformed contact profile remains the same as in Hertz's theory, but with additional attractive interactions outside the area of contact [28]. Their expression for the contact radius a is,

$$a = \frac{3R}{4E^*}\left(P + 2\omega_0\pi R\right)^{1/3} \tag{1.7}$$

and the pull-off force,

$$P_{pull-off} = -2\omega_0\pi R. \tag{1.8}$$

As we can see, the magnitudes of the pull-off force predicted by the JKR and DMT theories are different, although the scaling is the same. Then, *which theory is more suitable to explain the contact area dependence on the normal load?*

Tabor [33] pointed out that JKR and DMT theories are valid at the two extreme values of a parameter λ (Tabor parameter), that measures the impact of the interaction stresses on the surface deformations, and is given by [32]:

$$\lambda = \frac{\sigma_0}{\left(\frac{\omega E^{*2}}{\pi R}\right)^{1/3}} \tag{1.9}$$

where σ_0 is the amplitude of the attractive interaction stresses. Then, JKR theory describes compliant and adhesive materials for which λ is large and DMT theory describes stiff and weakly adhesive materials with small values of λ.

However, real situations are intermediate between these two extremes. A theory in this intermediate region, *i.e.* valid for a range of the Tabor parameter, was proposed by Maugis [34], which is a general case describing the contact, while both the JKR and DMT theories are special cases (see Figure 1.6).

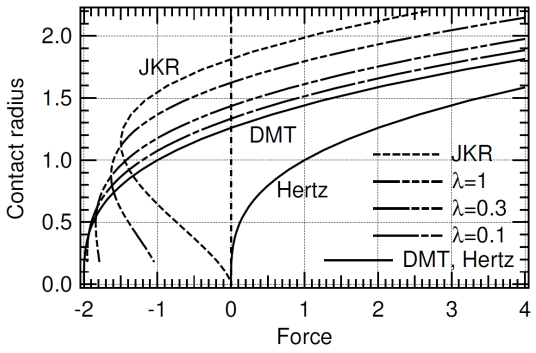

Figure 1.6: Evolution of the contact radius as a function of the normal force for Hertz, DMT, and JKR models. Maugis model with different values of Tabor parameter λ is also shown. Figure from [32].

1.2.4 Sheared contact in rough and single-asperity interfaces

A large part of the literature is concerned with contacts under purely normal load, while the case of sheared contacts has been much less investigated. And when that is the case, the pressure state is often supposed to be unchanged with respect to that in the normal loading case. Following the pioneer work of Cattaneo-Mindlin [35, 36], numerous models and experiments were proposed in the literature to expand these works toward more and more realistic cases. As we will see below, some of those studies try (i) to directly address the case of rough interfaces (see Figure 1.1 (b)) and others try (ii) to address the specific perfectly smooth sphere/plane contacts under shear (see Figure 1.1 (c)) always expecting, as it was the case for pure normal loading, that going back to the initial rough problem is possible.

Model approach for sheared interfaces

In addition to the contact problem under pure normal loading, the case of subsequent tangential loading was first addressed by the classical Cattaneo (1938) [35] and Mindlin (1949) [36] studies. They consider that the Hertz contact pressure is not affected by the application of a tangential load, which is a reasonable assumption in the case of elastomer/glass contacts, because the elastomer is incompressible and much softer than the glass. In these conditions, the normal/tangential decoupling is expected to be perfect. If the interface was fully stuck (no slip allowed), the shear stress field on the circular contact would diverge at the contact edges. Assuming a local Coulomb friction law, the contact edge is also a region of vanishing slip threshold. Both features indicate that, in reality, slip must occur at the contact periphery, as soon as the slightest shear force is applied to the contact. Slip thus initiates as a peripheral annulus, which will grow radially inward as the tangential load increases, with a size controlled by the value of the local friction coefficient μ [37]. The central stick zone thus shrinks progressively, until it completely disappears when macroscopic sliding sets in, *i.e.* when $Q = \mu P$ [30, 38].

Note that the Cattaneo-Mindlin model contains a physical inconsistency. Indeed, on the one hand, it is based on Hertz's theory, which considers a perfectly smooth contact. On the other hand, it assumes a local Coulomb's friction law, which implies that the macroscopic friction force is proportional to the normal load. The latter implication is at odds with $Q_s = \sigma A_R$ (Equation 1.3), which has been found to be valid for smooth sphere/plane contacts. Indeed, due to the non-linearity between P and A_R in Hertz's theory, Equation 1.3 is incompatible with a proportionality between Q_s and P. Then, Cattaneo and Mindlin do not seem to be usable to model perfectly smooth sphere/plane contacts under shear.

In the last decades, more adequate models have been developed by the rough contact mechanics community in two main directions (see Vakis et al. [8] for a recent review).

First, asperity models in which the contact interface is divided into well-defined micro-contacts actually carrying the normal and tangential loads applied to the contacting solids (Braun and Röder [39], Ciavarella, Delfine, and Demelio [40], and Violano

and Afferrante [41]). Each micro-junction is ascribed a set of individual properties (*e.g.*, its height, radius of curvature and friction coefficient) necessary to apply some assumed behaviour laws (*e.g.*, any contact (Johnson [30]) or friction law (Bot et al. [42])) when submitted to an external stimulus. The macroscopic behavior of the interface is then the emerging collective response of the population of micro-contacts (Trømborg et al. [43], Braun and Peyrard [44], and Costagliola, Bosia, and Pugno [45]).

Second, the contact, with adhesion, of a sphere and a half-space in which there is both normal and tangential loading was first considered by Savkoor and Briggs [46]. They use a combination of linear elastic fracture mechanics (LEFM) and contact mechanics, extending JKR theory (mode I) to tangential forces (mode II/mode III). They found that, as a result of increasing the tangential load, the surfaces tend to peel apart, and hence, the contact area decreases progressively. In their model, however, they did not account for frictional resistance as the contact evolves and have underestimated the interfacial toughness, which is the resistance to crack growth along an interface. This led to an overestimation of the reduction of the contact area with increasing tangential force. For many interfaces, it has been observed an increase of the interfacial toughness under mixed modes due to various phenomena such as friction, plasticity, etc [47]. Then, this mode combination effect has been accounted for by various models [48–53] in which an empirical Mode-Mixity Function (MMF) $f(\psi)$ [54] is introduced to tune the interaction modes:

$$G_c = f(\psi) G_{Ic}, \tag{1.10}$$

where G_c is the critical energy release rate, G_{Ic} is the mode I critical factor (or surface energy in Griffith's concept) and ψ is the phase angle that defines the ratio of mode I and II loading, defined as

$$\psi = \arctan\left(\frac{K_{II}}{K_I}\right), \tag{1.11}$$

where K_I and K_{II} are, respectively, the stress intensity factors in mode I and mode II (along the shearing direction).

$$K_I = \frac{P_H - P}{2a\sqrt{\pi a}}, \quad K_{II} = \frac{Q}{2a\sqrt{\pi a}}, \tag{1.12}$$

where $P_H = 4E^* a^3/3R$ is a compressive Hertzian load, with a denoting the radius of the contact area and Q the tangential force.

The three most popular versions of such a model in the literature [49, 52, 54] have a similar quadratic form at low K_{II}/K_I for the function $f(\psi)$:

$$f(\psi) \simeq 1 + (1-\lambda)\psi^2 + O(\psi^4) \tag{1.13}$$

where $0 \leq \lambda \leq 1$ is an empirical parameter. $\lambda = 1$ is the uncoupled limit mode with no effect of the tangential load on the contact area upon shearing. $\lambda = 0$ corresponds to the "ideally brittle" fracture of Savkoor and Briggs [46] model. λ can be adjusted to find the best agreement with the observed area decrease with the tangential load.

From all previous equations, the fundamental equation that governs the contact area reduction while the shear load is increased, for any mode-mixity function $f(\psi)$ can be expressed as:

$$P = \frac{4E^* a^3}{3R} - \sqrt{8\pi E^* G_{Ic} a^3 f(\psi) - Q^2}. \tag{1.14}$$

From Equation 1.14, it is now possible to predict the real contact area during the shearing of a sphere as function of the normal force P. Figure 1.7 presents the results for three different versions of the $f(\psi)$ function.

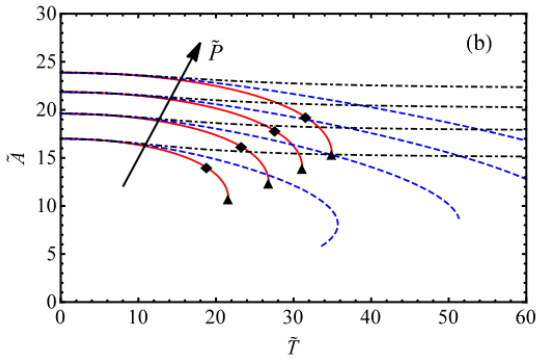

Figure 1.7: Evolution of the normalized contact area $\tilde{A}$ as a function of the normalized shear load $\tilde{T}$ for different normalized normal loads $\tilde{P}$ using three different versions [49, 52, 54] of the $f(\psi)$ function in Equation 1.14 (lines with different colors). Figure from [52].

So far, in the literature, LEFM-based models have been shown to quantitatively reproduce experimental results on the decay of the contact area under mixed-mode loading, and also to reproduce the anisotropic properties of the area changes. However, the overall contact area evolution depends on the MMF form [48–53]. Due to the same lack of understanding of the mode mixity, other adhesion models, like the numerical ones of Mergel et al. [55], Salehani, Irani, and Nicola [56], and Mergel, Scheibert, and Sauer [57] or the theoretical one of McMeeking et al. [58], also require *ad hoc* descriptions of the local interfacial behavior under coupled normal and tangential loading. More recently, adhesionless models based only on hyper-elasticity, to better account for the high deformation in elastomers, also have been suggested [57, 59, 60] and they will be discussed in further detail in Chapter 3.

To date, there is no universally accepted friction model for sheared elastomer contacts, and the different modeling strategies mentioned above do not always converge towards a unified vision of the mechanisms responsible for the area reduction/shrinkage observed in experiments. However, they may not all be equally relevant for all loading ranges. Indeed, one can easily imagine that the respective weights of the various mechanisms possibly involved (adhesion, large deformation, etc.) can vary according to the applied load.

Sheared interface experiments

While there are many theoretical models, the literature remains very poor on the experimental side. In the following, we will restrict our overview of the experimental literature to elastomeric sheared interfaces using PDMS (Polydimethylsiloxane), because they represent the central point of this study.

In the first set of experiments, performed by Chateauminois, Fretigny, and Olanier [61] and Prevost, Scheibert, and Debregeas [62], the authors studied the local transition to sliding by performing *in-situ* strain field measurements during shearing of an elastomeric interface. In the second set of experiments, performed by Waters and Guduru [49], Mergel et al. [55], and Sahli et al. [63], the authors study the area reduction that occurs during shearing of elastomeric interfaces and that was first experimentally demonstrated by Savkoor and Briggs [46].

Chateauminois, Fretigny, and Olanier [61] performed torsional friction experiments using an experimental setup, sketched in Figure 1.8(a), where a rigid glass sphere contacting a soft PDMS substrate was rotated around its symmetry axis. The use of torsion to shear the interface allows reducing the viscous effects. Indeed, in steady torsional sliding, the strains in the PDMS are time invariant.

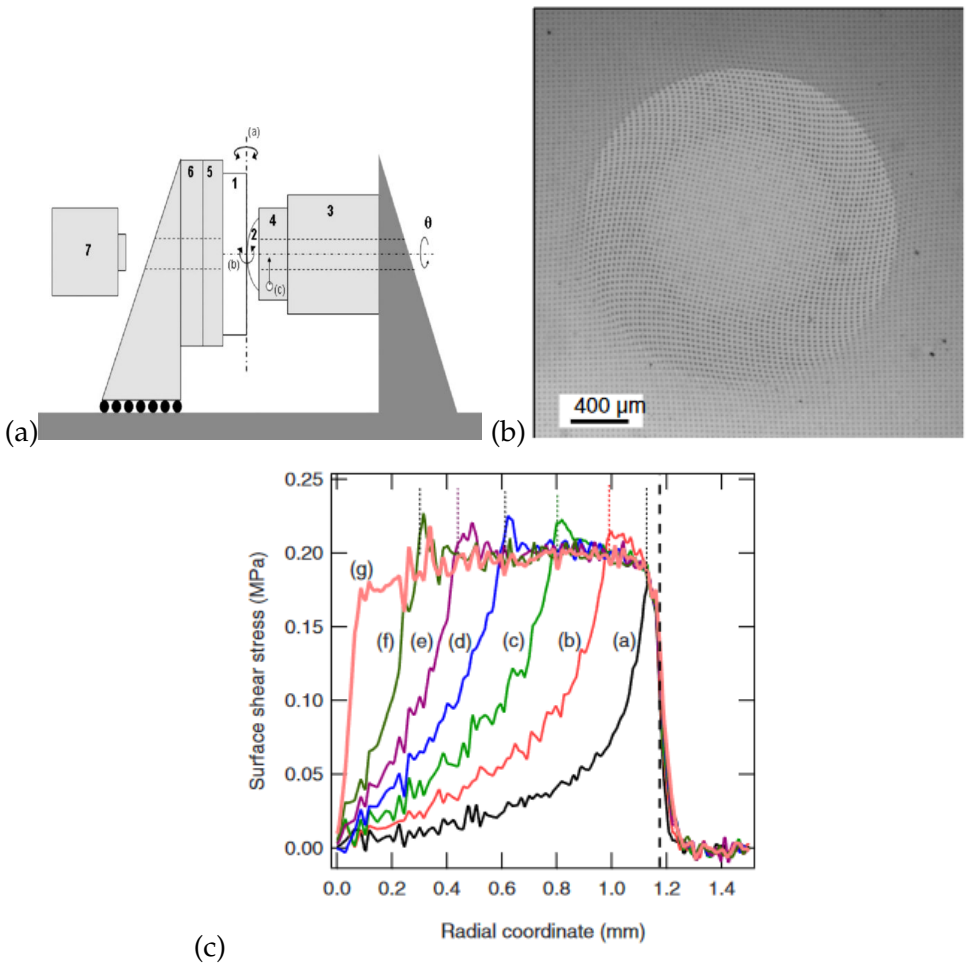

Figure 1.8: (a) Schematic description of the torsional contact apparatus. (b) Image of a twisted contact between a glass sphere and a PDMS substrate during stiction. (c) Orthoradial surface shear stress profiles obtained from the inversion of the measured surface displacement field at different stages of the stiction process. The large dotted line delimits the contact zone. Small dotted lines indicate the location of the adhesive zone. Figures from [61].

In order to monitor contact-induced surface displacements, a square network of tiny cylindrical holes (diameter 8 μm, depth 11 μm, and center-to-center spacing 40 μm) was created on the PDMS surface using standard microlithography procedures (see Figure 1.8(b)). The in-plane displacements were then measured by following the displacement of each cylindrical hole on the surface of the PDMS as a function of the twist angle. It was then shown that a micro-slip occurs in an annulus near to the contact

edge while a central circular contact zone stays in adhesive contact (see Figure 1.8(b)). During the stiction regime, the inner radius of the micro-slip annulus shrinks until it invades the entire contact region. Throughout the stiction process, no change in contact size was observed. Typical orthoradial shear stress distributions, obtained using an inversion of the displacement fields, are shown in Figure 1.8(c) at various stages of the stiction process.

Prevost, Scheibert, and Debregeas [62] investigated the micro-mechanics of a sheared multi-contact interface between a smooth rigid sphere and a flat but rough elastomer block using the experimental set-up sketch shown in Figure 1.9(a).

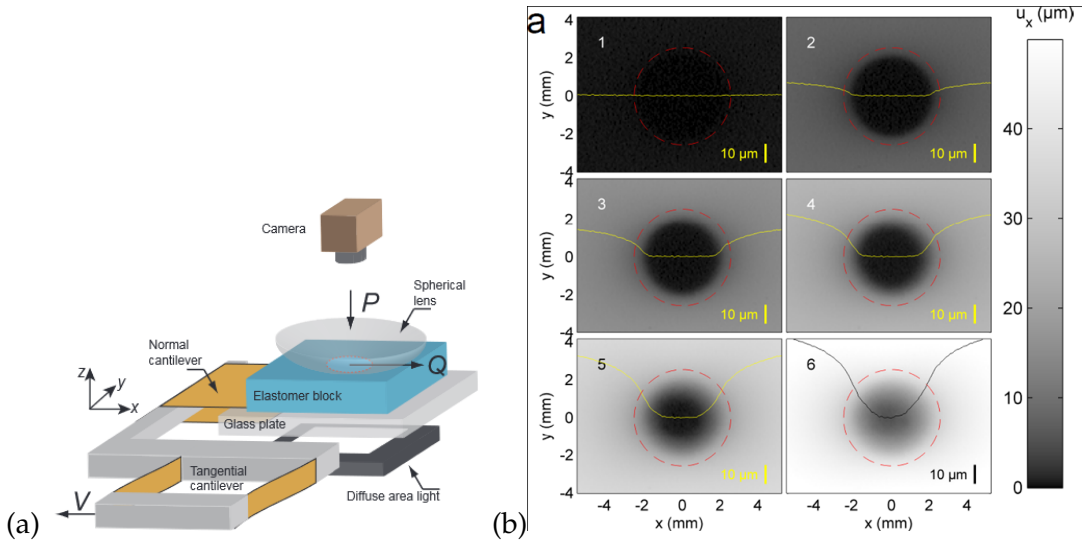

Figure 1.9: (a) Sketch of the experimental setup and (b) snapshots of the 2D displacement fields u_x in gray scale at $P = 0.5\,\mathrm{N}$. Red circle is contact area and yellow lines are cuts of the displacements fields at $y = 0$. Figures from [62].

The in-plane elastomer deformation was then observed during the incipient sliding, *i.e.* during the transition between static and sliding regimes. They could determine the displacement fields by image correlation between time t with a reference at $t = 0$ (no tangential force). Figure 1.9(b) shows the typical u_x (along the shear direction) displacement field under $P = 0.5\,\mathrm{N}$ at 6 different instants during the incipient tangential loading. Also here, as soon as Q increases, an annular slip region, in coexistence with a central stick region, is found to progressively invade the contact, up to the moment where this stick region vanishes marking the onset of the macroscopic sliding phase. They could compare quantitatively those fields with the predictions of the Cattaneo-Mindlin model. The agreement was quantitatively satisfactory, without any adjustable

parameters. However, systematic second order deviations were found, related to the presence of small scale roughness at the surface of the elastomer block and not accounted for in such a simple model. Note that in this experimental configuration, *i.e.* a rigid sphere on a soft plane, the strains in the PDMS are constantly evolving under the steady sliding rigid sphere. Therefore, viscous effects can play a role in the mechanisms involved at the interface.

Waters and Guduru [49] performed shearing experiments using a microtribometer, shown in Figure 1.10(a), to study the adhesive contact of a glass sphere and a smooth PDMS plane for tensile and compressive normal loadings, in the millinewton range, while continually recording images of the contact area evolution. Figure 1.10(b) shows their results for tangential loading T *vs* time for a range of normal loads and the evolution of the contact area for tensile (1-4) and compressive (A-D) normal loadings.

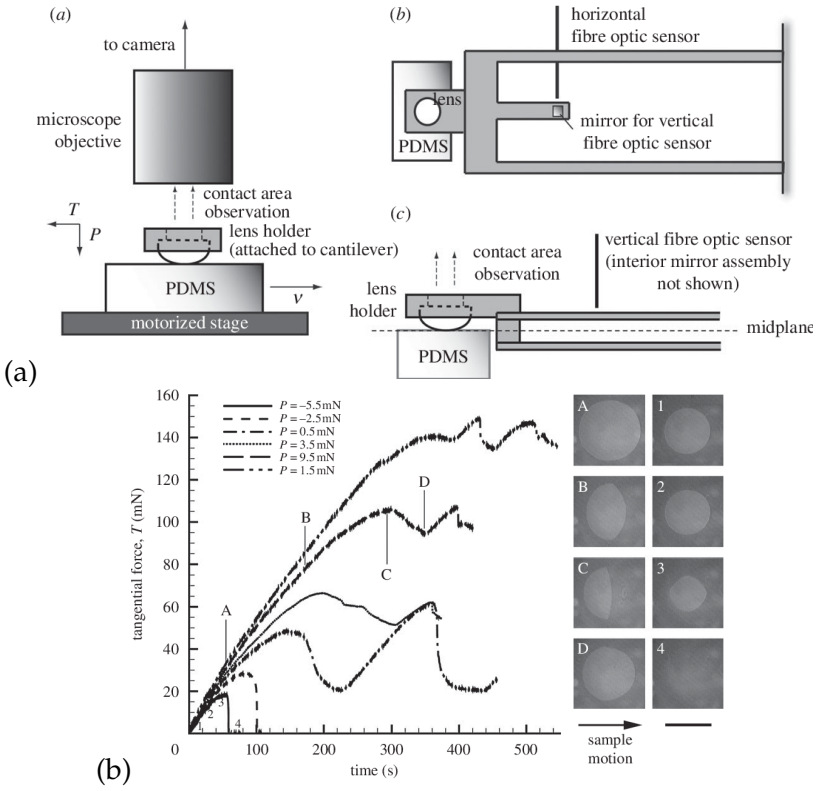

Figure 1.10: (a) Sketch of the experimental setup. (b) Evolution of tangential force *vs* time at various constant normal loads, and contact area images (1-4) for tensile normal loading ($P = -5.5\,\text{mN}$) and (A-D) for compressive normal loading ($P = 9.5\,\text{mN}$). In the images, sample motion relative to the spherical indenter is from left to right. Scale bar: 1 mm. Figures from [49].

The authors observed that under tensile loading, the contact area reduces axi-symmetrically and remains circular until separation at a critical tangential load. In contrast, under compressive loading, after a phase of symmetric peeling, the contact area becomes

asymmetric with significantly more peeling occurring at the trailing edge of the contact compared to the leading edge.

More recently, Sahli et al. [17] and Sahli [64], using an experimental set-up similar to that of [62] (see Figure 1.11), carried out shearing experiments for contacts between a glass plate and a smooth (single asperity) or a rough (multiple asperity) PDMS samples under large compression in the newton range.

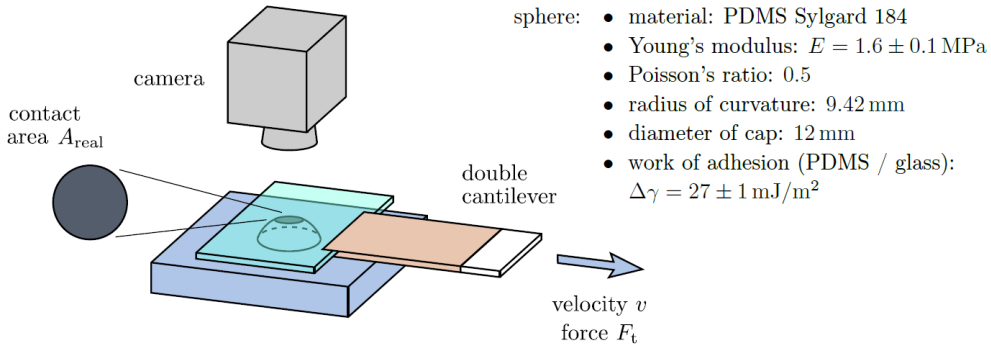

Figure 1.11: Sketch of the experimental setup for shearing experiments on a glass plate and an elastomer sphere used in Sahli et al. [17] and Sahli [64] and Mergel et al. [55]. Figure from [55].

Then, by analyzing the real contact area A_R evolution in a rough interface sheared toward macroscopic sliding, the authors found that A_R decreases by up to approximately 30 % (multi-contact) when the tangential force Q reaches its peak value (see Figure 1.12). And, as can be seen in Figures 1.12 and 1.13(b), the reduction starts as soon as Q starts increasing and continues until the macroscopic sliding regime is established, in which A_R remains nearly constant around its minimum.

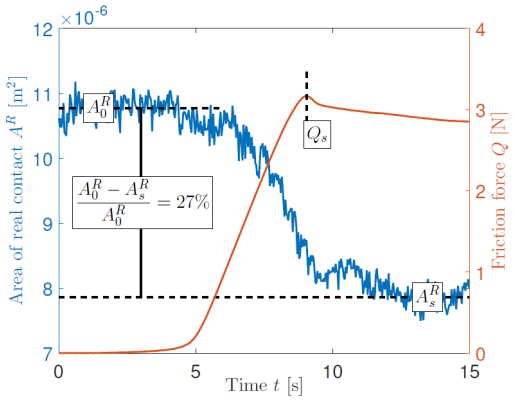

Figure 1.12: Typical evolution of the real contact area (blue) and the tangential force (red), of the multi-contact interface between a rough elastomer and a smooth glass substrate, as a function of time. Figure from [17].

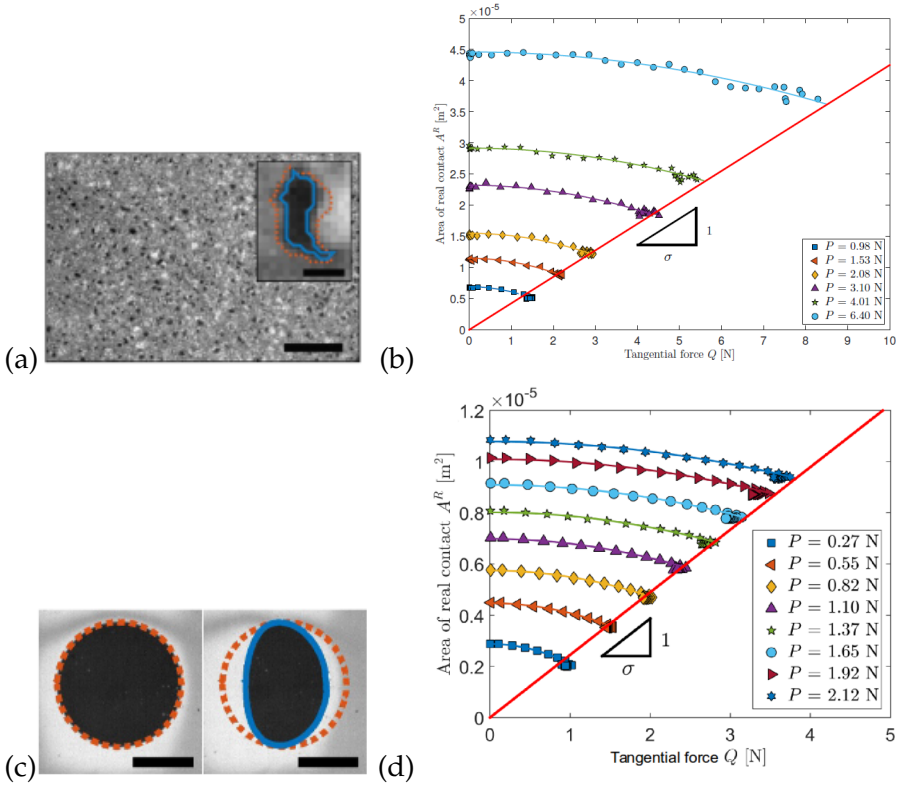

Figure 1.13: (a) Multi-contact interface between a rough PMDS and a smooth glass plate. The inset shows a zoom-in on a micro-asperity where the red line (resp. blue line) corresponds to the contour for no tangential force ($Q = 0$) (resp. under shear, at the onset of sliding Q_s). Scale bar: 100 μm. (b) A_R *vs* Q for the interface showed in (a) submitted to various normal loads P. (c) Images of a sphere/plane contact for $P = 0.55$ N, showing on the left $Q = 0$ and on the right $Q = Q_s$. Scale bars: 1 mm. (d) A_R *vs* Q, for the interface showed in (c). Figures from [17].

By analyzing the behavior of individual asperities, they also showed that such a macroscopic reduction originates from the reduction of each asperity, shown in the inset of Figure 1.13(a), where the red line (resp. blue line) corresponds to the contour for no tangential force ($Q = 0$) (resp. under shear, at the onset of sliding Q_s). Indeed, each asperity has a behavior similar to the one of a single sphere/plane contact (see Figures 1.13(c) and (d)).

Then, by plotting A_R as a function of Q (Figures 1.13(b) and (d)) for both single- and multi-contacts (Figures 1.13(a) and (c)), they were able to propose two laws:

- an empirical quadratic law of the form, $A_R = A_0 - \alpha_A Q^2$, to describe the contact area reduction. The rate of the decrease is thus quantified by the parameter of reduction, α_A, being A_0 the initial real contact area;

- a threshold law, $Q_s = \sigma A_s$, to characterize the interface shear strength, σ. The interface shear strength is deduced from the experimental data by fitting with a

linear expression the position of the tangential force peak Q_s at different normal forces in a $A = f(Q)$ diagram, where A_s is the corresponding real contact area to Q_s (see red lines in Figures 1.13(b) and (d)).

These laws have been shown to be relevant regardless of the applied normal force (valid on more than four orders of magnitude) and the type of the interface (rough or smooth), as shown in Figure 1.14, where α exhibits a power-law behavior over four decades as a function of the initial contact area A_0, *i.e* as a function of the initial normal load. Note that in this figure, the authors have concatenated data coming from single sphere on plane experiments (at large A_0) and from the analysis of the behaviour of micro-contact in a rough interface (at small A_0).

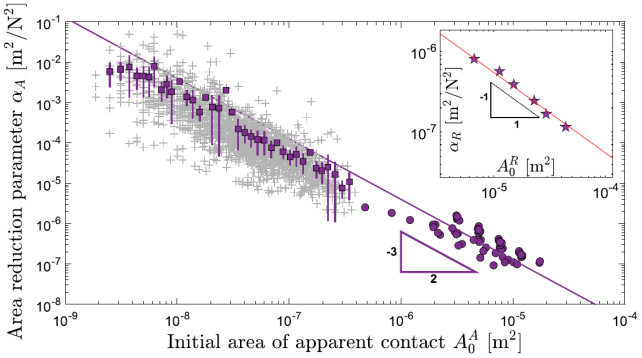

Figure 1.14: Area reduction across scales: α_A *vs* A_0 (PDMS/glass interface). Circles: sphere/plane contacts. V = 0.1 mm/s. +: raw data for micro-junctions within multi-contacts (*rms* roughness 26 μm). Squares: average of the data divided into 40 classes. Bars show the standard deviation within each class. Line: guide for eyes with slope -3/2. Inset: α_R *vs* A_0 for the same multi-contacts. Inset line: guide for eyes with slope -1. Figure from [17].

Later, using the same experimental set-up as Sahli et al. [17] (see Figure 1.11), Mergel et al. [55] performed shearing experiments on the onset of sliding of a smooth glass plate on a smooth PDMS sphere under small normal loads (from -1 mN to 8 mN). Their results about the typical behavior of shearing elastomers are shown here in Figure 1.15: (a) the tangential load increases, first almost linearly and then with a weakening slope, reaches its maximum (the static friction peak), and then rapidly decreases before entering a macroscopic sliding; (b) the contact area reduces as the interface is progressively sheared up to reach a macroscopic sliding and remains stable. And, in agreement with Waters and Guduru [49], contacts with the smallest initial areas (small normal load) immediately vanish when sheared, before entering a macroscopic sliding.

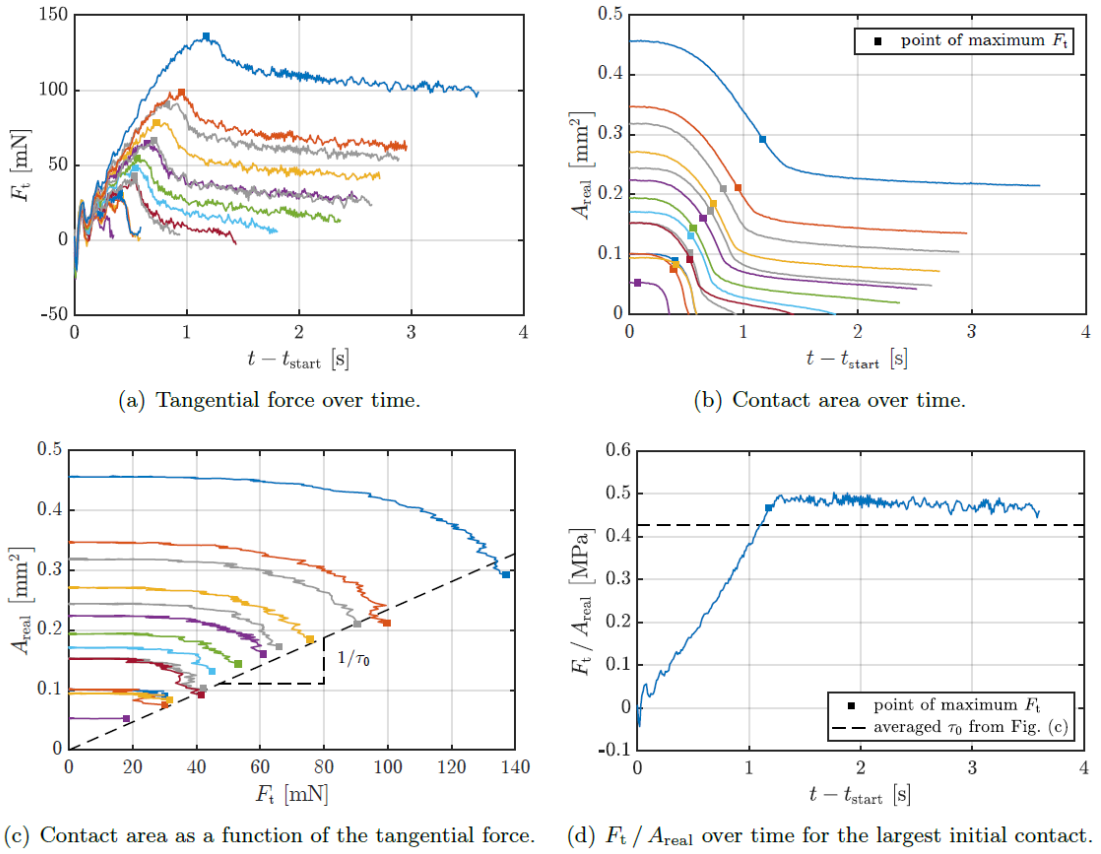

(a) Tangential force over time.

(b) Contact area over time.

(c) Contact area as a function of the tangential force.

(d) F_t / A_{real} over time for the largest initial contact.

Figure 1.15: Friction force (noted F_t) and real contact area (noted A_{real}) measured under low normal loads for the onset sliding of a interface between a glass plate and an elastomer sphere. Each color corresponds to a different initial contact area. The square markers indicate the moment of the tangential force peak. t_{start} is the instant when the motor starts to move at velocity $V = 0.1\,\mathrm{mm/s}$. Figure from [55].

In Figure 1.15(c), they find a good agreement with the threshold law proposed by Sahli et al. [17] on identical smooth sphere/plane contacts, but for large normal loads ($> 0.27\,\mathrm{N}$), that is, the friction force and the contact area are proportional to each other. This finding is also consistent with experiments on rough contacts involving soft materials [15, 17, 23]. However, they report experimental results in which the decay of the contact area is not quadratic for the entire range of observations and thus does not follow the empirical relation proposed by Sahli et al. [17]. Their findings indicate that the classical law by Coulomb and Amontons (with a linear dependence between the normal and tangential loads) is not applicable for strong adhesion or small roughnesses. In this case, the friction force is also affected by an additional adhesion term.

Finally, all the experimental studies presented in this section have some limitations to investigating the contact area evolution that can be highlighted:

- they are concentrated in different normal force ranges (either large or small), thus leaving an intermediate gap that has not been investigated (see Chapter 4);
- they have been performed in different experimental conditions, making a quantitative comparison between experiments, theory, and simulations even more complicated;
- the setup of most recent experimental studies does not allow direct measurements of the resulting normal force, which is only known initially (dead weight) [17] or estimated from the initial contact area using JKR theory [55] (see Chapter 2)
- they are limited to constant normal loading (see Chapter 5);
- their experimental optical observations do not provide insight into what occurs within the contact area, *i.e.* the local origin of the mechanisms of contact area variation (see Chapter 3).

1.3 Objectives and contents of the thesis

Despite the great progress that has been made in the last decades in the fundamental understanding of friction, in particular the mechanics of adhesive contacts subject to tangential forces, there remains a lot to explore, mainly due to the complexity of friction associated with the phenomena involved. Thus, the main objective of this thesis is to deepen the understanding of the onset of dry sliding elastomeric contact with a focus on the analysis of a model sphere/plane interface. All upcoming analysis will thus be based on a model sheared experiment of a smooth PDMS sphere on a glass plane with simultaneous monitoring of the normal and tangential force and *in-situ* visualization of the real contact area.

In a specific approach, an attempt will be made to bring the sphere/plane model towards more realistic contact mechanics. As illustrated in Figure 1.16, and previously mentioned, real surfaces contain irregularities of various orders, which cause contact to occur at discontinuous contact spots, that is, between their asperities. Then, the first specific objective will be (i) to identify the fundamental mechanisms that play a role during single-asperity shearing under constant normal loading. Additionally, such asperities can have different heights, which causes the contact spots to be subjected to

different local normal loadings, ranging from millinewtons to newtons. The second specific objective will consist (ii) of exploring the behavior of a sheared interface over a wide range of normal loadings. Furthermore, due to the slope of the asperities, the contact spots can be submitted to local normal loading variations, and this is the third specific objective, *i.e.* (iii) to study the influence of the normal loading trajectory.

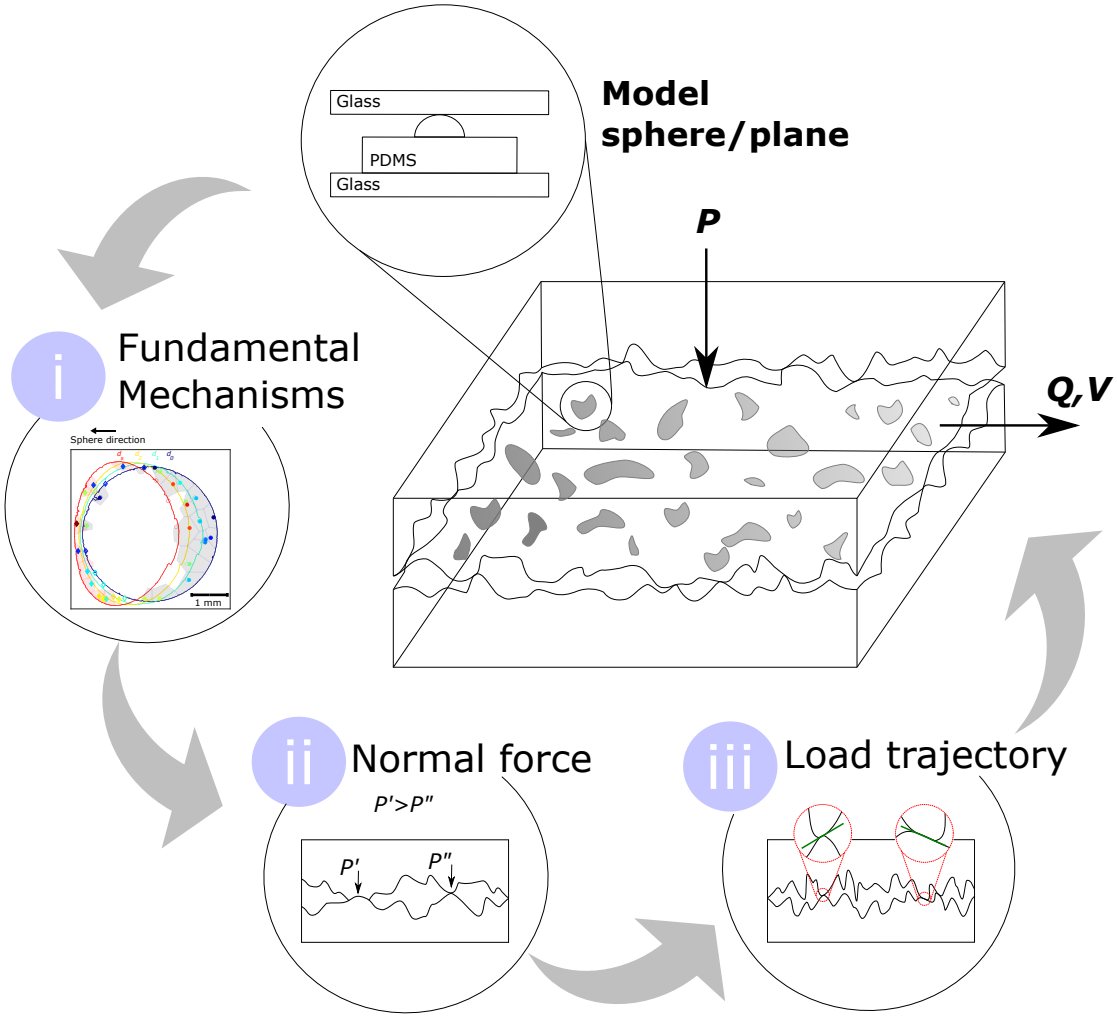

Figure 1.16: Graphical overview of the specific objectives of this thesis.

To achieve these objectives, this thesis is organized as follows:

Chapter 2 introduces in detail the equipment used to conduct the experimental study of the shear-induced behavior of elastomer/glass contacts, the details about the materials used, and the experimental procedures and techniques.

Then, in order to identify the elementary mechanisms and their effects on the contact area reduction, Chapter 3 presents an original experiment on an elastomer/glass

interface, similar to those of Sahli et al. [17, 63], but allowing *in-situ* access to the interface displacement field. The strategy is based on the incorporation of particles near the surface of the elastomer and on their use as local motion tracers of the frictional interface during the onset of tangential loading. The relevance of the detected mechanisms is compared with a non-adhesive model that shows a quantitative agreement with recent large-load experiments, with no adjustable parameters.

Chapter 4 is dedicated to improve the understanding of shear-induced area reduction over a wide range of normal loadings by describing the features of model sphere/plane experiments, from millinewtons up to newtons, in terms of contact area morphology, area reduction parameter, and interfacial shear strength. Thereby, covering, in one work, the ranges of normal load available in the literature data and bridging the gap between them.

Chapter 5 addresses the influence of the loading trajectory. In particular, the variation of the normal load during shearing is investigated.

Finally, Chapter 6 concludes this thesis with some important highlights obtained in previous chapters and presents some prospects for future work.

Chapter 2

Experimental methods

As we have seen in the last chapter, for a better understanding of the elementary mechanisms in sliding contacts of macroscopic bodies, it is important to characterize the interface. In this context, the present study considers the sliding contact of a sphere and a plane, under normal load, as a model for the contact of a single asperity with a rough interface. To do this, model experiments were performed on an optomechanical instrument, sketched in Figure 2.1, that enables monitoring the interface by *in-situ* optical measurements, while measuring normal and tangential forces.

This chapter introduces in details: (i) the materials involved in the model interfaces, (ii) the setup used to carry out the experimental study of the properties of sheared contacts, and (iii) some of the experimental procedures and techniques used to analyse the data.

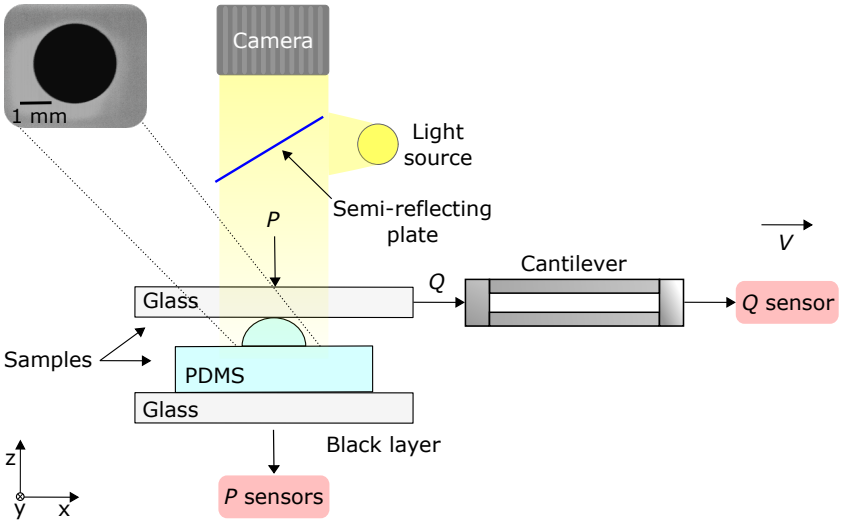

Figure 2.1: Sketch of the optomechanical instrument. P is the applied normal force, Q is the tangential force, and V is the motor translating velocity. The instrument is also presented in more detail and in a more realistic view in Figure 2.4.

2.1 Samples

To guarantee the required transparency in the optomechanical instrument that allows *in-situ* observation of the real contact area, two transparent samples are used, a glass substrate and an elastomer. Note that the refractive index of the glass (~ 1.50 [65]) and of the elastomer (~ 1.40 [66]) are quite similar, so that refraction effects at the PDMS/glass interface are expected to be negligible.

2.1.1 Glass substrate

Smooth bare glass plates (Mirit Glass) with dimensions $46\,\text{mm} \times 38\,\text{mm} \times 5\,\text{mm}$ are used both as a slider and as the bottom support for the PDMS samples (that will be described in Section 2.1.2). The glass roughness is considered as negligible as it is several order of magnitude lower than the PDMS sphere radius of curvature.

Before use, the glass surface is gently mechanically pre-cleaned with distilled water using a lens cleaning tissue. Then, it is sonicated in three different baths, each for 15 min, in the following order: (i) soapy water ($\sim 5\,\%$ solution of Decon 90 with water), (ii) ethanol, and (iii) distilled water. Between the baths, the glass is rinsed in distilled water to avoid cross-contamination. Finally, it is dried in an oven (Prolabo, Astel) at 90°C for 15 min. This process ensures a clean glass surface by removing dust and organic contaminants. It also ensures a good adherence of the PDMS/glass in the production of PDMS samples (Section 2.1.2).

2.1.2 Elastomer samples

The elastomer used is a cross-linked PolyDiMethylSiloxane (PDMS, kit Sylgard 184, Dow Corning) known for its elastic behavior with a Poisson ratio of $\sim$0.5 (incompressible), chemical inertness, mold-release properties and ability to replicate features down to the nanoscale, with low shrinkage during cure (around 1 %) [67–69].

The PDMS samples are prepared as follows. The two components, elastomer base and curing agent, are mixed in a weight ratio of 10:1, respectively, and degassed in a desiccator under vacuum to remove air bubbles introduced during mixing. Next, two different types of samples are molded:

- **Sample of the type S1R9:** PDMS samples with a single sphere (S1) of a radius of curvature of 9.42 mm (R9). For this type of sample, a plano-concave glass lens, with a radius of curvature of 9.42 mm (45-014, Edmund Optics) and a roughness of the order of a nanometer, is placed at the bottom of a cylindrical cavity (11 mm of height and 30 mm of diameter) coated with an aluminum foil, as illustrated in Figure 2.2(a). The aluminum foil (not illustrated) is used to assist in the demolding process. Then, the cavity is filled with the PDMS mixture, Figure 2.2(b), covered with the glass plate (46 mm$\times$38 mm$\times$5 mm), Figure 2.2(c), and cured at room temperature for 48 h. After, the PDMS sample is demolded by carefully raising the tip of the aluminum foil causing the cavity to be removed. And at last, with the aid of a scalpel, the PDMS sample is cut around the lens to remove any excess of PDMS and to ensure that the sphere is indeed the highest point in the sample (*i.e.* the unique contact point in the upcoming contact experiments). The final configuration is a cylindrical-like shape attached to a glass plate with a height of 6 mm, the top of which features a spherical smooth cap with a radius of curvature of 9.42 mm with a summit 2 mm higher than the top surface of the cylinder-like, Figures 2.2(d) and (e). As for the glass plate, the roughness of the PDMS sphere is negligible as it is of the order of a nanometer (the roughness of the lens). This process maintains the attachment of the PDMS to the glass by Van der Waal's bonds [70] and preserves the required transparency of the samples. The PDMS/glass interface is completely invisible.

- **Sample of type S1R9P:** PDMS sample with a single sphere (S1) of radius of curvature of 9.42 mm (R9) and a layer of particles (P). The objective here is to introduce a layer of particles that will be used to estimate the displacement field at the interface by a tracking method (see Section 3.2.2). This layer of particles must be as thin as possible to avoid 3D effects and as close as possible to the interface. However, it must also not be precisely at the interface to avoid modifying its frictional behaviour. Thus, for this type of sample, the cross-linking is performed in two steps. In the first step, a drop of PDMS mixture is poured into the plano-concave glass lens with a radius of curvature of 9.42 mm (the same as for sample

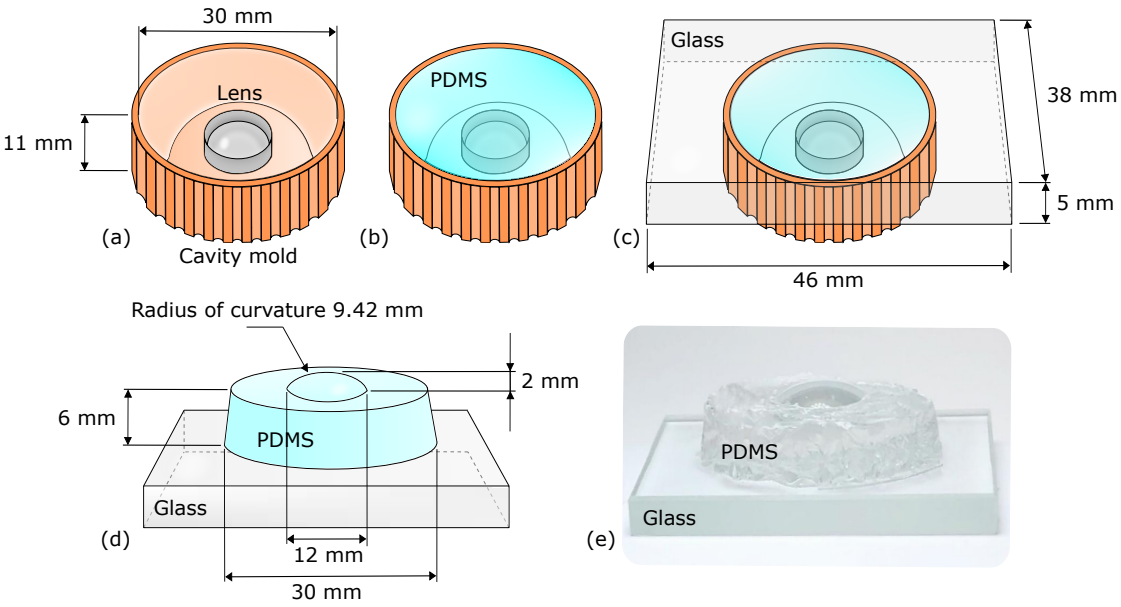

Figure 2.2: Sketch of sample of type S1R9 preparation. (a) A plano-concave glass lens is placed at the bottom of a cylindrical cavity coated with an aluminum foil (not illustrated), (b) the cavity is filled with a PDMS mixture, and (c) a glass plate is used to cover the cavity. (d,e) The final configuration is a cylinder-like shape PDMS sample attached to a glass plate with a spherical cap on top.

of type S1R9) , Figure 2.3(a). Then, the drop is spin-coated (SPIN 150, Spincoating) for 30 s at 2500 rpm, Figure 2.3(b), and cured in an oven (Prolabo, Astel) at 80°C for 20 min, to obtain a thin cross-linked PDMS layer of approximately 16 μm in thickness. The exposed surface of this layer is then sprinkled with silver particles, Figure 2.3(c), obtained from drying a silver-based coating (Electrodag 1415 M, Agar Scientific) diluted in acetone. The second step follows the same molding and demolding procedure as previously described for sample of type S1R9, except that a coated lens is used. Finally, with the exception of a layer of particles located $\sim$16 μm from the surface of the spherical cap, the sample is very similar to the sample of type S1R9 in terms of shape, see Figure 2.3(d).

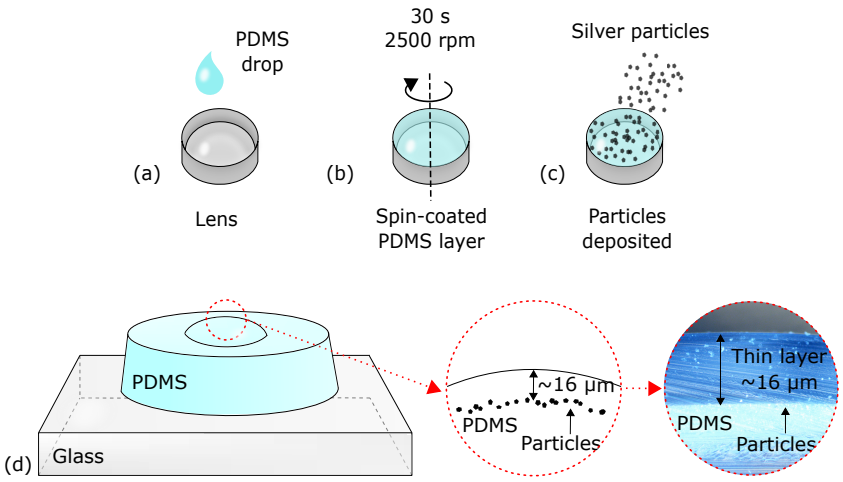

Figure 2.3: Sketch of sample of type S1R9P preparation steps. First, (a) a drop of PDMS mixture is poured into a plano-concave glass lens, (b) spin-coated and (c) cured in an oven at 80°C for 20 min to obtain a thin cross-linked PDMS layer which is sprinkled with silver particles. Second, the same preparation procedure as for sample S1R9 is used in Figure 2.2 using the coated lens. (d) The final configuration is the same as for sample of type S1R9, except for a layer of particles located $\sim$16 μm from the surface of the spherical cap.

2.2 Optomechanical test

2.2.1 Instrument overview

A custom-built experimental setup was used to carry out the optomechanical tests. The instrument is an upgrade from those used in [17, 53, 55, 63] and is shown in Figure 2.4. The main improvements include replacing the single cantilever beam with a double one, adding force sensors to measure the normal load, and adding goniometers to ensure the alignment (i) between the top sample plane and the direction of the motorized translation and (ii) between the top and bottom sample. This new setup integrates the following systems:

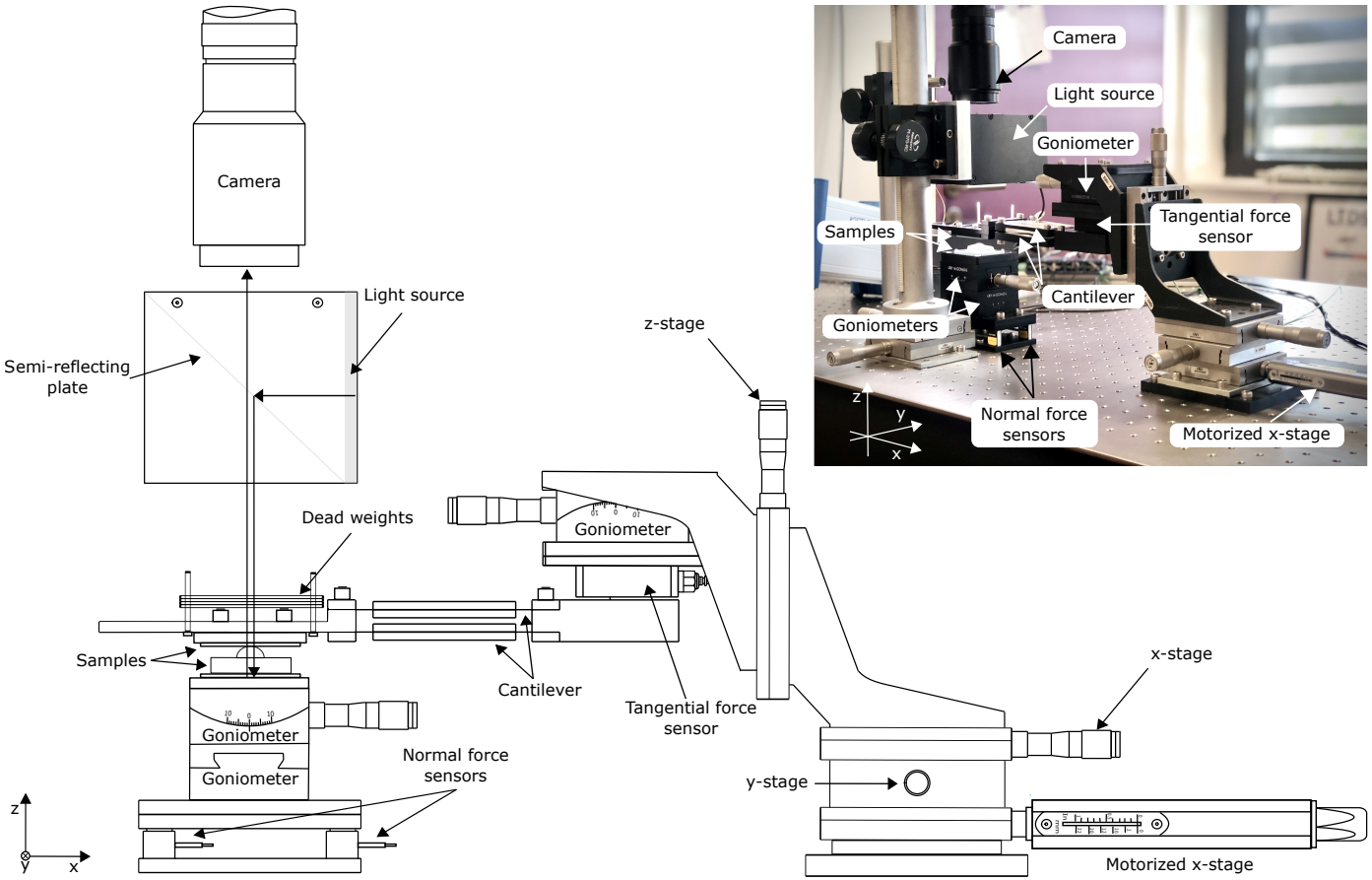

Figure 2.4: Optomechanical instrument. A PDMS sample is fixed to an optical table, while a glass plate is attached at the free extremity of a double cantilever and is driven at a constant velocity V by a motorized x-stage. Tangential force is measured by a force sensor located at the fixed extremity of the double cantilever and normal force is measured by four force sensors located between the optical table and a sample attachment. The contact interface is illuminated from the top and imaged in reflection with a camera. An inverse configuration (glass fixed and PDMS slid, see Figure 2.5) is also allowed since the glass plate onto which the PDMS sample is crosslinked and the glass plate used as a slider are identical. The inset shows a real picture of the instrument to aid in visualization

(i) Sample attachment system: in the sample attachment system two configurations are possible, a normal and an inverse, as illustrated in Figure 2.5.

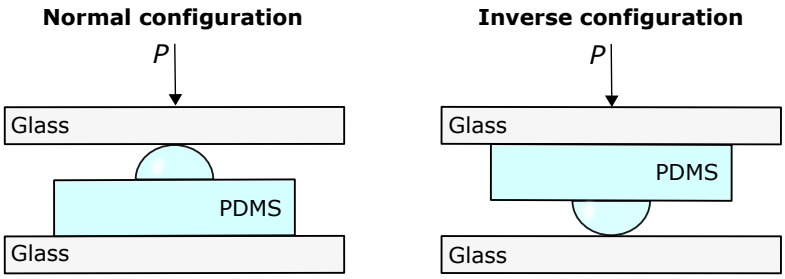

Figure 2.5: Sample attachment configurations.

In a normal (resp. inverse) configuration, the PDMS sphere (resp. glass plate) sample is fixed to the optical table, while the glass plate (resp. PDMS sphere) is attached at the extremity of the moving cantilever.

To ensure that the motion of the upper part, during normal loading of the tested interface, is as vertical as possible and with negligible rotation, a double cantilever beam, composed of two identical steel arms, with low vertical stiffness is placed between the sample and the tangential force sensor. The cantilever has a stiffness k_z of $177 \pm 1\,\mathrm{N/m}$ in the vertical z-direction (normal to the contact interface) and is essentially rigid in the x- and y-directions (parallel to the interface) allowing a quasi-perfect transmission of the forces from the interface to the sensor. Its stiffness calibration is presented in Figure 2.6, showing the force measurement as a function of an imposed cantilever vertical displacement by the z-stage. The slope of the fitted line gives the cantilever stiffness $k_z = 177\,\mathrm{N/m}$. As an example, for a normal load in the contact of 1 N, the typical indentation is of the order of 300 μm which gives a force exerted by the double cantilever beam of approximately 0.05 N.

(ii) Translation system: a motorized x-stage allows the displacement of the whole assembly made up of the slider sample, the cantilever, and the tangential force sensor. The motion is ensured by using a linear motor (LTA-HL, Newport) and its motion controller (SMC100CC, Newport). The maximum displacement stroke of the motor is 25 mm with a resolution of 50 nm, at a maximum speed of 1 mm/s and with a maximum pulling force of 100 N. The whole ensemble - slider sample, cantilever, and tangential force sensor - also can be moved by additional manual stages (UMR8.25, Newport) in the y- and z-directions.

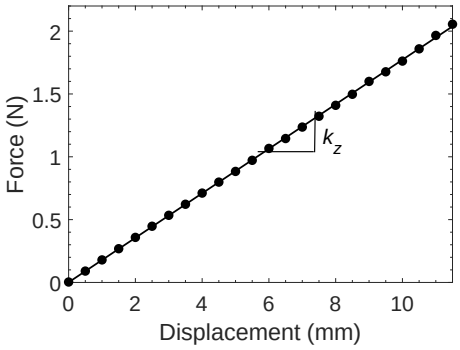

Figure 2.6: Force as a function of imposed cantilever vertical displacement. The slope of the fitted line provides the cantilever stiffness k_z of $177 \pm 1\,\mathrm{N/m}$ in the direction normal to the contact interface.

(iii) Force acquisition system: the force acquisition system allows the simultaneous measurement of the tangential force Q and the normal force P. Q is measured by a piezoelectric force sensor (Type 9217A, Kistler), placed just above the fixed end of the cantilever and connected to a charge amplifier (Type 5018A, Kistler, long measuring mode, 100 Hz low pass filter). Q measurements can be performed in tension and compression with a measuring range from -500 N to 500 N and a threshold measure of 1 mN. P is measured by four force sensors (LSB200, Futek) localized between the optical table and the fixed sample holder. P also can be performed in tension and compression within a maximum range of ~ 8.9 N.

(iv) Optical acquisition system: in this system the contact interface zone is illuminated from above with a white LED panel and is monitored optically in reflection mode using a CCD camera (2M360 MCL, Flare, 8 bits, 2048×1088 square pixels, 340 fps max.) connected to a variable-zoom objective lens (7000 type C, Navitar) and controlled by a software (Hiris, R&D vision). The software allows a direct adjustment of the acquisition frequency, exposure time, gain and offset of the camera. The camera is then put into *edge-triggered* mode and waits for an external image acquisition trigger signal sent by a LabVIEW^{TM} (National Instruments Corporation) code. All the images and their acquisition times are acquired and stored on the computer that drives all settings.

Figure 2.7 schematically shows the fundamental optical principles involved, and two typical grayscale images of the contact: one for an interface between PDMS(S1R9)/glass and the other for an interface between particle layer PDMS(S1R9P)/glass.

In the images, see right side of Figure 2.7, the contact area corresponds to the largest

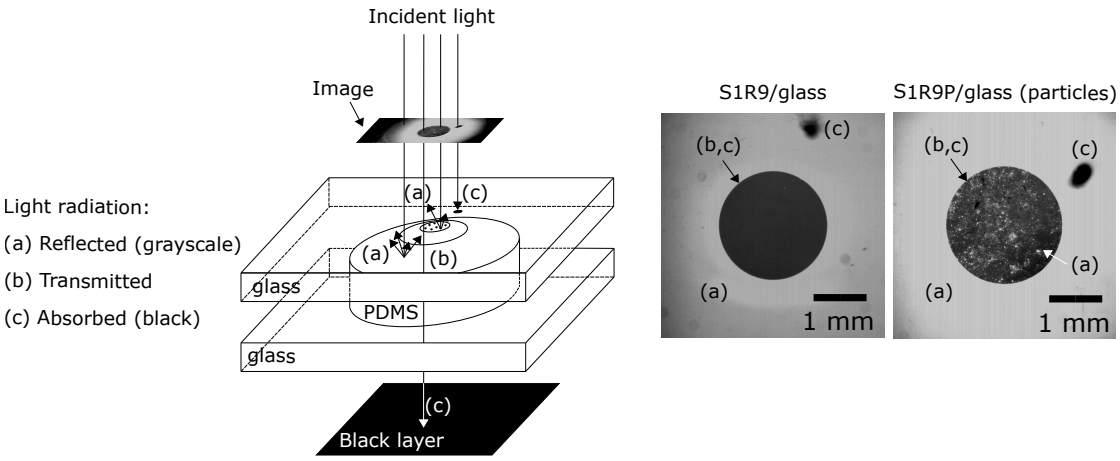

Figure 2.7: Sketch of the optical principles involved in the images acquisition.

region of dark pixels, because light is quasi-perfectly (b) transmitted through the PDMS/glass interface and is then (c) absorbed by a black layer which is placed under the bottom sample. Outside the contact area, *i.e.* at the interface between the glass and the air and at the interface between the air and the PDMS, part of the light is (a) reflected back to the camera, resulting in the lighter gray background in the image. The small area of dark pixels seen in the upper right corner of the contact is due to a black marker, intentionally drawn on the top surface of the glass substrate, that (c) absorbs the light. The marker is used as a tracker to follow the motion of the glass plate slider. In the image from the particle layer PDMS(S1R9P)/glass interface the contact area is not uniformly dark, as it was for PDMS(S1R9)/glass interface images and previous experiments from [17, 53, 55, 63]. In contrast, it is sprinkled with random bright spots which are due to the (a) reflection of light on the particles that were introduced close to the PDMS sample surface (detailed in Section 2.1.2, sample S1R9P). These spots will be used as tracers of contact area evolution in further analyses (see Chapter 3).

Figure 2.8 shows series of typical grayscale images of the contact interface during an experiment for PDMS/glass interface (in the first row) and particle layer PDMS(S1R9P)/glass (in the second row). Note that both samples show a similar behaviour of changing morphology, indicating that the introduction of the particles into the elastomer sphere is not significantly affecting the mechanical response of the interface.

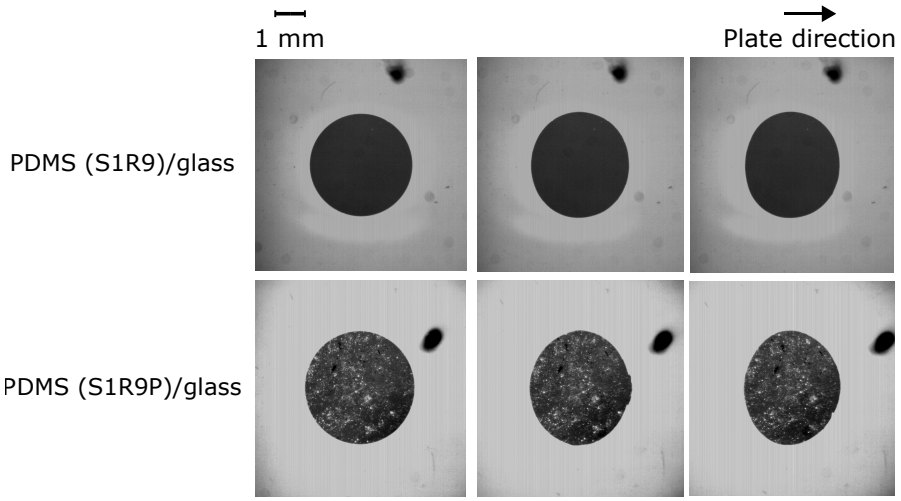

Figure 2.8: Typical images from the optomechanical instrument. Normal force P of 1.85 N and velocity V of 0.1 mm/s. First row: grayscale images of the PDMS(S1R9)/glass contact interface. Second row: grayscale images of the particle layer PDMS(S1R9P)/glass contact interface. The main dark region is the contact area; the bright spots inside the contact area, in the second row, are the particles; and the small dark region, in the top right corner, is a marker drawn on the glass plate slider to follow its displacement.

(v) Alignment system: three goniometers are used to align the instrument. Two of them are located under the sample holder (M-GON65-U and L, Newport), enabling to tilt the sample around the y- and x-direction, with an angular ranging from -10° to 10° and -5° to 5°, respectively. The third one (M-GON65-U, Newport) is placed above the tangential force sensor, capable of rotating the whole assembly made of the tangential force sensor, cantilever, and sample (attached at the free end of the cantilever) around the y-axis, with an angular ranging from -10° to 10°.

In this PhD thesis, a particular attention has been paid to the alignment of the various mechanical components of our experimental device. Indeed, as we will see in Chapter 5, this alignment is critical to the quality of the results obtained, and even a small angle variation can produce significant modifications in the measurements.

The alignment is made using a stainless steel ball (Young's modulus of ~ 210 GPa) fixed on a glass plate to avoid any large normal deformation. Firstly, the upper goniometer, located above the tangential force sensor, is set. For this, the ball sample is placed in a normal sample attachment configuration (*i.e.* a fixed ball with a glass slider). Then, the glass slider is brought into contact with the ball under several normal forces and displaced by around 15 mm. During this displacement, the normal force P is recorded by the P sensors, and the system is considered aligned if P remains constant. Otherwise, the setting of the goniometer is modified and the procedure is carried

over again. Secondly, the lower part of the device is aligned (the one located under the sample holder) by setting the two other goniometers. For this, a similar procedure is performed for an inverse sample attachment configuration (a fixed glass plate with a sliding ball) both in x- and y-direction. The whole system is considered aligned when P remains constant in both sample attachment configurations. The alignment is checked occasionally based on the use of the instrument.

(vi) Control system:

All the physical signals coming from the sensors and the motors are digitized with a DAQ card (NI-PCI-6281, National Instruments), via a shielded connection block (NI-BNC-2110, National Instruments), and transferred at high frequency (up to 3kHz) to a computer. Control of the camera settings is directly done through the Camera Link serial port.

The set-up is fully controlled through an interface developed in the laboratory using LabVIEW^{TM}software (National Instruments Corporation). Figure 2.9 shows a sketch of the data acquisition components, and their relationship to each other. This graphic interface allows in particular to control and program the displacement of the motor and the measurement of the force sensors, to trigger the camera and finally, to export all the data that are saved on the computer. Triggering the camera is of prime interest as it allows to have a perfect synchronisation between the force measurement and the image acquisition. A MATLAB ® (The MathWorks, Inc.) code has been developed to perform this synchronization of the data with the images (see Section 2.3).

2.2.2 Experimental procedure

Using the optomechanical instrument just introduced, the complete process of a typical shear-induced experiments will be described in this section.

The experimental process is divided into three main phases: preparation, test, and post-test. All experiments that will be presented have been performed in air and at room temperature, and followed this process.

Preparation

First, the experimental parameters are determined: (i) pre-waiting time (before the motor starts): 40 s; (ii) motor displacement, d: 2 mm; (iii) motor velocity, V: 0.1 mm/s;

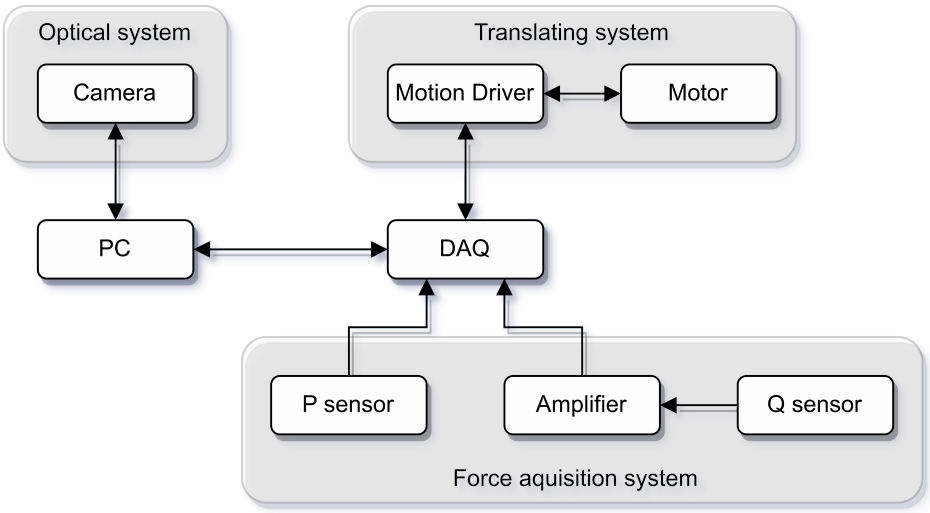

Figure 2.9: Data acquisition flow of the optomechanical instrument.

(iv) image acquisition frequency: 100 fps; (v) post-waiting time (after the motor stops): 10 s.

Second, the normal force P is settled. For this, the whole ensemble of slider sample, cantilever, and tangential force sensor is moved vertically bringing the slider sample in contact with the fixed sample in a position in which they just snap into contact due to adhesion. The normal force P is applied by adding dead weights on the latter configuration, except for small normal forces (< 0.2 N) where P is obtained by pushing the sliding sample on the fixed one via the z-stage. Then, P is verified by comparison with the output of the P sensors.

Test

At the beginning of the test sequence and during all its duration, all the data coming in particular from the motor displacement d, the normal P and tangential Q forces, and the trigger signal of image acquisition, are launched and recorded at a rate of 2 kHz.

The test phase is subdivided into three periods: pre-waiting, shearing, and post-waiting, as shown in Figure 2.10.

Pre-waiting period (40 s): this first period is used to mitigate the effect of area aging due to relaxation process [13], by letting the contact age by about a constant time before shear. For this, the contact is removed and then recreated using a thread tied to the

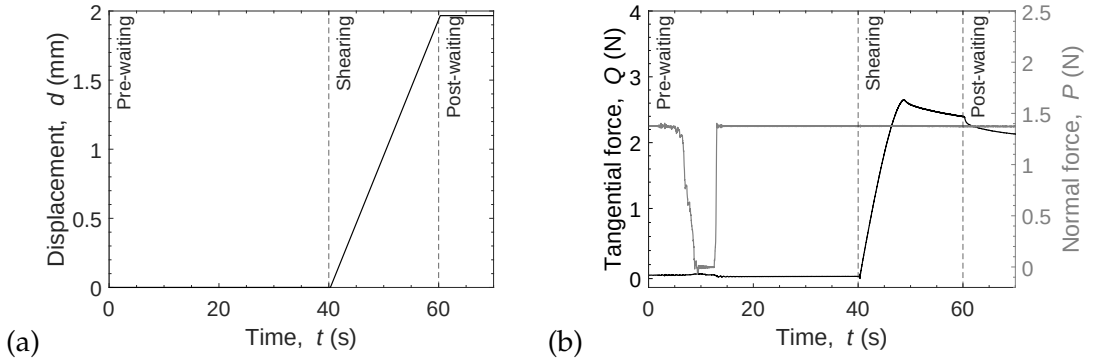

Figure 2.10: (a) Motor displacement d as a function of the time t. (b) Time evolution of the tangential force Q (black line, left axis), and the normal force P (grey line, right axis).

free end of the cantilever, that gently lifts and drops the slider sample. This process of contact recreation can be seen as an abrupt decline on the normal force P on the right axis of Figure 2.10(b). Also, during the cantilever lifting (in absence of contact between the PDMS and the glass samples), the tangential force sensor is re-scaled to zero, as seen on the left axis of Figure 2.10(b), to avoid the sensor drift and to remain within the optimal conditions of operation, less than 120 s, as recommended by the sensor manufacturer.

Shearing period (20 s): after the pre-waiting period of 40 s, a 100 Hz periodic square wave is generated to simultaneously trigger the displacement and the image acquisition. Indeed, at the first rising edge of the signal, the motor starts to run and the fixed extremity of the cantilever is pulled horizontally at a constant velocity V of 0.1 mm/s, over a total distance d of 2 mm, as specified during the preparation phase. While the motor is running and also from the first rising edge of the square signal, the system starts to record images at a frame rate of 100 fps. In the periodic square signal, each rising front edge imposes the acquisition of a single image, as shown by the red dots in the inset of Figure 2.11 for 10 successive images in an interval of 0.1 s.

Post-waiting period (10 s): 10 s after the stop of the motor displacement the acquisition data stops and the outputs of the shear-induced experiment are generated in the form of several files containing (i) the parameters specified in the preparation phase, (ii) the acquired signals of the motor displacement, the normal force, the tangential force, and the image trigger, (iii) the frequencies of data acquisitions, and (iv) the recorded images.

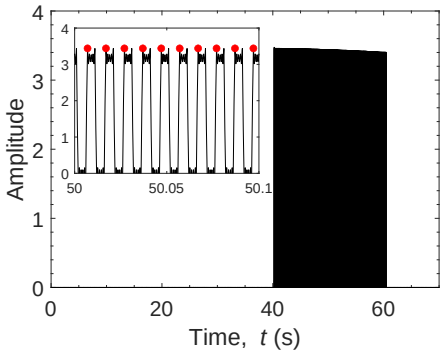

Figure 2.11: A 100 Hz periodic square (pulse) wave trigger signal used to trigger and control the camera image acquisition. The inset shows an interval of 0.1 s where each rising front edge (red dots) indicates the acquisition of a single image.

Post-test

An Excel file labels each carried out experiment and it is filled out with some details such as the file location of stored data, information about PMDS samples fabrication, and the ambient temperature and humidity.

At the end of a set of the experiments, an image of a ruler is taken on the same plane as the PMDS/glass interface for the purpose of calibration of the images in metric units. As shown in Figure 2.12, for a given zoom, a line with a known metric distance is drawn on the image of the ruler. Then, the known distance in metric units is divided by the length of the line in pixels, resulting in the size of each pixel in metric units/pixel, *i.e.* a calibration coefficient to convert pixels in metric units.

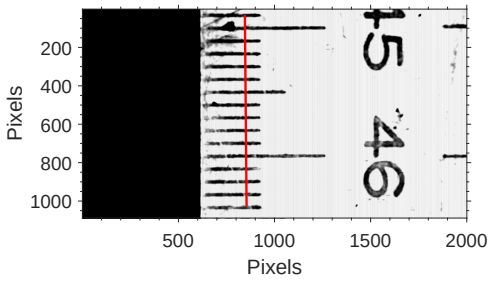

Figure 2.12: Image of a ruler taken on the same plane as the PMDS/glass interface for calibration of the images. A line with a known metric distance is drawn on this image. Then, the known distance in metric units is divided by the length of the line in pixels, which gives the size of each pixel in metric units/pixel.

2.3 Data processing

One can notice that images (100 Hz) and others acquired data (2 kHz) are recorded at different frequencies, and in order to analyze those data it is necessary to synchronize them. This process is possible using the trigger signal (Figure 2.11) that has been generated at 2 kHz and contain all the exact instants of the image acquisition starting.

To improve the data analysis and management, a Graphical User Interface (GUI) has been developed with MATLAB ® software (The MathWorks, Inc.), during this PhD thesis, to synchronize the recorded data and also to visualize the results. The interface comprises point-and-click controls providing organized and simple access to the data. It allows a rapid process of the raw data (data synchronization, image processing, parameter evaluation, and so forth.), contains some visualization tools and returns a structure array containing information and processed data for each experiment. Figure 2.13 shows the data flow diagram of the GUI. The essential GUI interactions and their outputs will be described in the coming sections.

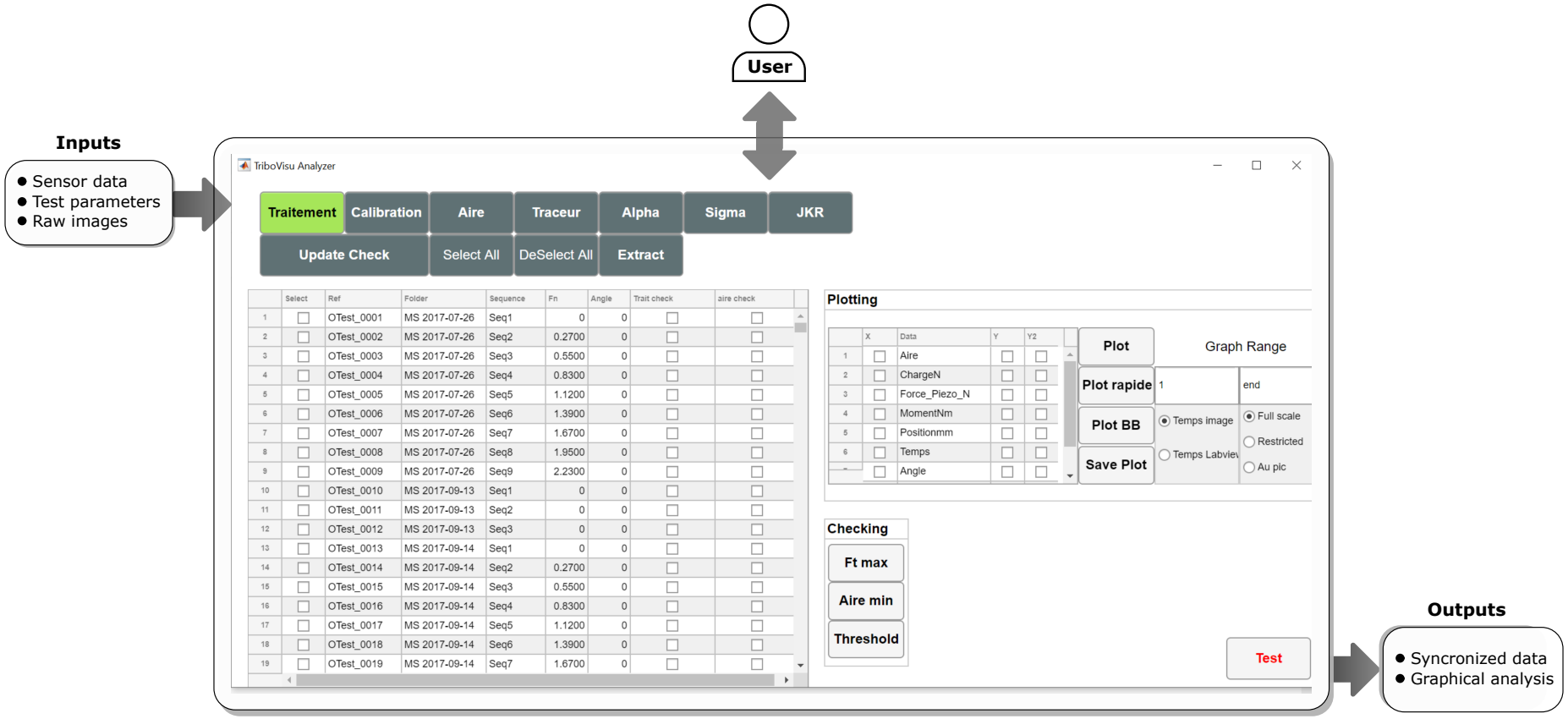

Figure 2.13: Data flow diagram of the Graphical User Interface (GUI) developed for the data processing.

2.3.1 Image processing

In this section, the procedures performed for the image analysis will be presented. The methods used to segment the recorded grayscale images (8-bit), to evaluate the contact area from and to measure the glass displacement will be detailed. Note that, for the use of the image processing techniques, the images are considered as a two-dimensional function $f(x, y)$, where x and y are spatial (plane) coordinates of a certain point, called *pixel* (picture element), and the amplitude of f at any pair of coordinates (x, y) is called the intensity or gray level of the image. This function can be mathematically represented in the form of matrices, where each element of this matrix is the amplitude of f and the coordinates x and y correspond to the columns and rows, respectively [71].

Segmentation

The first step in the image processing is the segmentation of the grayscale images into in- and out-of-contact pixels. Inside the GUI, the segmentation is initiated at the click of the button "Aire". First, the images are cropped in a region of interest around the contact area, thus excluding the marker on the glass substrate (see top right black spot in Figure 2.8) and also all noisy zones at the edge of observation zone. Then, the cropped images are converted into binary images by thresholding. A threshold level, T, for the image intensity distribution is found by using the MATLAB® function *graythresh*, that uses Otsu's method [72]. As a result, every pixel turns black or white according to whether its intensity is greater or less than T:

$$\text{A pixel becomes } = \begin{cases} \text{white if its gray level is } > T, \\ \text{black if its gray level is } \leq T. \end{cases}$$

The threshold value is found for the initial image and is kept constant for all images of a same test.

Figure 2.14 first and second rows show the result of these operations on the images of Figure 2.8.

In view of the operations to be performed next, the black and white images are reversed using the MATLAB® function *imcomplement*, resulting in binary images in

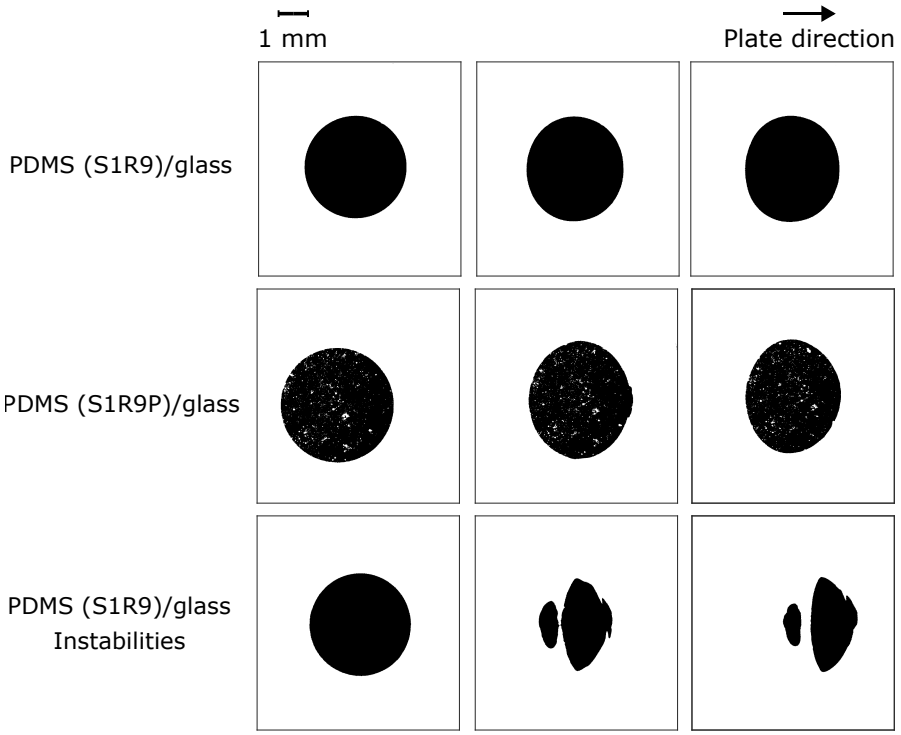

Figure 2.14: Segmentation of images. First row: segmented images of the PDMS/glass contact interface shown in Fig 2.8 first row. Second row: segmented images of the particle layer PDMS/glass contact interface shown in Fig 2.8 second row. Third row: segmented images of a case with instabilities at the interface. The main dark region is the contact area and the bright spots inside the contact area, on the second row, are the particles.

which the contact area is indicated by 1 (white) and out-of-contact area is indicated by 0 (black).

In the particular case of binary images of samples S1R9P, the particles are seen as holes (out-of-contact) area within the contact zone. Then, to compute these "holes" as in-contact areas, they are filled using the MATLAB ® function *imfill* with the argument *holes*.

Contact area

The second step consists in using the binary images to measure the real contact area A by using the MATLAB ® function *regionprops*. This function identifies connect components, called objects, and measures the contact area through the number of pixels of the object. This function also returns properties such as centroid, and the position and size of the smallest box containing the object. When multiple objects are identified, which is the case when there are instabilities in the interface, as seen in the third row of Figure 2.14, the features of each object are stored and the total area is considered as

the sum of the areas of all objects. Then, by using calibration coefficients (described in Section 2.2.2, Post-test), the total number of the contact area pixels is converted into metric units.

Glass displacement

The last step of the image processing, done by clicking on the button "Traceur" on the GUI, aims at tracking the displacement of the black marker drawn on the top of the glass plate slider to evaluate the glass displacement (as seen in Figures 2.8 and 2.14). The whole raw images are cropped in a region of interest around the black marker. Then, the same segmentation process, as presented above in Section. 2.3.1 is applied. The centroid's coordinates of the object detected in each image, as determined by the MATLAB ® function *regionprops*, are stored. The evolution of these coordinates are used to translate the images to set them in the slider's frame, in such a way that this tracer remains at a constant position. In other words, we place our images in the frame of the glass slider which actually moves from left to right at velocity V in the laboratory frame.

2.3.2 Force measurements processing

This data processing starts, after a click on the bottom "Traitement" on the GUI, by synchronizing the acquired signals (2 kHz) with the images (100 Hz).

First, the effective starting time of the shearing period is defined, *i.e.* the precise moment at which the displacement starts. For this, a piece-wise method is used dividing the displacement signal into two pieces. The first piece uses displacement data at a time interval between the nominal starting of 40 s and 2.5 s before it. This first piece is expected to correspond to a constant position for the motor. The second piece uses a time interval between the nominal starting of 40 s and 2.5 s after it. This second piece is expected to correspond to a constant velocity for the motor, and thus a linear evolution of the displacement. Then, each of the two pieces is fitted by a linear regression (dashed red lines in Fig 2.15), and their intersection defines the effective starting time (vertical dotted line in Fig 2.15). This method allow to account for the acceleration phase at the beginning of the motion.

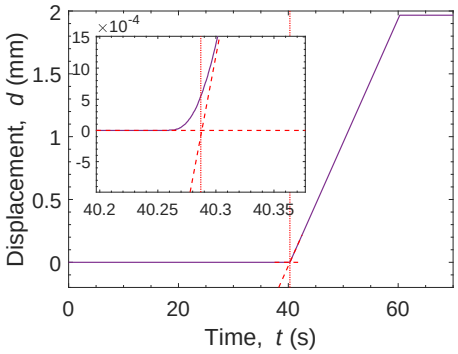

Figure 2.15: Motor displacement d as a function of time t. The inset is a zoom showing the piece-wise method for defining the effective start position. Displacement data is split into two pieces: one, 2.5 s before the nominal starting of 40 s and other, 2.5 s after it. These two pieces are fitted by linear regression represented by the dashed red lines, and their intersection defines the effective starting time, represented by the vertical dotted line.

Second, the trigger signal (see Figure 2.11) employed to control the camera image acquisition is used to find the temporal index of each image, *i.e.* taking each front edge in the trigger signal and find its correspondence, in time, in the other signals, as shown in Figure 2.16.

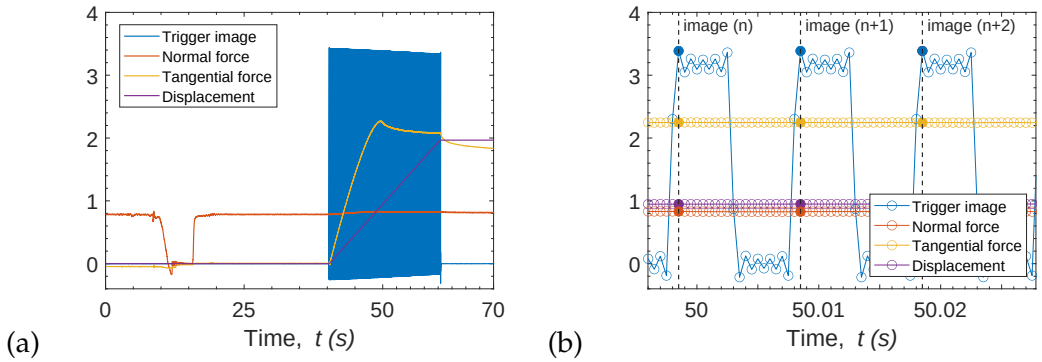

Figure 2.16: Synchronization of force and displacement signals with images. (a) All acquired signals - trigger image, normal force, tangential force, and motor displacement - as a function of the time t. (b) Zoom in on (a) where it is shown that the synchronization of the signals and the images is done using the trigger signal of image acquisition and taking each front edge and its temporal correspondence in the other signals.

As outputs of this data processing, we have all signals - normal force, tangential force, and displacement - at the time of the images, as shown in Figure 2.17.

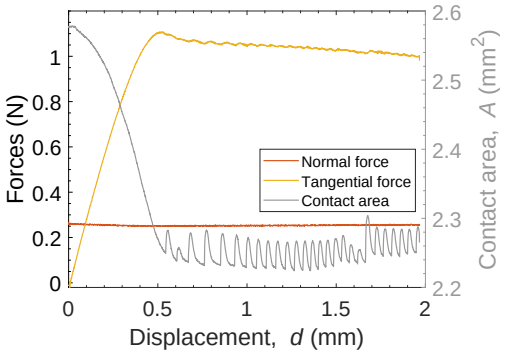

Figure 2.17: Evolution of the normal and tangential forces (left axis), and of the contact area A (right axis) as a function of the displacement d, after the synchronization of all data.

2.4 Other procedures

2.4.1 Tangential force peak determination

The peak of tangential force Q_s is usually used to define the transition between stuck state and macroscopic sliding, and is used in analyses that will be discussed in more details in the following chapters.

To find the tangential force peak, the MATLAB ® function *max* is used. This function returns the maximum of the tangential force curve. However, in some exceptions, the maximum of the tangential force is not found at the expected transition to macroscopic sliding, as in the two examples shown in Fig 2.18.

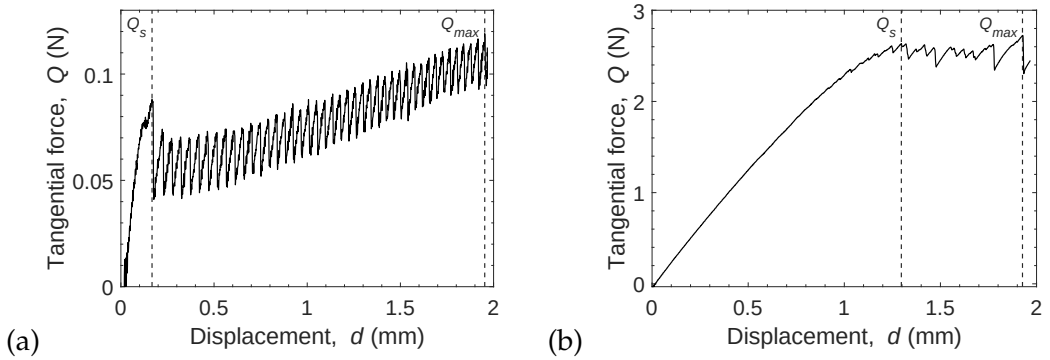

Figure 2.18: Tangential force Q as a function of the displacement d. (a) $P = 0.004\,\mathrm{N}$. (b) $P = 0.546\,\mathrm{N}$. Q_s is the force at the transition to macroscopic sliding, while Q_{max} is the absolute maximum of the tangential force curve.

Therefore, this operation is visually inspected to check whether the maximum point is indeed located in the transitional zone. If not, the procedure is performed, but in a manually restricted region of interest around to the transition region.

2.4.2 Oscillating curves' envelope

In further analyses a correspondence between the tangential force peak Q_s and the contact area is carried out by evaluating the contact area at the moment of Q_s and denoted as A_s, see vertical dashed lines in Figure 2.19(a). However, when instabilities occurs at the interface (see Figure 2.14 third row), they generate oscillations in both the tangential force and area evolution curves, as shown in Figure 2.19(b). In this case, performing a direct correspondence of such curves can be a potential source of error, since the oscillation of curves are rarely in phase. Indeed, at the time of Q_s, the instantaneous value of A, namely A_s, can take any value between a local peak and a local valley in the oscillating curve, as shown in Figure 2.20.

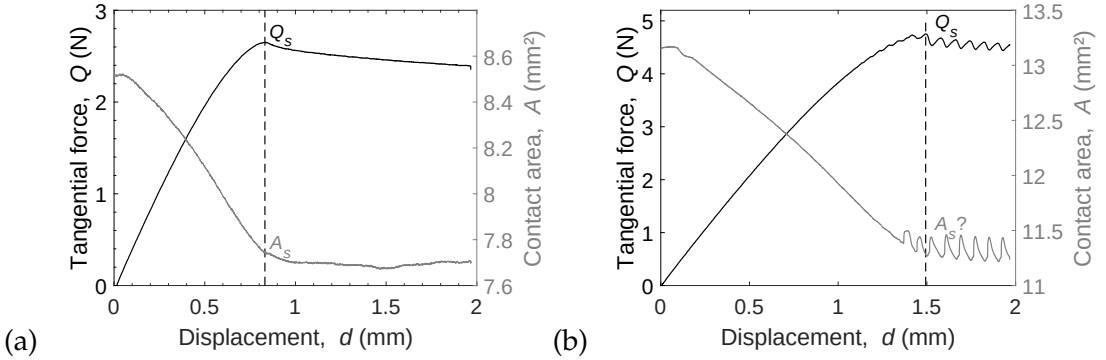

Figure 2.19: Evolution of the tangential force Q (solid black curve, left axis) and of the contact area A (solid grey curve, right axis) as a function of the imposed displacement d. (a) Case of a direct correspondence between the peak of the tangential force Q_s and the contact area A_s reduction curve. (b) Case with the presence of instabilities in the interface, when a direct correspondence in such curves can be a potential source of error.

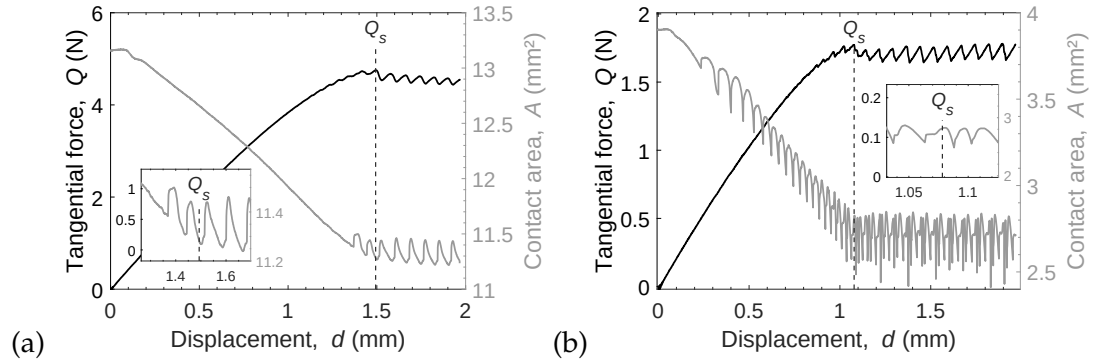

Figure 2.20: Evolution of oscillating curves showing the tangential force Q (black line, left axis) and the contact area A (grey line, right axis) as a function of the displacement d. The peak of the tangential force Q_s is shown as a vertical dashed line. The inset shows a zoom in the A signal when Q_s matches (a) a valley in the A curve or (b) a peak.

To minimize the potential error made on the evaluation of A_s, we made the strong assumption that the lower envelope of the $A = f(d)$ curve is representative of the behaviour of an interface in absence of instabilities. Indeed, in Figures 2.19 and 2.20, the lower envelope of the oscillations appears to be the natural continuation of the beginning of the curve, when no oscillation is present yet. Thus, a numerical method to evaluate the lower envelope of the oscillated signal is implemented. The lower envelope is a curve outlining the signal, by interpolation over local minima. Here, the lower envelope is constructed, using some MATLAB ® functions, as follow:

(i) the contact area curve is smoothed, in order to eliminate small peaks (noise), using the function *smooth* with a *rloess* method and a *smoothing factor* of 0.002;

(ii) after, the prominence of all local minina (or valley) are detected applying the function *findpeaks* with the argument *peak prominences* on the reverse of the smoothed contact area curve. The prominence of a local minimum measures how the valley stands out with respect to its depth and location relative to other valleys;

(iii) then, the local minina prominence's average is used as a threshold T_p, so that the function *findpeaks* can return only those peaks that have a prominence of at least the value of T_p. For it, the function *findpeaks* is applied again on the reverse of the smoothed contact area curve, but this time with the argument $MinPeakProminence = T_p$ found in (ii);

(iv) the found local minima are interpolated using the function *interp1* with the method *linear*;

(v) finally, the lower envelope was constructed by concatenating the smoothed curve until the first oscillation (first local minima) and the resulting from the interpolation of the local minima.

Figure 2.21 shows an example of the final result of these operations, where the smoothed contact area is represented as black lines. In (a) the found local minima from operation (iii) and the interpolated curve from operation (iv) are shown as red circle marks and solid red line, respectively. In (b) the constructed lower envelope is show as a solid blue line.

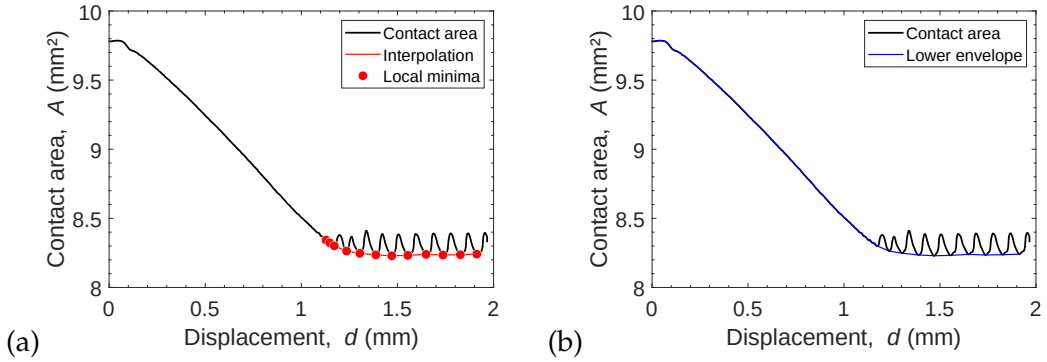

Figure 2.21: Evolution of oscillating smoothed contact area (black lines). (a) Red dots indicate the local minima and red line the linear interpolation of them. (b) The blue line represents the final lower envelope.

2.4.3 Measurement of elastic modulus and adhesion energy

Experimental data are also used to estimate the adhesion energy ω_0 of the interfaces (PDMS/glass) and the elastic modulus E of the PDMS samples. Using the same method apply in Waters and Guduru [49] and Vorvolakos and Chaudhury [73], the data are fitted according to the Johnson, Kendall, and Roberts (JKR) adhesion theory [27]. The original JKR relation between the load and the contact radius (at zero tangential force) is rearranged as:

$$\frac{a^{3/2}}{R} = \frac{9}{16E^*}\frac{P}{a^{3/2}} + \frac{3}{4}\sqrt{\frac{6\pi\omega_0}{E^*}} \tag{2.1}$$

where a is the contact radius, R is the radius of curvature of the sphere, and P is the normal force.

Therefore, by performing a linear fit of $a^{3/2}/R$ as a function of $P/a^{3/2}$, it is possible to find the equivalent E and ω_0 from its slope and y-intercept, respectively. An example of this approach is shown in Figure 2.22.

2.5 Repeatability

Any analysis of experimental measurements can be confirmed after repeating a set of tests several times. However, in our case, it is challenging to establish comparisons between different sets of measurements. The main difficulty is experienced when one attempts to compare the results from two different PDMS samples, due to the variability of properties found even when the same protocol of fabrication is carefully followed.

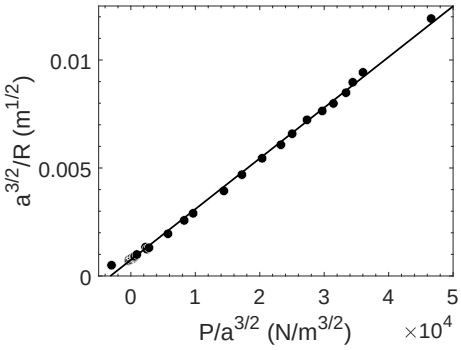

Figure 2.22: Contact radius a as a function of the normal force P from experimental data at zero tangential force. In this example, the value of $E = 3.19 \pm 0.05$ MPa and $\omega_0 = 125 \pm 23$ mJ/m^2, are obtained from a linear fit to the experimental data using Equation 2.1.

In these circumstances, a wide set of experiments, shown in Figure 2.23, was carried out in the laboratory group to check the repeatability of shear-induced experiments perform on a given PDMS sample. The results indicate that around fifty tests (2 mm of total displacement each one) can be performed remaining reproducible. In view of these concerns, in this thesis, a PDMS sample is used to a reduced extent, around 30 tests.

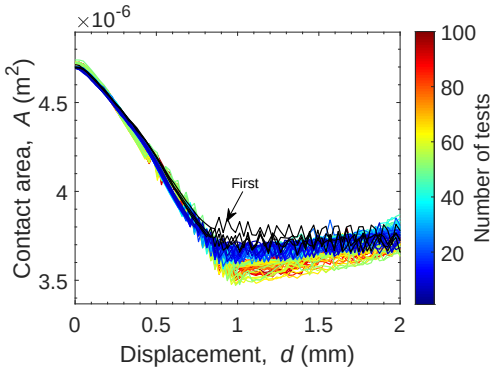

Figure 2.23: Evolution of the contact area A with the imposed displacement d, for 100 shearing experiments (tests).

Interestingly, a greater tangential force was observed at each beginning of a set of experiments, *i.e.* for the two or three first sliding experiments, which may be due to the orientation, extension and/or pull-out of the PDMS chains, a phenomenon evidenced by some authors [14, 74–76]. For this reason, in this manuscript, the first four tests of a set of experiments were rejected most of time. The cases in which the first tests were considered will be indicated.

In addition, in all this work, the sets of experiments with different normal forces were carried in a random order of normal force, to ensure that the observations are

consistent with the evolution of the normal force, and have no relation to any aging or temporal modification of the system.

Chapter 3

Elementary mechanisms of shear-induced contact area reduction

3.1 Introduction

Solid contacts of soft materials such as elastomers and human skin have revealed complex changes to the contact morphology when submitted to an additional shear loading. Not only is the overall real contact area significantly reduced [17, 77], but it also becomes increasingly anisotropic [63]; two effects that have not been satisfactorily explained yet. For both effects, smooth sphere/plane contacts have been shown to obey similar behaviour laws as rough contacts [17, 63]. It is therefore appealing to investigate anisotropic shear-induced area reduction in such simpler, single sphere/plane contacts between smooth solids.

Experimentally, elastomeric sphere/plane contacts are known to evolve from a circular area under pure normal load to a smaller, ellipse-like area in macroscopic sliding regime. In order to identify the underlying mechanisms responsible for such contact area evolution, Barquins and Courtel [78] and Barquins [79] monitored the shape of a straight line scratched on the polymer surface perpendicular to the direction of motion ("passing line" method), showing that the contact area shrinkage occurs by a peeling process; and also confirmed the existence of an adhesive zone, whereas partial slip takes place in an annular region adjacent to the edge of the contact area. Later, Waters and Guduru [49] performed a similar experiment to the "passing line" method; their results showed that there was no slip visible within the contact area while it remained symmetric, as the line appeared to remain straight inside the entire contact area. They

concluded that the contact area reduction under shearing is due to a peeling process rather than a slip propagation. Note that the difference in terms of loading conditions (normal loadings and shearing speed) in the above-mentioned studies may play a role in the observed discrepancies. It should be also noted that both findings, from Barquins and Courtel [78] and Barquins [79] and Waters and Guduru [49], are made only along the observation of the shape of a straight central line of the contact, and the presence of the scratched line can affect the mechanical behavior of the interface.

In this context and in order to take the first step toward the main objective of the thesis, this chapter presents an experimental analysis of an elastomer/glass interface, similar to those of Sahli et al. [17, 63], to identify the elementary mechanisms responsible for contact area reduction and their relative contributions. The strategy is based on the incorporation of particles at the proximity of the elastomer surface and on their use as local tracers for the motion of the entire frictional interface during incipient tangential loading under several constant normal loads. The relevance of the detected mechanisms will be compared with a non-adhesive model that shows a quantitative agreement with recent large-load experiments, with no adjustable parameter.

3.2 Experimental procedure

3.2.1 Tangential loading experiments

The custom-built setup presented in Section 2.2.1 was used to shear the interface between a smooth glass plate and a cross-linked PDMS sample (nearly incompressible, $E = 1.5 \pm 0.1\,\text{MPa}$) with a spherical cap seeded with a layer of particles about $16\,\mu\text{m}$ below the surface (see details in Section 2.1.2, sample of the type S1R9P). The experiments were performed in a normal sample attachment configuration, as illustrated in Figure 2.5, under 4 different constant normal loads, $P = 1.85\,\text{N}$, $0.54\,\text{N}$, $0.25\,\text{N}$, and $0.05\,\text{N}$. Respectively, 21 s, 14 s, 13 s, and 22 s, after the contact has been created for each experiment, a constant driving velocity $V = 0.1\,\text{mm/s}$ was imposed on the glass plate, over a total distance of 2 mm. Images of the interface were acquired during the glass displacement with a lateral square pixel of $7.7\,\mu\text{m}$ for $P = 1.85\,\text{N}$, and $9.0\,\mu\text{m}$ for the others normal loads, in the contact plane. See section 2.2.2 for more specifications and a detailed description of the experiment.

The evolution of the tangential force Q as a function of the imposed displacement d of the glass plate for the different normal loads is shown in Figure 3.1 (solid black line, left axis). The incipient tangential loading of the interface reaches a maximum, denoted as the static friction force Q_s (at displacement d_s), before a full sliding regime during which $Q < Q_s$.

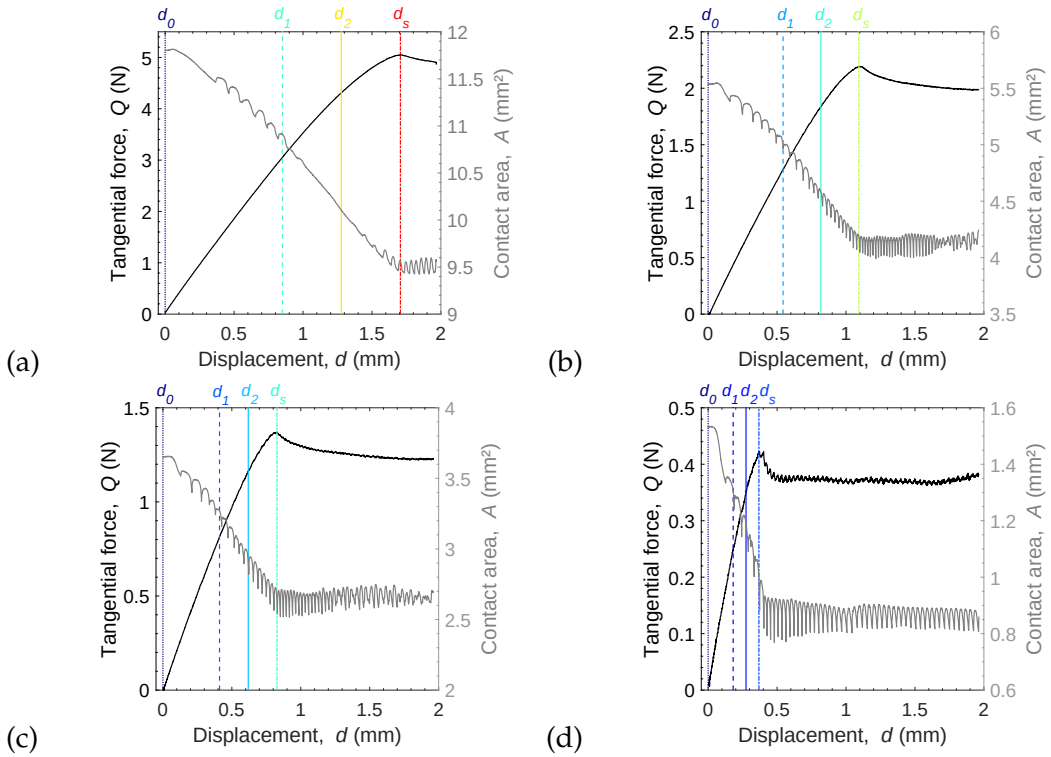

Figure 3.1: Evolution of the tangential force Q (solid black line, left axis) and of the contact area A (solid grey line, right axis) as a function of the imposed displacement d of the glass substrate. Four displacement values are indicated, which will be used in further figures. The static friction force Q_s occurs at displacement d_s. $V = 0.1\,\mathrm{mm/s}$. (a) $P = 1.85\,\mathrm{N}$, (b) $P = 0.54\,\mathrm{N}$, (c) $P = 0.25\,\mathrm{N}$, and (d) $P = 0.05\,\mathrm{N}$.

The incorporation of particles into the proximity of the PDMS sphere surface is the strategy that allows us to observe any local phenomenon occurring within the contact area during tangential loading. However, in order to carry out such observation, some specifications are required: (i) the particles must be visible by the camera regarding their sizes and light reflection ability, providing high contrast in the contact area; (ii) they must be located close to the sphere surface, but not on the very surface to avoid affecting the mechanical response of the interface; (iii) the layer of particles thickness must be thin to avoid differential displacement due to different depths; (iv) the particles in the layer must be well scattered and sufficiently isolated from one another to be monitored individually by a PIV (Particle Image Velocimetry) type procedure.

Among several tested particles candidates (*e.g.*, aluminum oxide, boron carbide, and glass micro-spheres), silver particles were the ones that best satisfied these requirements, however they have random shapes with a mean area of 9.2 $\times 10^2 \mu m^2$ (ranging from 2.9 $\times 10^2 \mu m^2$ to 67.1 $\times 10^2 \mu m^2$).

Typical raw images of the contact interface, for the four normal loads, are shown in Figure 3.2(a–d) for four different displacements (shown in Figure 3.1): d_0 before any shear, d_s the displacement at the static friction peak Q_s, and d_1 and d_2 two intermediate displacements. Full movies are available, as supplementary material, in Appendix A, as Movies M185, M054, M025, and M005 for $P = 1.85\,N$, $0.54\,N$, $0.25\,N$, and $0.05\,N$, respectively. The contact region corresponds to the biggest region of dark pixels. In all subsequent figures, the leading (resp. trailing) edge is always on the left (resp. right) side. As mentioned in the description of the optical acquisition system in Chapter 2, the contact regions are not uniformly dark, but are sprinkled with random bright spots that are due to light reflection on the particles incorporated close to the elastomer surface. The upper right dark region is a marker drawn on the glass substrate to monitor its macroscopic motion.

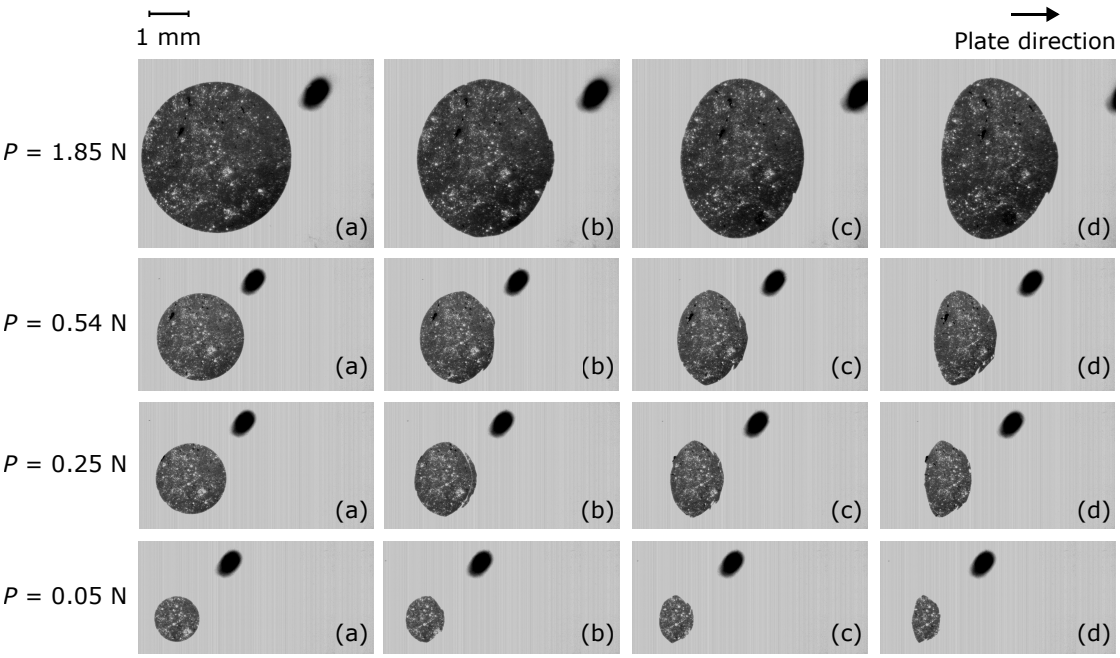

Figure 3.2: Raw images of the contact interface at the four displacements shown in Figure 3.1. (a): d_0, (b): d_1, (c): d_2, and (d): d_s, for the four normal loads, 1.85 N, 0.54 N, 0.25 N, and 0.05 N. The main dark region is the contact area, bright spots are the particles, and the upper right dark region is a marker drawn on the glass substrate to monitor its macroscopic motion. The images are in the frame of the camera and the leading edge is on the left side.

Figures 3.3(a–d) show typical contours of the contact, the inner area of which defines the contact area A. The evolution of A as a function of the imposed displacement of the glass plate is shown in Figure 3.1 (grey lines, right axes). For all experiments, both, Q and A curves, in Figure 3.1 present the same qualitative behavior as previous experiments in the literature [17, 49, 55], which shows that the insertion of particles into elastomer spheres does not significantly affect the mechanical response of the interface. The oscillations observable in the $A(d)$ curves in Figure 3.1 originate from the so-called detachment folds [79] occurring at the trailing edge of the contact.

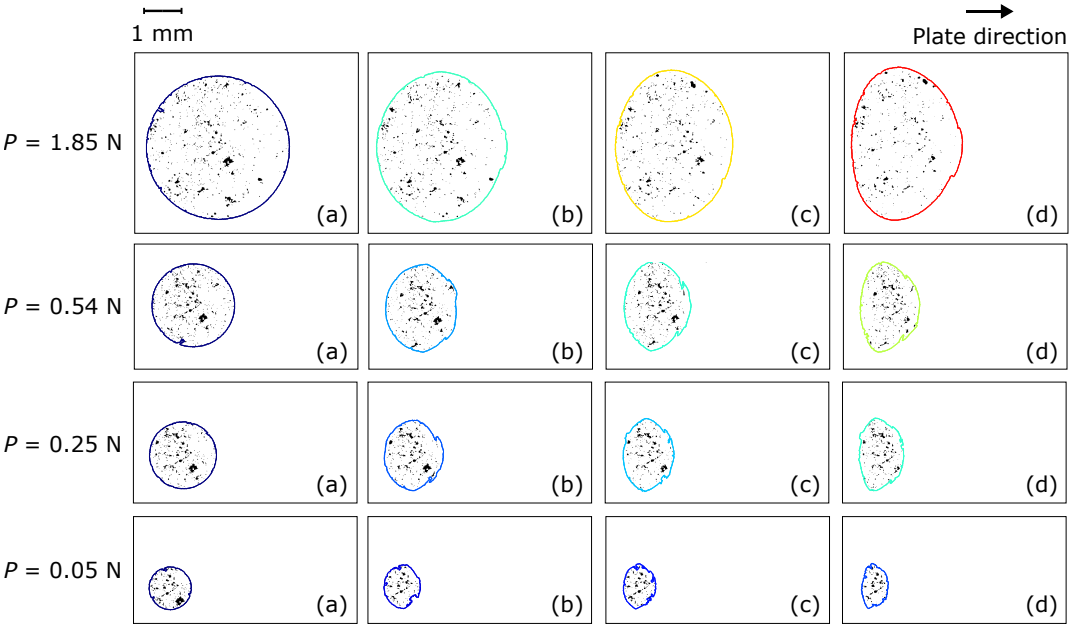

Figure 3.3: Segmented images from raw images of Figure 3.2 at the four displacements, (a): d_0, (b): d_1, (c): d_2, and (d): d_s, for the four normal loads, 1.85 N, 0.54 N, 0.25 N, and 0.05 N. In (a-d) of each experiment, the contours are those of the contact (same colors as in Figure 3.1), the inner area of which defines the contact area; black spots correspond to the particles. The images are in the frame of the moving glass plate. The leading edge is on the left side.

3.2.2 Image processing: segmentation and particle tracking

The bright spots present in the images of Figure 3.2 were used as tracers of the contact evolution by applying a homemade tracking procedure detailed hereafter. The main aim of this tracking code is to generate a data set in which the x- and y-positions of each tracer are given for each image/time-step. Note that only the tracers at the vertical of the contact regions are visible.

Image analysis followed the operations described in Section 2.3.1 and after the segmentation process, where basically the raw images are classified into in- and out-of-contact pixels, a noise reduction process was performed on all images. In this denoising process, all objects (set of connected pixels) with an area of a single pixel are removed by successively performing two morphological operations, erosion and dilation, with a 3×3 square structuring element (set of coordinate points whose width is 3 pixels). Then the closest remaining objects are connected by successively performing the two same operations in reverse order, *i.e.* dilation and erosion. This results in connecting all the objects within a distance of less than 23 μm for $P = 1.85\,\mathrm{N}$ and less than 27 μm for the other normal loads. In such operations, the center pixel of the structuring element, called the origin, is aligned with each pixel in the image that has a value of 1 (white) and each pixel of the structuring element is included (resp. excluded) in the dilated (resp. eroded) image. Those binary images were then used as inputs to the tracking code.

The tracking processing, as described in Algorithm 1, identifies, only on the initial image, objects whose area is strictly larger than 4 pixels. Those objects are then considered as tracers of the contact evolution for upcoming analyses. For each tracer, the centroid (C_x and C_y) and the x- and y-widths of the smallest rectangle enclosing it (W_x and W_y) are stored. Next, the trajectory of each tracer is found by searching for its successive positions in all images. For two successive images, the following procedure is applied to each tracer:

- extracts two sub-images from both successive images (at steps i and i+1): their common extraction positions correspond to the position, $C_x(i)$ and $C_y(i)$, of the tracer and their widths correspond to $W_x(i)$ and $W_y(i)$ increased by 5 pixels on all four sides to account for the dilation operation performed on the next process. This sub-image procedure is implemented to improve computing performance by significantly increasing the image processing speed in MATLAB ® (The MathWorks, Inc.).

- performs a dilation operation with a 3×3 square structuring element only on the sub-image at step i. This dilation enlarges the boundaries of the tracer by a larger

amount than the expected theoretical travel distance ($\Delta d_{\max}$) of the slider between two successive images in the steady sliding regime, $\Delta d_{\max} = 1\,\mu$m ~ 0.14 pixel.

- multiplies pixel by pixel the two resulting sub-images, *i.e.* the dilated one at step i with the unmodified one at step i+1.

- finds all objects in the image resulting from the multiplication and stores the position of the object as the coordinates, $C_x(i+1)$ and $C_y(i+1)$, of its center of mass in the full image. If multiple objects are detected, only the closest object to the center of the sub-image at step i is considered. If there is no object, then the trajectory ends.

Therefore, the outcome of the tracking process is a data set in which the centroid position, $C_x(i)$ and $C_y(i)$, of each tracer is given in the laboratory frame, for all image, *i.e.* for each time step. Then, all tracers containing non-realistic trajectory changes (greater than 3 pixels, that is, greater than 23 μm for $P = 1.85$ N and 27 μm for the other normal loads) in the position of the tracer between two consecutive images were removed. Finally, the displacement of the glass plate was subtracted from all trajectories (for instructions on glass displacement extraction, refer to Section 2.3.1). In other words, we place the trajectories in the frame of the glass substrate.

3.3 Results and analysis

In this section, based on the results of the particle tracking procedure, a thorough analysis of the tracers' behavior (appearance/disappearance and relative motion with respect to their initial position and adjacent tracers) is conducted. First, the existence of elementary mechanisms of contact area evolution on the onset of the macroscopic sliding is searched. Second, the evolution of the tracers displacement throughout the entire experiment is investigated.

3.3.1 Elementary mechanisms of contact area evolution

As mentioned in Section 3.2.1, the particles are only visible in the vertical direction of the contact area, which provides the possibility to investigate the existence of elementary mechanisms responsible for the contact area evolution.

Algorithm 1: Particles tracking code

Input: Segmented images
Output: Data set of tracer trajectories

```
1  begin
2      detection of the number of objects in the first image;
3      define as tracer all objects whose area > 4 pixels;
4      store the position of all tracers as the coordinates (C_x(i) and C_y(i)) of its
         centroid;
5      store x- and y-widths (W_x(i) and W_y(i)) of the smallest rectangle enclosing
         each tracer.
6      for images do
7          take two successive images at steps i and i+1.
8          for tracers do
9              extract two sub-images from the couple successive images at i and
                 i+1: their common extraction coordinates correspond to the
                 position, C_x(i) and C_y(i), of the tracer and their widths correspond
                 to W_x(i) and W_y(i) increased by 5 pixels on all sides to account for
                 the dilation operation that is performed on the next process.
10             perform a dilation operation with a 3x3 square structuring element
                 only on the sub-image at step i
11             multiply pixel by pixel the sub-image (dilated) at step i and the
                 sub-image (unmodified) at step i+1
12             find the number of objects (connected pixels) in the image resulting
                 from the multiplication
13             if object = 1 then
14                 save tracers as coordinates (C_x(i+1) and C_y(i+1)) of its centroid
                     in the full image.
15             else if object > 1 then
16                 only the closest object to the center of the sub-image at step i is
                     considered.
17             else
18                 tracer trajectory ends.
```

Tracers that were initially in contact and no longer exist at the onset of the macroscopic sliding (at Q_s), means that they have been lifted out-of-contact. This first elementary mechanism of area variation is then named "contact lifting" (or simply "lifting"). On the contrary, tracers that were initially out-of-contact, but came into contact during the incipient loading phase demonstrate the second elementary mechanism of area variation, that is named "contact laying" (or "laying"). Finally, the third elementary mechanism is related to inhomogeneous slip and in-plane deformation within the contact zone and leads to either "in-plane compression" or "in-plane dilation".

In an attempt to quantify those mechanisms we make use of two graphical approaches: Voronoi tessellation and Delaunay triangulation. In an overview definition, Voronoi tessellation of a finite set of unique sites is a collection of regions, called cells, that divide up an Euclidean space. Each cell corresponds to one of the sites, and all the sites in one region are closer to the corresponding site than to any other site [80]. Its dual graph is a Delaunay triangulation, where two sites are connected by an edge in the Delaunay triangulation if they belong to adjacent Voronoi cells. Delaunay triangulation is formed by a net of triangles satisfying the empty circumcircle criterion: (i) the circumcircle of each triangle contains only the vertices of the triangle, and (ii) there are no site of other triangles inside the circumcircle. Delaunay triangulations also maximize the minimum angle of all triangles in the triangulation [80, 81]. Figure 3.4 illustrates an example of a Voronoi diagram (solid black lines) and its dual Delaunay tessellation (dashed red lines) for a set of 11 sites (open black disks).

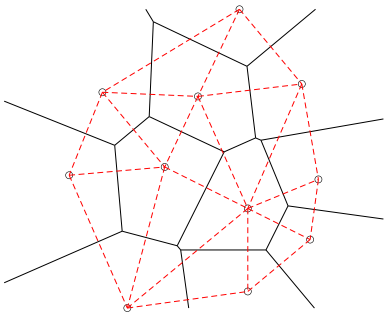

Figure 3.4: A Voronoi diagram (solid black lines) and its dual Delaunay tessellation (dashed red lines) for a set of 11 sites (open black disks).

Contact lifting

The feature of local contact lifting is that a tracer disappears from the image when it is reached by a moving contact edge, which means that a point of the elastomer initially in contact with the glass has been lifted out-of-contact. Such criterion of being close to the contact edge is used to distinguish tracers that are truly lifted from tracers that disappear due to noise in the images and tracking procedure.

In practice, we look for the tracer's trajectory which ends at a position less than 20 pixels from the contact edge (*i.e.*, 154 μm for $P = 1.85\,\mathrm{N}$ and 180 μm for the others normal loads). All these tracers are represented as disks in Figure 3.5. Filled disks correspond to the position of the lifted tracers in the initial image (at d_0), and open disks indicate the position when the tracers disappear.

It appears that a considerable amount of tracers are indeed lifted during the incipient tangential loading of the contact for all normal loads. The majority of them are located at the trailing edge of the contact (on the right side), where points of the glass are continuously driven out-of-contact region. Some of them are located at the leading edge of the contact, but may be tracers that were initially close to the contact edge and disappeared due to tracking noise. However, for the smallest normal load, $P = 0.05\,\mathrm{N}$, shown in Figure 3.5(d), it seems that a real lifting also occurs at the contact leading edge since the contour on the left side moves inward the contact area.

The color of each disk in Figure 3.5 corresponds to the glass displacement at which the tracer disappears. It seems that the colors of the filled disks are spatially organized, from blue (early disappearance) for the rightmost disks to red (late disappearance) for the leftmost disks. Such a pattern indicates that lifting occurs through an inward front propagation, starting from the trailing edge of the contact (and also from the leading edge for the small load, $P = 0.05\,\mathrm{N}$, see Figure 3.5(d)).

In order to quantify the contact area lost due to lifting, we assign a representative individual area to each tracer. To this end, we performed a bounded Voronoi tessellation of the centroid of the tracers in the initial image, the boundary being the contact contour. Each tracer was thus assigned the area of its Voronoi cell. In Figure 3.5, the grey cells correspond to all Voronoi cells assigned to lifting in the final image (at d_s). Then, for each image, the lifted area is calculated as the sum of the Voronoi cells area of

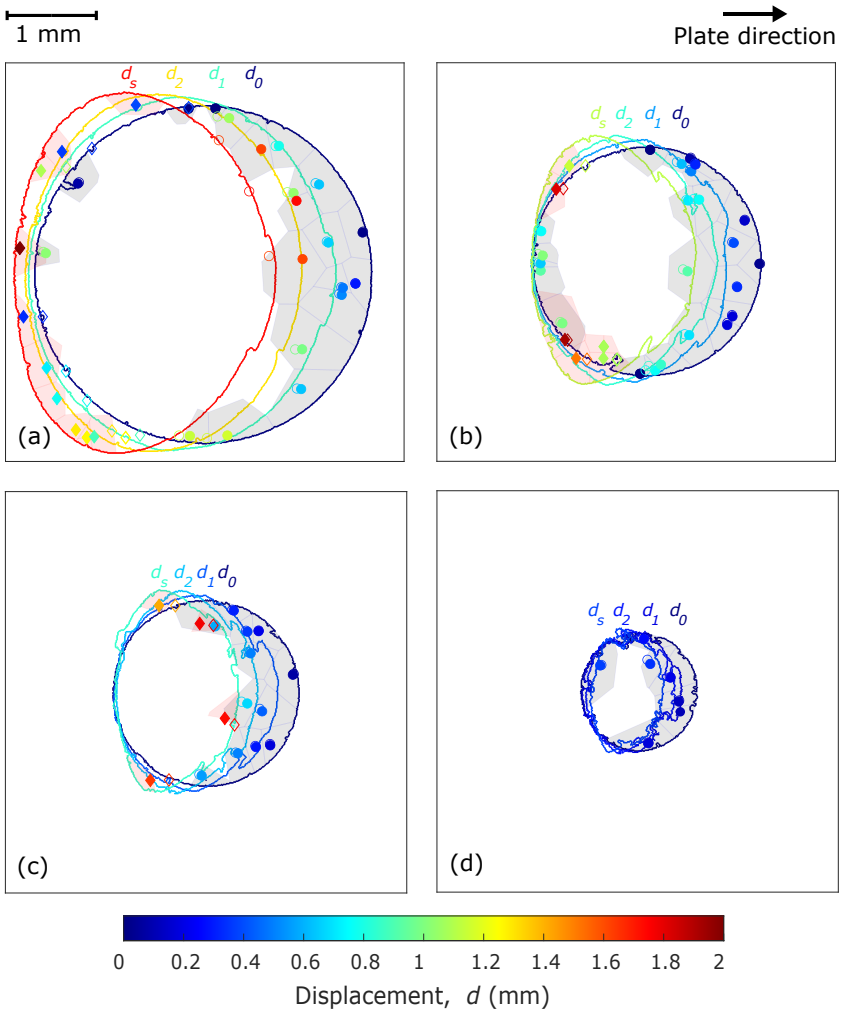

Figure 3.5: Measurement of the lifted and laid areas. (a) $P = 1.85\,\mathrm{N}$, (b) $P = 0.54\,\mathrm{N}$, (c) $P = 0.25\,\mathrm{N}$, and (d) $P = 0.05\,\mathrm{N}$. Solid colored lines: contours of the contact at the four selected displacements (same colors as in Figures 3.1, 3.3, and 3.9). The contours are in the frame of the moving glass plate. The leading edge is on the left side. Open (resp. filled) disks: position of the lifted particles when they disappear (resp. at d_0). The symbol color corresponds to the displacement at which the particle is lifted (same color code as for the contours). Grey cells: cells of the Voronoi tessellation at d_0 associated to lifted particles at d_s. Filled (resp. open) diamonds: position of the laid particles at d_s (resp. when they appear). The symbol color corresponds to the displacement at which the particle are laid. Red cells: cells of the Voronoi tessellation at d_s associated to laid particles at d_s.

all lifted tracers so far. The evolution of the lifted area along the experiments is shown in blue in Figure 3.6 and is stair-like because each lifting event abruptly increases the lifted area by a finite amount (a cell area). The estimated final lifted area for each normal load is shown in Table 3.1. It can be seen that the contact area reduction increases with the decrease of the normal load P, from $\sim 19\,\%$ to $\sim 35\,\%$; one expects the lifted area to behave in the same way. However, the values of lifted cells presented on Table 3.1 must be carefully observed, since, for $P = 1.85\,\mathrm{N}$ and $P = 0.54\,\mathrm{N}$ (see Figures 3.5(a) and (b)), it is taking into account the lifted cells, on the leading edge (left side), presumably

associated to a noise in the images and not to a real contact lifting. This misattribution leads to an overestimation of the lifted area of $\sim 2\,\%$ and $\sim 7\,\%$, respectively.

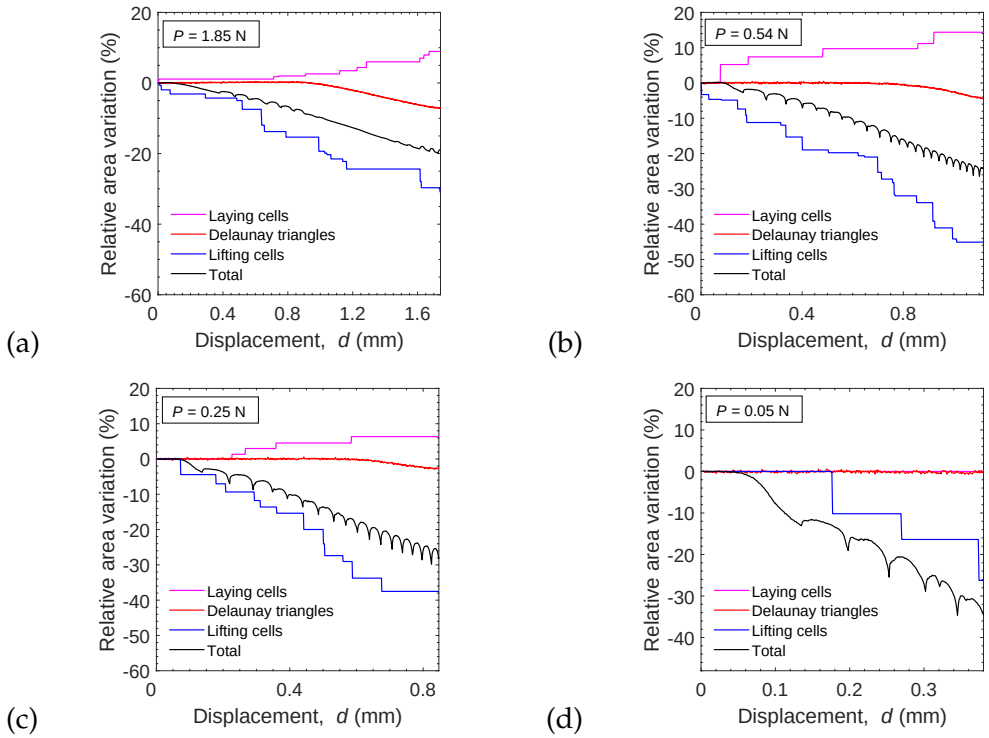

Figure 3.6: Contributions of the various mechanisms to the area variation. (a) $P = 1.85\,\mathrm{N}$, (b) $P = 0.54\,\mathrm{N}$, (c) $P = 0.25\,\mathrm{N}$, and (d) $P = 0.05\,\mathrm{N}$. Relative area variation, $\Delta A/A_0$, *vs* the imposed displacement, d. Black: reduction of the total contact area. Blue (resp. magenta): area lost (resp. gained) by lifting (resp. laying), measured as in Figure 3.5. Red: area variations due to slip-induced in-plane deformation, measured as in Figure 3.7.

Table 3.1: Estimated contribution of contact area reduction mechanisms.

P	Area reduction	Lifted cells	Laid cells	Delaunay triangles
1.85 N	$\sim 19\,\%$	$\sim 31\,\%$	$\sim 9\,\%$	$\sim 7\,\%$
0.54 N	$\sim 24\,\%$	$\sim 45\,\%$	$\sim 14\,\%$	$\sim 4\,\%$
0.25 N	$\sim 28\,\%$	$\sim 38\,\%$	$\sim 6\,\%$	$\sim 3\,\%$
0.05 N	$\sim 35\,\%$	$\sim 46\,\%$	$0\,\%$	$< 1\,\%$

Contact laying

The mechanism of laying, *i.e.* points of the elastomer getting into contact with the glass plate upon shearing, can be analyzed similarly to lifting. The same analysis as in the previous section is performed here, but backward in time: the first image considered is the one at the static friction peak (at d_s), while the last one is the initial image (at d_0). In doing so, tracers appearing close to the contact periphery in forward time are the one disappearing in backward time and therefore those detected by our reverse procedure.

Figure 3.5 shows the results of this analysis, where the locations of the laid tracers are shown in the final configuration (at d_s, filled diamonds) or where they appear (open diamonds). Laid tracers are found at the leading edge of the contact, beyond the initial contact region. Only for $P = 0.25\,\mathrm{N}$ (Figure 3.5(c)), there are two laid tracers found at the trailing edge of the contact (right side), but as mentioned in the lifting analysis, these tracers may initially be located at the proximity of the contact edge and disappeared in backward time due to noise in the images. The filled diamonds color, evolving from blue to red, corresponds to the displacement at which they appear and is again spatially organized, indicating that contact laying occurs through an outward front propagation starting at the leading edge of the contact. No laid tracer is found for $P = 0.05\,\mathrm{N}$ (Figure 3.5(d)), indicating that laying mechanism may not occur under such small normal load, a regime in which adhesion stresses are expected to dominate [49]. However, the very low resolution of our analysis in such a small contact area with very few tracers does not fully validate this hypothesis and further investigations are required.

The amount of contact area gained via laying is estimated using a bounded Voronoi tessellation performed in the final contact configuration (at d_s). In Figure 3.5, the red cells correspond to the area assigned to laying in the final image (at d_s). At each instant, the laid area is counted as the sum of the areas of all laid tracers. The evolution of the area gained due to laying is shown in magenta in Figure 3.6. Unlike lifting, the laying mechanism initiates only after a finite shear is applied, and it seems to increase as the normal load increases, as shown in Table 3.1. The values of laid cells consider the ones attributed to noise in the images in $P = 0.25\,\mathrm{N}$ (Figure 3.5(c)) with tracers located at the trailing edge of the contact and in $P = 0.54\,\mathrm{N}$ (Figure 3.5(b)) with tracers located inside the initial contour at the leading edge, resulting in an overestimation of the laid areas of $\sim 3\,\%$ for both $P = 0.54\,\mathrm{N}$ and $P = 0.25\,\mathrm{N}$.

In-plane deformation

In previous analyses of tracers' displacement, it is observed that a peripheral slip region gradually invades the contact replacing a central stuck area as shear increases. Moreover, in both contact lifting and laying, the filled and open markers have different

locations regarding the glass plate (see Figure 3.5), which clearly means that slip occurs between the two instants. Local lifting is preceded by a slip, while local laying is followed by a slip. In both analyses, slip is found to be roughly parallel, but opposed to the glass plate motion, and it occurs in both the leading and trailing regions of the contact.

From the combination of backward slip at the trailing edge and a stuck zone at the contact center, one expects in-plane compression of the elastomer in the trailing half of the contact. Symmetrically, in-plane dilation is expected in the leading half. The overall effect of both types of in-plane deformation must lead to a change in contact area that was estimated as follows.

Only the tracers present in the initial image and that could be followed from d_0 to d_s, thus excluding the lifted and laid ones, were considered. A Delaunay triangulation was performed to mesh these tracers in the initial image, as shown as a grey network in Figure 3.7(a). As shear increases, the tracers move relative to each other. By keeping the same connectivity within the mesh, but updating the position of the tracers (sites), the relative changes of the areas of all the triangles of the initial Delaunay triangulation were monitored and the local in-plane deformation is thus estimated as these relative area changes.

Figure 3.7 shows, for the four normal loads (in the rows), the evolution of the in-plane deformation field as shear increases (cold colors for compression, warm ones for dilation). Before d_1 (b) no deformation is observed, presumably because the slip front has not reached yet the fraction of initial contact covered by the Delaunay triangulation. Between d_1 (b) and d_2 (c), a compressed region sets in at the trailing side of the contact; the absence of a detectable symmetrical dilated region on the leading side suggests that the propagation of the slip front is not axisymmetrical, as usually considered in models of the incipient shear loading of circular linear-elastic contacts [82]. At d_s (d), a heterogeneous slip-induced in-plane deformation field is fully developed, with a large compression region on the trailing side and a smaller dilation region on the leading one. Those field measurements are qualitatively consistent with previous measurements of Barquins and Courtel [78] and Barquins [79] on a similar system, but made only along the central line of the contact in steady-state sliding.

The evolution under shear of the sum of the total area contained in the deforming

Delaunay triangulation is shown in red in Figure 3.6. This area remains essentially unchanged during the first half of the experiment, and then progressively decreases by up to about 7 %, 4 %, 3 %, and <1 % of the initial contact area for $P = 1.85\,\mathrm{N}$, 0.54 N, 0.25 N, and 0.05 N, respectively.

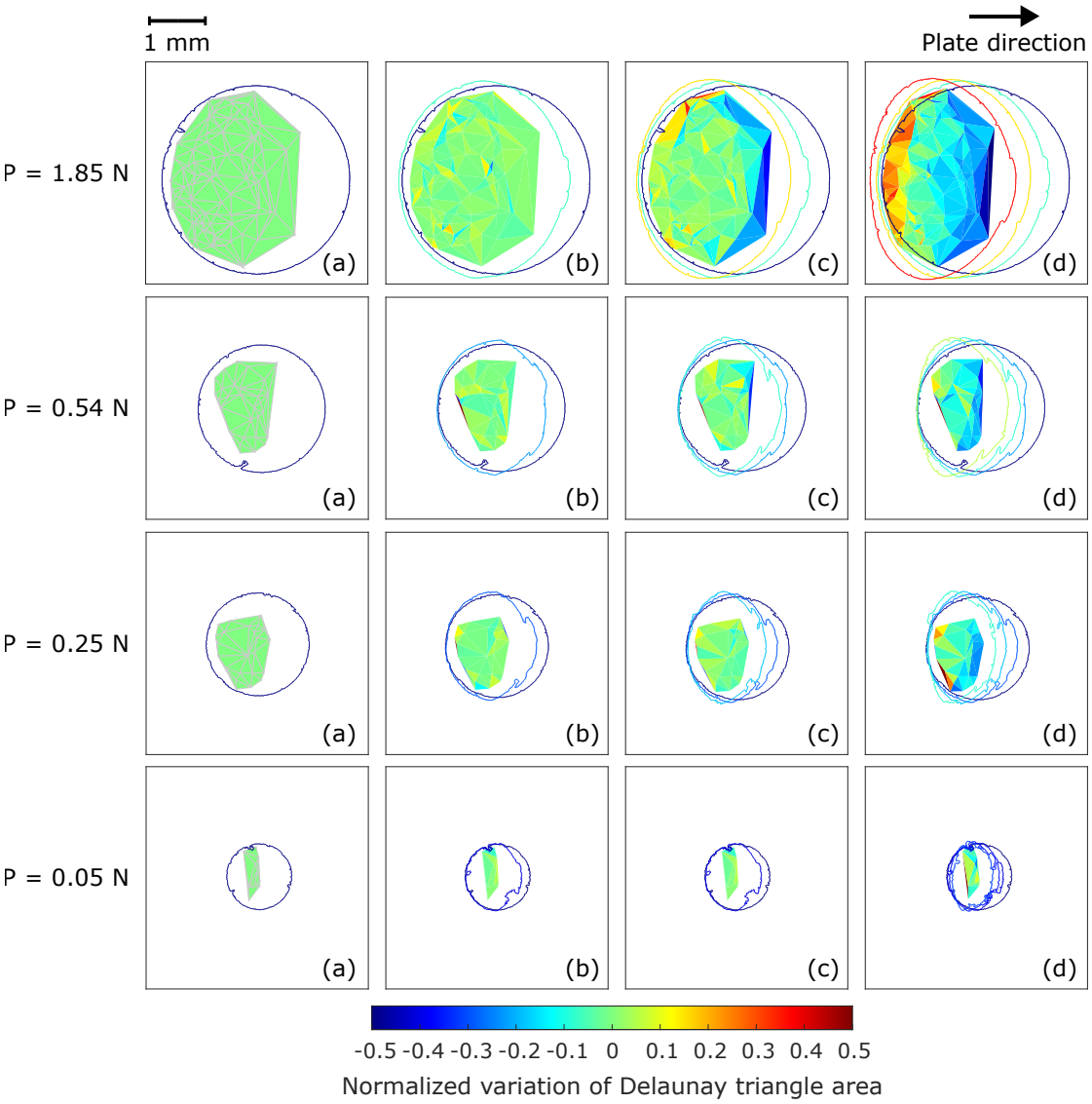

Figure 3.7: In-plane deformation measurement. (a) Grey network: Delaunay triangulation based on all tracers of the first image (at d_0) that can be tracked until d_s. (b-d) Snapshots of the evolution of the Delaunay triangles (defined at d_0) at successive instants: d_1 (b), d_2 (c), and d_s (d). Solid lines are the contours of the contact at d_0, d_1, d_2, and d_s with the same color code as in Figures 3.1, 3.3 and 3.5. The color of each triangle corresponds to its relative area change with respect to the situation at d_0 (see colorbar). Colder (resp. warmer) colors mean in-plane compression (resp. dilation).

Uncertainties on the area changes evaluation

The uncertainties of the above experimental measurements are mainly related to the finite surface density of useful tracers. Table 3.2 shows the number of tracers larger than 4 pixels in the initial image of each experiment, on which the tracking procedure has been applied. As well as the the amount of tracers useful for the Voronoi (*i.e.* corresponding either to lifted or laid tracers) and Delaunay analysis. Not all the tracers were used in the analyses due to the exclusion of the tracers containing non-realistic trajectories, see Section 3.2.2.

Table 3.2: Number of tracers applied on the analyses.

P	Tracers	Voronoi analysis	Delaunay analysis
1.85 N	263	31	174
0.54 N	140	30	48
0.25 N	89	16	34
0.05 N	48	7	12

Table 3.3 summarizes the average Voronoi area of the useful cells and their fraction of the initial contact area. In practice, due to the randomness of the tracers' location, the individual areas varied considerably, as show in the fourth column. Because the Voronoi cells are the smallest units of area involved in the lifting (resp. laying) analysis, the evolution rate of the estimated lifting (resp.laying) area suffers from large fluctuations. In fact, each drop (resp. rise) in the blue (resp.magenta) curves of Figure 3.6 are linked to the simultaneous subtraction (resp.addition) of one or more Voronoi cells with a radom area.

Table 3.3: Voronoi areas.

P	Avg. Voronoi area (mm^2)	Avg. Voronoi area (%)	Range of Voronoi area (%)
1.85 N	0.15	1.33	0.21 - 3.99
0.54 N	0.12	2.20	0.21 - 5.27
0.25 N	0.10	2.74	1.66 - 4.71
0.05 N	0.10	6.76	3.55 - 9.86

Avg: average

In addition, the final estimate of the lifted area is actually an overestimation. Because, for the latest lifted cells, the fraction of area at the left of the tracer has not been really lifted yet. The same discussion applies to the estimation of the final laid area. Both effects would be reduced with a larger density of tracers, resulting in smoother curves with smaller step amplitudes.

Concerning the estimate of in-plane deformation, the region probed by the Delaunay-based analysis is only a fraction of the target region (the part of the initial contact that never lifts nor lays during the experiment). This is apparent for instance in Figure 3.7(a), for all normal loads P, with the white strip between the leading part of the contact contour and the Delaunay triangulation. An analogous strip is also lost on the trailing side, between the Delaunay triangulation and the lifted region. Those strips are due to the fact that only the tracers that could be followed from d_0 to d_s (excluding the lifted and laid ones) were considered in this analysis. Because the largest strains are precisely expected to be found on the periphery of the Delaunay triangulation (see Figure 3.7(d)), the estimate of the area lost by in-plane deformation may be subject to a significant error. The values in Table 3.1 of area reduction due to this mechanism must then be taken with caution.

3.3.2 Evolution of tracers displacement

The displacement of each tracer relative to its initial position in the contact area Δd_t is measured and show in Figure 3.8 as a function of the time t for the four normal loads. The instant of the static friction force Q_s is indicated as a vertical line. The trajectory of tracers considered to be lifted out-of-contact (see Section 3.3.1) before the end of the experiment are shown in black, while colored lines represent the tracers present from the initial (at $t = 0\,\mathrm{s}$) to the end of the experiment (at $t = 20\,\mathrm{s}$). Cold colors are for the smallest displacements and warm colors for the largest ones at Q_s.

We can see in Figure 3.8 that each particle, basically, has two main regimes. The first one, at a low times/tangential displacements, corresponds to a stuck regime during which the particles stay nearly at the same position in the glass moving frame, which means that they are stuck to the moving glass plate. In reality, one can notice that in this regime, especially for the highest loads, the position of each particle does not remain exactly unchanged (vanishing displacement). This small unexpected displacement can presumably be attributed to the bulk deformation of the PDMS under shear. Indeed, the particles are not precisely located at the interface ($\sim 16\,\mu$m in depth) and thus they can be slightly displaced in the direction of the shear even if no relative displacement (slip) occurs at the interface. Note that a similar phenomenon was observed at a rough contact interface in [62]. The second regime, at large times/tangential displacements,

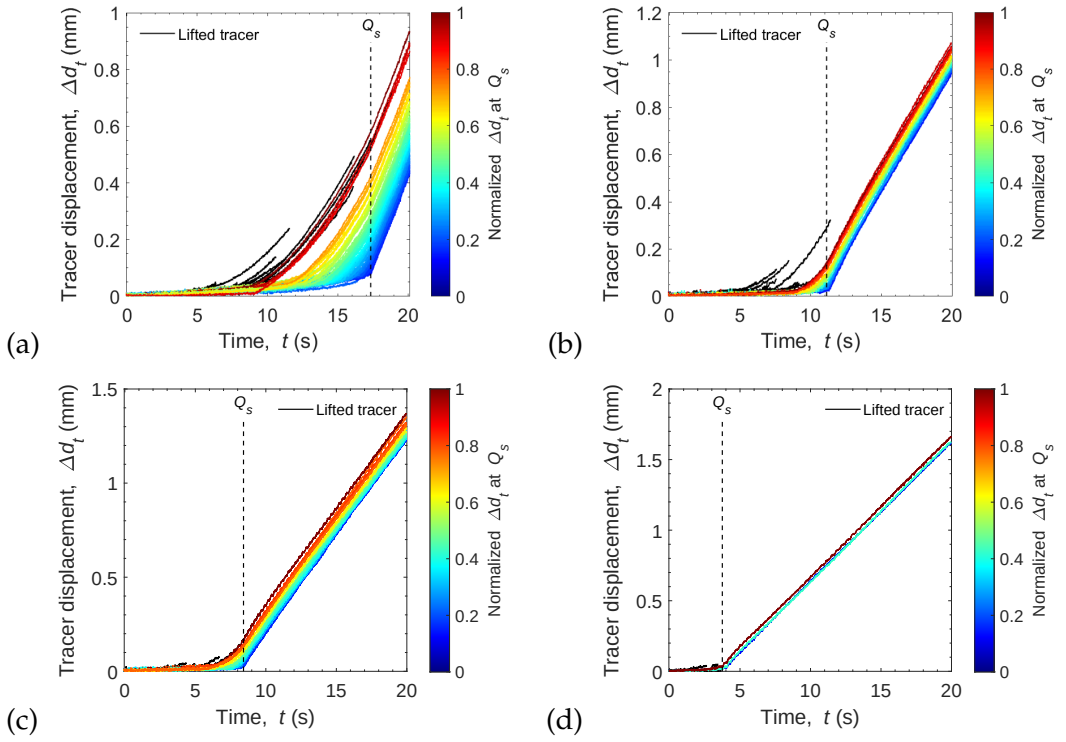

Figure 3.8: Tracers displacement *vs* time. (a) $P = 1.85\,\mathrm{N}$, (b) $P = 0.54\,\mathrm{N}$, (c) $P = 0.25\,\mathrm{N}$, and (d) $P = 0.05\,\mathrm{N}$. Vertical line indicates the instant of the static friction force Q_s. Black lines: tracers' trajectories that are lifted out-of-contact before the end of the experiment (at $t = 20\,\mathrm{s}$). Colored lines: tracers present from the beginning to the end of the experiment. Cold colors are for the smallest displacements and warm colors for the largest displacements at Q_s.

corresponds to a full sliding regime during which the particles stay in place in the laboratory frame, *i.e.* move at the glass velocity in the glass frame.

By focusing on the transitions between those two regimes, for each particle, three important observations can be made: (i) the transitions at the various tracers are spread over a period of approximately half the duration to reach the peak; (ii) the order of departure of the transition respects the color code used which means that the first particles that have slipped (warm color) are those in the end which have slipped the most; and, (iii) the larger the time/displacement at which the transition occurs, the more abrupt it is: the last particle which slips (*i.e.* the one corresponding to the darkest blue curve) clearly shows a sharp kink between the two regimes.

All of these observations seem to indicate that there is a temporal and spatial organization in the transition to sliding within the interface. Then, to better spatially address each tracer displacement in the contact area, their magnitude is represented by iso-displacement contours in Figure 3.9.

As in Figure 3.8, cold colors are for the smallest displacements and warm colors for

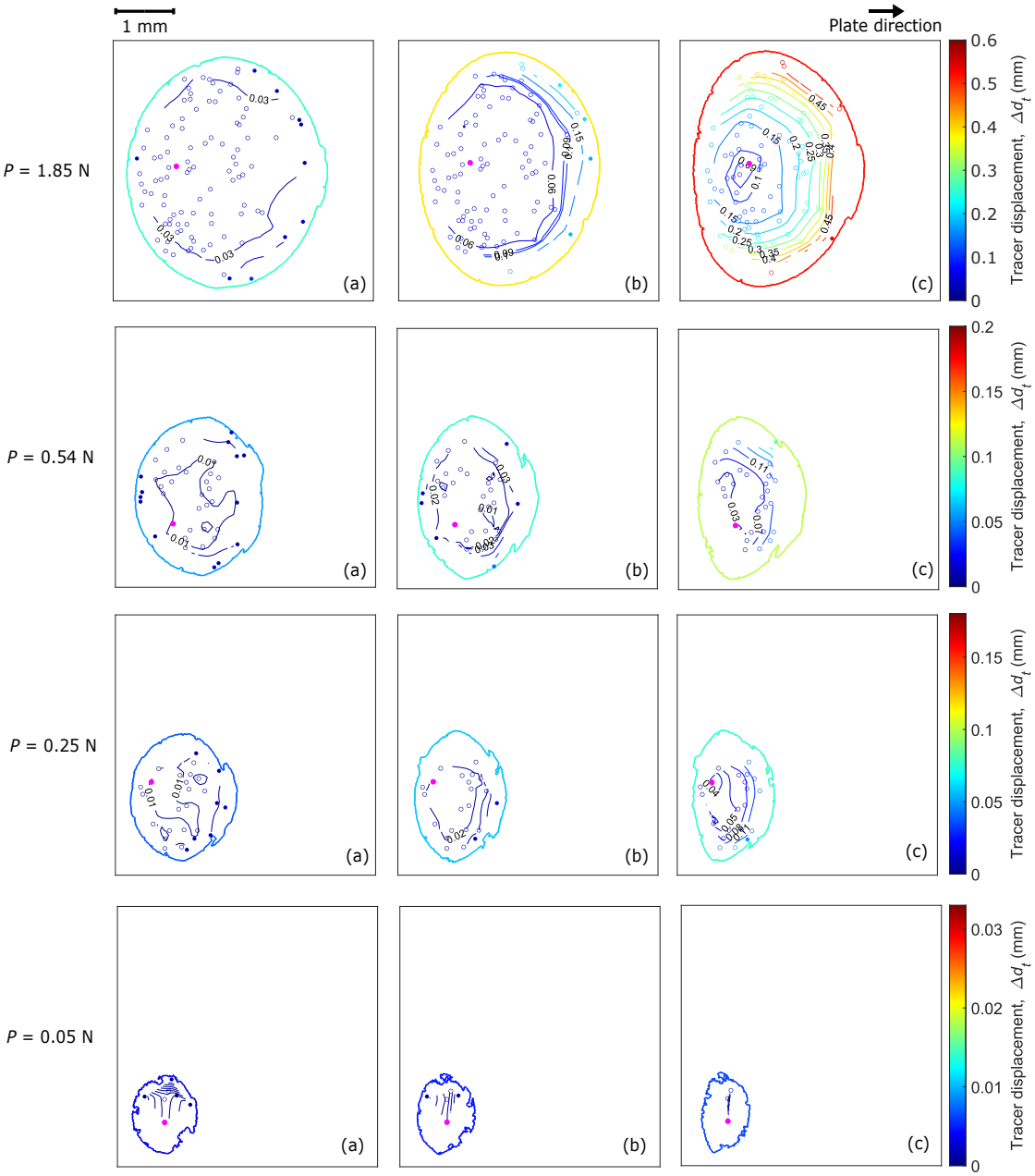

Figure 3.9: Iso-displacement contours of the tracers displacement for all normal loads. The outer contour defines the contact area at the instants (a) d_1, (b) d_2, and (c) d_s with the same color code as in the previous Figures 3.1 and 3.3. Lifted tracers at Q_s, *i.e.* tracers that up to Q_s will be lifted, are represented as filled disks (•), while open disks (○) are for tracers present throughout the experiment (from $t = 0\,\mathrm{s}$ to $t = 20\,\mathrm{s}$); their color is the same of the sets of iso-displacement contours. Cold colors are for the smallest displacements and warm colors for the largest ones for both tracers and iso-displacement contours. The filled magenta disk (•) is the last tracer to slip.

the largest ones at Q_s. The outer contour defines the contact area at the instants (a) d_1, (b) d_2, and (c) d_s with the same color code as in the previous Figures 3.1 and 3.3. The tracers lifted during the experiment are represented as filled disks, while open disks are for tracers present throughout the experiment; their color follows the same

color code that of the sets of iso-displacement contours, *i.e.* showing the magnitude of the tracers displacement. We assumed a displacement greater than 0.03 mm as a slip. This threshold (not equal to 0) is set to account for the unexpected displacement of the particles in the stuck regime due to their depth relative to the interface. Note that this fixed threshold should, ideally, be considered as a function of the PDMS bulk deformation under shear.

By following the evolution in time of the 0.03 iso-value curve, *i.e.* the limit between stuck and slip region, it can be seen that a micro-slip front moves inward from the contact periphery as shear increases. As expected, at $d = d_s$, this slip front converges and disappears around the last tracer to slip (show as a filled magenta disk in Figure 3.8).

Both figures, Figure 3.8 and Figure 3.9, are consistent with a context of a partial slip, which is classical in sheared sphere/plane contacts, either rough [62] or smooth [61]. This scenario is also apparent in the movies (M185, M054, M025, and M005) where a peripheral slip region gradually invades the contact, replacing a central stuck area. Those observations are less evident to be performed with small normal loads, due to the lower density of tracers in such normal loads, hindering a more conclusive analysis.

To draw attention to some specific points of Figure 3.8, Figure 3.10 shows, on the left axis, the displacement curves for the last tracer to slip (blue line), the first never lifting tracer to slip (red line), and the first lifted tracer to slip (black line) as a function of time; on the right axis (grey color), $Q(t)$ is shown. The slope of the hatched area represents the velocity of the moving glass ($V = 0.1\,\mathrm{mm/s}$). Highlighting the evolution of those three tracers allows us to identify different stages during their evolution:

Stuck state (1-2): from the beginning of the displacement (1) when the glass plate starts to move, the tracers are dragged with the glass (no relative tracers displacement), up to the instant that the first tracer slips (2). Note that the first tracer to slip (black line) belongs to the set of tracers that will be lifted (in the four normal loads).

Partial slip (2-4): the slip of the first tracer (2) means that local slip occurs very soon after the onset of the shear. During the branch (2-4) more and more tracers start to slip at different instants as a slip front propagates inward (as can be seen in Figure 3.9). This slip front defines the frontier between a slip and a stick region, meaning that during all this period the interface is under partial slip condition. At the instant (3) the first never lifted point starts to slip, and in (4) the last tracer slips and the macroscopic sliding

regime initiates. This moment corresponds with the tangential force peak Q_s, at least for the highest explored normal load. At lower loads, the lack of resolution of our set of experiment does not allow such a conclusion with high certainty. Note that the last tracer to slip is located in a central region on the contact area (filled magenta disk in Fig 3.9). The fact that the tracers start to slip at different instants results in a heterogeneous slip field, thus leading to the in-plane deformations discussed previously in Section 3.3.1.

Transient sliding (4-5): at the very beginning of sliding of each tracer, the slope of the curves seem to increase, meaning that the velocity of each tracer accelerates reaching a velocity even greater than the glass velocity V, *i.e.* the slope of the curves greater than the slope of the hatched area, before stabilising at V. Such transient sliding may be due to a process of interfacial relaxation, and its duration increases with the increase of the normal load, from (d) to (a) in Figure 3.10. Note that for $P = 1.85\,\mathrm{N}$, the experiment duration was not sufficient to allow all tracers to stabilize their velocity at V.

Steady state sliding (5-end): after the accelerated sliding period, all slipping tracers reach the same velocity as the glass (5), *i.e.* the slopes of the curves and of the hatched area are the same, meaning that a steady macroscopic sliding is reached.

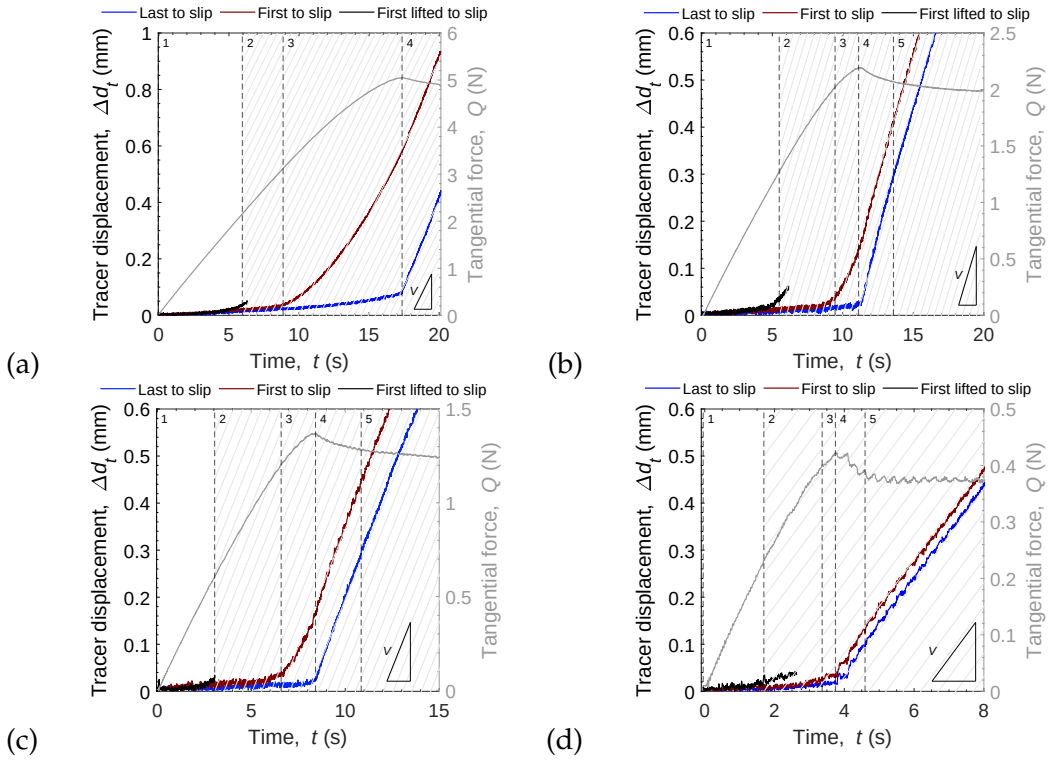

Figure 3.10: Evolution of the tracers for (a) $P = 1.85\,\mathrm{N}$, (b) $P = 0.54\,\mathrm{N}$, (c) $P = 0.25\,\mathrm{N}$, and (d) $P = 0.05\,\mathrm{N}$. Left axis (black color) is shown the last tracer to slip (blue line), the first never lifted tracer to slip (red line), and the first lifted tracer to slip (black line) as a function of the time; the right axis (grey color) shows $Q(t)$. Evolution states of the tracers: (1-2) stuck state, (2-4) partial slip, (3) first never lifted tracer to slip, (4-5) transient sliding, and (5) steady state sliding. The slope of the hatched area represents the velocity of the glass $V = 0.1\,\mathrm{mm/s}$.

3.3.3 Finite-strain modelling of shear-induced contact area reduction

In collaboration with J. Lengiewicz and S. Stupkiewicz from Institute of Fundamental Technological Research (IPPT), Polish Academy of Sciences, a 3D model that combines a hyperelastic bulk and a non-adhesive but frictional interface was developed to evaluate the findings of the experimental analysis in terms of elementary mechanisms of shear-induced contact area reduction - lifting, laying, and in-plane deformation. The model results were prepared to be matched quantitatively with the literature experiments of [17, 63]. However, those literature results are similar enough to the ones obtained earlier in this chapter to enable a qualitative comparison with the same model. The results were presented in the published article "Finite deformations govern the anisotropic shear-induced area reduction of soft elastic contacts" [60], and a summary of the model and simulation part will be presented here.

Computational model: finite-strain framework and Tresca friction

The finite strain framework and Tresca friction model (see below) without adhesion are the two basic features of the model. They are combined with a finite element method as a suitable spatial discretization scheme. The contact problem under consideration, sketched in Figure 3.11 from Lengiewicz et al. [60], corresponds to normal, and then tangential loading of a hyperelastic spherical solid in (adhesionless) frictional unilateral contact with a rigid plate.

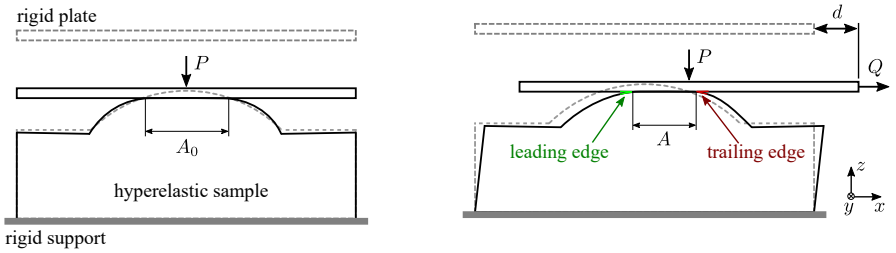

(a) (b)

Figure 3.11: 2D sketch of the (3D) soft-sphere/rigid-plane contact under study. The initial (dashed lines) and deformed (solid lines) configurations are shown for two stages: (a) under pure normal load P and (b) when an additional tangential displacement d is applied, giving rise to a tangential load Q. In all subsequent figures, the leading (resp. trailing) edge is always on the left (resp. right) side. A_0 and A indicate the contact areas in the initial and deformed configurations, respectively. Figure from [60].

Hyperelasticity is treated using the nearly-incompressible isotropic neo-Hookean model. Such a model is used for predicting the nonlinear stress-strain behavior of materials, like elastomers and polymers, undergoing large deformations [83]. For the frictional behaviour of the contact interface, the Tresca model is employed. In this model, no local slip occurs until the contact shear strength σ is reached, and σ is assumed constant and independent on the normal contact traction. It was chosen because it is the simplest model that produces a proportional relation between the friction force of sphere/plane contact interface and its contact area, a relationship reported experimentally in many frictional contacts (see, *e.g.*, Sahli et al. [17] and references therein). In the Tresca model, the proportionality constant will simply be the contact shear strength, σ.

The model parameters were taken to match their experimental counterpart in [17, 63]. The elastic properties of the elastomer sample are specified by the shear modulus μ and bulk modulus κ. Assuming a nearly incompressible response with the Poisson's ratio of $\nu = 0.49$, the Young's modulus has been identified as $E = 1.80\,\text{MPa}$. The

relationship between the parameters (E, ν) and (μ, κ) is given by $\mu = E/(2(1+\nu))$ and $\kappa = E/(3(1-\nu))$ and corresponds to a shear modulus of $\mu = 0.60\,\text{MPa}$ and a bulk modulus of $\kappa = 0.40\,\text{MPa}$. A value of $\mu = 0.60\,\text{MPa}$ was derived in a unique manner using the experimental values of P and $A(Q=0)$. Similarly, a value of $\sigma = 0.41\,\text{MPa}$ was derived using the experimental values of A_s and Q_s. Note that the ratio σ/μ is significant, such that shear strains exceeding 50 % are expected. This is far beyond the range of validity of the small-strain theory, and of linear elasticity in particular, so that the finite-strain framework used in this study is, actually, essential. At those large strains, the mechanical behaviour of the elastomer used in the experiments of Sahli et al. [17, 63] (Sylgard 184) is already well beyond its linear range [84, 85].

Shear-induced contact area reduction

Firstly, using the computational model described above, the shear-induced contact area reduction in the literature sphere/plane experiments of Sahli et al. [17, 63] were simulated and qualitatively compared in Fig 3.12. Figure 3.12(a) directly compares the predicted $A(Q)$ curves with those of Sahli et al. [17] (see their Figure 2C). The solid red line correspond to the relation $Q = \sigma A$. Figure 3.12(b) compares the predicted contact sizes along and orthogonal to shear, $\ell_{\parallel}$ and $\ell_{\perp}$ respectively, with those of Sahli et al. [63] (see their Figure 3b). In both cases, the amplitudes and shapes of the curves are well captured, although the model slightly underestimates A and does not capture the slight increase of $\ell_{\perp}$ observed in the experiments.

Elementary mechanisms of contact area reduction

Secondly, a thorough analysis of the simulation results of this model was used to validate the experimental findings of Section 3.3.1, to test whether the elementary mechanisms - lifting, laying and in-plane deformation - responsible for contact area reduction in the experiment can also be identified in the model.

Figure 3.13 shows the evolution of the contact area, for the normal loads $P = 0.27\,\text{N}$ and $P = 2.12\,\text{N}$, during the incipient tangential loading at five selected displacements of the rigid plate: $d_0 = 0$, d_s at the onset of global sliding and three intermediate configurations (d_i). The nodes of the elastic surface are labeled in red if they have undergone some local slip, in blue if they are still stuck to the same point of the rigid plate, and

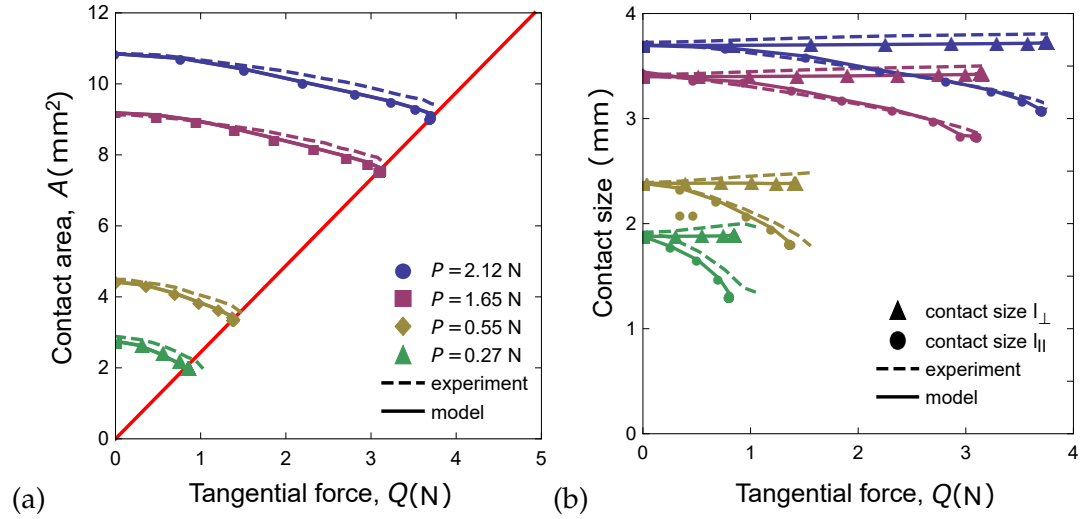

Figure 3.12: Comparison of the model predictions obtained for the model, for all normal loads, to the experimental results of [17, 63]. (a) A *vs* Q. Solid straight red line: $Q = \sigma A$. (b) Contact size along ($\ell_\parallel$) and perpendicular to ($\ell_\perp$) the shear loading direction *vs* Q. Figure adapted from [60].

in green if they were initially in contact and not anymore at the onset of macroscopic sliding.

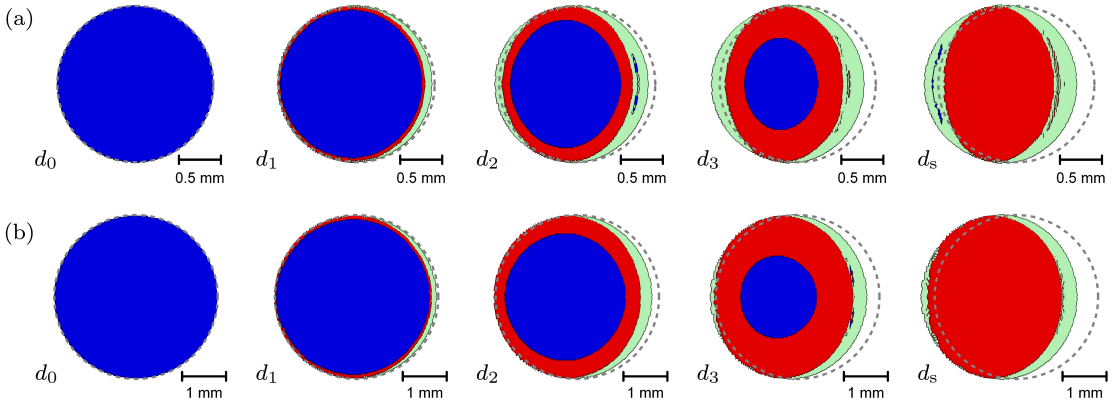

Figure 3.13: Evolution of the contact zones for (a) $P = 0.27\,\mathrm{N}$ (d_1, d_2, d_3: 35, 61, 81 % of $d_s = 0.45\,\mathrm{mm}$) and (b) $P = 2.12\,\mathrm{N}$ (d_1, d_2, d_3: 29, 58, 80 % of $d_s = 1.04\,\mathrm{mm}$) shown in the frame attached to the moving rigid plate. Dashed circles indicate the boundary of the initial contact zone (at d_0). Blue and red regions denote the stick and slip zones, respectively. Green regions indicate the current (deformed) location of the initial contact zone that has been lifted. The leading edge is on the left. Figure from [60].

As in the experimental findings observed earlier in this chapter and in the experiments of Sahli et al. [63], the contact zone and the stick zone have an elliptical shape, the related shear-induced anisotropy increases with increasing displacement d and is higher for the lower normal loads.

The labeled nodes allow us to identify the same mechanism as those found in the experiments. First, the region of contact lifting clearly corresponds to the green region

around the final contact zone, *i.e.* the region that corresponds to nodes that have been lifted out-of-contact during the incipient loading due to the shear-induced deformations of the elastic sphere. Second, region of contact laying correspond to small parts (hardly visible in Figure 3.13 d_s) of the final contact which are found outside the deformed initial contact region (shown as a green region in the current configuration). These nodes were initially out of contact, but laid into contact during the incipient tangential loading. Finally, in-plane deformation, related to inhomogeneous slip, is also find in the model within the contact zone and leads to either "in-plane compression" or "in-plane dilation". Indeed, in Figure 3.13, the slip zone advances from the contact periphery towards the centre at the expense of the stick zone until the stick zone vanishes and full sliding occurs. As in our experiments (see Figure 3.9), an inward slip front, corresponding to the boundary of the blue region (*i.e.* the frontier between the stick and slip zones) can be identified and is responsible for the inhomogeneous strain field at the interface. Such deformations extend beyond the contact region, which explains why the boundary of the green zone does not coincide with the dashed circle.

The partial slip configurations, as those seen in Figure 3.13, are classically found (with a circular stick zone) in models of sheared frictional linear elastic sphere/plane contact [30, 82]. They typically correspond to heterogeneous slip fields, thus causing in-plane deformations.

Figure 3.14 provides a detailed insight into this last mechanism, by showing the field of local surface dilation/compression. For each contact node i, its tributary area (*i.e.* the area associated with the node) is computed both in the initial configuration (at d_0), A_0^i, and in the current configuration, A^i. The color map in Figure 3.14 corresponds to the local surface dilation/compression, $(A^i - A_0^i)/A_0^i$. Surface dilation is observed close to the leading edge while compression is observed close to the trailing edge. The decreasing green elliptical region in the middle of the contact zone, in which the local surface dilation/compression is equal to zero, corresponds to the stick zone in Figure 3.13.

Figure 3.15 compares the individual contributions of all mechanisms to the total relative contact area change in the model. For all normal loads, the model predicts that lifting represents about 90–95 % of the total shear-induced area reduction, indicating it as the primary mechanism responsible for the area reduction. The contributions of

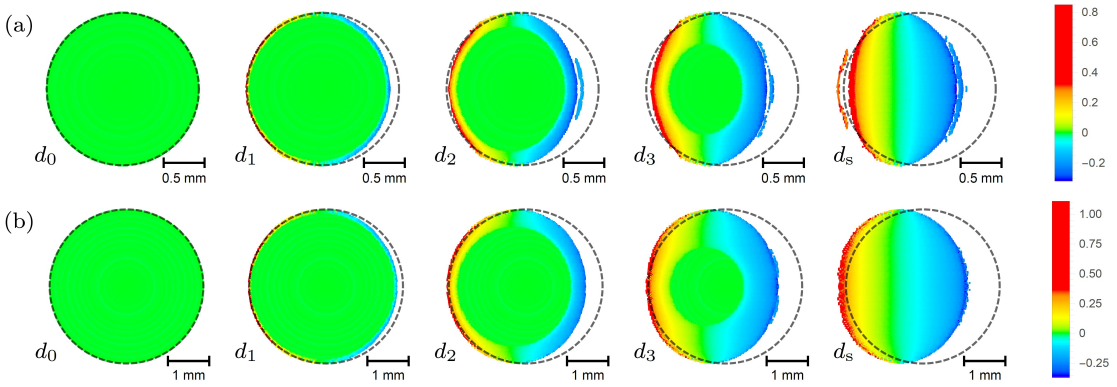

Figure 3.14: Evolution of the field of surface dilation/compression, $(A^i - A^i_0)/A^i_0$, shown in the frame attached to the moving rigid plate for (a) $P = 0.27\,\mathrm{N}$ and (b) $P = 2.12\,\mathrm{N}$, and for the same select displacements as in Figure 3.13. Dashed circles indicate the boundary of the initial contact zone. The leading edge is on the left. Figure from [60].

dilation and compression are individually significant, however, they essentially cancel each other out, so that the in-plane deformation is responsible only for about 5–10 % of the total area reduction. Contact laying is rarely observed (if so, at the leading edge only), therefore its contribution to the total area reduction is essentially negligible in the model.

We emphasize that the relevant lifting in our model is a local lifting due to shear deformations of the elastic sample, rather than a shear-induced global lifting of the rigid plate. Such a global lifting, although existing in the constant normal load setting of the model, has been found to be only about 4 % of the normal displacement associated with the initial, purely normal loading. Thus, it is far from sufficient to explain the 15–30 % area reduction observed in Figure 3.15.

Summary

The model just presented has been shown to capture quantitatively the experimental results of [17, 63] about the anisotropic shear-induced area reduction of sphere/plane elastomer contacts for relatively large normal loads (Figure 3.12) and also the results of the experimental observations presented in this chapter. The agreement was obtained without any adjustable parameter, in the sense that virtually all model parameters are set by independent measurements on the same experimental system. Those

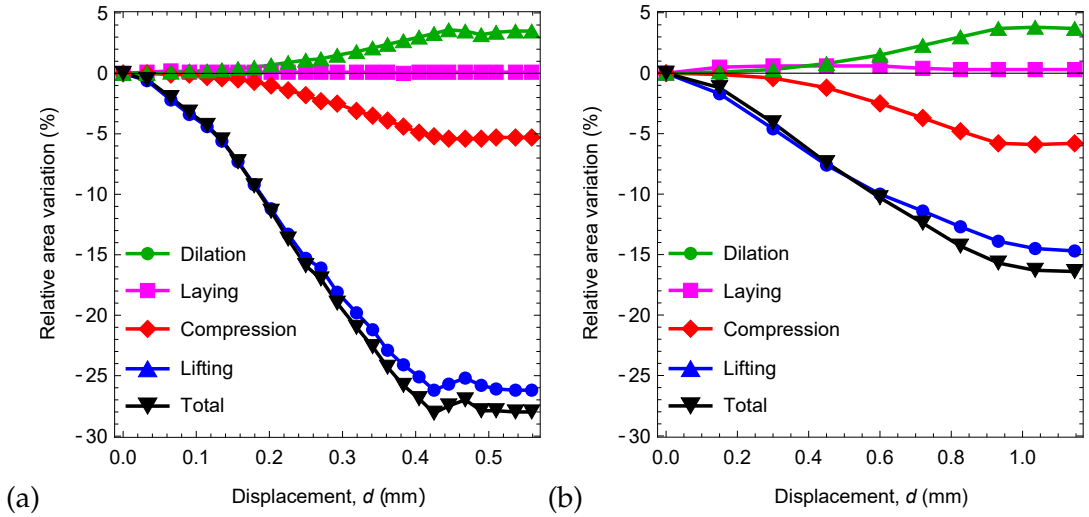

Figure 3.15: Evolution of the individual contributions of the various elementary mechanisms to the total relative area variation $\Delta A/A_0$ as a function of the rigid plate displacement d. (a) $P = 0.27\,\mathrm{N}$ and (b) $P = 2.12\,\mathrm{N}$. Figure adapted from [60].

parameters are: the geometry of the hyperelastic neo-Hookean sample, its shear modulus, and the contact shear strength of the PDMS/glass interface. This absence of adjustable parameters provides the presented model with a decisive comparative advantage over competing models with reduced contact area induced by shear. Especially, fracture-like adhesion-based models, that in order to offer a good quantitative agreement with experiments [53, 86], require a prescription of finely-tuned mode-mixity functions [52]. The presented 3D model also captures the anisotropic evolution of the contact shape, whereas most fracture-based adhesive models assume axisymmetry of the contact (see Papangelo et al. [53] for the only exception, to our knowledge).

The direct implication of the model is that finite-deformation effects and the non-linear elasticity of elastomers are presumably the key ingredients explaining the experimental results, rather than viscoelasticity or adhesion. Nevertheless, the model has only been applied to contacts submitted to relatively large normal load, in the newton range [17], while other experiments have used much smaller normal loads, in the millinewton range [46, 49, 55]. For those smaller loads, adhesive stresses may be of the order of, or even exceed, contact stresses, and non-linear elasticity may be not the only dominant ingredient for shear-induced contact shrinking anymore. Identifying the normal load regimes in which adhesion needs to be accounted for is an important goal not only for future contact mechanics models but also for experiments. In face of this, we will present in Chapter 4 an experimental study in a wide range of normal loads.

3.4 Discussion

An original experimental analysis using an elastomer sphere seeded with particles identified different stages during the sliding process and the presence of three elementary mechanisms - lifting, laying, and in-plane deformation - responsible for the anisotropic contact area reduction. Although a higher area density of tracers would be desirable to reduce the measurement uncertainties, particularly at small loads (Section 3.3.1), lifting is presumably the dominant area reduction mechanism, while a non negligible contribution of the laying and in-plane mechanisms exists as the normal load increases. The observations suggest that the contributions of those mechanisms are load-dependent and that different phenomena govern at small and large normal loads.

A typical transition between a stuck state to a sliding one, *i.e.* the transition between the static to kinetic friction is usually defined by a peak in a tangential-time curve followed by an abrupt decrease. However, experimentally, such a peak is not well apparent, which leads us to question: *where is the onset of sliding?* The observations in Section 3.3.2 show that the frictional sliding undergoes different stages and partial slip starts well below the static friction force Q_s with micro slip occurring at different instants, for different tracers, until Q_s. The profile of tracers' trajectory has shown a quite asymmetrical displacement in the contact zone and a less pronounced transition to macroscopic sliding as the normal load increases. Surprisingly, the velocity of the tracers reached a velocity even greater than the glass velocity V before finally reaching it. As pointed out, such observation may be due to a process of interfacial relaxation, that is, the interface is in a deformed state, it has stored elastic energy, and part of this elastic energy must be restored to return to a less-deformed state during the macroscopic sliding state.

The incipient shear-loading of smooth sphere/plane elastic contacts is characterized in the experiments and in the model by two propagating fronts: a lifting front at the contact periphery, and a non-circular micro-slip front within the contact area. The existence of those two different fronts, although explicitly acknowledged by some authors [58, 87], has never been properly described in fracture-based adhesive models. Indeed, in those models, the additional energy dissipation in the contact due to frictional micro-slip, and described via the mode-mixity function, is assumed to be located

at the contact periphery, and not within a growing, finite region of the contact.

For the first time, the elementary mechanisms of area change were quantified. And, as in the experiments, the modeling results suggest that for the experimental conditions used in [17, 63], local lifting is the main mechanism explaining the significant area reduction observed and its anisotropy (Figure 3.15). For all normal loads explored, this conclusion is true, with the total area reduction being dependent on the normal load (as also observed experimentally).

In summary, lifting is presumably the main area reduction mechanism in both experiments and model. While experiments revealed a potentially larger contribution of the laying and in-plane mechanisms for large normal loads, a definitive quantitative comparison with the model is hindered by the finite experimental resolution. Also note that, due to the higher contact shear strength (0.53 rather than 0.41 MPa) and smaller Young's modulus (1.5 rather than 1.8 MPa) of this chapter's experiments compared to those of [17, 63], the numerical model could not converge in those more severe conditions, thus impeding direct comparison between model and tracer-based experiments. Such a comparison is also an important challenge for future work.

Finally, the simplicity and generality of the model assumptions suggest that the results may be also relevant to other systems than the elastomer sphere/plane contacts studied here. First, non-linear elasticity being a generic feature of soft materials, from gels to human skin, we expect it to be a likely mechanism for contact area reduction in all studies involving such materials. It would thus be interesting to re-interpret recent experiments like those of e.g. [86] on polyacrylonitrile or those of [17, 88] on human fingertips, from the standpoint of finite-deformation mechanics. Second, [17, 63] argued that the mechanisms of shear-induced anisotropic contact area reduction may be the same in millimetric sphere/plane contacts and in individual micrometric junctions within rough contact interfaces. Such a similarity across scales suggests that the present conclusions may also be used to further understand the shear behaviour of soft material multicontacts, the modelling of which may require non-linear elasticity. This may in particular be an explanation for the fact that, in [89], a multi-asperity model based on linear elasticity failed to reproduce quantitatively the multicontact results of [17].

3.5 Conclusion

An original experimental analysis was proposed to show the existence of elementary mechanisms responsible for the evolution of the contact area under shear. First, it was demonstrated that contact lifting and contact laying do occur and can be quantified using Voronoi tessellation. Second, using Delaunay triangulation, the progressive development of a heterogeneous in-plane strain field within the contact area was illustrated. The existence of those mechanisms seems to be normal load-dependent. Under large load, contact lifting and contact laying occur on opposite sides of the periphery of the contact area, while under small load, contact lifting occurs at both sides. The challenges associated with the experimental approach has been thoroughly discussed.

With the tracking of the particles we could measure their displacement relative to its initial position in the contact area and identify a micro-slip front that moves from the contact periphery inward the contact region as shear increases, replacing a central stuck area. We highlighted different stages during their evolution: a stuck state, a partial slip, a transient sliding, and steady state sliding.

The findings, under large load, were qualitatively compared with a developed model proposing for the first time a non-adhesive, non-viscous model of shear-induced contact area reduction in soft materials. Quantitative agreement with the recent experimental results of Sahli et al. [17, 63] on sphere/plane elastomer contacts has been obtained, with no adjustable parameter, using the Tresca friction law and the neo-Hookean hyperelastic model. The necessary ingredients for this agreement are finite deformations and non-linear elasticity.

All results suggest a new perspective on the phenomenon of shear-induced contact area reduction in soft materials. This currently highly debated topic has been dominated by interpretations based on a leading role of adhesion. Here, instead, it was suggested that finite-deformation effects and non-linear elasticity can be equally important, all the more so as large normal loads are considered. Clarification of the validity domains where adhesion and/or finite deformations need to be accounted for remains a major open issue on the topic.

Chapter 4

Shear-induced area reduction over a wide range of normal loadings

4.1 Introduction

Elastomer friction between dry surfaces in relative motion is a complex phenomenon due to mechanical, chemical, and physical interactions, each operating at their own force scale. Adhesion and deformation components have the most significant contributions to the overall friction force [90, 91].

In the previous Chapter 3, we were focused on the investigation of a simple model problem, *i.e.* a sphere/plane contact involving an elastomer and a rigid smooth surface. We have shown that deformation at the interface and lifting/laying at the contact edges are the main mechanisms governing the contact area reduction under shearing under relatively large normal loads. This investigation raises a direct and natural question: *do the same mechanisms occur over a wider range of normal forces?*

Despite many scientific groups have carried out theoretical [49, 52, 92] and numerical simulation [56, 59, 60] studies on sheared model interfaces for different range in terms of normal force, experiments are mainly performed under small compression (or even tension), *i.e.* for very small normal loads [46, 49, 55]. Only recently, a few experiments have been conducted under much higher normal loads [17] but still leaving a gap in the range of load explored. In addition to this experimental gap, the different conditions of the available experimental data (see Figure 4.1) make a quantitative comparison between experiments, theory and simulations from the literature even more

complicated. Indeed, the frictional behavior of the interface depends strongly on material, elastic modulus, surface energy, contact geometry, equipment/procedure, sliding velocity, temperature, and so forth, making it impossible to have a unified view of the behavior of a single sphere on plane sheared contact over a wide range of normal forces.

Within this scenario and to proceed to the next step in our study, which will consist in going towards more realistic frictional sliding configurations, the objective of this chapter is to improve the understanding of shear-induced area reduction from mN up to N in order to cover and fill the experimental gap found in literature. In particular, we will study the evolution of the main features and parameters that allow describing the model sphere/plane experiments: contact area morphology, area reduction parameter, and interfacial shear strength over a wide range of normal loadings.

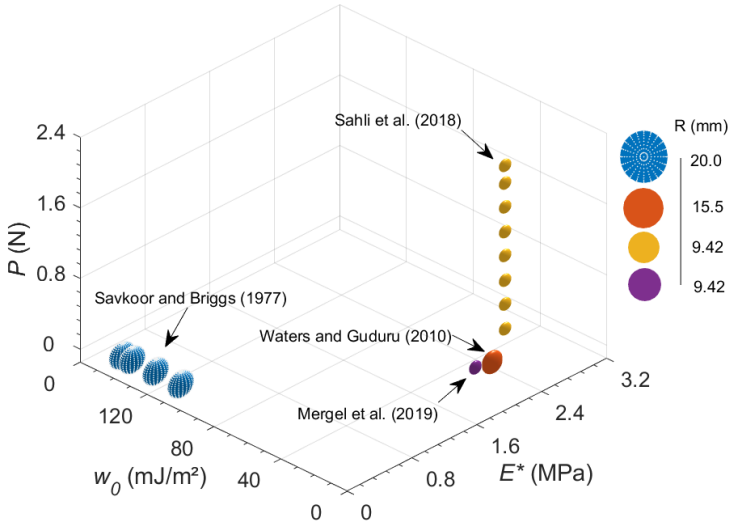

Figure 4.1: Illustration of the spreading of experimental conditions found in the literature for model sphere/plane sheared interfaces. The axes show the range of normal forces P, the effective elastic modulus E^*, and the surface energy ω_0. The marker size indicates the sphere radius R. All studies used PDMS against glass, except Savkoor and Briggs [46] that used a rubber dielectric gel (indicated with a white dot texture on the marker).

4.2 Tangential loading experiments

To address the objective of this chapter, three sets of experiments have been performed using the optomechanical instrument presented in Section 2.2.1 on S1R9 samples (one sphere with a radius of curvature of 9.42 mm, see Section 2.1.2) against a glass

plate, for a wide range of normal forces P, as shown in Table 4.1. The normal load was applied by adding dead weights, except for P smaller than 0.25 N. In this small load case, the normal load was applied by pushing the whole cantilever on the sphere (resp. glass plate) in a normal (resp. inverse) attachment configuration via the z-stage (see Figures 2.4 and 2.5). The normal force P was measured with the normal load sensors and it remains constant throughout the experiments. The tangential force results from the displacement of the glass plate (normal configuration) or of the sphere (inverse configuration) at a constant velocity $V = 0.1\,\mathrm{mm/s}$. Images of the contact area during the test were taken with a lateral square pixel of 7.75, 8.08, and 8.09 μm for Set 1, 2, and 3, respectively. In each set, a different PDMS sphere was used and, although they were carefully manufactured in a similar way, some parameters were difficult to control, such as the elastomer base and curing agent batch and the delay in the effective use of the sphere after the defined curing time of 48 h. For each set, the experiments were carried out in random order, in terms of normal loads, to avoid systematic errors. Full details and specifications of the experimental procedure are given in Chapter 2.2.2.

Table 4.1: Sets of tangential loading experiments.

Set	Range of P	Sample	Attachment configuration*
1	-14.1 mN to 5.2 N	S1R9 (1)	Normal
2	-0.2 mN to 3.2 N	S1R9 (2)	Inverse
3	-2.1 mN to 1.4 N	S1R9 (3)	Inverse

* As illustrated in Figure 2.5.

4.3 Results and analysis

In this section the results and analyses of the three sets of experiments will be presented. In order to properly define the wide range of normal forces, hereafter small loads correspond to tests with $P \leq 0.25\,\mathrm{N}$ and large loads to tests with $P > 0.25\,\mathrm{N}$. This threshold value has been chosen based on data found in the literature. Indeed, the literature maximum normal force is 15.5 mN in the small load range [49], and the minimum normal force is 0.27 N in the large load range [17].

4.3.1 Adhesion energy and elastic modulus

The adhesion energy ω_0 of the PDMS/glass interfaces and the effective elastic modulus E^* of the PDMS samples were estimated for each set from the contact area under no tangential load ($Q = 0$) by JKR theory [27] using the method described in Section 2.4.3. The fits for Set 1 (●,—), Set 2 (▲,· ·), and Set 3 (♦,- -), using Equation 2.1 in which E^* and ω_0 are the two fitting parameters, are show in Figure 4.2 for three distinct ranges of P: (a) entire, (b) large load, and (c) small load. The points in the large load range are represented by filled markers and the small load range by open markers (also shown in the insets). The parameters, E^* and ω_0, are shown in Tables 4.2 and 4.3, respectively.

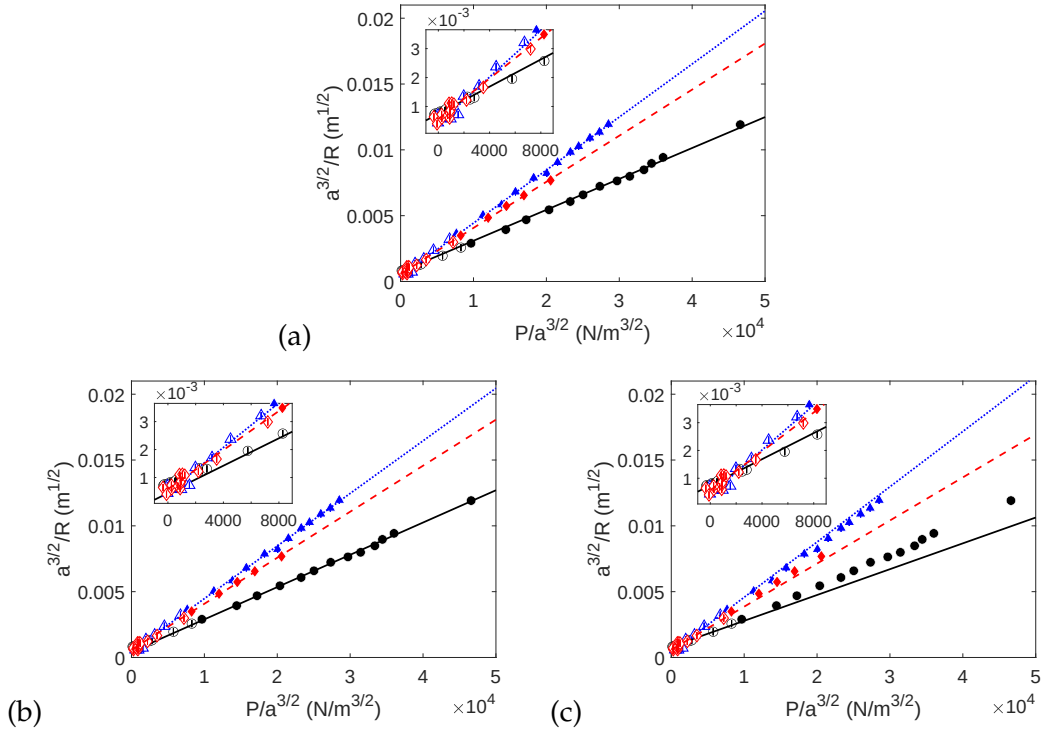

Figure 4.2: Estimation of the adhesion energy ω_0 of the PDMS/glass interfaces and the effective elastic modulus E^* of the PDMS samples by JKR theory [27] using the method described in Section 2.4.3. Set 1 (●,—), Set 2 (▲,· ·), and Set 3 (♦,- -). The points in the large load range of P are represented by filled markers and the small load range by open markers (also shown in the insets). The lines represent the fits (Equation 2.1) of each set of data in three distinct ranges of P: (a) entire, (b) large load, and (c) small load.

Table 4.2: Effective elastic modulus E^* of the PDMS samples.

Set \ Range of P	Entire	Large	Small
1 (●,—)	3.19 ± 0.05 MPa	3.06 ± 0.08 MPa	3.82 ± 0.39 MPa
2 (▲,· ·)	1.86 ± 0.02 MPa	1.87 ± 0.06 MPa	1.78 ± 0.20 MPa
3 (♦,- -)	2.14 ± 0.06 MPa	2.20 ± 0.15 MPa	2.29 ± 0.33 MPa

Table 4.3: Adhesion energy ω_0 of the PDMS/glass interfaces.

Set \ Range of P	Entire	Large	Small
1 (●,—)	$125 \pm 23\ \mathrm{mJ/m^2}$	$42 \pm 33\ \mathrm{mJ/m^2}$	$182 \pm 8\ \mathrm{mJ/m^2}$
2 (▲,· ·)	$22 \pm 7\ \mathrm{mJ/m^2}$	$30 \pm 31\ \mathrm{mJ/m^2}$	$18 \pm 8\ \mathrm{mJ/m^2}$
3 (♦,- -)	$48 \pm 12\ \mathrm{mJ/m^2}$	$85 \pm 72\ \mathrm{mJ/m^2}$	$56 \pm 11\ \mathrm{mJ/m^2}$

We can see in Figure 4.2 and Tables 4.2 and 4.3 that the entire range of P fits (solid black lines) are mainly dominated by the experiments in the large load range. Another observation is the huge variation in the evaluation of the adhesion energy ω_0 of the PDMS/glass interfaces and also of the effective elastic modulus E^* of the PDMS samples, between the sets. Those differences may be due to the difficulty of controlling all parameters in PDMS sample preparation, as mentioned in Section 4.2. All PDMS samples of this work were prepared at room temperature. However, they were prepared during different periods (*e.g.*, summer and winter) and a temperature variation of around 10 °C between them was detected afterwards. Since the cross-linking process depends strongly on temperature, the non-control of this parameter can result in an incomplete cross-linking after 48 h, which causes a variation in the final properties of the PDMS samples. Incomplete cross-linking leads to an imperfect network with free chains (not linked to the network) and dangling chains (connected to the network only at one extremity). This results in a lower elastic modulus ("the more the PDMS is crosslinked, the less it is elastic" [93]) and in a transfer of free chains to the glass plate over the successive experiments, reducing the surface energy thereby the adhesion energy [94, 95]. These findings were made later in the timeline of this thesis and, unfortunately, they could not be taken into account in the subsequent results. However, it has led to enhancements to the PDMS sample preparation process under temperature control for future work.

Therefore, thereafter, we will not be able to compare quantitatively the results between the three different sets of experiments as was initially our intention. We will just compare them qualitatively. Indeed, E^* and ω_0 are key parameters in the response of the interface (all the more at small load for ω_0).

4.3.2 Tangential and normal forces

Figure 4.3 shows the evolution of the tangential force Q plotted versus the tangential displacement d. On the left side, the entire range of normal loads is presented for (a) Set 1, (b) Set 2, and (c) Set 3. The curves color scale goes from blue for the smallest P to red for the largest P for each set. To allow a better visualization, the small loads are also shown on the right side of the figure. We can observe, for each curve, the typical behavior: Q increases linearly at the very beginning, followed by a progressive slope reduction, before reaching a maximum Q_s; then Q decreases and enters a macroscopic sliding regime. In a simple theory of friction, due to Bowden and Tabor [25], when the tangential force reaches its maximum Q_s (indicated as a circle marker) is the the start of sliding, *i.e.* the sudden transition from static to kinetic friction. Experimentally, here, such transition is more marked when P is small and becomes smoother as P increases. Also with the increase of P, we can observe the expected increase of Q_s, likewise, we see that both the displacement d to reach it and the slope of the curves in the static region increase. One can notice, in the three sets, that the $Q(d)$ curves present stick-slip-like oscillations appearing sometimes even before Q_s. We can identify a tendency for such instabilities to arise at lower normal force values. Such oscillations are thought to be the result of detachment waves from a compressive zone to a tensile one, so-called Schallamach waves, occurring due to surface instability [79]. The conditions for such instability are very difficult to control and still remain unclear in the literature. In this study, we have hypothesized that these oscillations did not have a major effect on the results.

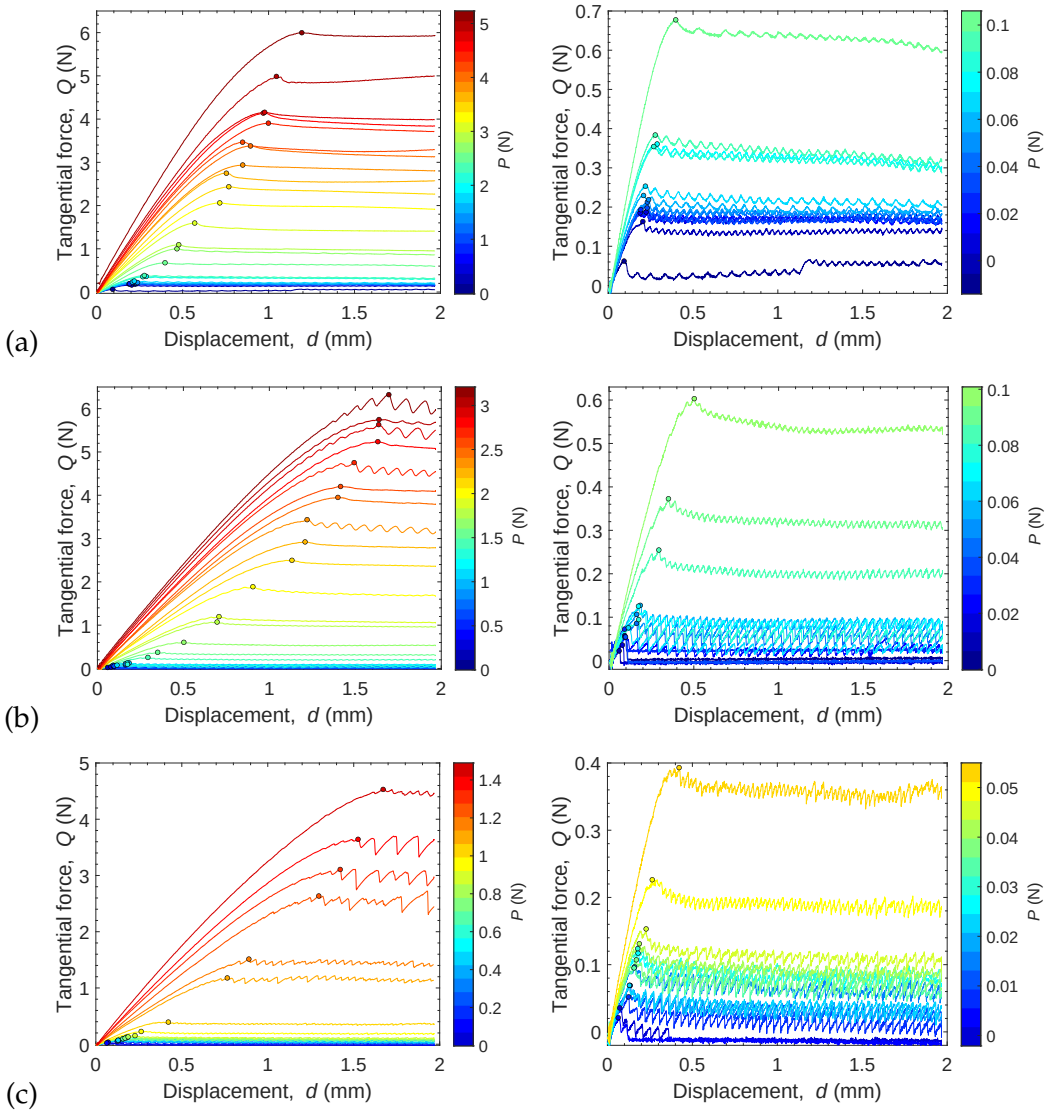

Figure 4.3: Tangential force Q as a function of displacement d for (a) Set 1, (b) Set 2, and (c) Set 3. The entire sets of normal loads are shown on left side; the small loads are show on the right side. Curves color scale goes from blue (smallest P) to red (largest P). The moment of the tangential force peak Q_s is shown as a circle marker.

Figure 4.4 shows the evolution of the normal load as a function of the displacement d associated to the tests presented in Figure 4.3. Again, the left side shows the entire range of P for (a) Set 1, (b) Set 2; and (c) Set 3, and the right side shows a zoom in the small loads. The moment of the tangential force peak Q_s is shown as a circle marker. A slight increase, on Set 2 and 3, and decrease, on Set 1, can be seen in the static region, up to Q_s, due to the presence of a small residual angle between the shear direction and the plane. This slight variation in the normal force does not explain the large reduction in the contact area A that is observed (see next section 4.3.3). In the case of increased P, it is even against the reduction of A. The effect of the presence of a small angle will be

discussed in detail in Chapter 5.

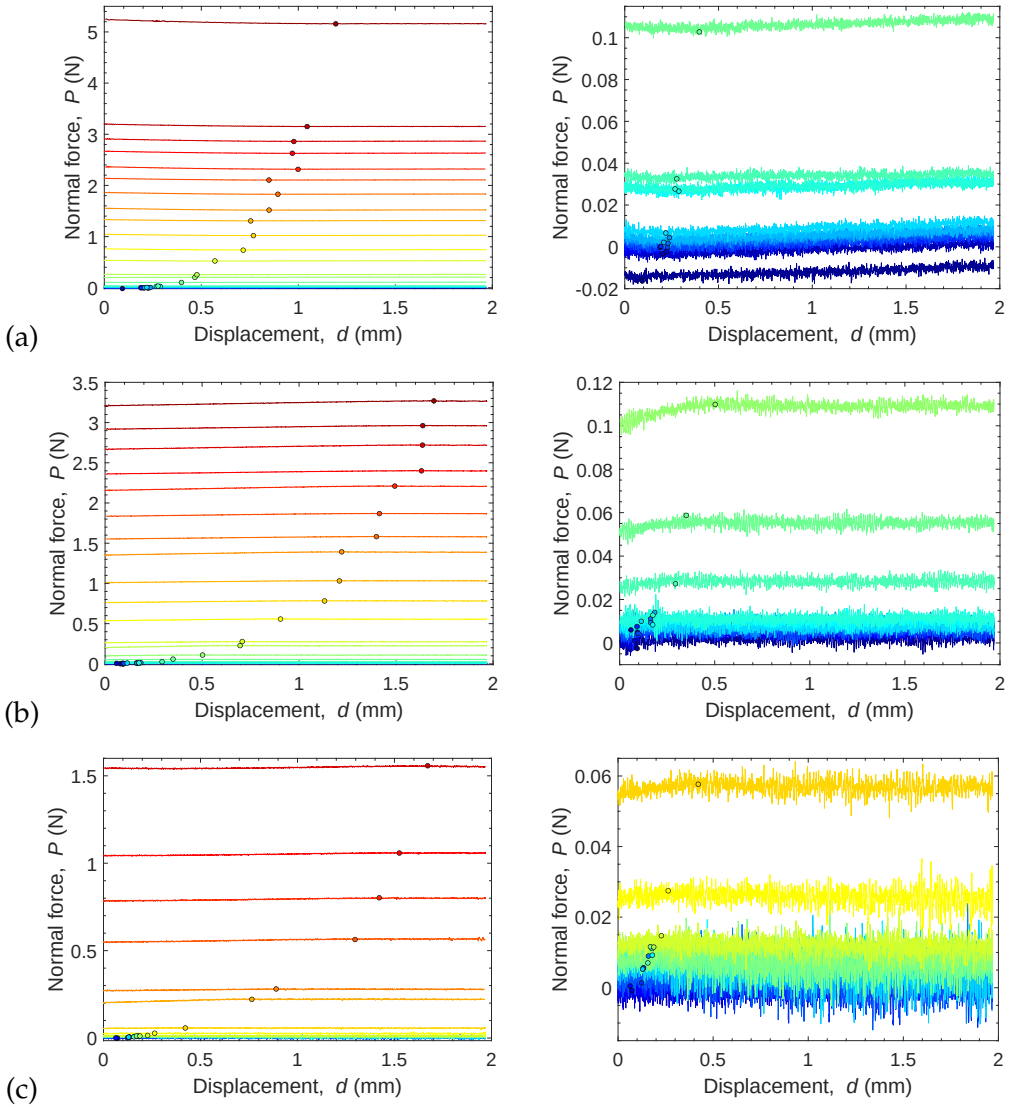

Figure 4.4: Normal force P as a function of displacement d for (a) Set 1, (b) Set 2, and (c) Set 3. The entire sets of normal loads are shown on left side; the small loads are show on the right side. The moment of the tangential force peak Q_s is shown as a circle marker.

4.3.3 Contact area evolution

Figures 4.5, 4.6 and 4.7 present the raw images of the three sets of experiments for two small normal loads and two large normal loads (specified in the figures). In each figure, the first column of images shows the initial contact area before shearing ($Q = 0$), the last column shows the contact area at the tangential force peak ($Q = Q_s$), and the second and third columns correspond to two intermediate displacements. At $Q = 0$, all the contact areas are, as expected, perfectly circular and their size increases with the

normal load P. At $Q = Q_s$, we can observe a clear area reduction, and as, for example, in Sahli et al. [17], the area reduction is not axisymmetric and evolves from a circular to a prolate shape as the reduction is much larger in the sliding direction. Moreover, the prolate shape is not quite symmetrical about the vertical axis (perpendicular to the sliding direction) as the reduction is larger at the trailing edge of the contact (right side on the images). Note that in some images, one can clearly see the presence of the detachment waves that propagate at the trailing edge of the contact.

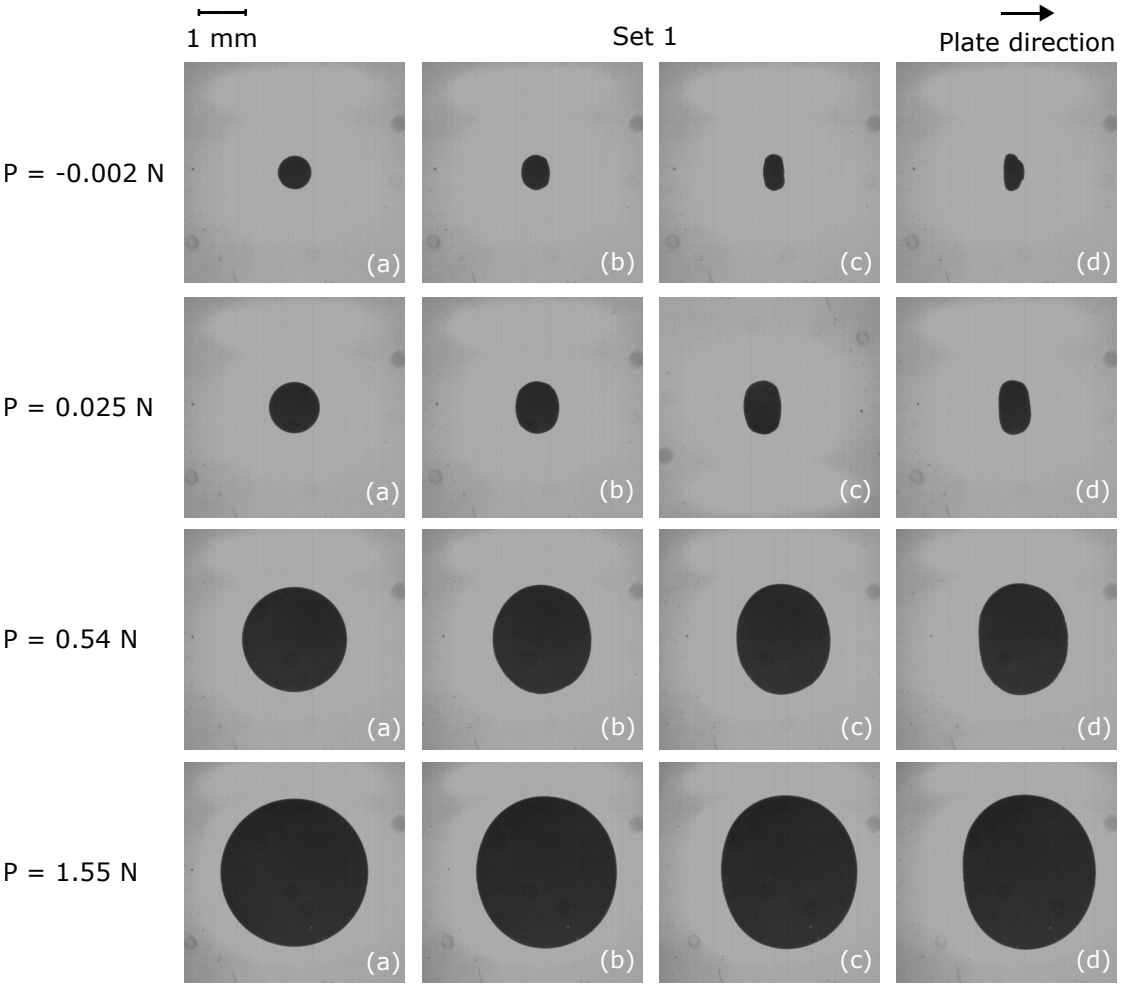

Figure 4.5: Raw images of Set 1 for four normal forces showing the contact area evolution under shearing for four displacement steps: (a) at $Q = 0$, (b-c) at two intermediate displacements, and (d) at $Q = Q_s$.

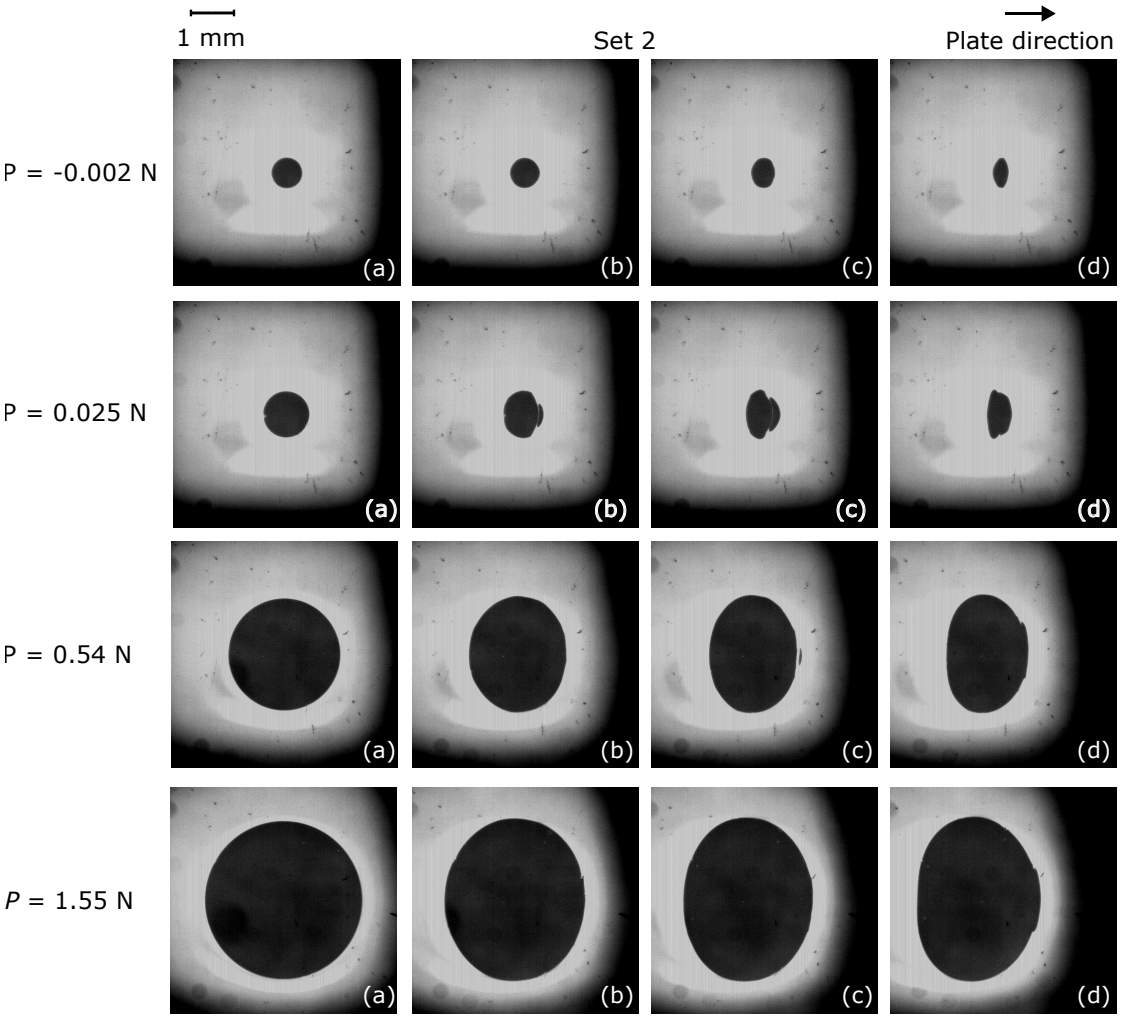

Figure 4.6: Raw images of Set 2 for four normal forces showing the contact area evolution under shearing for four displacement steps: (a) at $Q = 0$, (b-c) at two intermediate displacements, and (d) at $Q = Q_s$.

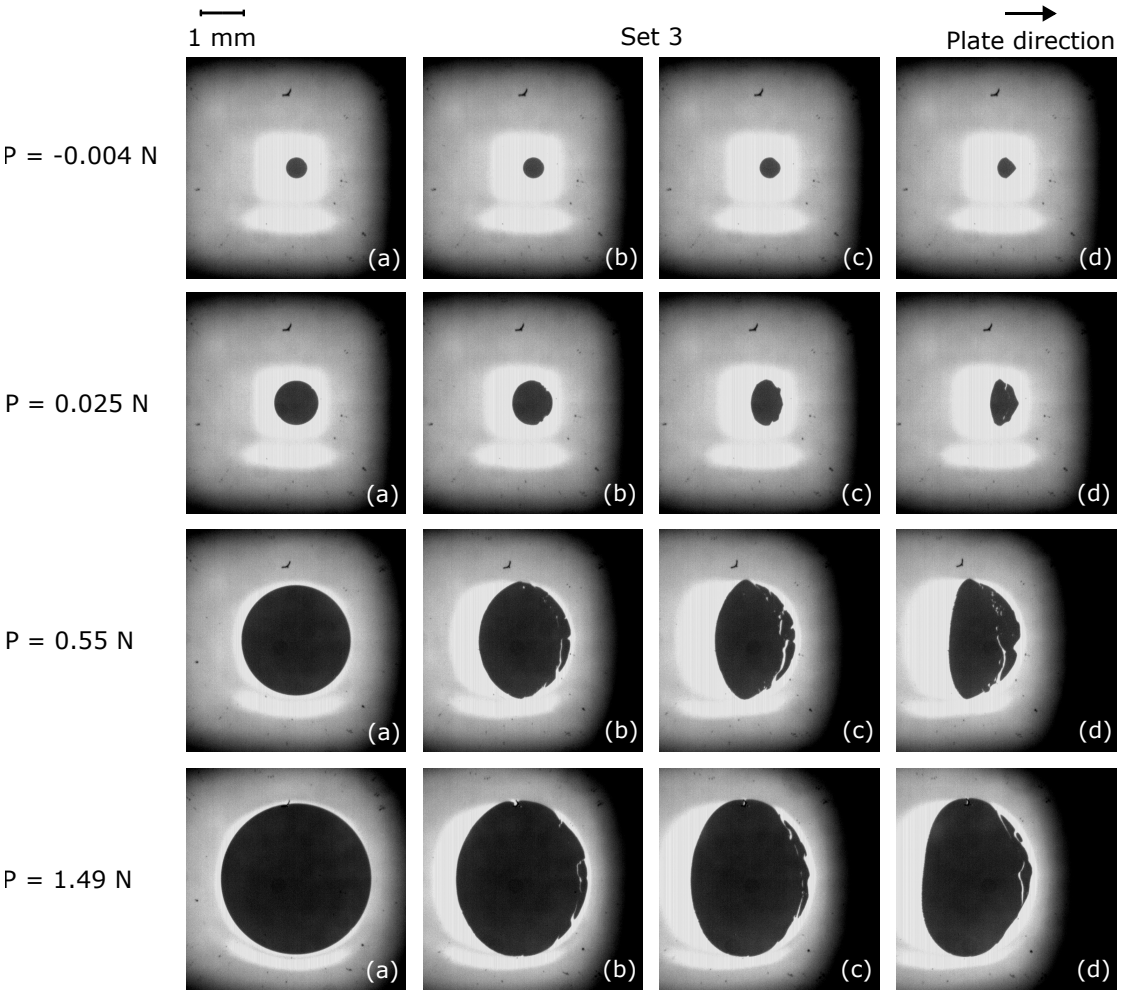

Figure 4.7: Raw images of Set 3 for four normal forces showing the contact area evolution under shearing for four displacement steps: (a) at $Q = 0$, (b-c) at two intermediate displacements, and (d) at $Q = Q_s$.

From all the images, such as those shown in Figures 4.5, 4.6, and 4.7, we can now evaluate the contact areas A using the procedure described in Section 2.3.1. Figure 4.8 shows the evolution of these contact areas A during the displacement d. On the left side is shown the entire range of P for (a) Set 1, (b) Set 2, and (c) Set 3; and on the right side is shown a zoom in the small loads. The curves color scale goes from blue for the smallest P to red for the largest P for each set. The moment of the tangential force peak Q_s is shown as a circle marker. As soon as the displacement d starts, the contact area A begins to reduce in all experiments (*i.e.* for all normal loads). Note that some curves exhibit a stick-slip-like aspect (periodic oscillations), as for $Q(d)$, which is again the consequence of the detachment waves.

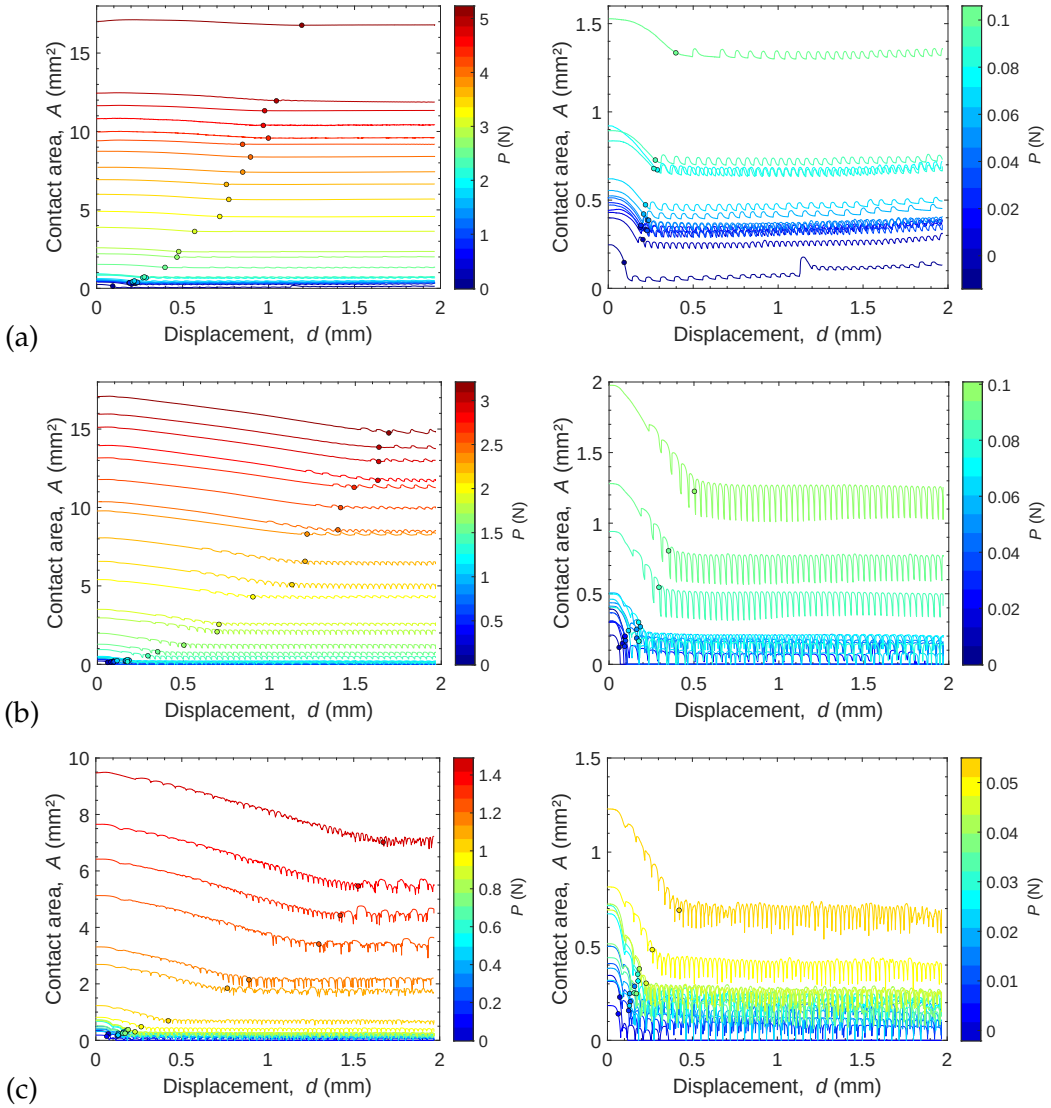

Figure 4.8: Contact area A as a function of displacement d for (a) Set 1, (b) Set 2, and (c) Set 3. The entire set of normal loads are shown on the left side; the small loads are shown on the right side. Curves color scale goes from blue (smallest P) to red (largest P). The moment of the tangential force peak Q_s is shown as a circle marker.

Figure 4.9 shows the percentage of area reduction at Q_s as a function of A_0 for Set 1 (●), Set 2 (▲), and Set 3 (♦). The points in the large load range of P (large A_0) are represented by filled markers and in the small load range (small A_0) by open markers. The inset shows a zoom in the small loads. We can see that, in all sets, the reduction of the contact area increases with the decrease of A_0 (decrease of P). However, their overall contact area reduction levels are significantly different. The difference in the values between the sets is attributed to the difference in terms of properties of the PDMS spheres.

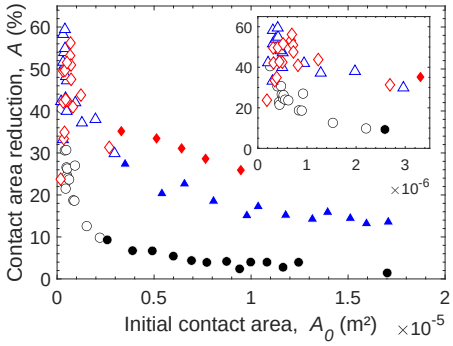

Figure 4.9: Contact area reduction at Q_s versus the initial contact area A_0. The points in the large load range of P (large A_0) are represented by filled markers and in the small load range (small A_0) by open markers. The inset shows a zoom in the small load range. Set 1 (●), Set 2 (▲), and Set 3 (♦).

Recently, a contact area decrease by up to 30 % for smooth (single asperity) and rough (multiple asperity) contacts, was reported in the literature on the range of large P [17].

Even if much more investigation would be necessary to be able to quantify the relation between the contact area reduction and the PDMS properties, we can observe that Set 1 presented the smallest reduction in the contact area while having the highest values of elastic modulus and adhesion energy (see Tables 4.2 and 4.3).

4.3.4 Analysis

As suggested by Sahli et al. [17], plotting and analyzing the evolution of the contact area as a function of the tangential force from $Q = 0$ to $Q = Q_s$, as shown in Figure 4.10, allows extracting the two main parameters that characterized the behavior of the involved interface: (i) the decay of contact area under shearing and (ii) the shear strength of the interface. In this section, we will investigate those two parameters for the three sets of experiments over a wide range of normal loads.

Contact area reduction rate

To evaluate the contact area reduction, from Figure 4.10, we use the quadratic decay expression proposed by Sahli et al. [17] for a range of large normal loads in both smooth sphere/plane and rough interfaces:

$$A = A_0 - \alpha_A Q^2, \tag{4.1}$$

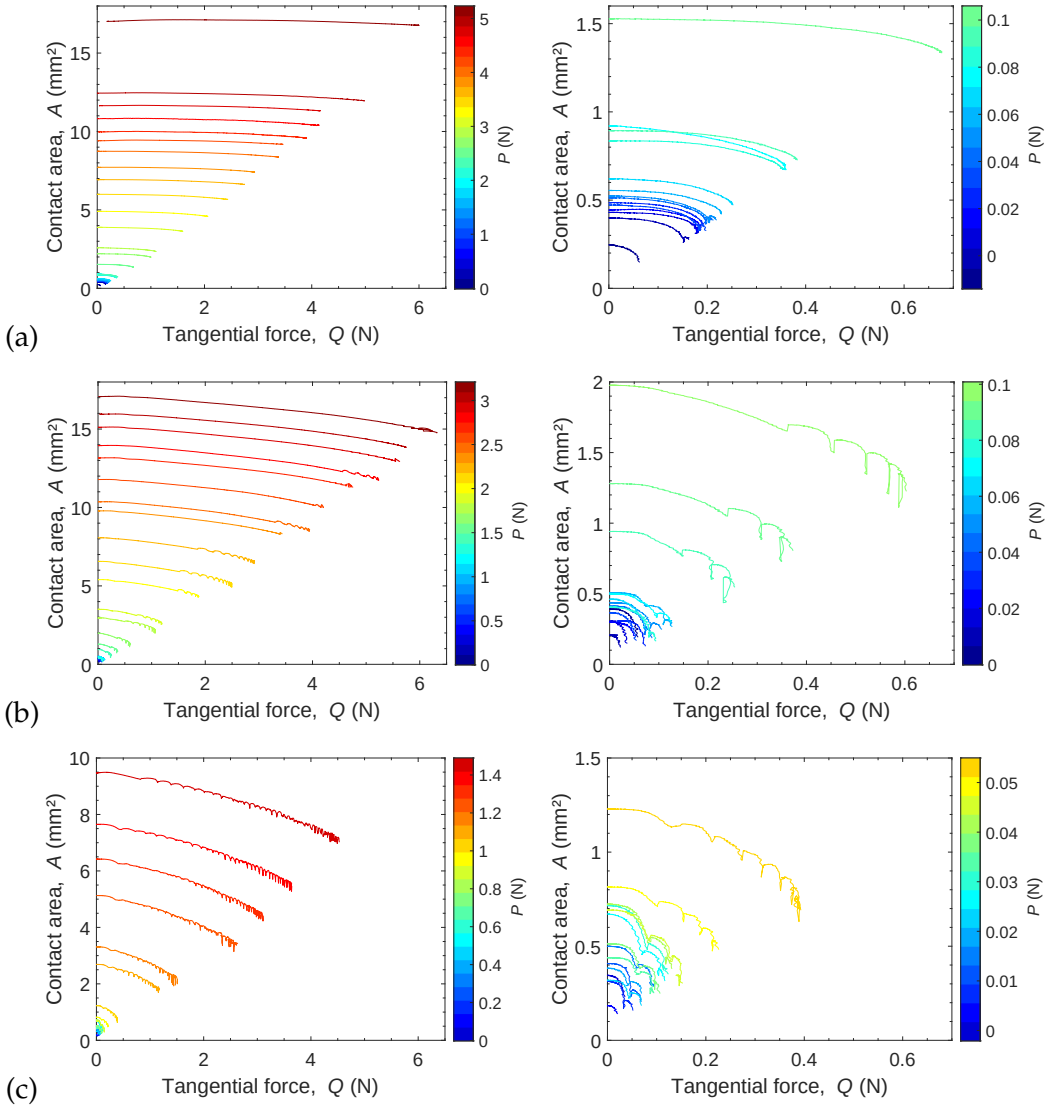

Figure 4.10: Evolution of the contact area A with the tangential force Q for (a) Set 1, (b) Set 2, and (c) Set 3. The entire set of normal loads are shown on left side; the small loads are show on the right side. Curves color scale goes from blue (smallest P) to red (largest P).

where A_0 is the initial contact area (at $Q = 0$).

The authors in [17] found that the contact area rate α_A obeys a well-defined scaling law,

$$\alpha_A = \beta (A_0)^{\gamma}, \tag{4.2}$$

with $\gamma \simeq -3/2$ over four orders of magnitude of A_0. However, in their study, the authors have used different samples to explore a such wide range of A_0 (*i.e.* of normal loads P). In particular, they have used a single PDMS sphere for large normal loads, while for small ones, they employed a rough interface. Indeed, for their rough sample,

they extracted the behavior of each micro-asperity contact and considered it as a single independent spherical contact.

Using the quadratic decay law (Equation 4.1), each $A(Q)$ curve (Figure 4.10) of the three sets of experiments was fitted with the single adjustment parameter: α_A. It thus allows to extract α_A for each normal load P, *i.e.* for different initial contact area A_0. Figure 4.11 shows, *e.g.*, the results of the fit (red lines) of the experimental data (black lines) for one small P (left side) and one large P (right side) of (a) Set 1, (b) Set 2, and (c) Set 3. For small P, a smaller and relatively poor coefficient of determination (R-square = 0.93) is found, in comparison with the one for large P (R-square = 0.98).

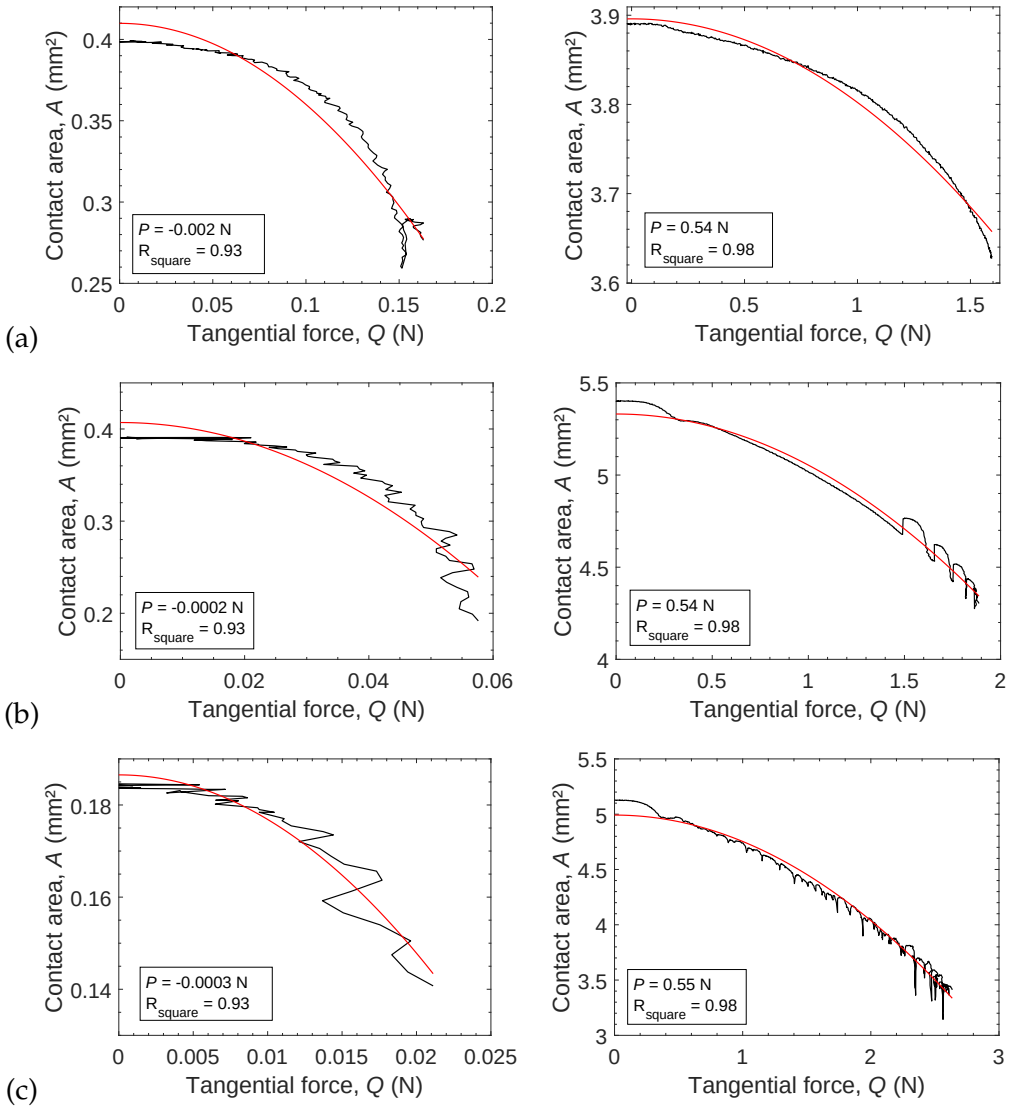

Figure 4.11: Contact area A as a function of the tangential force Q for (a) Set 1, (b) Set 2, and (c) Set 3. Left side: small P. Right side: large P. Black lines are the experimental data and red lines the fits using the quadratic decay law (Equation 4.1).

In Figure 4.12(a), the evolution of α_A (Equation 4.1) is plotted as a function of A_0 for Set 1 (●), Set 2 (▲), and Set 3 (♦). Figure 4.12(a) also shows the result of a fit performed by using Equation 4.2 on the entire range of normal loads (colored lines with the same color as the corresponded fitted set). We can see that, for each set, the points are well aligned and in good agreement with a power-law evolution, as expected by Equation 4.2. However, the level of the curve seems to vary from one set to another (mainly for Set 1). In addition, the points are well aligned at large loads (large A_0), but less well aligned - larger dispersion - at small loads (small A_0). This observation is validated by Figure 4.12(b) which shows a rather good fit agreement (high R-square) with the experimental data at large loads, *i.e.* in the same range as in Sahli et al. [17] (■ in Figure 4.12). However, as in Mergel et al. [55] (▼ in Figure 4.12), for small normal loads, the quadratic law does not fit well the experimental data (lower R-square).

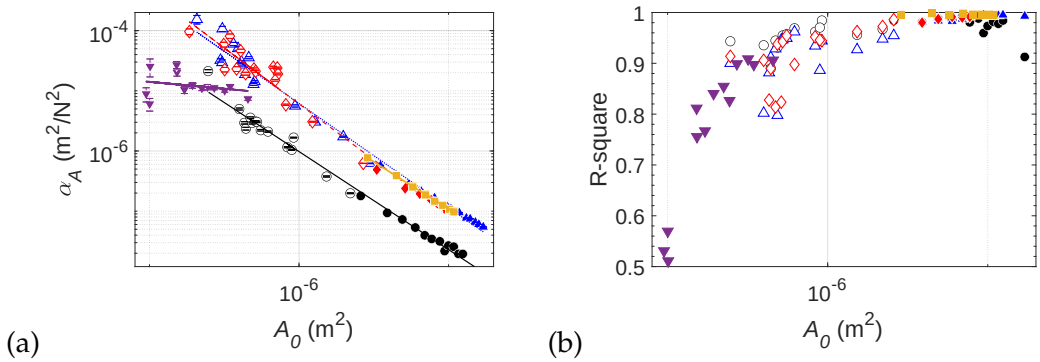

Figure 4.12: (a) Decay rate of contact area under shearing α_A *vs* the initial contact area A_0. Set 1 (●,—), Set 2 (▲,· ·), and Set 3 (♦,- -). The lines represent the power-law fits performed by using Equation 4.2 on the entire range of normal loads. The points in the large load range of P are represented by filled markers and the small load range of P by open markers. The literature data are also shown for large loads as ■,— (Sahli et al. [17]) and for small loads as ▼,— (Mergel et al. [55]). (b) Evolution of the coefficient of determination R-square of the fits (Equation 4.1) *vs* A_0.

To go further in the verification of the validity of Equation 4.2 over a wide range of normal loads, we also fit the three sets of data, as well as the literature experimental data from small [57] and large [17] loads for a single sphere/plane contact in two sub ranges of normal loads: large loads (see lines in Figure 4.13(a)) and small loads (see lines in Figure 4.13(b)). Tables 4.4 shows the fit parameter γ derived from the use of Equation 4.2. We can observe that γ is affected by the sample properties, however, most importantly, γ is significantly affected by the range of normal loads employed

to perform the fit. Indeed, it seems that the exponent γ varies with the range of normal force involved, and so may be influenced by the dominant mechanisms at play depending on the normal load: non-linear elasticity or adhesion.

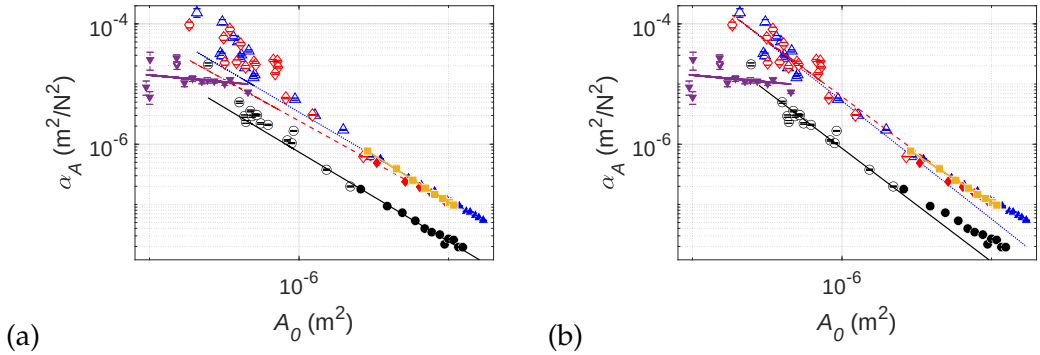

Figure 4.13: Results of the power law fits performed on the data of Figure 4.12 for sub ranges of normal loads: (a) large loads and (b) small loads.

Table 4.4: Power-law fit exponent, γ, of Equation 4.2.

	Power-law fit exponent, α		
Set \ Range of P	Entire	Large	Small
1 (●,—)	-1.63 ± 0.06	-1.48 ± 0.13	-1.88 ± 0.29
2 (▲,· ·)	-1.73 ± 0.08	-1.46 ± 0.04	-1.96 ± 0.30
3 (♦,- -)	-1.86 ± 0.17	-1.37 ± 0.21	-1.84 ± 0.44
Sahli et al. [17] (■,—)		-1.57 ± 0.04	
Mergel et al. [55] (▼,—)			-0.20 ± 0.58

We have just seen that the power-fits (Equation 4.2) do not work well with a single exponent over the wide range of normal loads. Interestingly, in the literature, some studies question the validity of the quadratic decreasing of contact area, especially at small loads. Indeed, Mergel et al. [55], using a similar set-up as the one of this study, but with small normal loads, report experimental results in which the decay of the contact area is not quadratic for the entire range of their observations. More recently, Salehani, Irani, and Nicola [56] carried out simulations on sphere/plane contacts for compressive and tensile loads, and found that under tensile load, when the onset of sliding is approached, the rate of contact area reduction increases. Recent models also seem to confirm that the decay of contact area under small loads may no longer be associated with a power of 2 [52, 53, 56]. In face of those discrepancies at small normal loads where the decay of contact area law (Equation 4.1) may not be strictly quadratic,

Papangelo et al. [53] proposed to use a power-law function with a variable exponent n to describe area reduction:

$$A = A_0 - \alpha_B Q^n, \tag{4.3}$$

from which the best-fit exponent n is to be obtained. Using a nonaxisymmetric model based on linear elastic fracture mechanics, the authors showed, in their Figure 10(b) [53], a value of n close to 2 under large loads (for P in the order of 1 N, $n \sim 1.8$–1.9), and pointed out that under small loads n increases (for P in order of 10^{-3}–10^{-2}, $n \sim 3 \pm 0.5$).

Accordingly, we used Equation 4.3 to fit the data in our three sets of experiments. In Figure 4.14, the evolution of the exponent n is plotted as a function of the initial contact area A_0 both for our data (Set 1 (●), Set 2 (▲), and Set 3 (♦)) and for those of the literature (Sahli et al. [17] (■) and Mergel et al. [55] (▼)). We can see that the exponent n is quite constant at large loads, and is close to 2 (quadratic form as in Sahli et al. [17]) for Set 2 and 3, but close to 3 for Set 1. This exponent variation between the sets, raises the question of the exponent's dependence on the properties of the PDMS. For small loads, as in the literature [55], we find an exponent which tends to increase.

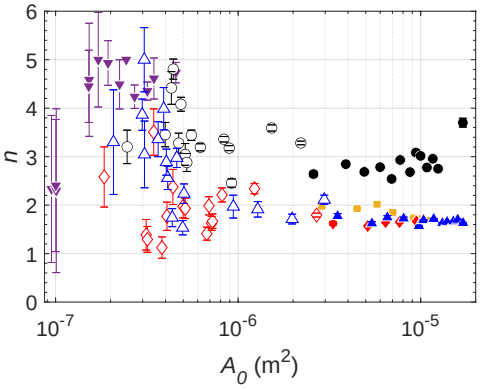

Figure 4.14: Evolution of the best-fit exponent n (Equation 4.3) as a function of the initial contact area A_0. The points in the large range of P are represented by filled markers and the small range by open markers. Set 1 (●), Set 2 (▲), and Set 3 (♦). The literature data are also shown as ■ (Sahli et al. [17]) and ▼ (Mergel et al. [55]).

Comparison with mode-mixity fracture model

In addition to all previous analyses and still to evaluate the contact area reduction, we compared our experimental data sets to a recent mode-mixity model proposed

by Papangelo and Ciavarella [52] which predicts the contact area reduction of an adhesive contact under shearing by taking into account the dependence of the interfacial toughness on the phase angle $\psi = \arctan(K_{II}/K_I)$; K_{II} and K_I being, respectively, the mode II and mode I stress intensity factors (defined in Equation 1.13 and Equation 1.12). This model is an improved version of the LEFM-based models, which all require at least one empirical coefficient λ within one mode-mixity function $f(\psi)$ [54] to describe the critical condition for the propagation of an interfacial crack. The expression for $f(\psi)$ proposed by Papangelo and Ciavarella [52] is:

$$f(\psi) = [1 + (\lambda - 1)\sin^2(\psi)]^{-1} \tag{4.4}$$

To access $f(\psi)$ from our experimental data, we use the fracture mechanics model rewritten in the form [52]:

$$\frac{G_c}{G_{Ic}} = f(\psi) = \frac{\left(\frac{4E^* a^3}{3R} - P\right)^2 + Q^2}{8\pi E^* a^3 G_{Ic}} \tag{4.5}$$

where G_{Ic} corresponds to the adhesion energy of the interface, *i.e.* ω_0. Then, the ratio G_c/G_{Ic} as a function of ψ can be obtained directly from our experiments and compared with the proposed model (Equation 4.4) to extract the value of the unique adjustment parameter λ. We used the elastic and adhesive properties, E^* and ω_0, for each set of experiments from the parameters related to the JKR fit in the entire range of P performed in Section 4.3.1 (refer to the parameters in Figure 4.2 and Tabs. 4.2 and 4.3). As we have seen in the previous Section 4.3.1, the parameters E^* and ω_0 in our experiments are mainly dominated by the experiments in the large load range of P and we could not notice a significant difference using the other parameters. Also, we use a value of P estimated from JKR's theory, that is : $P = \frac{4E^* a^3}{3R} - \sqrt{8\pi E^* a^3 G_{Ic}}$.

The proposed model (Equation 4.4) was used to fit our results on the contact area decay under shearing. Figure 4.15 shows an example of how the experimental data (represented by markers) are fitted (represented by green lines). One can notice that for Sets 2 (Figure 4.15(b)) and 3 (Figure 4.15(c)) the oscillations at the ends of the curves disturb the fit, resulting in a relatively low coefficient of determination (R-square).

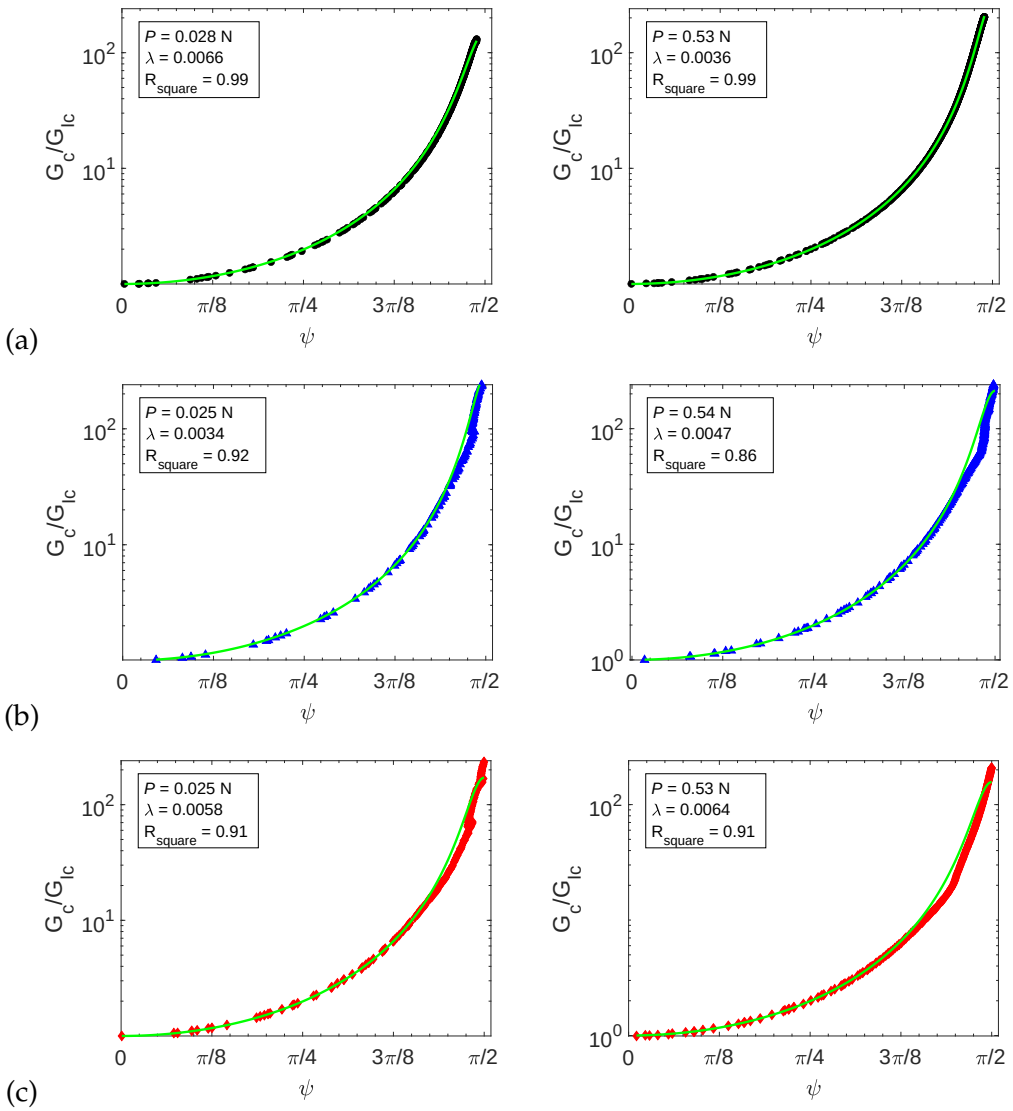

Figure 4.15: Ratio G_c/G_{Ic} as a function of ψ for (a) Set 1, (b) Set 2, and (c) Set 3. Left side: small P and right side: large P. Markers are from the experimental data and green lines are the fits using Equation 4.4).

Then, in Figure 4.16, we plotted, as a function of the normal forces P, (a) the coefficient λ that best fits our three sets of experimental data and (b) the coefficient of determination R-square of the fits. First, as observed in the previous analyses for α, the values of λ vary from one set of experiment to the other. Second, contrary to Papangelo and Ciavarella [52] that suggested an almost constant value of λ for a given set of experiment, we point out that, at low loads, this does not seem to be exactly the case. The values of λ for small loads are more scattered, see inset of Figure 4.16(a)).

To try to see if this evolution of λ at low load is of prime interest, we have evaluated a unique λ value for all three set of experiments by fitting the experimental data of all

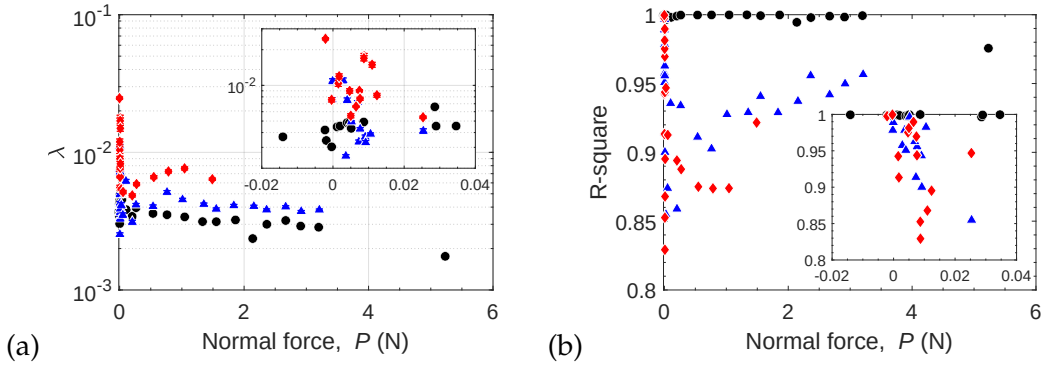

Figure 4.16: (a) Best fitted λ as a function of the normal force P. (b) Fit coefficients of determination (R-square) as a function of the normal force P. The insets show a zoom in the small loads.

the normal forces, as shown in Figure 4.17. Again, λ vary from one set of experiment to the other and the oscillations at the ends of the curves result in a relatively low coefficient of determination (R-square). Then, in Figure 4.18, the aforementioned empirical forms of mode-mixity functions, $f(\psi)$, as described by Equation 4.5, were used to plot the prediction of the evolution of the contact area as a function of the tangential force Q using $\lambda = f(P)$ (red lines) and λ = const (blue lines). Those predictions can thus be compared to our experimental data (black line). Note that Figure 4.18 only presents the results for two representative normal loads (small and large) of Set 1 as, all other case presents the exact same qualitative tendency.

At large loads, Figure 4.18(b), both predictions seem to capture the experimental evolution. However, using $\lambda = f(P)$, *i.e* a single value of λ for each $A = f(Q)$ curve, always yields slightly better results. Nevertheless, at low loads, Figure 4.18(a), the prediction based on a single value of λ does not capture the experimental evolution at all, in contrast to the prediction based on $\lambda = f(P)$.

Finally, we can see that the amplitude of the mode-mixity function (controlled by the value of λ) has a strong influence on the prediction of contact area evolution. For a wide range of normal loads, the experimental results can be fitted well only by using the appropriate value of λ. The dependence of λ versus P remains to be understood, in order to be properly accounted for in such LEFM-based models.

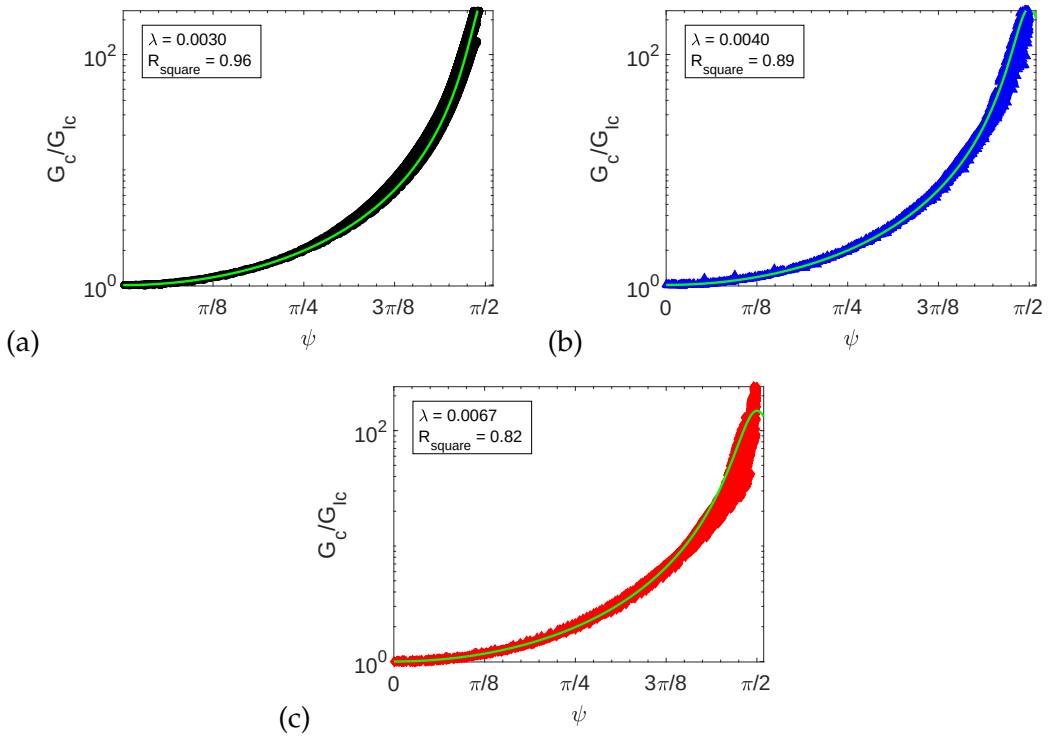

Figure 4.17: Ratio G_c/G_{Ic} as a function of ψ of all normal forces P for (a) Set 1, (b) Set 2, and (c) Set 3. Markers are from the experimental data and green lines are the fits using Equation 4.4).

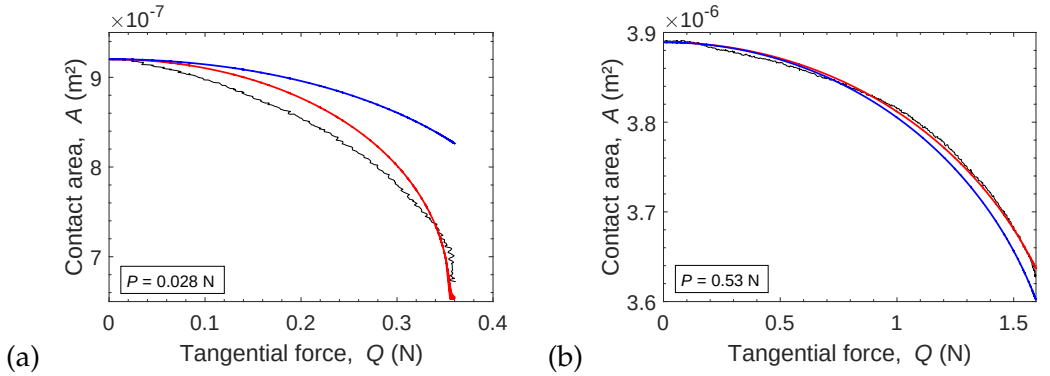

Figure 4.18: Contact area A as a function of the tangential force Q for two normal loads P, (a) in the range of small P and (b) in the range of large P, for Set 1. Black lines are the experimental data, red lines are the prediction of the contact area evolution using $\lambda = f(P)$, and blue lines using λ = constant.

Interface shear strength

For the analysis of the interface shear strength σ, we fitted the endpoints of the curves in Figure 4.10 using the threshold equation also proposed by Sahli et al. [17],

$$A_s = aQ_s, \tag{4.6}$$

with a single adjustment parameter a such that $\sigma = 1/a$. Figure 4.19 shows, for the

three sets, the endpoints of Figure 4.10, *i.e.* A_s (A at the moment of Q_s) as a function of Q_s. And, as in previous figures, large loads are shown on the left side and small loads on the right one. The fits have also been performed on (a) entire, (b) large, and (c) small ranges of P. Literature data of large loads (Sahli et al. [17]) and small loads (Mergel et al. [55]) were fitted separately. The fit results are shown in Table 4.5 in terms of shear strength σ.

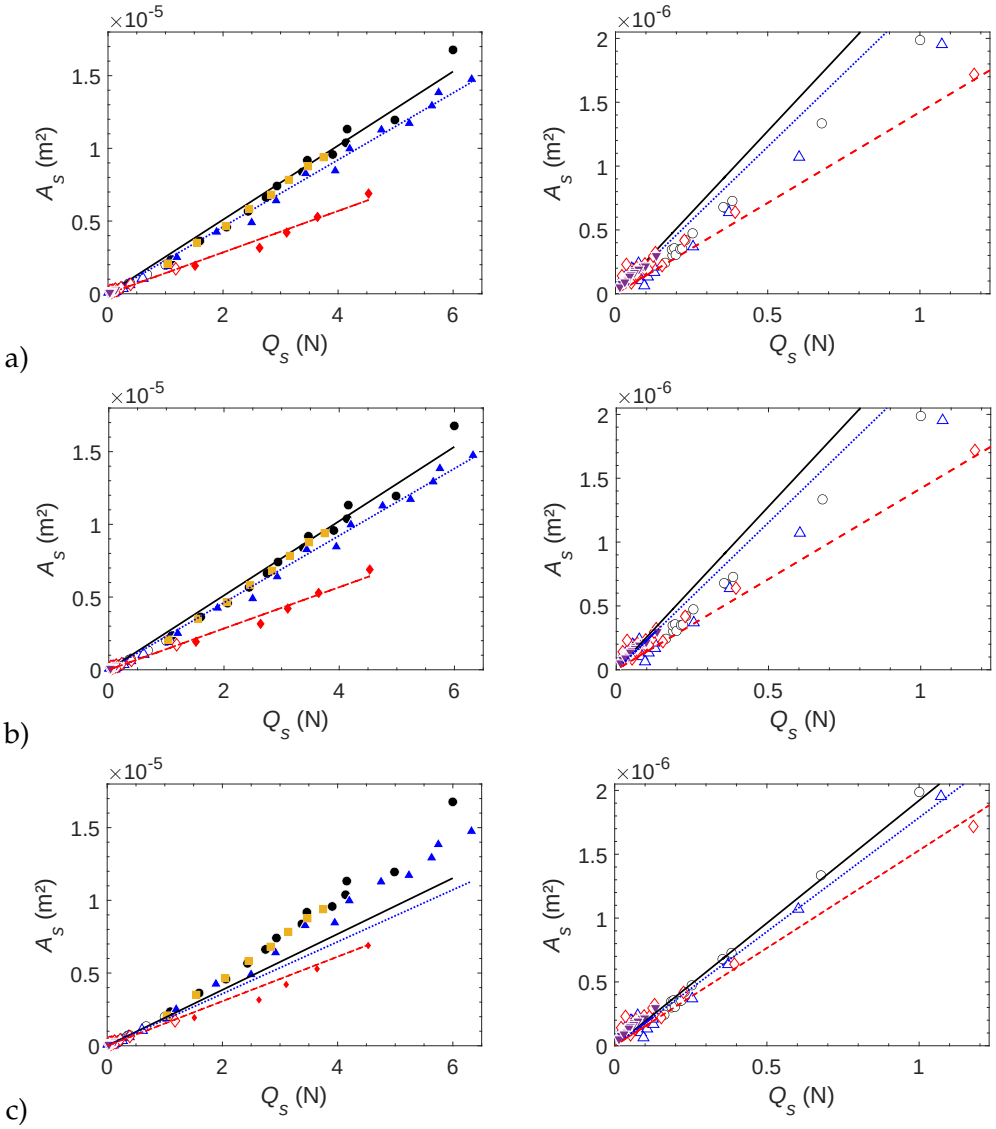

Figure 4.19: Contact area A_s at the moment of the peak of tangential force Q_s, as a function of Q_s. Left side: fit on the (a) entire, (b) large, and (c) small range of P. Right side: zoom in the small range of P. Set 1 (●, —), Set 2 (▲, · ·), and Set 3 (♦, - -). The points in the large range of P are represented by filled markers and the small range by open markers. Literature data are also shown as ■ (Sahli et al. [17]) and ▼ (Mergel et al. [55]).

We can see in Figure 4.19(a) that the fits on the entire range are dominated by large load points. In (b), the fits of the large loads do not seem to capture the small ones, and

Table 4.5: Interface shear strength σ in MPa.

Set \ Range of P	Entire	Large	Small
1 (●,—)	0.39 ± 0.01	0.39 ± 0.02	0.52 ± 0.01
2 (▲,· ·)	0.43 ± 0.01	0.43 ± 0.01	0.55 ± 0.04
3 (♦,- -)	0.70 ± 0.02	0.70 ± 0.08	0.65 ± 0.06
Sahli et al. [17] (■)		0.36 ± 0.01	
Mergel et al. [55] (▼)			0.43 ± 0.01

vice versa in (c) where the fits of the small loads do not seem to capture the large ones. Then the interface shear strength σ for the large load range is lower than for the small one, except for Set 3, as shown in Table 4.5. This exception, however, is probably due to the fact that there are too few points available at large loads in this set, resulting in a value of σ possibly poorly estimated. The literature data also indicate a lower σ value for the small load range data, which is consistent with the σ results of the sets.

In the linear relation of Equation 4.6, the authors of [17] only considered large normal loads, then they postulated that the straight line goes through the origin. However, when we expand this range of normal load by considering large and small loads together, such a linear relation does not seem to work well. In face of this and based on a previous study by Nguyen et al. [96], that suggests a power-law relationship between the local shear stress and the local pressure for PDMS in contact with a sandblasted glass surface, we applied the following power-law equation to fit the data:

$$A_s = \rho(Q_s)^{\kappa}. \tag{4.7}$$

Then, Figure 4.20 shows the same points as Figure 4.19 on a log-log scale, that is, A_s as a function of Q_s fitted using the power-law Equation 4.7 over (a) the entire range of P, (b) the large load range, and (c) the small load range. The fit results are shown in Tab. 4.6.

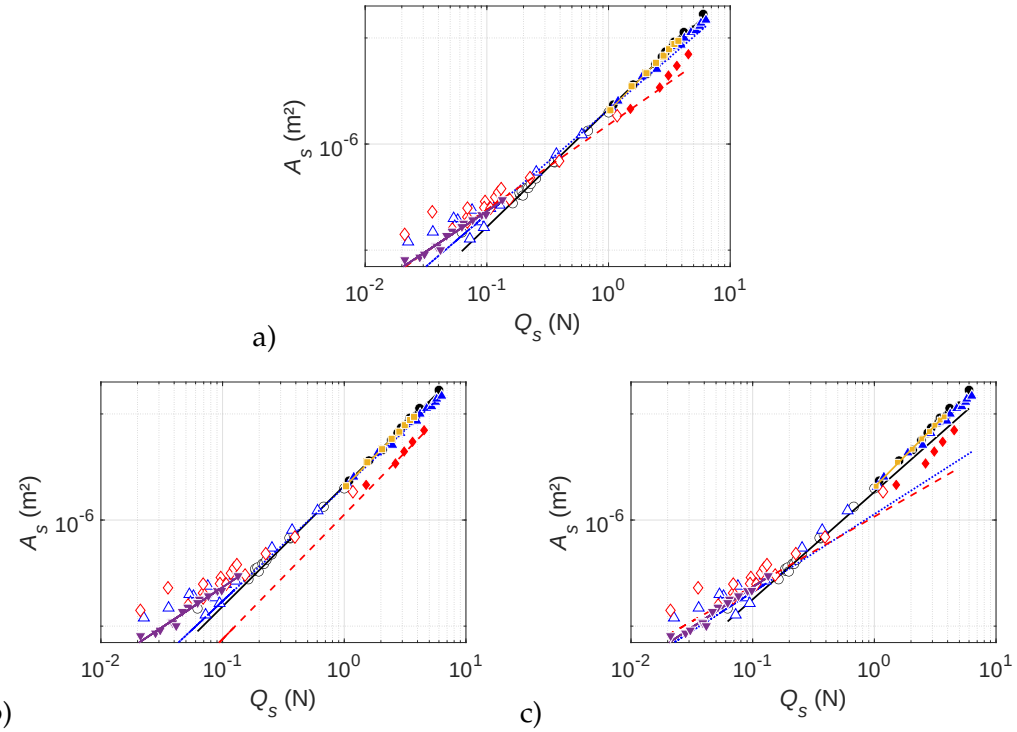

Figure 4.20: Contact area A_s, at the moment of the peak of tangential force Q_s, as a function of Q_s in a log-log scale. Fits using the power-law Equation 4.7 to (a) the entire range of P, (b) the large load range, and (c) the small load range. The points in the large range of P are represented by filled markers and the small range of P by open markers. Set 1 (●, —), Set 2 (▲, · ·), and Set 3 (♦, - -), Sahli et al. [17] (■,—), and Mergel et al. [55] (▼, —).

Table 4.6: Power-law fit exponent, κ, of Equation 4.7.

Set \ Range of P	Entire	Large	Small
1 (●, —)	1.11 ± 0.03	1.14 ± 0.06	1.01 ± 0.01
2 (▲, · ·)	0.98 ± 0.09	1.07 ± 0.07	0.73 ± 0.02
3 (♦, - -)	0.80 ± 0.09	1.17 ± 0.28	0.66 ± 0.02
Sahli et al. [17] (■, —)		1.17 ± 0.04	
Mergel et al. [55] (▼, —)			0.76 ± 0.07

Table 4.7: Power-law fit constant of proportionality, ρ, of Equation 4.7.

Set \ Range of P	Entire	Large	Small
1 (●, —)	2.13 ± 0.08	2.10 ± 0.15	1.84 ± 0.30
2 (▲, · ·)	2.09 ± 0.36	2.04 ± 0.19	1.13 ± 0.77
3 (♦, - -)	1.52 ± 0.30	1.12 ± 0.36	1.08 ± 0.53
Sahli et al. [17] (■, —)		2.04 ± 0.07	
Mergel et al. [55] (▼, —)			1.33 ± 0.28

All values in the magnitude order of 10^{-6}.

Even if, qualitatively, the difference between the fits performed on the different

range of normal force seems to be less important than when a linear relation is used, one can see, in particular in tables 4.6, that the values of the exponent differs with the range of normal forces that is considered. Again, as for α and λ, the interfacial shear strength σ exhibits a dependency toward the normal load P.

4.4 Discussion

To date, studies in the literature on the onset of sliding of elastomer sphere/plane contacts have focused on various and quite narrow ranges of normal forces. It is important to note that a wide range of experimental data is difficult to address experimentally due to the difficulty in controlling the various parameters involved in the process. Besides the difficulties, the setup of most recent experimental studies for small loads in Mergel et al. [55] and for large normal loads in Sahli et al. [17] does not allow direct measurements of the normal force really at play at the interface, which is only known through a dead weight [17] or estimated from the initial contact area using JKR theory [55].

In this chapter, the tangential force experiments on a model sphere/plane interface have been carried out over the widest range of normal forces in the literature. They even cover all the ranges of normal forces that we have identified. Thus, as intended, they filled the gap between all existing data and also improved the normal force measurements.

The characterization of the model interfaces followed generally the literature laws: (i) the empirical quadratic law, $A = A_0 - \alpha_A Q^2$, to describe the contact area reduction, (ii) the latest version of LEFM-based models and (iii) the threshold law, $Q_s = \sigma A_s$, to characterize the interface shear strength. However, if one looks much more in detail, it does not appear that these laws and models allow the experimental results to be adequately explained in a single and satisfying way over the entire range of normal forces that have been investigated. First, the quadratic exponent of the area reduction law and the LEFM based models seem to not well describe the decay of the contact area, in particular for small P (small A_0) (see Figure 4.14 or Figure4.18), not to mention the variation due to different E and ω_0 (from different samples). Second, the threshold law seems to work well only when using a limited range of force P (small or large

P). In other words, we have constant behaviors by ranges of normal force, but with different values of σ. However, when we try to unify the ranges of P, the scenario becomes more complicated and σ is not constant anymore (Figure 4.19 and Table 4.5). Even a power-law for σ (Equation 4.7) seems to not fit the very small loads (Figure 4.20 and Table 4.6). Such difficult unification may be due to the relative contribution of the elementary mechanisms responsible for the contact area reduction, which may differ for small and large normal loads, as previously suggested in Chapter 3.

4.4.1 Transition to kinetic sliding

Our experiments have shown that a quantitative comparison of the experimental results from different sets can be misleading. Nevertheless, it is still possible to indicate overall trends, which is the focus of the following discussion.

One trend which can be brought out is the aforementioned gradual transition to a kinetic sliding. According to Bowden and Tabor [25], when a tangential force Q is applied to an interface between two solids, the force increases quasi-statically with time t. Once Q reaches a peak Q_s, the interface starts to slide and Q suddenly decreases to a kinetic sliding Q_k (Figure 4.21, left side). However, experimentally, we observed a gradual transition to a kinetic sliding Q_k (Figure 4.21, right side), that is more evident in the large normal forces, as we could see in the Figure 4.3.

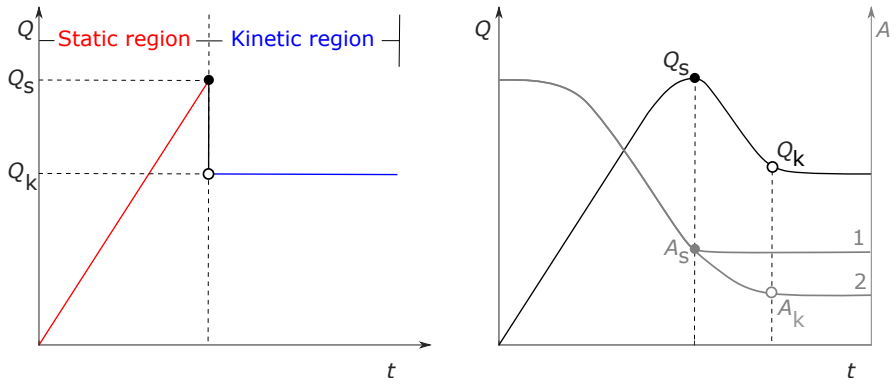

Figure 4.21: Time t evolution of the tangential force Q. Scheme of a theoretical abrupt (on the left side) and a more realistic gradual (on the right side) transition from a static region Q_s to a kinetic region Q_k. Scenario 1: the minimum contact area A_s is related to the static peak Q_s. Scenario 2: the minimum contact area A_k is related to the kinetic point Q_k.

In face of this gradual Q transition, we can rise some questions about the behavior of the contact area during this process: *Where is the minimum of the contact area? Is it*

related to the static peak Q_s (scenario 1 in Figure 4.21, right side)? Or to the kinetic point Q_k (scenario 2 in Figure 4.21, right side)?

To answer these questions, we revisit Figure 4.8, where, after reaching Q_s (indicated by a circle marker), the contact area continues to decrease (even more so for small loads) before entering the steady sliding regime. This means that the area associated with the tangential force peak Q_s is different and higher than the one in the steady sliding regime Q_k which seems to correspond more to scenario 2 in Figure 4.21 (right side). This observation about the continuation of the reduction of the contact area after Q_s can also be seen in the literature data from Mergel et al. [55] in their Figure 5(b), represented here in Figure 4.22. In this figure, the time t evolution of the contact area A is shown for a range of very small normal loads (from -0.46 mN to 7.74 mN), and we can clearly see that the contact area A continues to reduce after Q_s (indicated as a filled circle marker).

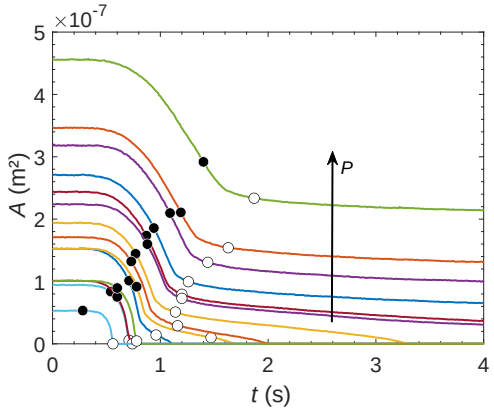

Figure 4.22: Contact area A evolution over time t adapted from Figure 5(b) of Mergel et al. [55]. The filled circle markers show the time of the tangential force peak Q_s and the open circle markers (not present in the original figure in [55]) a critical minimum area A_{crit} before entering a steady sliding regime.

Therefore, these literature data [55] and our three sets were analyzed to find the critical area A_{crit} before entering the steady state in the kinetic sliding regime. In theory, this regime is described as constant, but from an experimental point of view, we usually observe that there is indeed a slight slope (positive or negative), attributed to the presence of a residual angle in the experimental device. This slope makes the detection of A_{crit} a little more complicated. For it, we have used the following procedure: (i) for the literature data, the MATLAB® function *findchangepts* was used to find the point where the mean value and slope of the contact area curve (using linear statistics) changed most abruptly. This function was applied in a curve interval between Q_s and

$1.5 \times Q_s$. The found A_{crit} are shown in Figure 4.22 as open circle markers; (ii) for our three experimental sets, the same identification A_{crit} method was used. However, due to the great oscillations in some curves, the method was applied to the lower envelope of them (see Section 2.4.2) and a visual inspection was performed to confirm that the automatically found A_{crit} was in a critical zone to a steady sliding regime. If not, a manual identification was performed. And to avoid manual user error, a simple click-and-point interface was developed, asking 7 volunteers to indicate the critical point on the curves and the average of the answers was taken into account. An asterisk will be used to indicate cases where A_{crit} manual detection was used.

Thus, the normalized difference between A_s and A_{crit} was plotted in Figure 4.23 *versus* the initial contact area A_0. The experiments in which the contact abruptly vanishes during shearing were not considered here since they do not enter a clear steady sliding regime, as for example, the bottom light blue curve in Figure 4.22.

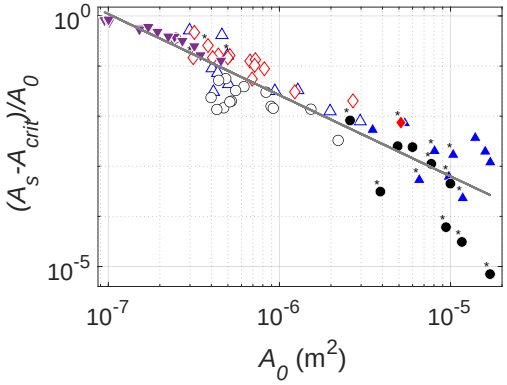

Figure 4.23: Normalized difference between the contact area at the moment of tangential force peak A_s and the area before entering a steady state in the kinetic sliding regime A_{crit} *versus* the initial contact area A_0. Set 1 (●), Set 2 (▲), and Set 3 (♦). The points in the large range of P are represented by filled markers and the small range by open markers. Literature data for small loads are also show as ▼ (Mergel et al. [55]). Asterisks denote cases where A_{crit} was manually detected.

The points of Figure 4.23 are well fitted by using a power-law relation ($f(x) = ax^k$) with an exponent of -1.61 $\pm$ 0.17 (see grey line). This means that at large initial contact area A_0 (*i.e.* at large P), the difference between A_s and A_{crit} is very small or even almost zero. Therefore, A_{crit} is almost simultaneous with the tangential force peak Q_s, and more related to scenario 1 in Figure 4.21 (right side). Contrarily, the more A_0 decreases (*i.e.* the more P decreases), the further the A_{crit} seems to move away from Q_s, indicating

that the area reduction mechanisms continue after Q_s, which is more similar to scenario 2 in Figure 4.21 (right side).

In the case of scenario 2, we can propose two hypotheses: (i) macroscopic sliding starts at Q_s and the contact area reduction continues after it, that is, during the macroscopic sliding. However, in this case, what would be the mechanisms, since lifting and deformation require a stuck area?; (ii) macroscopic sliding starts after the tangential peak, that is, it starts at Q_{crit} when A reaches A_{crit}. In that case, is adhesion playing a dominant role in the transition to sliding? Due to the fact that these observations occur close to a dynamic phase of the contact's evolution in which the micro-slip front finishes invading the interface, experiments in the presence of particles (tracers) with a high temporal resolution are required to validate these hypotheses.

4.4.2 Alternative interpretation of the interface shear strength

The non-correspondence between Q_s and A_{crit}, that is when they do not occur at the same time, poses an issue in the definition of the interface shear strength σ. So far, σ has been defined as the ratio Q_s/A_s, and in order to evaluate it, the static stresses stored in the interface must be entirely relaxed down to their kinetic counterpart, *i.e.* the interface must be in a full sliding regime.

Is this still the case with small loads? Should one take into account the adhesion (either with analytical model or with numerical methods). The current problem (in the course of resolution) is that the analytical model are in simple elasticity and the numerical models do not take into account the adhesion. One can wonder if the simultaneous taking into account of the two phenomena is necessary and if each one is dominant on the other according to the range of force.

In view of these observations, we propose an alternative shear strength, defined as Q_{crit}/A_{crit}. Figure 4.24 shows, in a log-log scale, the critical contact area A_{crit} as a function of its corresponding tangential force Q_{crit}. Due to the presence of oscillations in the tangential force Q curves, Q_{crit} was taken from the lower envelope of Q, constructed at the same way of the area lower envelope (see Section 2.4.2).

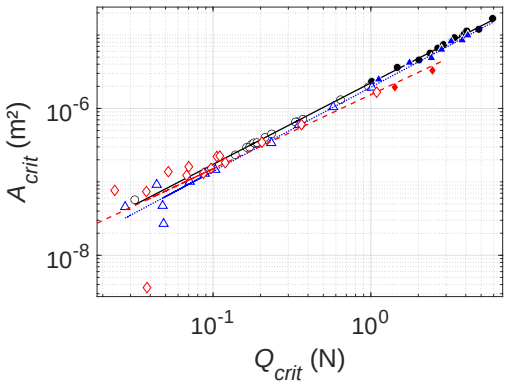

Figure 4.24: Critical contact area A_{crit} as a function of Q_{crit} (Q at the moment of A_{crit}) in a log-log scale. The points in the large range of P are represented by filled markers and the small range by open markers. Set 1 (●, —), Set 2 (▲, · ·), and Set 3 (♦, - -). Lines are the power-law fits ($f(x) = ax^k$) with the same color as the corresponded fitted set

Given how well aligned the points in Figure 4.24 appear, we fitted them with a power-law equation ($f(x) = ax^k$), shown as lines in Figure 4.24 (colored lines with the same color as the corresponded fitted set). The fit exponent results are 1.11 ± 0.01 (Set 1: ●, —), 1.14 ± 0.05 (Set 2: ▲, · ·), and 1.01 ± 0.23 (Set 3: ♦, - -). We can observe that the fits are in better agreement with the points than the fits of the classic definition of σ (see Figure 4.20).

For a better comparison we show in Figure 4.25 as filled marker: A_s and Q_s; and as open markers: A_{crit} and Q_{crit}. A vertical shift was applied between the experimental sets by an offset on the points for a better visualization.

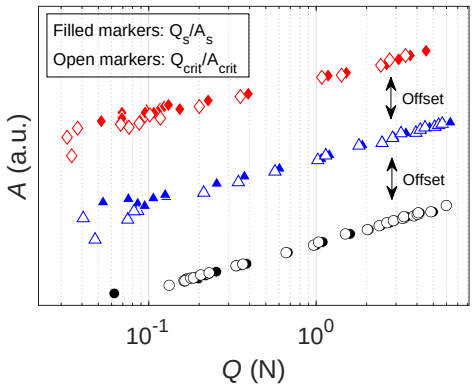

Figure 4.25: Contact area A as a function of the tangential force Q in a log-log scale for Set 1 (●), Set 2 (▲), and Set 3 (♦). A vertical shift was applied between the sets by an offset on the points to a better visualization.

We can see in Figure 4.25 that the critical points seem to be better aligned than the points at tangential force peak. Also, the difference between the two sets of points

seems to increase with the decrease in the normal load. Then, a scenario 2 which the hypothesis (ii) that the macroscopic sliding starts after the tangential peak (as discussed in Section 4.4.1) seems to be more reasonable.

4.4.3 The effect of normal load on contact area reduction mechanisms

A qualitative visual analysis of the contact area images by superimposing frames of the initial contact area (at $Q = 0$) and frames at the static friction peak (at Q_s) in the frame of the moving glass plate was performed and is shown in Figure 4.26. In this figure, the leading edge of the contacts is on the left side. The black region, in the middle, shows the contact area presents during the onset of sliding (from $Q = 0$ to Q_s); the blue region, on the right edge, shows the area presents at $Q = 0$ and not at Q_s; and the red region is the area not presents at $Q = 0$ but presents at Q_s. Images for four normal forces are presented (in the columns), two in the small load range (a and b) and two in the large load one (c and d), for the three sets (in the rows).

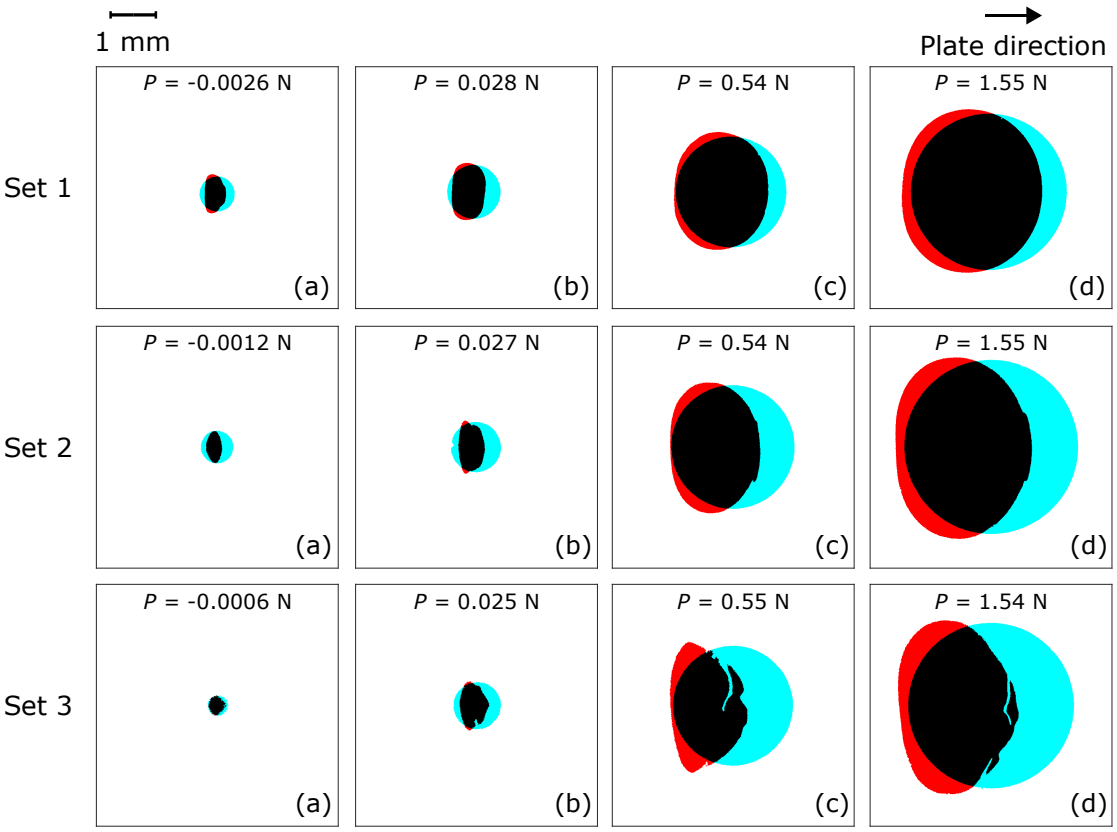

Figure 4.26: Superimposed images of the initial contact (at $Q = 0$) and images of the contact area at the static friction peak (at Q_s) in the frame of the moving glass plate. The leading edge of the contacts is on the left side. The black region is the contact area presents both at $Q = 0$ to Q_s; the blue region the area presents at $Q = 0$ and not at Q_s; and the red region the area not presents at $Q = 0$ but presents at Q_s.

In a first qualitative analysis of Figure 4.26, we can see that in the large loads, Figure 4.26(c-d), the lost contact area at Q_s (in blue) occur at the trailing edge of the contact and the new contact area at Q_s (in red) on the leading one. While, under small load, Figure 4.26(a-b), the lost contact area at Q_s (in blue) appears on both edges. These observations are consistent with the disappearance/appearance of contact area due to the elementary mechanisms of lifting/lay down seen in the previous Chapter 3. This seems to confirm that the relative contributions of the elementary reduction mechanisms on the contact area reduction under shear depend on the normal force and also that these relative contributions are the reason of the higher rate of reduction α observed under small loads. It is worth noting, however, that we cannot make a direct and conclusive comparison between these observations of Figure 4.26 and the mechanisms observed in Chapter 3 since there are no particles to validate them.

In a second qualitative analysis of Figure 4.26, now comparing the three sets, we can see that they present the same trend of lost contact and new contact areas, however there is an increase of both contributions from Set 1 to Set 3. Set 3 even presents a slight difference in the morphology. Those observations indicate that the area reduction also depends on the material properties and possible uncontrolled parameters like surface contamination.

4.5 Conclusion

This chapter aimed at improving the understanding of shear-induced area reduction from millinewtons up to newtons normal force, covering the gap of experimental data in the literature that so far was concentrated in distinct normal load ranges. We thus performed the first experiments to bridge the gap between those two ranges with the very same sample and experimental setup.

By analysing the experimental data, the main features and parameters were discussed along with the literature experimental data, and we have shown that a quantitative comparison between experiments obtained from the same equipment/procedure is already challenging. Therefore, comparing theoretical and numerical results with experimental data from different teams and labs may result in misleading conclusions.

We have confirmed the already raised discussion about a higher rate of contact area reduction under small normal loads, and indicated the possibility of a PDMS properties dependence. In particular, for small normal loads, we also show that area reduction continues after the tangential peak force, which calls into question the definition of the exact moment of the transition to sliding.

The results indicate that the large normal load behavior holds down to about 0.1 N, below which adhesive effects presumably become non-negligible, *i.e.* the results seems to indicate a different contribution of the mechanisms of contact area reduction from that at larger normal loads. Ideally, the introduction of particles, as was performed for large loads in Chapter 3, would enable verification of the contact area reduction mechanisms and their relative contributions in different ranges of normal force.

Chapter 5

Sliding friction under normal loading variation

5.1 Introduction

When two rough surfaces move relative to each other, first, during purely normal contact, their roughness causes contact to occur at discontinuous contact spots, that is, between their asperities, which might have not only random sizes and heights (as often taken into account in the literature [97]), but also differ in terms of the mean plane of their macroscopic contact interface. Such an interface may have a different inclination than nearby micro-contacts, and be different from the mean plane of the contact interface macroscopic, *e.g.*, two opposite asperities in contact, whose summits are not confused. Second, during relative motion, these micro-contacts have finite life-times (constantly coming in- and out-of-contact), causing the local loading conditions between them to vary significantly.

Unfortunately, these two characteristics - inclination and temporal evolution of the load - are not taken into account by the approach classically used in contact mechanics, which often considers a constant normal loading and a contact model sphere and shear plane parallel to the plane of interface.

In this chapter, in order to study more realistic contact problems, which integrate these non-standard conditions, we will investigate the influence of the loading trajectory on sheared model interfaces. In particular, the variation of the normal load during shear and its influence in terms of coefficient of friction, contact area variation, area reduction parameter and interfacial shear strength will be studied.

5.2 Experimental set-up

The experiments were carried out using the tribometer presented in Section 2.2.1 on S1R9 samples (a single smooth sphere with a radius of curvature of 9.42 mm, see Section 2.1.2) against a smooth glass plate. Shearing tests with simultaneous normal loading variations were performed by introducing a slight tilt between the glass plate and the direction of the tangential loading. For this, two representative cases were considered:

Case A - Tilt of the sliding plate: the tilt was introduced using the goniometer located above the tangential force sensor and the cantilever. In this case, not only the sliding plate was tilted, but also the cantilever and the tangential force sensor, see Figure 5.1. In this case, we used a normal attachment configuration (defined in Figure 2.5) - fixed sphere at the bottom (in blue) and plate at the top (in red).

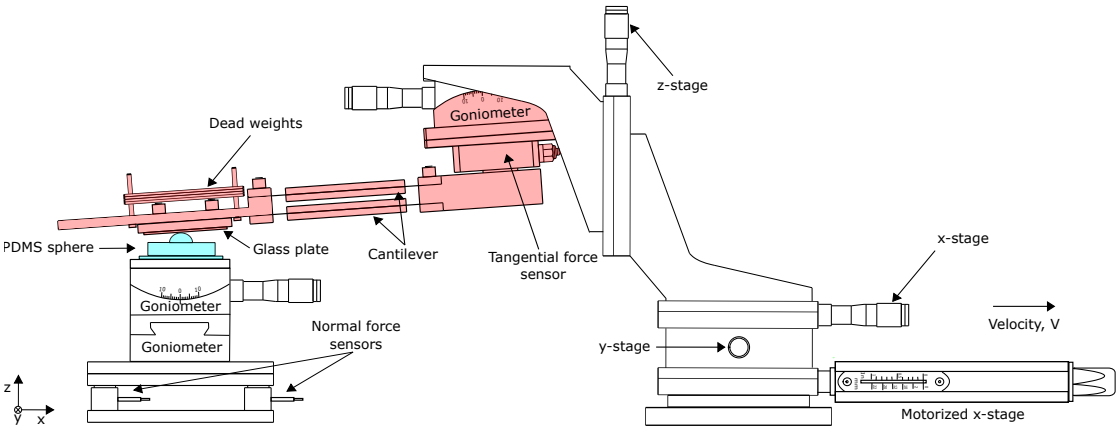

Figure 5.1: Setup for Case A - Tilt of the sliding plate.

Case B - Tilt of the fixed plate: the goniometer located under the fixed plate was used for introducing the tilt, as shown in Figure 5.2. In this case, we used an inverse attachment configuration (also defined in Figure 2.5) - sliding sphere at the top (in blue) and the fixed plate at the bottom (in red).

Note that these presented cases are only two of the possibilities of introducing a tilt in one tribological test among many others. Nevertheless, they were chosen because they illustrate, as we will see later, the two main configurations that are expected, the other configurations being reduced to one or the other of these two cases if we focus only on the contact interface.

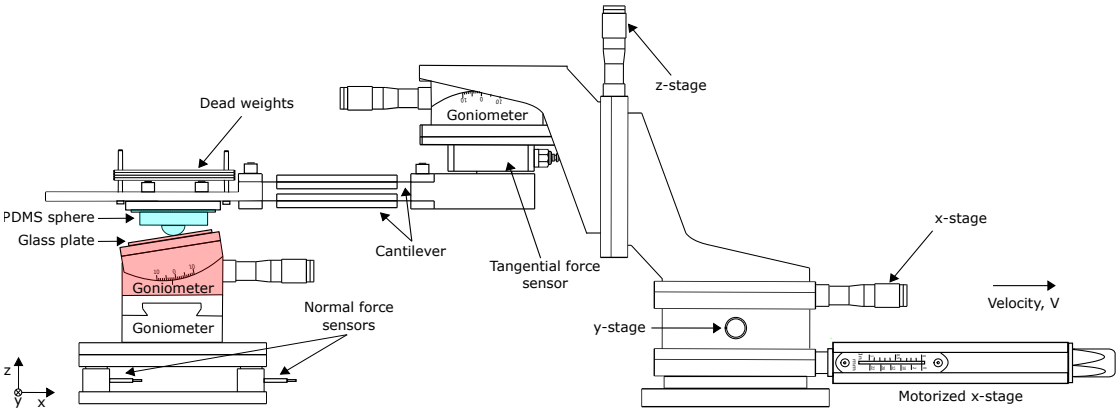

Figure 5.2: Setup for Case B - Tilt of the fixed plate.

For each case, the normal load was first applied by adding dead weights, and then the tilt was set up using the respective goniometer. After that, the initial value of normal force was verified with the normal load sensors and adjusted, if necessary, to reach the target normal force value, via the z-stage, which pushes the whole ensemble of tangential force sensor, cantilever and slider sample on the sphere (resp. plate) in a normal (resp. inverse) attachment configuration. The tilt is defined as the angle ϕ between the contact interface plane and the xy-plane. Note that, in both configurations, the motor displacement is applied only in the x-direction, and therefore parallel to xy-plane. Positive angles have been defined as the ones corresponding to a motion of the sphere upwards on the glass plate, as shown in Figure 5.3.

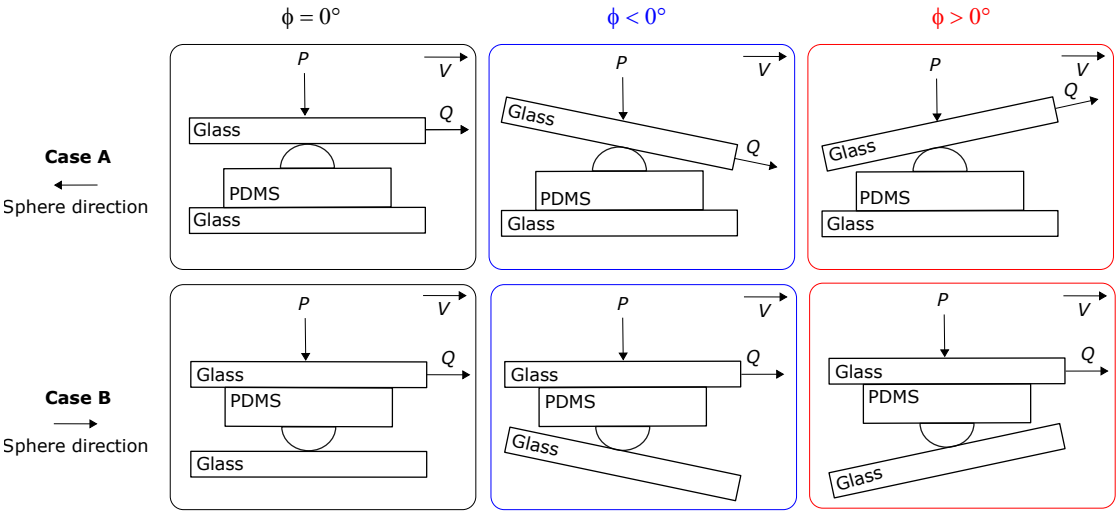

Figure 5.3: Definition of the tilt angle ϕ. Case A: Tilt of the sliding plate. Case B: Tilt of the fixed plate. Left: aligned configuration ($\phi = 0°$), centre: $\phi < 0°$, and right: $\phi > 0°$.

The tangential motion was imposed to the plate (resp. sphere) for Case A (resp. Case B) at a constant velocity $V = 0.1\,\mathrm{mm/s}$. Images of the contact area during the

running of the tangential force were recorded at 100 fps. The lateral square pixel varied in the range of 7.90 μm - 9.06 μm for the different sets of experiments. The contact area A was obtained from the images following the image processing described in Section 2.3.1, where, basically, each image is segmented by applying a threshold on the image intensity distribution using Otsu's method [72]. Consequently, the images are binarized into in- and out-of-contact regions according to their intensity level with respect to the threshold. Then, the total number of in-contact pixels is multiplied by the square of the pixel size to evaluate the apparent contact area A_{app} seen by the camera, in squared meters. Note that, due to the tilt of the interface, the camera is no longer perpendicular to it and thus a correction is required to access the real contact area A. As A_{app} is the projection of A onto the xy-plane, we applied the following correction: $A = A_{app} / \cos\phi$.

Table 5.1: Sets of experiments.

Case	Range of ϕ	P_0	Sample
■ A	-4 to 4°	0.78 N	S1R9 (4)
▲ B(i)	-2.5 to 4°	0.78 N	S1R9 (4)
♦ B(ii)	-3 to 4°	0.78 N	S1R9 (5)
▼ B(iii)	-2.5 to 4°	0.10 N	S1R9 (5)
● B(iv)	-2°	-0.6 mN to 3.20 N	S1R9 (2)
● B(iv)	0°	-0.2 mN to 3.21 N	S1R9 (2)
● B(iv)	2°	-2.3 mN to 3.19 N	S1R9 (2)

Table 5.1 lists all experiments that have been performed. Cases A and B(i) were carried out under the same initial normal force P_0 of 0.78 N and with the same sphere, S1R9 (4). Cases B(i) and B(ii) were performed under the same initial normal load P_0 of 0.78 N and different spheres, S1R9 (4) and S1R9 (5). For the same sphere, S1R9 (5), two different normal forces were tested, $P_0 = 0.10$ N B(iii) and $P_0 = 0.78$ N B(ii). Finally, to test the influence of the tilt on a wide range of initial normal loading, three sets of experiment, named B(iv), with two opposite angles, -2° and 2°, and an aligned case, 0°, were performed with the same sphere, S1R9 (2).

For Case A, the aligned experiment $\phi = 0°$ was carried out first. Then, we performed the ones with $\phi > 0°$ in an ascending order and last, the ones with $\phi < 0°$ in a descending order. For Cases B(i,ii, and iii), the experiments were performed in the following order: $\phi = 0°$, $\phi < 0°$ (descending order), and $\phi > 0°$ (ascending order). In Case B(iv), the experiments were carried out randomly in relation to the applied initial

normal load, and ϕ was modified every 5 tests in the following order: $\phi = 0°$, -2°, and 2°. For example, 5 different initial normal loads (randomly selected) at $\phi = 0°$ were tested. Then the same 5 initial normal loads were tested for $\phi = -2°$, and last the same 5 initial normal loads for $\phi = 2°$. For Cases B, the contact area was difficult to be correctly detected for angles smaller than $-2.5°$, because, in such conditions, the projected contact area touches the edge of the field of view detected by the camera, making the detection of the contact area difficult.

5.3 Results and analysis

In this section, we will present the results and analyses, first, for Case A (tilt of the sliding plate) and second, for Case B (tilt of the fixed plate).

5.3.1 Case A: tilt of the sliding plate

Raw experimental results

Figure 5.4 shows the evolution of (a) the tangential force Q and (b) the normal force P during the displacement d.

In Figure 5.4(a) a typical tangential force-displacement curve behavior is observed for all angles ϕ, *i.e.* when the plate starts to move, Q increases linearly. Then, a small difference between the positive and negative angles can be noticed in the slight slope change before the curves reach their maximum Q_s. After Q_s, the curves decrease entering in a macroscopic sliding with, unlike a constant regime, a decay for $\phi < 0°$ (blue lines) and a rise for $\phi > 0°$ (red lines). As mentioned in Section 2.5, we found a greater tangential force at the beginning of the sets of experiments, which may be due to the orientation, extension, and/or pull-out of the PDMS chains [14, 74, 75]. For this reason, the first tests are usually eliminated, but as an exception here, they were considered. The higher Q_s values for $\phi = 0°$, 0.5°, and 1° may be due to this reason rather than a effect of the tilt. Excluding the first tests ($\phi = 0°$, 0.5°, and 1°), the values of Q_s are also a little different, of around 6 % for ϕ ranging between $-4°$ and 4°.

Concerning the normal force-displacement curves, shown in Figure 5.4(b), we can observe that, for $\phi = 0°$ (black line), the normal force is, as expected, constant during

the entire sliding process. However, with the addition of a positive (resp. negative) tilting, the normal force start to decrease (resp. increase) before entering the macroscopic sliding regime. We can observe a variation of the normal force at Q_s of around 33 % for a variation of ϕ in the range of -4° to 4°. In the subsequent sliding regime, the normal force remains nearly stable even if some variations, out of the scope of this work, can emerge at large angles, both positive and negative.

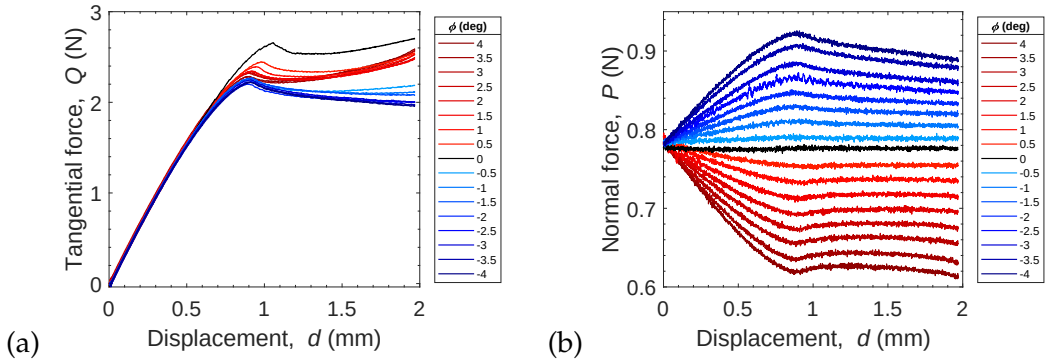

Figure 5.4: Evolution of (a) the tangential force Q and (b) the normal force P during the displacement d for Case A.

Figure 5.5 shows the evolution of the contact area A as a function of (a) the displacement d and (b) of the tangential force Q up to its peak. A typical behavior evolution of A, as in previous experiments in the literature [17, 55], can be seen in all curves, *i.e.* a reduction of A starting immediately withan increase of (a) the displacement d and (b) the tangential force Q, before reaching the macroscopic sliding regime during which A remains nearly constant. We also can identify here a discrepancy in the first tests ($\phi = 0^\circ$, 0.5°, and 1°), showing a greater reduction in the contact area, probably for the same reasons responsible for the modification of tangential force curves. Excluding them, a variation of the contact area at Q_s of around 5 % for a variation of ϕ in the range of -4° to 4° can be observed for all tilt angles. In light of these observations, the tilt does not appear to have a significant influence on the reduction of the contact area.

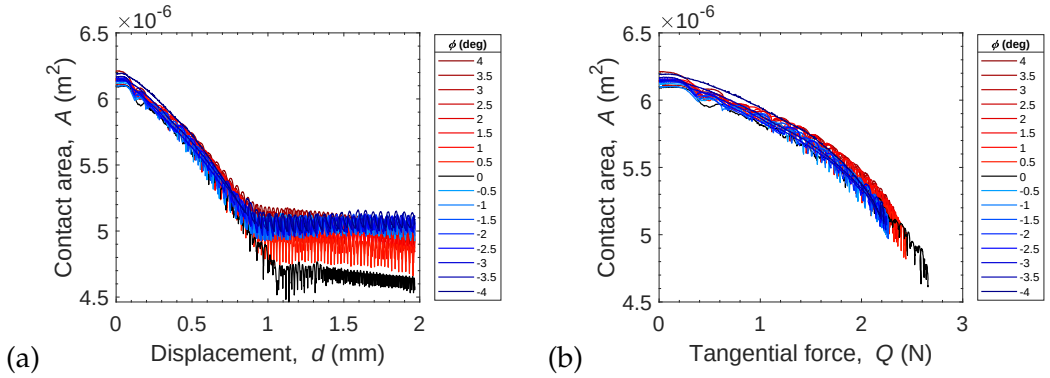

Figure 5.5: Contact area A as a function of (a) the displacement d and (b) the tangential force Q up to its peak for Case A.

Analysis: from raw to real force measurements

The results presented above lead us to some intriguing questions: *why does a 33 % variation in the normal force have no significant effect on the tangential force and on the contact area reduction? Have we really carried out the experiments we expected and applied a normal load variation? Is there something wrong with our measurements?*

In order to answer those questions, we will analyze the forces acting on the contact interface during the experiment in more details. The main objective is to see if they correspond to the forces that are measured by the sensors, as one expects in a well-designed experiment.

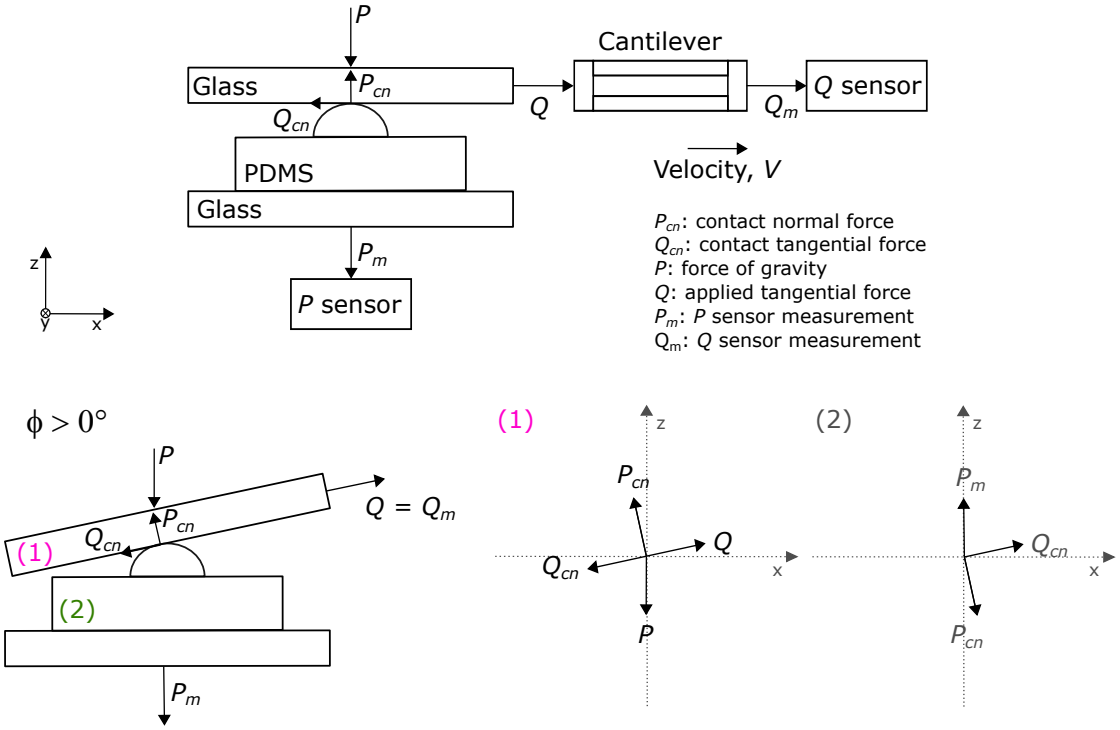

Figure 5.6: Force diagrams of Case A. Top panel: forces acting on an aligned system ($(\phi = 0°)$). Bottom panel: forces acting on a positive tilting position ($\phi > 0°$).

The top panel of Figure 5.6 shows all the forces at play in the Case A configuration. There are 4 forces acting on the system - the force of gravity $P = mg$ due the presence of a dead-weight in our experiment, the applied tangential force Q, and the contact tangential Q_{cn} and normal P_{cn} forces. P acts in a downward direction and is colinear with the normal force measured by the sensor P_m. Q is colinear with the tangential force measured by the sensor Q_m. We consider that P and Q are both directly measured by our normal/tangential force sensors. P_{cn} acts in a direction perpendicular to the contact plane and Q_{cn} parallel to it.

The bottom panel of Figure 5.6 shows the forces at play in a tilted configuration for a positive angle and the free body diagram on (1) the glass plate and on (2) the PDMS sphere for a positive tilting position. In all the tilting configurations, that is, for positive and negative ones, the forces must be balanced to fulfill the conditions of static equilibrium.

First, the cantilever equilibrium gives:

$$\|Q\| = \|Q_m\| \tag{5.1}$$

Analyzing the static equilibrium of (1) in the x- and z-direction, respectively, gives

$$\|Q_{cn}\| \cdot \cos(\phi) + \|P_{cn}\| \cdot \sin(\phi) = \|Q\| \cdot \cos(\phi) \tag{5.2}$$

$$\|P_{cn}\| \cdot \cos(\phi) + \|Q\| \cdot \sin(\phi) = \|P\| + \|Q_{cn}\| \cdot \sin(\phi) \tag{5.3}$$

or, in a parallel and perpendicular direction to the contact interface, it gives

$$\|Q_{cn}\| + \|P\| \cdot \sin(\phi) = \|Q\| \tag{5.4}$$

$$\|P_{cn}\| = \|P\| \cdot \cos(\phi) \tag{5.5}$$

The analysis of the static equilibrium of (2) in the z-direction (downward) gives

$$\|P_m\| = \|P_{cn}\| \cdot \cos(\phi) - \|Q_{cn}\| \cdot \sin(\phi) \tag{5.6}$$

In summary,

$$\|Q_{cn}\| = \|Q_m\| - \|P\| \cdot \sin(\phi) \tag{5.7}$$

$$\|P_{cn}\| = \|P\| \cdot \cos(\phi) \tag{5.8}$$

$$\|Q_m\| = \|Q_{cn}\| + \|P_{cn}\| \cdot \tan(\phi) \tag{5.9}$$

$$\|P_m\| = \|P_{cn}\| \cdot \cos(\phi) - \|Q_{cn}\| \cdot \sin(\phi) \tag{5.10}$$

From those equations, one can see that, in the tilted experiments, the forces acting on the contact (Q_{cn} and P_{cn}) do not correspond to the ones that are measured (Q_m and P_m). However, knowing the tilt angle and using the equations above, it is now possible to calculate them.

Figure 5.7 shows the real force-displacement curves acting in the contact both for (a) the contact tangential force Q_{cn} and (b) the contact normal force P_{cn}. The $Q_{cn}(d)$ evolution remains similar to $Q(d)$ evolution from Figure 5.4, showing only a slight reduction,

due to the subtraction of $P \cdot \sin(\phi)$ (see Equation 5.7). Indeed, $P < Q_{max}$ at least for elastomers and $sin(\phi)$ is small. However, for $P_{cn}(d)$, the corrections are huge, because during the entire experiment, the normal sensors progressively measure a growing portion of the tangential force that is projected onto the interface plane, $Q_{cn} \cdot \sin(\phi)$ (see Equation 5.10). Indeed, $\sin(\phi)$ is small but as Q continuously increases up to even become much higher than P, $Q \sin(\phi)$ becomes no longer negligible and its evolution is mainly responsible for the unexpected evolution of P that is measured. Once this contribution of the tangential force is removed, we note that the $P_{cn}(d)$ curves are nearly flat and constant; meaning that, from the contact's point of view, tilting the whole ensemble of tangential force sensor, cantilever and slider sample, has no effect on P_{cn}. Instead of 17 different experiments, we now understand that we have just replicated the same experiment 17 times, and the remaining Q_{cn} variation is only due to uncertainties (or maybe some secondary effects). The remaining small changes of about 4 % in the contact tangential force peak Q_{cns} are related to the also small relative changes of P_{cns} (at Q_{cns}) of about 1.5 %. Even though it is outside the scope of this work, which is focused on the onset of sliding, one can observe that, in steady sliding regime, both the tangential and normal forces seem to increase (resp.decrease) for positive (resp. negative) ϕ.

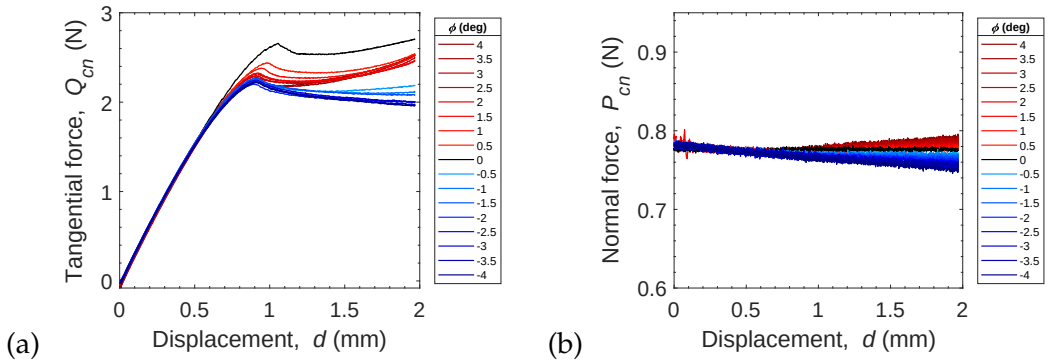

Figure 5.7: Evolution of the contact tangential force Q_{cn} and (b) the contact normal force P_{cn} during the displacement d.

5.3.2 Case B: tilt of the fixed plate

Raw experimental results

Figure 5.8 shows Case B(i) results, that has an initial normal force of 0.78 N (same as Case A) and a tilt variation between -2.5° and 4°. This figure shows (a) the tangential Q and (b) the normal P forces, directly measured by the sensors, as a function of the

displacement d; (c) the evolution of the contact area A as a function of the displacement d and (d) as a function of the tangential force Q up to its peak.

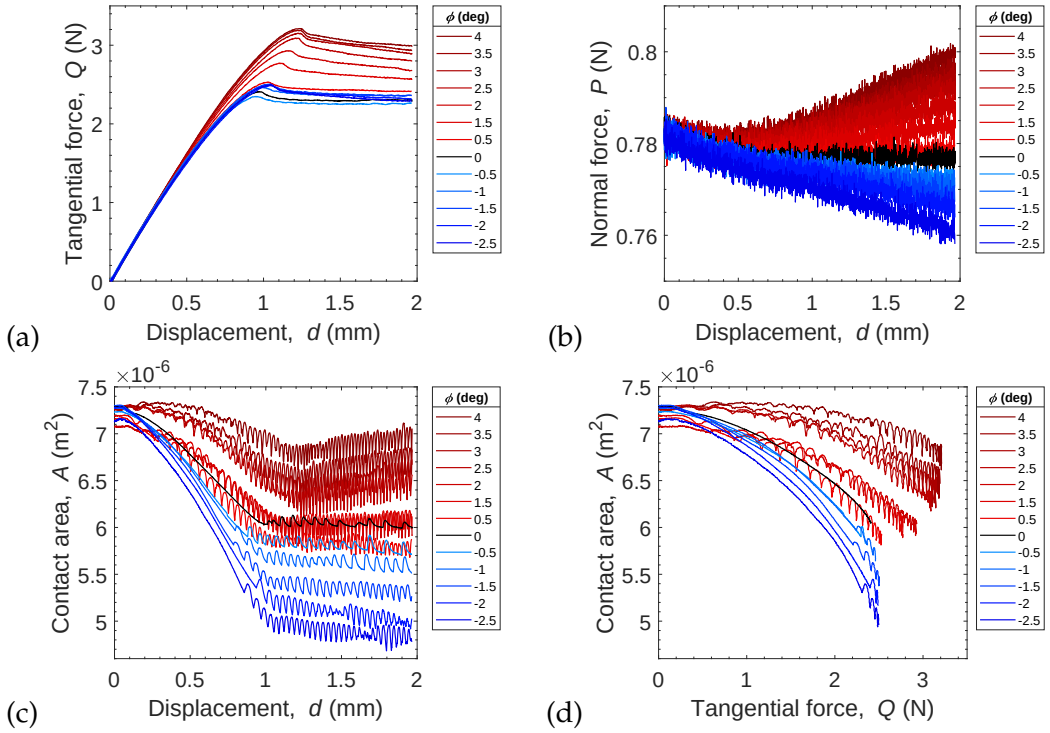

Figure 5.8: Results of Case B(i), where the initial normal force is 0.78 N and the tilt angle ϕ ranges between -2.5° and 4°. (a) Tangential force Q and (b) normal force P as a function of the displacement d; (c) contact area A as a function of the displacement d and (d) as a function of the tangential force Q up to its peak.

In Figure 5.8(a), as in Case A, we can also see the typical sphere/plane shear-induced behavior: the tangential force increases linearly, followed by a transition peak to a constant macroscopic sliding regime. Note that the tangential force peak Q_s increases with the positive tilt angles $\phi > 0$, whereas it seems to remain almost invariable for negative ones $\phi < 0$. Concerning the normal force measured by the sensors, in Figure 5.8(b), the addition of the tilt results in a different and nearly opposite behaviour when compared to Case A. The normal force is nearly constant until the tangential force reaches its peak Q_s, and, in the sliding regime, a large decay for $\phi < 0°$ (blue lines) or a large rise for $\phi > 0°$ (red lines) is observed. The evolution of the contact area A, in Figure 5.8(c), shows, in comparison to the aligned case (black line), a greater reduction for $\phi < 0°$ (blue lines) and a smaller reduction for $\phi > 0°$ (red lines). In Figure 5.8(d), the trajectory of the contact area reduction and the value of the endpoints, that is, the tangential force peak Q_s and the corresponding contact area A_s seem to be affected by

the tilt of the fixed plate. In this case, with a ϕ variation range of $-2.5°$ to $4°$, we observe a Q_s variation of $\sim$ 27 % and a A reduction at Q_s of $\sim$ 30 % while the normal force P remains essentially constant (less than 3 % variations).

Analysis: from raw to real force measurements

As in the previous case, those results lead us to some interesting and almost similar questions: *why do the tangential and the contact area vary so much when the normal force appears to be nearly constant? Have we really carried out the experiments that we expected, a test with a normal load variation? Is there something wrong with our measurements?*

In order to answer these questions, we will again analyze in more detail the forces acting on the contact interface during the experiment. The top panel of Figure 5.9 shows the forces at play in the Case B configuration, and the bottom panel a diagram of forces for a positive tilting case, which shows the free body diagram on (1) the glass plate and (2) on the PDMS sphere. Such forces, as in Case A, must be balanced for all the tilting configurations (positive and negative) to fulfill the conditions of static equilibrium.

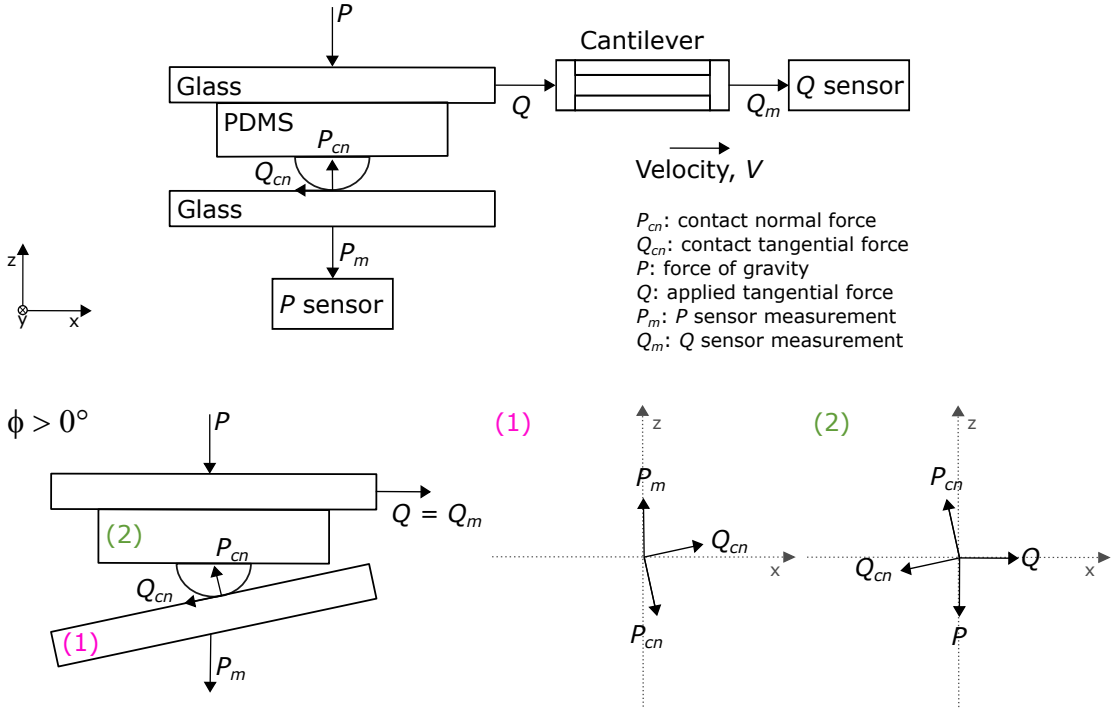

Figure 5.9: Force diagrams of Case B. Top panel: forces acting on an aligned system ($\phi = 0°$). Bottom panel: forces acting on a positive tilting position ($\phi > 0°$).

Thus, here again, the cantilever equilibrium gives:

$$\|Q\| = \|Q_m\| \tag{5.11}$$

And the static equilibrium of (1) in the z-direction gives

$$\|P_m\| = \|P_{cn}\| \cdot \cos(\phi) - \|Q_{cn}\| \cdot \sin(\phi) \tag{5.12}$$

The equilibrium of (2) in the x- and z-direction gives

$$\|Q_{cn}\| \cdot \cos(\phi) + \|P_{cn}\| \cdot \sin(\phi) = \|Q\| \tag{5.13}$$

$$\|P_{cn}\| \cdot \cos(\phi) = \|P\| + \|Q_{cn}\| \cdot \sin(\phi) \tag{5.14}$$

And in a parallel and perpendicular direction to the contact interface

$$\|Q_{cn}\| + \|P\| \cdot \sin(\phi) = \|Q\| \cdot \cos(\phi) \tag{5.15}$$

$$\|P_{cn}\| = \|P\| \cdot \cos(\phi) + \|Q\| \cdot \sin(\phi) \tag{5.16}$$

In summary,

$$\|Q_{cn}\| = \|Q_m\| \cdot \cos(\phi) - \|P\| \cdot \sin(\phi) \tag{5.17}$$

$$\|P_{cn}\| = \|P\| \cdot \cos(\phi) + \|Q_m\| \cdot \sin(\phi) \tag{5.18}$$

$$\|Q_m\| = (\|Q_{cn}\| \cdot \cos(\phi) - \|P_{cn}\| \cdot \sin(\phi)) / \cos(2\phi) \tag{5.19}$$

$$\|P_m\| = \|P_{cn}\| \cdot \cos(\phi) - \|Q_{cn}\| \cdot \sin(\phi) \tag{5.20}$$

After making the necessary corrections using the equations above, Figure 5.10 shows the real forces acting on the contact interface of Cases B(i,ii,iii, and iv). On the left (resp. right) side, the contact tangential force Q_{cn} (resp. contact normal force P_{cn}) is shown as a function of the displacement d. The $Q_{cn}(d)$ curves remain similar to $Q(d)$ curved from Figure 5.8, showing only a slight reduction, due to the subtraction of $P \cdot \sin(\phi)$ and multiplication of $cos(\phi)$ (see equation 5.17). Indeed, again, Q continuously increases

up to even become much higher than P, $sin(\phi)$ is small, and $cos(\phi) \sim 1$. However, for $P_{cn}(d)$, the corrections are huge (as in Case A), because during the entire experiment, the normal sensors progressively measure a tangential force component that is projected onto the interface plane, $Q_{cn} \cdot \sin(\phi)$. $\sin(\phi)$ is small but as Q increases to become even higher than P, $Q_{cn} \cdot \sin(\phi)$ becomes no longer negligible and is mainly responsible for the unexpected evolution of normal force that is measured. The $P_{cn}(d)$ curves actually vary significantly before the onset of sliding, progressively increasing (resp. decreasing) for positive (resp. negative) angles.

When entering the macroscopic sliding regime, Q_{cn} remains stable. We can identify a variation of P_{cn} at the instant of Q_s of more than 38 % for a variation of ϕ in the range of -4° to 4° which may explain the variation in the contact tangential force peak Q_{cns} ($\sim$ 29 %). Indeed, from Equation 5.18, one can see that, in this case, this is not the measurement of the normal force that is affected by a tiny part of the friction force but the normal force (P_{cn}) acting on the contact itself. There is a clear coupling between P and Q. In Case B, while we seem to measure a constant normal force, in reality, we are performing tests with progressively increasing normal loads. Figure 5.10 shows, on the right side, that the tilt angle ϕ significantly affects the normal force acting on the contact interface. The increase in the loading during the displacement of the contact is proportional to the friction force that develops progressively at the interface. Note that in the sliding regime, as Q is expected to remain constant, P also remain constant but at a higher (resp. lower) values than the one at the beginning for positive (resp. negative) angles.

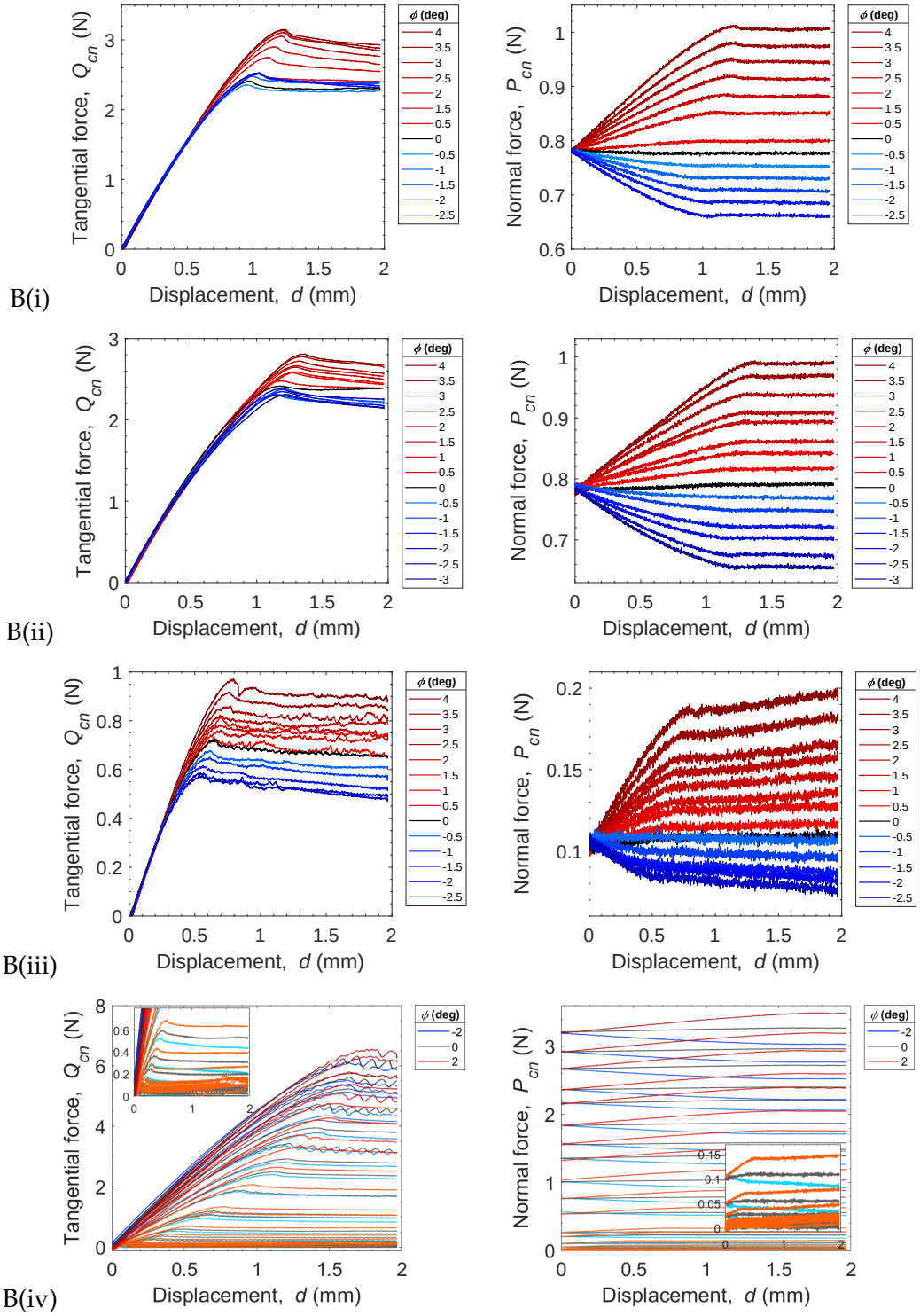

Figure 5.10: Evolution of the contact tangential force Q_{cn} (on the left side) and the contact normal force P_{cn} (on the right side) as functions of the displacement d. B(i): 0.78 N; B(ii): 0.78 N; B(iii): 0.1 N; B(iv): wide range of initial normal force for 3 different tilt angles (-2°: blue lines, 0°: black lines, and 2°: red lines). The color gradients for Cases B(iv) are in function of the initial normal force P_0; light colors for small P_0 and dark colors for large P_0. The insets on B(iv) show a zoom in the small P_0.

Analysis: effect on the real area evolution

Figure 5.11 shows the evolution of the contact area A as a function of displacement d (on the left side) and as a function of the contact tangential force Q_{cn} up to its peak (on the right side). We can see in this figure that, when compared to $\phi = 0^\circ$ (aligned cases, black lines), the A reduction is greater for $\phi < 0^\circ$ (blue lines), and it is smaller for $\phi > 0^\circ$ (red lines).

In order to know whether those variation in the contact area evolution can be understand knowing the real loading condition applied to the interface, *i.e.* a gradual increasing/decreasing of the contact normal force due to the coupling with the friction force, we will perform the usual analyses initially proposed by Sahli et al. [17]: evaluation of the area reduction rate α_A and of the interfacial shear strength σ.

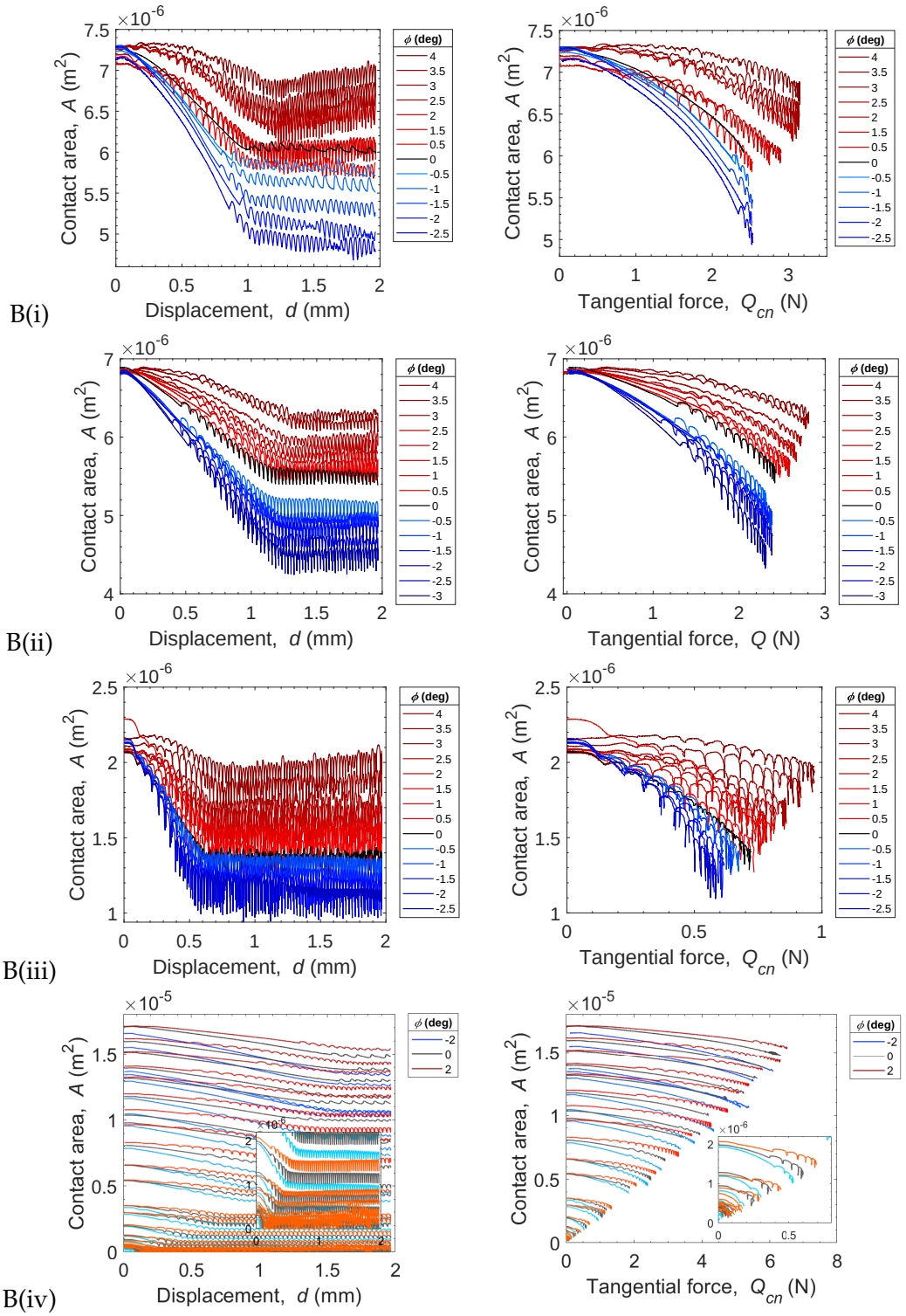

Figure 5.11: Contact area A as a function of the displacement d (on the left side) and of the tangential force Q_{cn} up to its peak (on the right side). B(i): 0.78 N; B(ii): 0.78 N; B(iii): 0.1 N; B(iv): wide range of initial normal force for 3 different tilt angles (-2°: blue lines, 0°: black lines, and 2°: red lines). The color gradients for Cases B(iv) are in function of the initial normal force P_0; light colors for small P_0 and dark colors for large P_0. The insets on B(iv) show a zoom in the small P_0.

Contact area reduction rate

First, to evaluate the area reduction rate, the quadratic-law equation $A = A_0 - \alpha_A Q_{cn}^2$ [17], where A_0 is the initial contact area at $Q_{cn} = 0$ and α_A is the area reduction rate, was used to fit all sets of experiments of Cases B. Figure 5.12 shows (a) α_A as a function of A_0 and (b) as a function of ϕ. The inset in (a) shows the coefficients of determination (R-square) of the quadratic-law fits as a function of A_0. Then, $\alpha_A(A_0)$ were fitted according to the scaling law, $\alpha_A = \beta(A_0)^\gamma$ [17]. The results are shown in Figure 5.12 and Table 5.2.

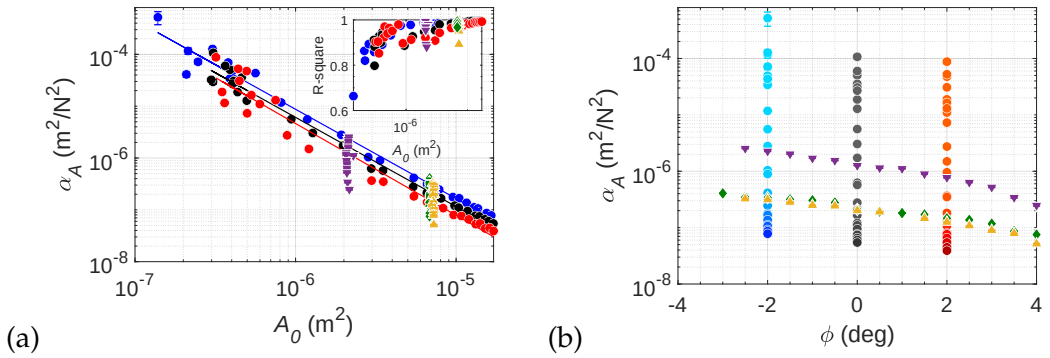

Figure 5.12: Evaluation of the contact area decay rate. (a) Area reduction decay rate α_A as a function of the initial contact area A_0 and (b) as a function of the tilt angle ϕ. ▲ B(i): 0.78 N; ♦ B(ii): 0.78 N; ▼ B(iii): 0.10 N; and a wide range of initial normal loadings for ● B(iv): ϕ = -2°, ● B(iv): ϕ = 0°, and ● B(iv): ϕ = 2°. The lines in (a) represent the power-law fits with the same colors as their fitted points. The color gradients for Cases B(iv) in (b) are in function of the initial normal force P_0; light colors for small P_0 and dark colors for large P_0.

Table 5.2: Power-law fitting results of $\alpha(A_0)$ for Cases B(iv).

Case	ϕ	γ	β^*
B(iv) (●,—)	-2°	-1.72 ± 0.09	3.98 ± 5.99
B(iv) (●,—)	0°	-1.72 ± 0.08	2.84 ± 3.97
B(iv) (●,—)	2°	-1.77 ± 0.15	1.09 ± 3.81

Values in the order of magnitude of 10^{-16}.

We can see in Figure 5.12(a) that, for Cases B(iv) (● B(iv): ϕ = -2°, ● B(iv): ϕ = 0°, and ● B(iv): ϕ = 2°), which have a wide range of initial normal loads, the results are consistent with those of Chapter 4: (i) the experimental points are in good agreement with a power-law evolution, and similar values of the exponent γ are found, see Table 5.2; (ii) there is a larger dispersion of points at small loads (small A_0) because the

quadratic-law does not seem to fit as well the experimental data (lower R-square) for such small normal loads (as discussed in Chapter 4).

Now, concerning the effect of the tilt, in Figure 5.12(a) the level of the points (*i.e.* the value of the prefactor β) seems to differ for each of the three set of experiments, leading to higher values of α_A for $\phi < 0°$ and lower for $\phi > 0°$ compared to the aligned case ($\phi = 0°$). Note that the variation of the β prefactor for the three B(iv) sets is of the same order of magnitude as that observed in [17], which could mean that the quality of the alignment (not measured in [17]) is a possible origin of the experimental uncertainties highlighted in that study. Figure 5.12(b) tends to confirm the dependence of α_A with the tilt. Indeed, the contact area decay rate gradually increases when the tilt angle decreases from 4° to -4° for all initial normal loads that have been tested. This effect can be easily seen for the three set of experiment performed at a single constant normal load (▲ B(i): 0.78 N, ♦ B(ii): 0.78 N, and ▼ B(iii): 0.10 N) and harder to see for the B(iv) sets, as both the angle and the normal force act on the values of α_A.

Since the quadratic law does not adequately describe the contact area reduction for small normal loads, we also looked into using the power-law relation $A = A_0 - \alpha_B Q_{cn}^n$, which was first proposed by Papangelo et al. [53] and allows accounting for different exponents. Figure 5.13 shows the evolution of the exponent n, for fits performed on all sets of experiments in case B, as a function of (a) the initial contact area A_0 and (b) the tilt angle ϕ. In agreement with the findings of Chapter 4 and of Papangelo et al. [53], in the range of large normal load (P larger than about 0.1 N, being here A_0 larger than about 10^{-6} m^2) n is close to 2, and increases for smaller and smaller normal loads (Figure 5.13(a)). But, when plotted as a function of ϕ, it seems than n is nearly constant for $\phi < 0°$ and increases for $\phi > 0°$ (Figure 5.13(b)).

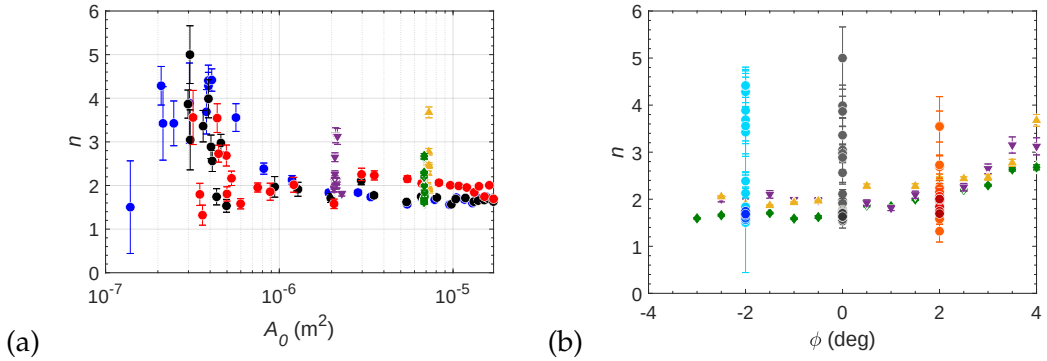

Figure 5.13: Evolution of the exponent n for fit performed on all sets of experiments in case B using the the power-law relation $A = A_0 - \alpha_B Q_{cn}^n$ as a function of (a) the initial contact area A_0 and (b) the tilt angle ϕ. ▲ B(i): 0.78 N; ♦ B(ii): 0.78 N; ▼ B(iii): 0.10 N; and a wide range of initial normal loadings for ● B(iv): ϕ = -2°, ● B(iv): ϕ = 0°, and ● B(iv): ϕ = 2°. The color gradients for Cases B(iv) in (b) are in function of the initial normal force P_0; light colors for small P_0 and dark colors for large P_0.

Interface shear strength

Second, to investigate the potential role of the tilt on the interface shear strength σ, we plotted in Figure 5.14, for all sets of experiments of Case B, the endpoints of the curves from Figure 5.11 (right side), *i.e.* the contact area at the moment of the tangential force peak A_s versus the contact tangential force peak Q_{cns}. The lines correspond to linear fits forced through the origin using the linear law, $A_s = aQ_s$ [17], in which the linear coefficients a is the inverse of the interface shear strength σ ($\sigma = 1/a$). The fit results, in terms of σ, are shown in Table 5.3.

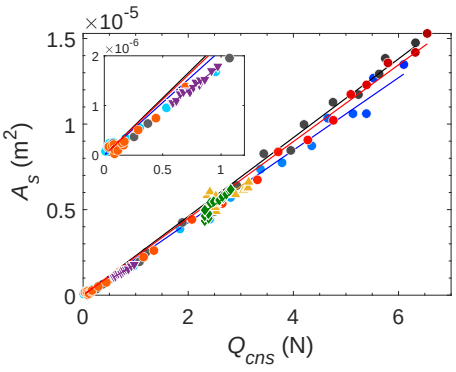

Figure 5.14: Contact area A_s, at the moment of the the peak of the contact tangential force Q_{cns}, as a function of Q_{cns}. The inset shows a zoom in the small contact normal forces. Cases: ▲ B(i): 0.78 N; ♦ B(ii): 0.78 N; ▼ B(iii): 0.10 N; and a wide range of initial normal loadings for ● B(iv): ϕ = -2°, ● B(iv): ϕ = 0°, and ● B(iv): ϕ = 2°. The color gradients for Cases B(iv) are in function of the initial normal force P_0; light colors for small P_0 and dark colors for large P_0. The lines correspond to linear fits with the same colors as their fitted points.

Table 5.3: Interface shear strength σ in MPa.

Case	P_0	σ
B(i) (▲,—)	0.78 N	0.47 ± 0.01
B(ii) (♦,—)	0.78 N	0.47 ± 0.01
B(iii) (▼,—)	0.10 N	0.55 ± 0.01
B(iv) -2° (●,—)	-0.6 mN to 3.20 N	0.47 ± 0.01
B(iv) 0° (●,—)	-0.2 mN to 3.21 N	0.43 ± 0.01
B(iv) 2° (●,—)	-2.3 mN to 3.19 N	0.44 ± 0.01

As in Chapter 4, in Figure 5.14 we observe that the fits are dominated by points at larger loads which causes σ determination to be of poor quality at low initial P_0 (see inset in Figure 5.14) and makes the analysis of the results all the more delicate. Also, we can see in Table 5.3 that the interface shear strength σ for large loads is smaller than for small ones. Overall, no major tilt effect on σ can be clearly seen.

Then, to take this analysis a step further, we measured an instantaneous interface shear strength, *i.e.* the ratio Q_{cns}/As for each curve, rather than a "global" σ resulting from a linear fit over all normal loads. Figure 5.15 shows σ_{inst} evolution as a function of (a) the tilt angle ϕ and (b) Q_{cns}.

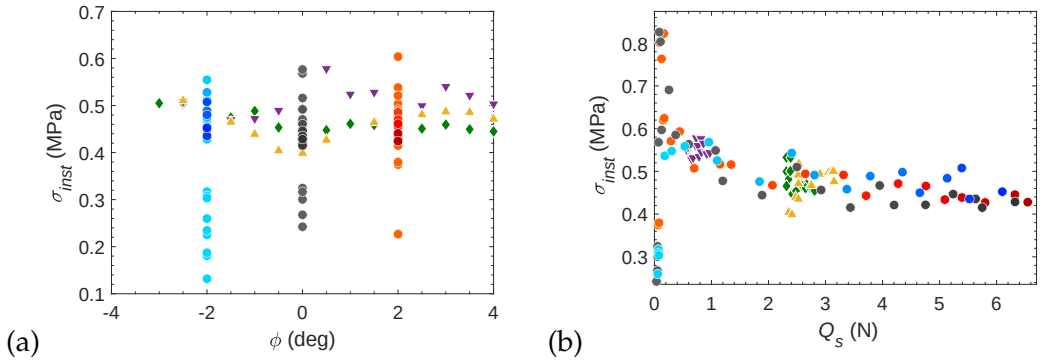

Figure 5.15: Instantaneous interface shear strength ($\sigma_{inst} = Q_{cns}/A_s$) as a function of (a) the tilt angle ϕ and (b) Q_{cns}. Cases: ▲ B(i): 0.78 N; ♦ B(ii): 0.78 N; ▼ B(iii): 0.10 N; and a wide range of initial normal loadings for ● B(iv): ϕ = -2°, ● B(iv): ϕ = 0°, and ● B(iv): ϕ = 2°. The color gradients for Cases B(iv) are in function of the initial normal force P_0; light colors for small P_0 and dark colors for large P_0.

In Figure 5.15(a), we can point out a slight increase in σ_{inst} in the presence of a tilt ϕ (negative and positive), however the dispersion of those values are of the same order of magnitude as the standard error that is made on this type of experiment. In Figure 5.15(b), the tendency for σ_{inst} to increase at low normal loads (consequently low Q_s) seems to be confirmed, but no clear dependency with the tilt seems to emerge.

At this point of the analysis of Case B experiments, the addition of a tilt seems to play a role in the contact area reduction (both on its amplitude and on its functional form (parameter n). On the other hand, the interfacial shear strength (σ) does not seem to be affected or at least at a level too low to be measured at present.

5.4 Discussion

5.4.1 Effect of a tilt on the friction coefficient evaluation

In this chapter, two tilting cases were presented and studied: Case A, in which the plate (slider), the cantilever, and the tangential force sensor were tilted simultaneously; and Case B, where the sphere was the slider and the tilt was applied to the fixed plate. It is worth mentioning again that these are just two representative cases of many other possible configurations.

In both cases, the results indicate the importance of considering the forces really at play at the contact interface. This consideration is crucial in any study in which the value or evolution of the normal force is a key parameter, such as for example when the coefficient of friction μ is to be determined. Indeed, friction between two solid surfaces is typically represented by μ, which is defined as the ratio of the peak tangential force to its corresponding normal force. Note that here, μ correspond to static friction coefficient. The evolution of μ as a function of the tilt angle is shown in Figure 5.16 for all sets of experiments of (a) Case A and (b) Cases B. In this figure, both the results based on the forces measured by the sensors (filled markers) and the corrected forces actually acting on the contact interface (open markers) are represented.

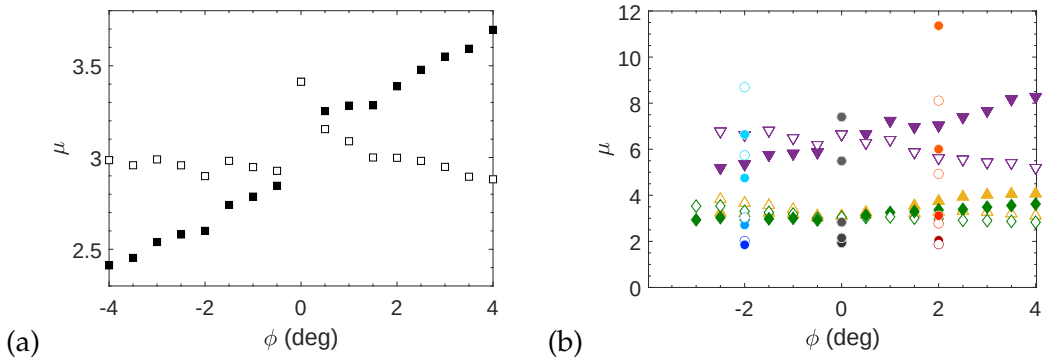

Figure 5.16: Friction coefficient μ as a function of the tilt angle ϕ for (a) Case A and (b) Cases B. Filled markers are for the forces measured by the sensors and open markers for the corrected forces acting on the contact plane. ▲ B(i): 0.78 N; ♦ B(ii): 0.78 N; ▼ B(iii): 0.10 N; and some initial normal loadings for the wide range of ● B(iv): ϕ = -2°, ● B(iv): ϕ = 0°, and ● B(iv): ϕ = 2°. The color gradients for Cases B(iv) in (b) are in function of the initial normal force P_0; light colors for small P_0 and dark colors for large P_0.

In Case A (Figure 5.16(a)), we can see that the coefficients of friction μ calculated from the sensors data (filled markers) increase linearly with the increase of the tilt angle ϕ. However, when considering the forces acting on the contact plane (open markers), μ is found to be nearly constant. Note that the discrepant points (for $\phi = 0°$, 0.5°, and 1°) are attributable to the first experiments of a sets of tests, which has been discussed previously in this chapter and in Section 2.5. In fact, in our sets of experiment, the normal force acting on the interface P_{cn} did not change with ϕ, and this tilt configuration had no effect on the contact normal force at the incipient shearing, *i.e.* the tilting configuration performed here has only modified the value measured by the sensor, but not the test itself when focusing on the interface.

In Cases B (Figure 5.16(b)), a similar situation to Case A is observed. When the sensors forces are considered (filled markers), μ also seems to increase linearly with the increase of the tilt angle ϕ. But considering the forces acting on the contact plane (open markers), μ seems to actually slightly decrease with the increase of ϕ. Such tilt configuration generates a variation of P_{cn} during the incipient sliding but as μ is just evaluated at the moment of the tangential force peak Q_s, and both values of Q_{cns} and its corresponding normal force P_{cns} increase (resp. decrease) for $\phi > 0°$ (resp. $\phi < 0°$), μ is not strongly affected.

All the above observations imply that a simple and direct friction coefficient μ calculation based on raw sensor measurements can be significantly affected in presence of a minor misalignment between the contact interface and the sliding direction, which

may lead to incorrect conclusions or additional experimental uncertainty. Indeed, in our experiments, the apparent evolution of μ from raw sensor data analysis is only reflecting the effect of an "error" in the conception of our experimental set-up. Here, the "error", *i.e.* the misalignment, was deliberate and mastered. However, this highlights the difficulty to correctly design an experimental set-up to evaluate the friction of elastomers. Indeed, due to their high friction coefficient, any slight misalignment can result in non-negligible variations in the normal force measurement due to the induced coupling with the tangential forces at the interface. Unfortunately, evaluating such misalignment is often quite difficult and rarely performed, which makes the comparison between experimental results from the literature sometimes hazardous. We emphasize the importance of analyzing the forces really acting on the interface. But, in order to do so, information on the misalignment as well as the normal force measurement are required, which is not always the case in experiments where normal loading is based on the use of dead weight.

Finally, in Case B, we have performed sets of experiments in which, contrary to classical ones, the normal load constantly evolved during the incipient shearing. This raise some questions up to now unanswered, including: *how to define a friction coefficient in such a loading condition, i.e. when the normal force is not constant? Is the definition of μ as the ratio Q/P at the peak of tangential force still valid? Does μ depend on the loading trajectory?*

5.4.2 Contribution of normal force variation in the contact area evolution

In order to better understand the effect caused by the tilting during Cases B experiments, we will analyze in more detail the respective contributions of the variation of the contact normal force P_{cn} and the contact tangential force Q_{cn}. Indeed, increasing/decreasing the normal load tends to increase/decrease the contact area, whereas shearing the contact tends to reduce it, so variations of both forces will contribute to the evolution of the contact area and to the resulting friction force. As a consequence, we think that one fraction of the final area reduction is due to the evolution of Q_{cn} and one fraction is due to the variation of P_{cn}.

In the following, we propose to modify the usual law of contact area reduction under shearing ($A = A_0 - \alpha_A Q_{cn}^2$ [17]) to account for the contribution of the contact normal loading variation. Successively, we will test two different scenarii by assuming respectively an **additive** and a **multiplicative** contribution. For the additive contribution, we will test two different equations based on the theory of Hertz and JKR, respectively.

Additive contribution based on Hertz's theory

First, according to Hertz's contact theory, we propose to account for an additive contribution of the contact normal force variation to the evolution of the contact area under shearing, in the following form:

$$A = A_0 - \alpha_{add} Q_{cn}^2 + A_0 \cdot \left[\left(\frac{P_{cn}}{P_{cn0}} \right)^{2/3} - 1 \right] \tag{5.21}$$

where A is the contact area, A_0 the initial contact area, α_{add} the fitting coefficient, Q_{cn} the contact tangential force, P_{cn} the contact normal force, and P_{cn0} the initial contact normal force. This equation allows us to define A_Q, which correspond to contribution of the the contact area corrected by the expected effect of the contact normal load P_{cn}, as:

$$A_Q = A - A_0 \cdot \left[\left(\frac{P_{cn}}{P_{cn0}} \right)^{2/3} - 1 \right] \tag{5.22}$$

Then, Figure 5.17 shows A_Q as a function of Q_{cn}. We can see that all curves seem to follow a single master curve. Indeed, the shearing contribution to contact area reduction seems to be similar for experiments under the same initial normal loading and the dispersion of the curves $A(Q_{cn})$ in Figure 5.11 was mainly due to the normal loading variations. However, a certain variation in the shape of the $A_Q(Q_{cn})$ curves between the negative (in blue) and positive (in red) angles can still be pointed out.

Note that caution must be taken when interpreting these $A_Q(Q_{cn})$ curves, because they connect two quantities with different physical representativity, *i.e.* one fraction only of the contact area (A_Q) *vs* the full contact tangential force Q_{cn}.

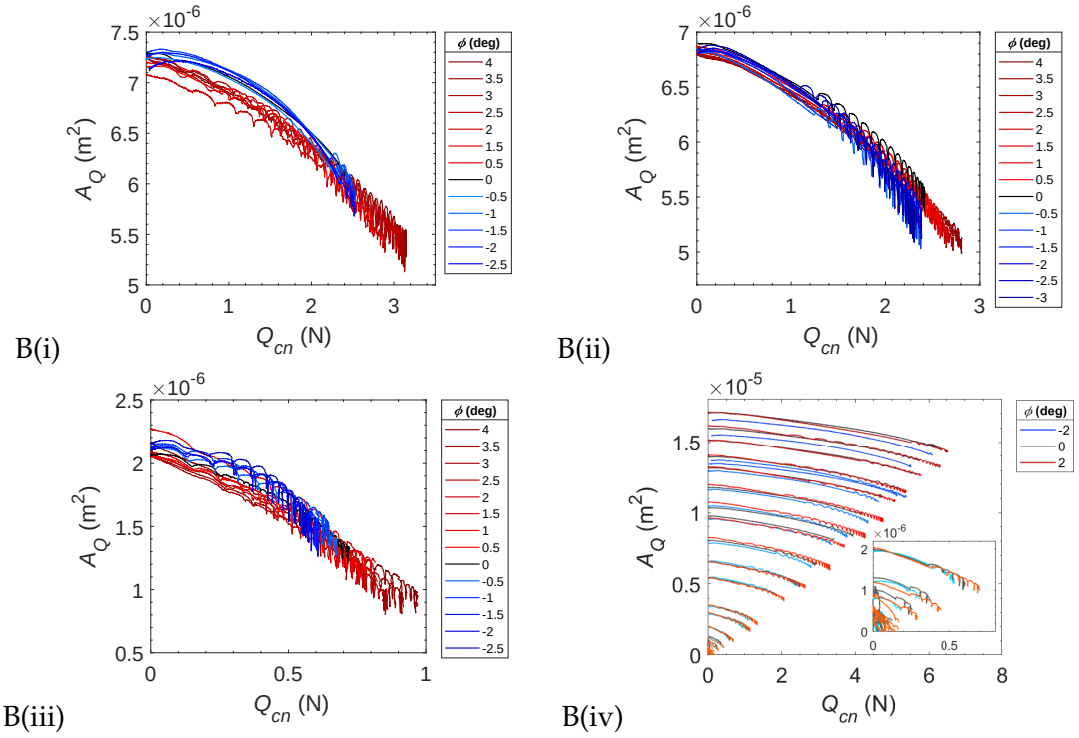

Figure 5.17: Fraction of the contact area A_Q attributed to the contribution of the contact tangential force Q_{cn} as a function of Q_{cn}. B(i): 0.78 N; B(ii): 0.78 N; B(iii): 0.1 N; B(iv): wide range of initial normal force for 3 different tilt angles (-2°: blue lines, 0°: black lines, and 2°: red lines). The color gradients for Cases B(iv) are in function of the initial normal force P_0; light colors for small P_0 and dark colors for large P_0. The inset on B(iv) shows a zoom in the small P_0.

All the curves of Figure 5.17 were used to evaluate the area reduction parameter α_{add} associated uniquely with shearing using quadratic-law: $A_Q = A_0 - \alpha_{add} Q_{cn}^2$. Then, Figure 5.18 shows the evolution of α_{add} as a function of (a) the initial contact area A_0 and of (b) the tilt angle ϕ.

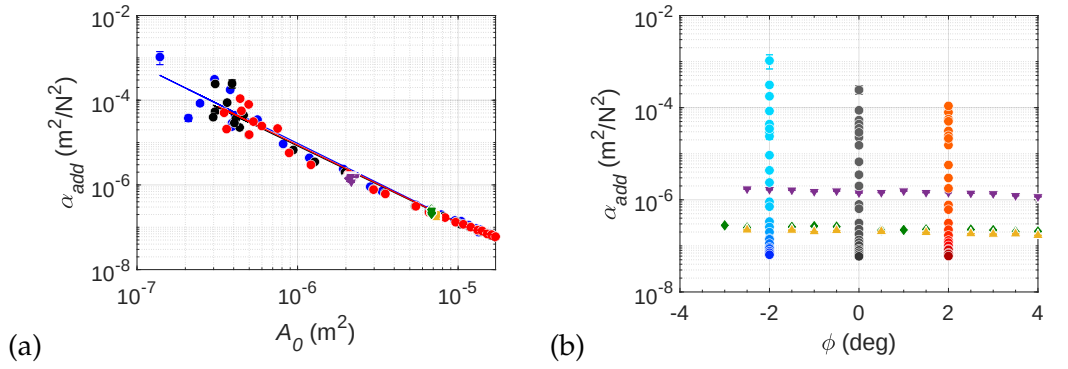

Figure 5.18: Area reduction parameter α_{add} (Hertz) as a function of (a) the initial contact area A_0 and of (b) the tilt angle ϕ. Cases: ▲ B(i): 0.78 N; ♦ B(ii): 0.78 N; ▼ B(iii): 0.10 N; and a wide range of initial normal loadings for ● B(iv): ϕ = -2°, ● B(iv): ϕ = 0°, and ● B(iv): ϕ = 2°. The lines in (a) represent the power-law fits with the same colors of their fitted points. The color gradients for Cases B(iv) in (b) are in function of the initial normal force P_0; light colors for small P_0 and dark colors for large P_0.

Comparing Figure 5.18 to Figure 5.12, we can see that the points are now regrouped into a single master curve, *i.e.* the dependence on the tilt has practically disappeared. The points can be very well fitted by the scaling law, $\alpha_{add} = \beta(A_0)^{\gamma}$ [17]. The result can be seen in the three lines of Figure 5.18 which are almost perfectly superimposed. Similar values of γ and β were also found for all three B(iv) experiments and thus, for all tilt angles (see Table. 5.4). This implies that the observed effect in Figure 5.12 was, in fact, a contribution to the variation of the contact normal force variation caused by the tilting and that using an additive contribution based on Hertz's theory is enough to account for the role of the normal load variation on the area reduction.

Table 5.4: Power-law fitting results of $\alpha_{add}(A_0)$ (Hertz).

Case	ϕ	γ	β^*
B(iv) (●,—)	-2°	-1.87 ± 0.15	0.57 ± 2.19
B(iv) (●,—)	0°	-1.83 ± 0.14	0.93 ± 2.83
B(iv) (●,—)	2°	-1.84 ± 0.14	0.79 ± 2.27

Values in the order of magnitude of 10^{-16}.

An area decreasing as Q_{cn}^{n} [53] was also considered, since the area reduction for small forces seem not to be well captured by a Q_{cn}^{2} evolution [55]. The exponent n is, then, plotted in Figure 5.19 as a function of (a) A_0 and (b) ϕ. Again, when compared to Figure 5.13, it seems that the dependency of n toward the tilt has nearly vanished, just remaining a slight decrease towards the positive angles.

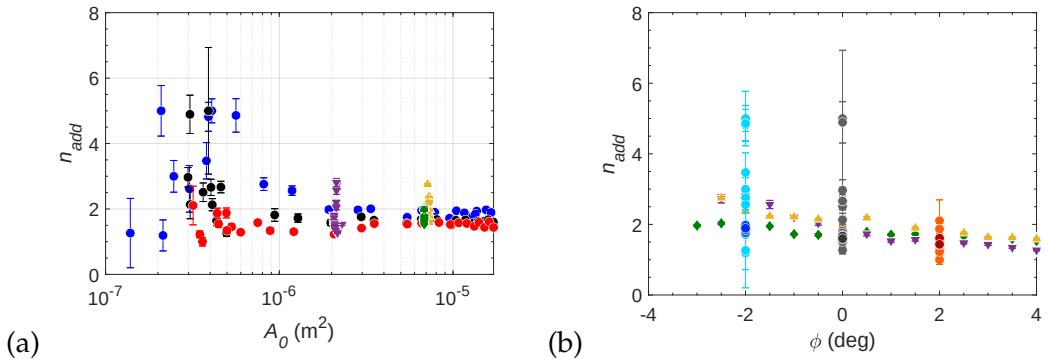

Figure 5.19: Exponent n as a function of (a) the initial contact area A_0 and of (b) the tilt angle ϕ. Cases: ▲ B(i): 0.78 N; ♦ B(ii): 0.78 N; ▼ B(iii): 0.10 N; and a wide range of initial normal loadings for ● B(iv): ϕ = -2°, ● B(iv): ϕ = 0°, and ● B(iv): ϕ = 2°. The color gradients for Cases B(iv) in (b) are in function of the initial normal force P_0; light colors for small P_0 and dark colors for large P_0.

Additive contribution based on JKR theory

Second, we proposed to account for an additive contribution of the contact normal force variation to the evolution of the contact area under shearing, according to JKR contact theory, in the following form:

$$A = A_0 - \alpha_{add} Q_{cn}^2 + A_0 \cdot \left[\left(\frac{P_{cn} + 6\omega_0 \pi R + \sqrt{12\omega_0 \pi R P_{cn} + (6\omega_0 \pi R)^2}}{P_{cn0} + 6\omega_0 \pi R + \sqrt{12\omega_0 \pi R P_{cn0} + (6\omega_0 \pi R)^2}} \right)^{2/3} - 1 \right] \tag{5.23}$$

where ω_0 is the adhesion energy of the interface and R is the sphere radius of curvature. The adhesion energy ω_0 of the PDMS/glass interfaces under $\phi = 0°$ was obtained, for each PDMS sample, from the initial contact area (at $Q = 0$) by JKR theory [27] using the method described in Section 2.4.3.

Then, as before, we define A_Q as the contact area corrected by the expected effect of the contact normal load, P_{cn},

$$A_Q = A - A_0 \cdot \left[\left(\frac{P_{cn} + 6\omega_0 \pi R + \sqrt{12\omega_0 \pi R P_{cn} + (6\omega_0 \pi R)^2}}{P_{cn0} + 6\omega_0 \pi R + \sqrt{12\omega_0 \pi R P_{cn0} + (6\omega_0 \pi R)^2}} \right)^{2/3} - 1 \right] \tag{5.24}$$

The evolutions of α_{add} (JKR) (see Figure 5.20) and n (see Figure 5.21) with (a) A_0 and (b) ϕ were obtained using the same approach as in the previous analysis.

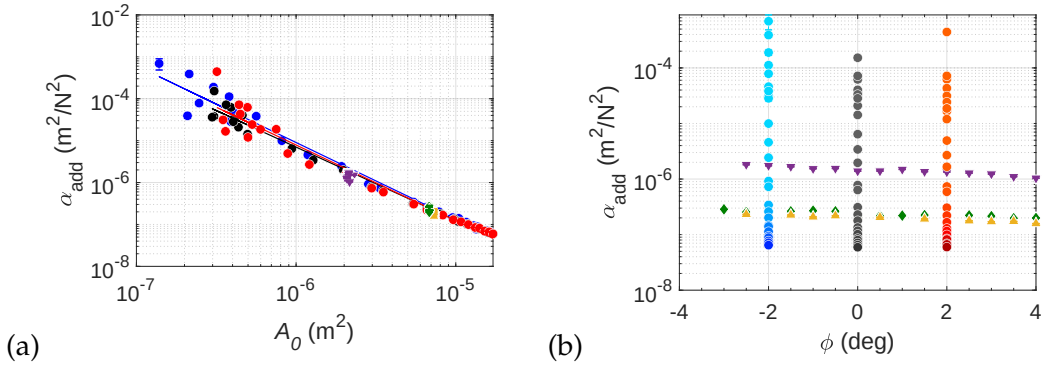

Figure 5.20: Area reduction parameter α_{add} (JKR) as a function of (a) the initial contact area A_0 and of (b) the tilt angle ϕ. Cases: ▲ B(i): 0.78 N; ♦ B(ii): 0.78 N; ▼ B(iii): 0.10 N; and a wide range of initial normal loadings for ● B(iv): ϕ = -2°, ● B(iv): ϕ = 0°, and ● B(iv): ϕ = 2°. The lines in (a) represent the power-law fits with the same colors of their fitted points. The color gradients for Cases B(iv) in (b) are in function of the initial normal force P_0; light colors for small P_0 and dark colors for large P_0.

Once again, the tilt effect has nearly disappeared, the points are also in agreement with the scaling law, $\alpha_{add} = \beta(A_0)^{\gamma}$ [17], see lines in Figure 5.20 and Table 5.5. However, the quality results are not substantially different from the Hertz-based additive contribution to justify the increase in complexity added by the use of JKR theory instead of Hertz's theory.

Table 5.5: Power-law fitting results of $\alpha_{add}(A_0)$ (JKR).

Case	ϕ	γ	β^*
B(iv) (●,—)	-2°	-1.83 ± 0.12	0.91 ± 2.29
B(iv) (●,—)	0°	-1.75 ± 0.09	2.36 ± 3.66
B(iv) (●,—)	2°	-1.81 ± 0.17	1.15 ± 5.14

Values in the order of magnitude of 10^{-16}.

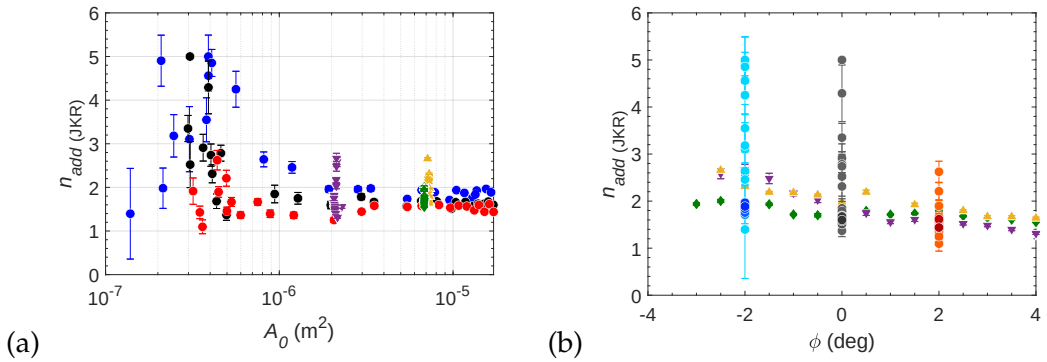

Figure 5.21: Exponent n as a function of (a) the initial contact area A_0 and (b) as a function of the tilt angle ϕ. Cases: ▲ B(i): 0.78 N; ♦ B(ii): 0.78 N; ▼ B(iii): 0.10 N; and a wide range of initial normal loadings for ● B(iv): ϕ = -2°, ● B(iv): ϕ = 0°, and ● B(iv): ϕ = 2°. The color gradients for Cases B(iv) in (b) are in function of the initial normal force P_0; light colors for small P_0 and dark colors for large P_0.

Multiplicative contribution based on Hertz's theory

Finally, again based on the Hertz's contact theory, we propose to account for a multiplicative contribution of the contact normal force to the evolution of the contact area under shearing, in the following form:

$$A = (A_0 - \alpha_{multi} Q_{cn}^2) \cdot \left(\frac{P_{cn}}{P_{cn0}} \right)^{2/3} \tag{5.25}$$

Once again, we performed the same analyses as in previous sections to obtain the evolution of α_{multi} (see Figure 5.22) and n (see Figure 5.23) as a function of (a) A_0 and (b) ϕ. The regrouping of the points into a single master curve for α_{multi}, the agreement with the scaling law (see lines in Figure 5.22 and values of the exponents in Table 5.6) and

the nearly vanishing of the influence of ϕ occur. However, the quality is not as good as for the additive contributions as can be seen by the more important dispersion of the data point especially at low A_0.

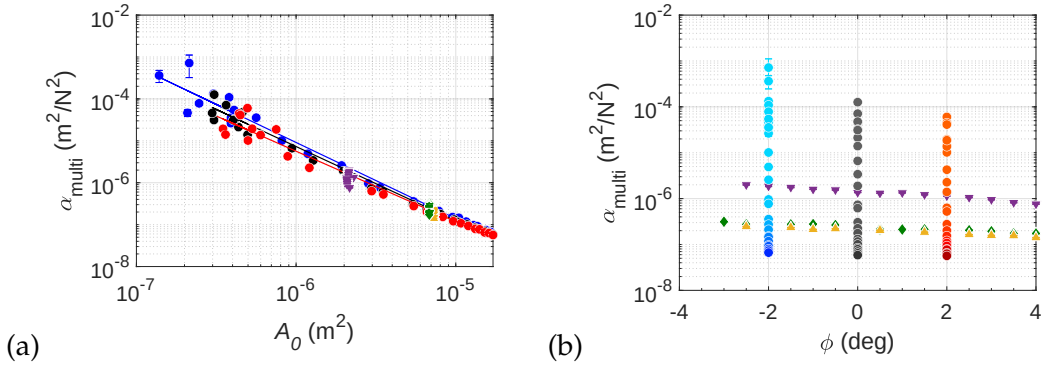

Figure 5.22: Area reduction parameter α_{multi} as a function of (a) the initial contact area A_0 and of (b) the tilt angle ϕ. Cases: ▲ B(i): 0.78 N; ♦ B(ii): 0.78 N; ▼ B(iii): 0.10 N; and a wide range of initial normal loadings for ● B(iv): ϕ = -2°, ● B(iv): ϕ = 0°, and ● B(iv): ϕ = 2°. The lines in (a) represent the power-law fits with the same colors of their fitted points. The color gradients for Cases B(iv) in (b) are in function of the initial normal force P_0; light colors for small P_0 and dark colors for large P_0.

Table 5.6: Power-law fitting results of $\alpha_{multi}(A_0)$.

Case	ϕ	γ	β^*
B(iv) (●,—)	-2°	-1.82 ± 0.12	1.14 ± 2.82
B(iv) (●,—)	0°	-1.77 ± 0.11	1.73 ± 3.40
B(iv) (●,—)	2°	-1.68 ± 0.13	4.67 ± 11.7

Values in the order of magnitude of 10^{-16}.

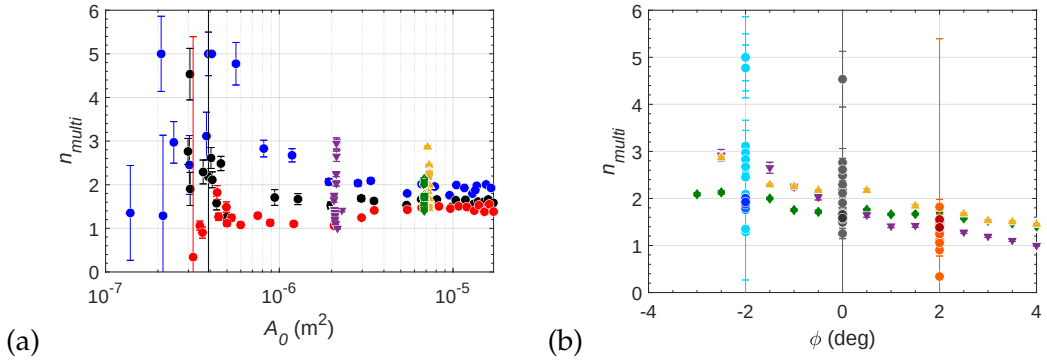

Figure 5.23: Exponent n of Equation 5.25 considering Q_{cn}^n as a function of (a) the initial contact area A_0 and (b) as a function of the tilt angle ϕ. Cases: ▲ B(i): 0.78 N; ♦ B(ii): 0.78 N; ▼ B(iii): 0.10 N; and a wide range of initial normal loadings for ● B(iv): ϕ = -2°, ● B(iv): ϕ = 0°, and ● B(iv): ϕ = 2°. The color gradients for Cases B(iv) are in function of the initial normal force P_0; light colors for small P_0 and dark colors for large P_0.

Summary

Two methods to account for the contribution of the normal force variation to the reduction of the contact area have been proposed: an additive, based on Hertz and JKR's theory, and a multiplicative based on Hertz's theory. By fitting the experimental data, we have observed the same trend in all proposed contributions, a regrouping of the area reduction decay parameter (α) as a function of the initial contact area on a single main curve, the additive method based on Hertz's theory being the best to account for the contribution of the normal force variation. However, even after eliminating the contribution of the normal force variation with the best method, it can be noticed that the shapes of the $A_Q(Q)$ curves are still somewhat different one from the others, refer to Figure 5.17.

The fit coefficient (α_{add}) captures well the rate of the quadratic based reduction of A_Q. However, the shape of such curves is better fitted when using a power-law based approximation Q^n. In fact, the fitting coefficient in the quadratic equation $A = A_0 - \alpha_A Q_{cn}^2$ [17] determines the rate of decreasing of the quadratic function, *i.e.* the steepness of the drop at its end, as shown in Figure 5.24(a). In contrast, the exponent n in the equation $A = A_0 - \alpha_A Q_{cn}^n$ [53] determines the shape of the curve, as shown in Figure 5.24(b). And, as seen in Figure 5.19, the exponent n seems to somehow depend on the tilt angle ϕ, leading us to assume that ϕ may have a slight effect on the contact area evolution.

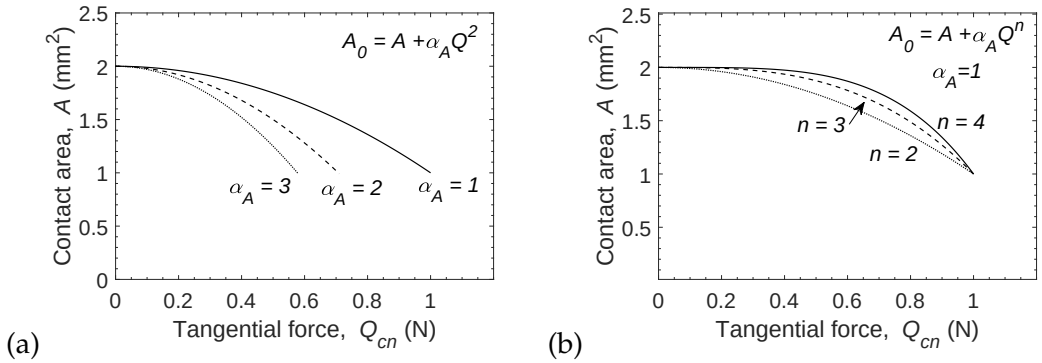

Figure 5.24: Influence on the contact area reduction of (a) the reduction rate α_A from the equation $A = A_0 - \alpha_A Q_{cn}^2$ [17] and (b) the exponent n from the equation $A = A_0 - \alpha_A Q_{cn}^n$ [53].

5.4.3 The effect of the tilt on contact area reduction mechanisms

A qualitative analysis of the images of the evolution of the real contact area for all tests in Case B is proposed here based on the findings of Chapter 3, which identified the main mechanisms responsible for the contact area reduction of large normal loads under shearing, namely interface deformation and lifting/laying at the contact edges. Although such mechanisms were observed with particle-based tests, which is not the case in present experiments, we have just superimposed frames of the initial contact area and at the moment of the contact tangential force peak in the frame of the moving glass plate, as in Chapter 4, to observe the variation of the real contact area at the onset of sliding. Figure 5.25 shows these two frames for different tilt angles, in the columns, $\phi = -2^\circ$ (left), $\phi = 0^\circ$ (centre), and $\phi = 2^\circ$ (right) and for the different experiments, in the rows, B(i), B(ii), B(iii), and two initial normal forces of cases B(iv): 0.10 N and 0.78 N. The black regions correspond to the contact areas always present during the incipient shearing; the blue regions are the areas present at $Q = 0$ and not at Q_s; and the red region are the areas not present at the beginning $Q = 0$, but present at Q_s.

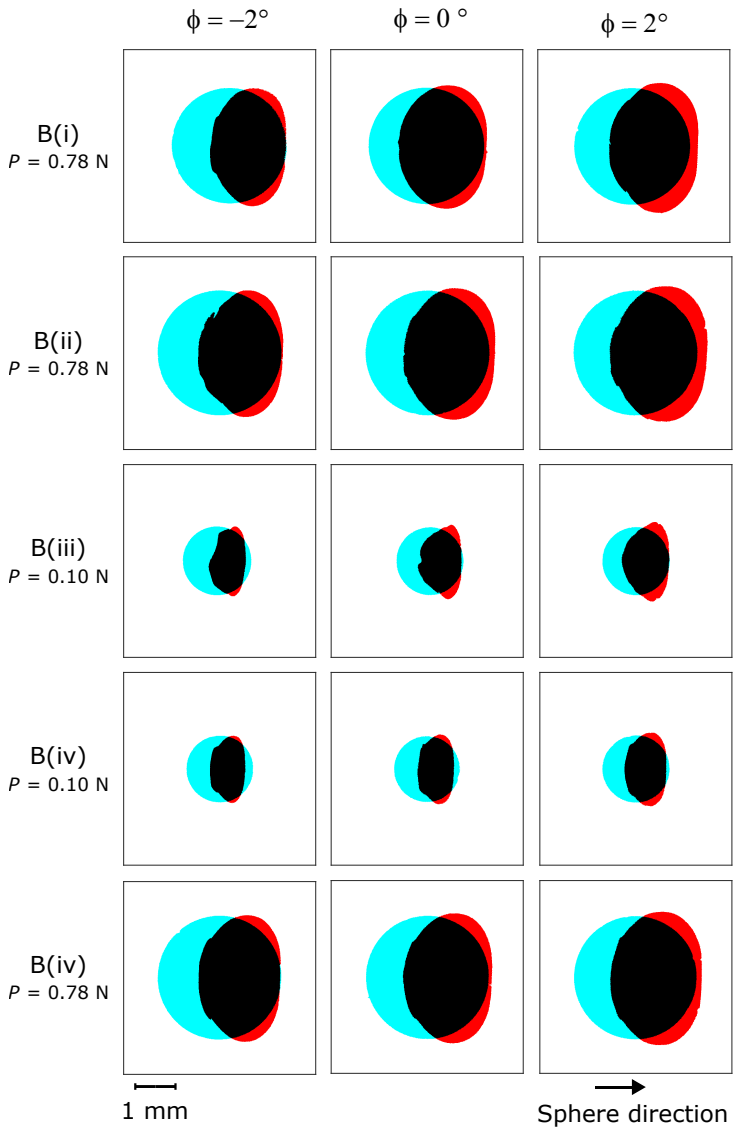

Figure 5.25: Superimposed images of the initial contact area (at $Q_{cn} = 0$) and images at the static friction peak (at Q_{cns}) for (in the columns) $\phi = 0°$, $-2°$, and $2°$ of (in the rows) the cases B(i), B(ii), B(iii), and two initial normal forces of cases B(iv): 0.10 N and 0.78 N. The leading edge of the images is on the right side. The black region is the contact area present during the whole incipient shearing; the blue region is the area present at $Q_{cn} = 0$ and not at Q_{cns}; and the red region is the area not present at $Q_{cn} = 0$ but present at Q_{cns}. The superimposed images are in the frame of the moving glass plate.

By performing a simple visual analysis, we can see that, relative to the aligned case ($\phi = 0°$), for all normal forces (all cases), the red area of the positives angles ($\phi = 2°$) has increased, while for negative angles ($\phi = -2°$) it has slightly decreased or remained the same. Despite the lack of an rigorous analysis such as the particle-based one to identify the exactly mechanisms playing a role here, we can suggest that the tilt, or the variation of the contact normal force, is affecting the contribution of the reduction area mechanisms at least by changing the proportion in between all of them.

5.5 Conclusion

In this chapter we have investigated the influence of the loading trajectory on the behaviour of a sheared model sphere on plane interface. In particular, variations of the normal load during shearing were imposed in a controlled way through the introduction of a small tilt angle at the interface, and its effect was studied for two representative tilting cases.

One of the most significant findings that emerge from this study is that a simple and direct static friction coefficient μ calculation for soft material based on raw sensor measurements can be very affected by the presence of a minor misalignment between the contact interface and the sliding direction, due to an induced coupling with the tangential forces. Such coupling may lead to incorrect conclusions or additional experimental uncertainty. With this study, we raised important questions about the definition of the friction coefficient when the normal force is not constant, a condition that closely represents the reality of bodies in contact, down to the single micro-contact scale.

After carefully correcting the force measurements to extract the real force at play at the interface, the effect of normal loading variation during shearing on the evolution of the contact area and on the resulting shear force was investigated. Our results show that, contrary to the interfacial shear strength which remains nearly unchanged, the area reduction is strongly affected by the load variation. To account for this variation, we proposed an empirical modification of the standard law of contact area reduction under shear ($A = A_0 - \alpha_A Q_{cn}^2$ [17]), which considers an additive effective contribution of the normal load based on Hertz's model. This law appears to be effective for the type of loading trajectories considered in this work. However, its validity must be tested for various other types of trajectories to assess its generality. Finally, with a visual analysis of the contact, we suggested that the tilt angle can affect the relative contributions of the mechanisms of the contact area reduction. These findings have significant implications for the understanding of the contact and friction behaviour of more realistic interfaces, including rough on rough contacts.

Chapter 6

Concluding remarks and future work

In this chapter, firstly, we will summarise and bring together the main areas covered in this work, highlighting the findings, improvements, challenges, and still open questions; and secondly, we will make recommendations for future work.

6.1 Summary of the work

The main objective of this thesis was to obtain a better understanding of the onset of dry sliding contact of elastomers for the simplest sphere/plane model experiment, to shed light on the phenomena potentially involved in more realistic and/or practical situations. To this end, comprehensive studies of a single elastomer contact in the incipient dry sliding process were performed using an optomechanical apparatus in order to achieve the following specific objectives: (i) investigate the elementary mechanisms that play a role during shearing under constant normal loadings, (ii) explore a wide range of normal loading, and (iii) investigate the effect of the normal loading trajectory.

In **Chapter 2 - Experimental methods**, we included a full description of the experimental setup and procedures of the materials and geometries of the samples, and of the data analyses used in this work. In addition, some improvements and difficulties have been reported, among which we can highlight:

- The improvement of the optomechanical setup, which was already used in [17, 53, 55, 63], by:

  - replacing the single cantilever beam by a double one;
  - allowing the direct measurement of the normal load by the addition of four force sensors;
  - adding goniometers to ensure the equipment alignment (which has been proven in Chapter 5 to be critical to the quality of the results obtained).

- The development of a graphical user interface (GUI) for data processing, management, and visualization.

- The repeatability challenge, due to the various properties of different PDMS samples, that resulted in improvements in the PDMS sample preparation process under temperature control for future work.

In **Chapter 3 - Elementary mechanisms of shear-induced contact area reduction**, we have taken a fundamental first step in our goal of understanding friction sliding in elastomers, *i.e.* identifying the mechanisms responsible for contact area reduction in the most simplified representation of contact mechanics, that is, a sphere/plane model interface.

For this, we performed an original experiment by introducing particles in the vicinity of the elastomeric surface and studied their local displacement during shearing at the onset of sliding under several constant normal loadings. Using a homemade particle tracking algorithm and some processing tools, we have been able to show that (i) contact lifting and (ii) contact laying do occur, and their contribution was quantified by a Voronoi tessellation based method. Additionally, using a method based on Delaunay triangulation, we demonstrated that (iii) a heterogeneous in-plane strain field develops progressively at the interface. We also noted that these mechanisms are dependent on normal load. However, under small loads, further research is required to validate this finding due to the low resolution of the presented study.

By tracking the motion of the particles during shearing, we measured their relative displacement compared to their initial position in the contact area and showed the existence of a micro-slip front moving from the contact periphery inward the contact region as shear increases. This allowed us to distinguish three different stages in the evolution of the contact interface:

- a **stuck stage** which is very short in time, meaning that the transition to slipping starts quite early for very low tangential force (*i.e.* well before the peak of the tangential force);
- a **partial slip** during which an annular-like slipping zone progressively replaces the central stuck area, which is in qualitative agreement with the classical Cattaneo-Mindlin [35, 36] approach;
- a classical **steady-state sliding** that seems to start when the tangential force reaches its maximum value, at least for large loads. At small loads, the lack of resolution of the presented method, due to too few tracers, does not allow a precise conclusion on this point.

For the first time in the literature, the findings, under large loads, were successfully qualitatively compared with numerical simulation based on a non-adhesive, non-viscous model of shear-induced contact area reduction in elastomers. Quantitative agreement with the recent experimental results of Sahli et al. [17, 63] on sphere/plane elastomer contacts has been obtained, with no adjustable parameter, using the Tresca friction law and the neo-Hookean hyperelastic model. Those results indicate that shear-induced contact area reduction is essentially a large strain effect.

In **Chapter 4 - Shear-induced area reduction over a wide range of normal loadings**, we carried out the second step of our study, which was to study more realistic frictional sliding. Considering that the contact spots in a real and rough interface are subject to very different local normal loadings, ranging from millinewtons to newtons, we performed three sets of shearing experiments on a model sphere/plane interface for a wide range of constant normal loads. This study was also motivated by (i) the fact that, in the literature, experimental studies on sheared sphere/plane interfaces are concentrated either on small normal loads [46, 49, 55] or on large loads [17], leaving a range of normal loads to be explored, and (ii) by the findings of the previous Chapter 3 on large normal loads that led us to question if the same mechanisms responsible for the contact area variation occur over a wider range of normal loads. Thus, we were able to:

- cover and fill the gap present in the data of the experimental literature;

- present for the first time a unified view of the behavior of a single sphere/plane sheared contact performed with similar conditions from millinewtons to newtons;
- show that a quantitative comparison between experiments obtained from the same equipment/procedure is still challenging unless the procedure to generate the samples is fully mastered. Therefore, comparing theoretical and numerical results with experimental data from different sources is even more challenging and may result in misleading conclusions;
- show that neither of the two area reduction parameters (α and λ) used in literature can be considered as constant over the entire range of normal loads that we tested and that dependence on normal load remains to be taken into account, especially at low normal loads;
- show that interfacial shear strength (σ) is also not constant over the entire range of normal loads that we tested and depends on normal load;
- confirm the already observed effect of a higher contact area reduction rate under small normal loads and its possible link with the increasing effect of adhesion;
- show that, for small normal loads, area reduction continues after the tangential peak force, which calls into question the definition of the exact moment of the transition to sliding and thus the method to evaluate the interfacial shear strength.

Considering all of these, experimentally in elastomers, the transition from the tangential force peak Q_s to the kinetic regime Q_k is much more complex than in Bowden and Tabor [90]. In particular, for large normal loads, it does not seem to be due to an abrupt instability, but rather to a gradual transition, most likely in connection with a micro-slip front that moves from the contact periphery inward the stuck contact region with the increase of tangential force, as discussed in Chapter 3. At low normal loads, the transition is even more complex and clearly needs further investigation to bring a definitive conclusion.

Even though we have not been able to show the existence of the contact area reduction elementary mechanisms highlighted in Chapter 3 for all normal loads, we raised the question about the load-dependence of their relative contribution in the contact area reduction process.

In **Chapter 5 - Sliding friction under normal loading variation**, we took the last step in this study. Indeed, in addition to the different local normal loading conditions that the contact spots encountered in a rough interface, they may also be submitted to local normal loading variations due to the transient nature of micro-contacts as antagonist asperities pass above each other. In this context, we investigated the influence of the loading trajectory by carrying out shearing experiments under a progressive increase/decrease of normal loading. For it, we studied two cases where the contact plane and the sliding direction were misaligned.

First, the most significant finding of this study was that a simple and direct static friction coefficient μ_s calculation for elastomers based on raw measurements can be significantly affected by the presence of a minor misalignment between the contact interface and the sliding direction. This finding is of main importance in the design of elastomer-specific tribometers.

Second, by studying the effects of normal loading variation during shearing, in particular by analyzing the evolution of contact area variation, area reduction parameter, and interfacial shear strength, we have been able to propose an empirical and practical extension of the usual law of contact area reduction under shear. Whether this extended law is specific to the type of loading trajectory used here or is more general remains to be assessed in future studies.

Third, the question of the potential effect of a tilt angle on the relative weights of the several elementary mechanisms occurring at the onset of sliding also remains open.

Finally, the analyses undertaken in this work make several fundamental contributions that improve our understanding of the progressive transition to sliding of elastomer interfaces and, in particular, the associated contact area reduction [17, 52, 53, 55, 56]. The findings provide significant insights into the mechanisms and their relative contributions to friction. All the presented experimental results for single contacts may now be integrated into probabilistic multi-contact analyses of rough surfaces and go beyond the case, a little too simplistic but whose in-depth study remains essential, of a mono-contact between a smooth sphere and a smooth plane.

6.2 Prospects for future research

Finally, for future work, in addition to the several prospective systems and questions that have been raised and that remain to be studied, two specific topics require special attention: the effect of roughness/patterning and sliding precursors.

6.2.1 Effect of roughness/patterning

Up to now, in this work, we have focused exclusively on the friction behavior of smooth interfaces, *i.e.* a smooth sphere sliding on a smooth glass plate. However, it is obvious that understanding the crucial role of roughness or patterning would be of major interest in deepening our understanding of the onset of dry sliding contact of elastomers.

In Figure 6.1(b), we show the results of shearing experiments performed between a patterned sphere and a smooth glass plate. The pattern was obtained by molding the PDMS directly on a homemade aluminum mold rather than on a smooth glass lens (see Figure 6.1(a)). A sphere with a radius of 9.42 mm was milled on the mold using a micro-milling machine equipped with a spherical mill cutter with a radius of 1 mm. As a consequence of this milling process, the mold surface was patterned with parallel grooves that correspond to the successive passes of the mill cutter. Then, the PDMS sphere was a negative replica of the mold and thus presents a pattern in the form of parallel cylindrical stripes with a height of ~ 0.25 mm as can be observed in Figures 6.1(a) and (c). Figure 6.1(b) shows the evolution of the tangential force Q for different normal loads P and two different sliding directions with respect to the pattern (parallel and perpendicular). Figure 6.1(c) Images of the patterned sphere/plane contact at no tangential force ($Q = 0$) for the parallel and perpendicular directions under normal loads of $P = 0.82$ N and $P = 0.82$ N, respectively.

As expected, the peak of the tangential force Q_s is affected by the normal load P, but it is also affected by the sliding direction. For each P, Q_s is higher when the sphere slides parallel to the pattern. This preliminary result emphasizes the crucial role of roughness and clearly shows that additional investigations are required to understand, for example, the influence of surface morphology on the elementary mechanisms of

contact area reduction and also on the propagation of the annular-like slipping front (see Chapter 3).

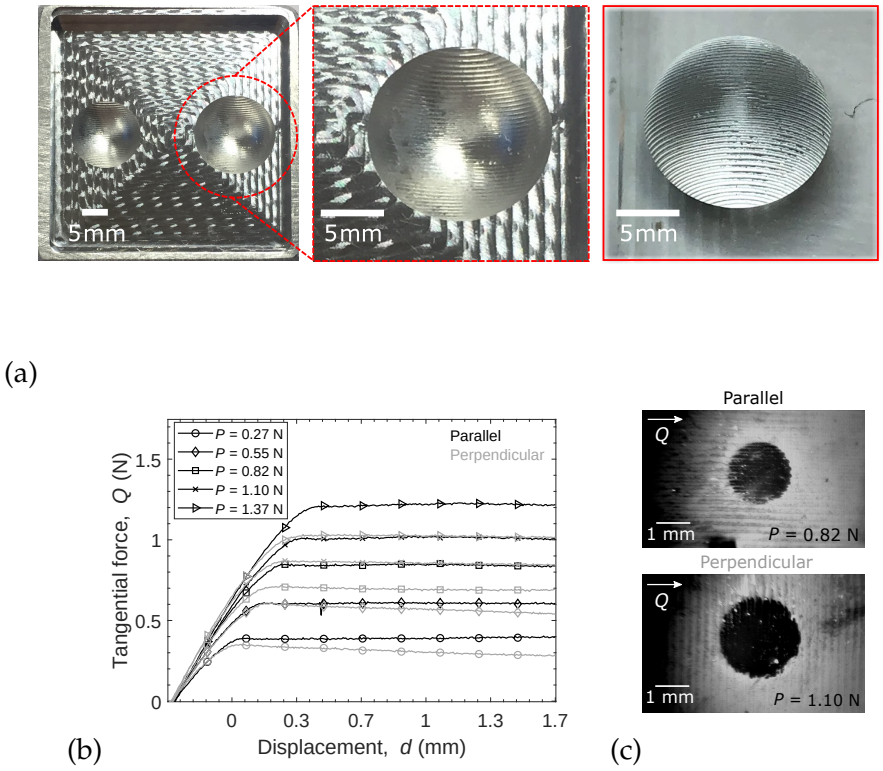

Figure 6.1: The use of (a) a milled aluminum mold allows generating a PMDS sphere of radius of curvature of 9.42 mm patterned with parallel stripes. (b) Tangential force evolution during shearing of a patterned sphere/plane contact for different normal loads P (different markers) and two different sliding directions with respect to the patterned sphere: parallel (black lines) and perpendicular (grey lines). (c) Images of the patterned sphere/plane contact at no tangential force ($Q = 0$).

6.2.2 Sliding precursors

Ultimately, one would like to be able to understand and predict frictional sliding. Indeed, a better understanding of the transition between static and dynamic friction is crucial for many technological, economic, and societal applications, because it is involved, for example, in the problems of gripping objects, in wear of nano-devices, in the physics of earthquakes, or even in more classic contact problems involving elastomers (*e.g.*, road/tire or piston/syringe). Prediction of sliding is a very complicated issue, but based on the work performed in this thesis, we can propose some strategies in that

direction. Indeed, we provide some new elements to now be able to design model surfaces that may allow the emergence and detection of sliding precursors early enough before global sliding occurs.

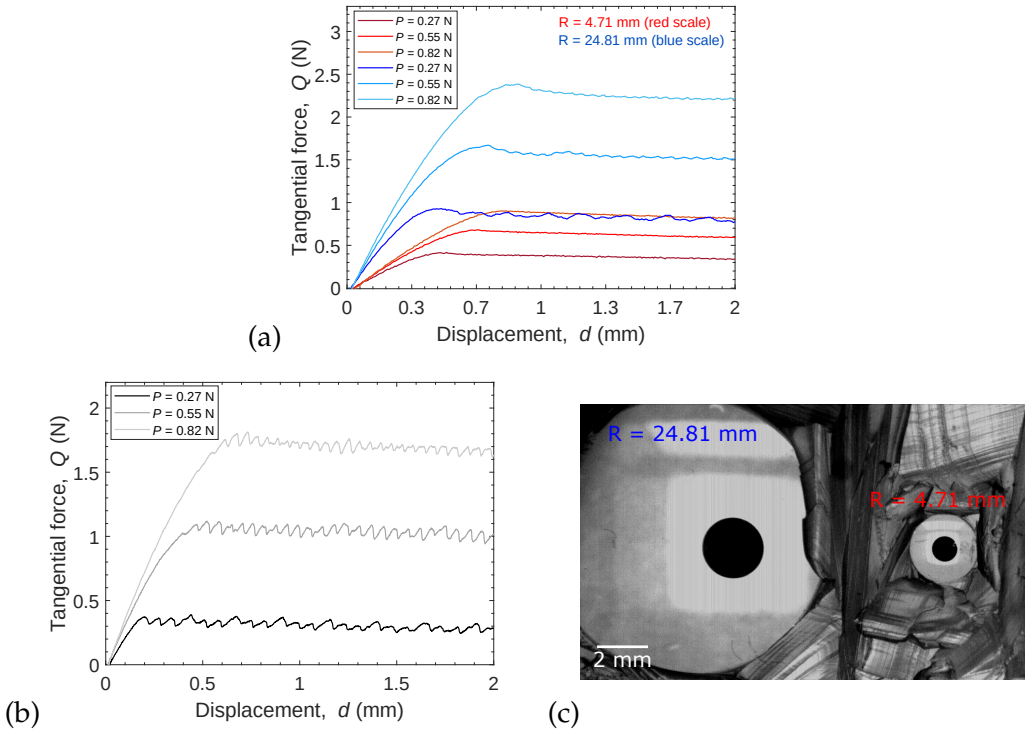

Figure 6.2: Tangential force Q evolution during shearing of a sphere/plane contact under different normal loads P for (a) two different spheres of radius of curvature R=4.71 mm (red lines) and R=24.81 mm (blue lines) and (b) for a patterned interface made of two spheres of respective radius of curvature R=4.71 mm and R=24.81 mm. (c) *In-situ* optical view of the real contact area (black spots).

Even if there is still a lot of progress and work to be done, some preliminary results, performed during this work, demonstrate that patterned surfaces can be used to induce the emergence of macroscopic sliding precursors. For example, when two smooth spheres of different radii are combined, they begin to slide at different sliding thresholds. Indeed, in Fig 6.2(a), which presents the evolution of the tangential force during shearing of two different spheres of radius 4.71 mm and 24.81 mm for three normal loads (0.27 N, 0.55 N and 0.82 N), we can observe as expected that the tangential force peak is both higher and shifted toward higher displacement when the radius of the sphere is higher. Thus, when the same two spheres of different radius are combined in one single interface, we expect the smallest to slide before. Provided that one is able to detect this event in the main friction curve, it could play the role of precursor to the

macroscopic sliding of the interface. In Figure 6.4(b), when the first sphere begins to slide, a small change in the slope of the curve can be observed by the naked eye, quite before the peak force (*e.g.* at about 0.45 mm for 0.82 N and 0.3 mm for 0.55 N). Unfortunately, such a subtle feature is nearly impossible to extract automatically from the curve. The problem becomes even more complex when more spheres are added to the interfaces, as can be seen in Figure 6.3 for the case of three spheres (two small and one large) or five spheres (four small and one large).

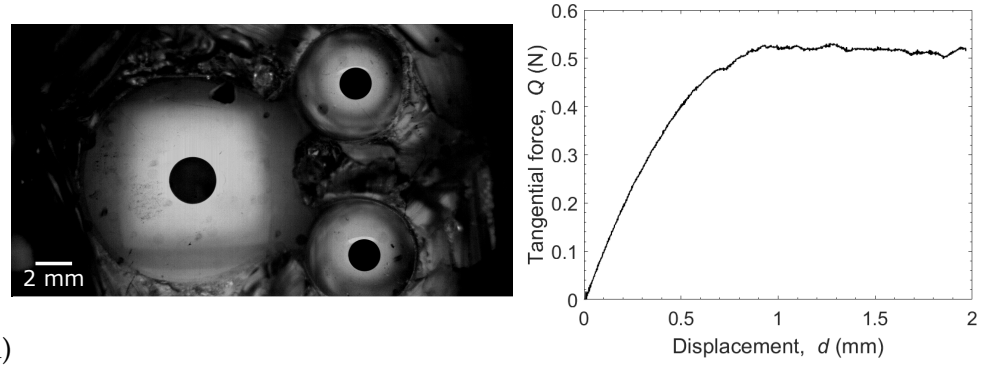

(a)

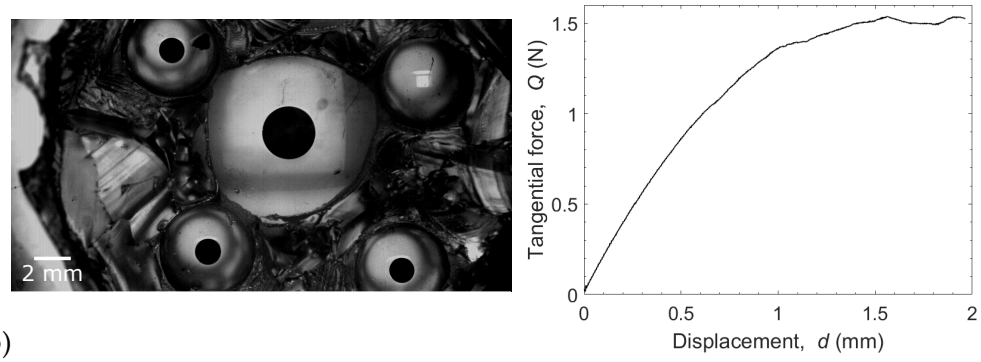

(b)

Figure 6.3: (a) Left side: *in-situ* optical view of the real contact area (black spots) for a three spheres/glass interface under normal load of 0.25 N. Right side: tangential force Q evolution during shearing of the three spheres/glass interface shown on the left side. (b) Left side: *in-situ* optical view of the real contact area (black spots) for a five spheres/glass interface under normal load of 1.05 N. Right side: tangential force Q evolution during shearing of the five spheres/glass interface shown on the left side.

Then, in Figure 6.4, we combined two textured spheres of same radius of curvature R=9.42 mm but with a height difference of 0.2 mm in a single interface. And similar to the case of two smooth spheres, a change in the slope of the evolution of the tangential force Q curve appears (*e.g.*, see red arrow in Figure 6.4(a)). The texture was obtained by molding the PDMS on a milled aluminum mold, using a fine pitch between the different circular milling passes to obtain a smoother surface than in Figure 6.1(a) for instance. In this case, stick-slip-like oscillations (a way in which instabilities during sliding in

soft adhesives manifest) occur as soon as one of the two spheres starts sliding. Those oscillations show up in the tangential force, which could facilitate the detection of the simultaneous slope change (see Figure 6.4(a)). However, a large part of the physics responsible for the appearance of such instabilities (like Schallamach waves [98] and re-attachment folds [78]) is still not fully understood and, as we have seen all along this work, mastering their presence is still a very challenging task. One way would be to extend the work done in Chapter 3 to 3D in order to access not only the mechanical field at the very interface but in the whole bulk of the sphere. This could be done numerically by using the same type of model that the one presented, or experimentally by using an *in-situ* 3D imaging method (such as X-Ray tomography) combined with Digital Volume Correlation (DVC).

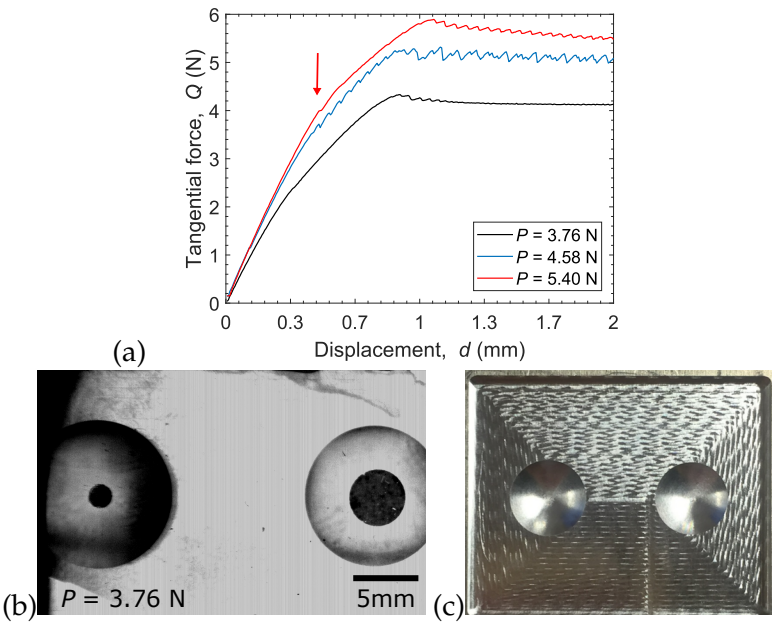

Figure 6.4: (a) Evolution of the tangential force Q during shear of a contact between two textured spheres, for three different normal loads P. (b) View of the real contact area (black spots) between the glass plate and the two spheres, that have a height different of 0.2 mm. (c) Top view of the milled aluminum mold used to create the PDMS sample. The spheres were milled by successive circular passes and a fine pitch.

Appendix A

Appendix A

A.1 Chapter 4 - Supplementary material

(a) (b)

(c) (d)

Figure A.1: Time-evolution of the tracer-seeded contact images in the laboratory frame, snapshots of which are shown in Figure 3.2(a–d). Real speed. The upper right area of dark pixels is the marker drawn on the glass plate slider to follow its displacement. The leading edge is on the left. (a) Video M185, $P = 1.85\,\mathrm{N}$, image size: 7.2 mm x 4.9 mm. (b) Video M054, $P = 0.54\,\mathrm{N}$, image size: 4.7 mm x 3.7 mm. (c) Video M025, $P = 0.25\,\mathrm{N}$, image size: 5.3 mm x 3.5 mm. (d) Video M005, $P = 0.05\,\mathrm{N}$, image size: 4.6 mm x 3.3 mm.

Bibliography

[1] Gang Sheng Chen. *Handbook of friction-vibration interactions*. Elsevier, 2014.

[2] Roberto C. Dante. *Handbook of friction materials and their applications*. Woodhead publishing, 2015.

[3] Jeong Young Park and Miquel Salmeron. "Fundamental Aspects of Energy Dissipation in Friction". *Chemical Reviews* 114.1 (2014), pp. 677–711.

[4] MB Uday et al. "Advances in friction welding process: a review". *Science and technology of Welding and Joining* 15.7 (2010), pp. 534–558.

[5] H Liang et al. "Wear phenomena in chemical mechanical polishing". *Wear* 211.2 (1997), pp. 271–279.

[6] Jacqueline Krim. "Surface science and the atomic-scale origins of friction: what once was old is new again". *Surface science* 500.1-3 (2002), pp. 741–758.

[7] Bo NJ Persson. *Sliding Friction: physical principles and applications*. NanoScience and Technology. Springer Berlin Heidelberg, 2000.

[8] AI Vakis et al. "Modeling and simulation in tribology across scales: An overview". *Tribology International* 125 (2018), pp. 169–199.

[9] Yonggang Meng et al. "A review of recent advances in tribology". *Friction* 8.2 (2020), pp. 221–300.

[10] Ian M Hutchings. "Leonardo da Vinci's studies of friction". *Wear* 360 (2016), pp. 51–66.

[11] Charles Augustin Coulomb. *Théorie des machines simples en ayant égard au frottement de leurs parties et à la roideur des cordages*. Bachelier, 1821.

[12] Frank Philip Bowden and David Tabor. *The friction and lubrication of solids*. Vol. 1. Oxford university press, 2001.

[13] James H Dieterich and Brian D Kilgore. "Direct observation of frictional contacts: New insights for state-dependent properties". *Pure and Applied Geophysics* 143.1-3 (1994), pp. 283–302.

[14] Anish Kurian, Shishir Prasad, and Ali Dhinojwala. "Unusual surface aging of poly (dimethylsiloxane) elastomers". *Macromolecules* 43.5 (2010), pp. 2438–2443.

[15] S Yashima et al. "Normal contact and friction of rubber with model randomly rough surfaces". *Soft Matter* 11.5 (2015), pp. 871–881.

[16] Shmuel M Rubinstein, Gil Cohen, and Jay Fineberg. "Detachment fronts and the onset of dynamic friction". *Nature* 430.7003 (2004), pp. 1005–1009.

[17] R Sahli et al. "Evolution of real contact area under shear and the value of static friction of soft materials". *Proceedings of the National Academy of Sciences* 115.3 (2018), pp. 471–476.

[18] Pauline Berthoud et al. "Physical analysis of the state-and rate-dependent friction law: Static friction". *Physical review B* 59.22 (1999), p. 14313.

[19] Olivier Ronsin and Karine Labastie Coeyrehourcq. "State, rate and temperature–dependent sliding friction of elastomers". *Proceedings of the Royal Society of London. Series A: Mathematical, Physical and Engineering Sciences* 457.2010 (2001), pp. 1277–1294.

[20] JF Archard. "Elastic deformation and the laws of friction". *Proceedings of the Royal Society of London. Series A. Mathematical and Physical Sciences* 243.1233 (1957), pp. 190–205.

[21] Robert W Carpick and Miquel Salmeron. "Scratching the surface: fundamental investigations of tribology with atomic force microscopy". *Chemical reviews* 97.4 (1997), pp. 1163–1194.

[22] Céline Cohen et al. "Incidence of the molecular organization on friction at soft polymer interfaces". *Soft Matter* 7.18 (2011), pp. 8535–8541.

[23] Fanny Wu-Bavouzet et al. "Effect of surface pattern on the adhesive friction of elastomers". *Physical Review E* 82.3 (2010), p. 031806.

[24] JA Greenwood and JBP Williamson. "Contact of nominally flat surfaces". *Proceedings of the royal society of London. Series A. Mathematical and physical sciences* 295.1442 (1966), pp. 300–319.

[25] FP Bowden and D Tabor. "Mechanism of metallic friction". *Nature* 150.3798 (1942), pp. 197–199.

[26] Heinrich Hertz. "Ueber die Berührung fester elastischer Körper." *Journal für die reine und angewandte Mathematik* 1882.92 (1882), pp. 156–171.

[27] KL Johnson, K Kendall, and AD Roberts. "Surface energy and the contact of elastic solids". *Proceedings of the royal society of London. A. mathematical and physical sciences* 324.1558 (1971), pp. 301–313.

[28] Boris V Derjaguin, Vladimir M Muller, and Yu P Toporov. "Effect of contact deformations on the adhesion of particles". *Journal of Colloid and interface science* 53.2 (1975), pp. 314–326.

[29] Bharat Bhushan. "Contact mechanics of rough surfaces in tribology: single asperity contact" (1996).

[30] KL Johnson. *Contact mechanics*. Cambridge, United Kingdom: Cambridge University Press, 1985.

[31] M Brogly. "Forces involved in adhesion". *Handbook of Adhesion Technology, Springer-Verlag, Heidelberg, Germany* (2011), pp. 39–63.

[32] Etienne Barthel. "Adhesive elastic contacts: JKR and more". *Journal of Physics D: Applied Physics* 41.16 (2008), p. 163001.

[33] D Tabor. "Surface forces and surface interactions". *Plenary and invited lectures*. Elsevier, 1977, pp. 3–14.

[34] Daniel Maugis. "Adhesion of spheres: the JKR-DMT transition using a Dugdale model". *Journal of colloid and interface science* 150.1 (1992), pp. 243–269.

[35] C Cattaneo. "Sul contatto di due corpi elastici. Accademia dei Lincei". *Rendiconti* 27 (1938), pp. 342–348.

[36] Raymond David Mindlin. "Compliance of elastic bodies in contact". *J. Appl. Mech., ASME* 16 (1949), pp. 259–268.

[37] James R Barber. "Nominally static frictional contacts under periodic loading". *The Journal of Strain Analysis for Engineering Design* 51.4 (2016), pp. 270–278.

[38] Valentin L Popov. *Contact mechanics and friction*. Springer, 2010.

[39] OM Braun and J Röder. "Transition from stick-slip to smooth sliding: an earthquakelike model". *Physical review letters* 88.9 (2002), p. 096102.

[40] M Ciavarella, V Delfine, and G Demelio. "A "re-vitalized" Greenwood and Williamson model of elastic contact between fractal surfaces". *Journal of the Mechanics and Physics of Solids* 54.12 (2006), pp. 2569–2591.

[41] G Violano and L Afferrante. "Contact of rough surfaces: Modeling adhesion in advanced multiasperity models". *Proceedings of the Institution of Mechanical Engineers, Part J: Journal of Engineering Tribology* 233.10 (2019), pp. 1585–1593.

[42] Alain Le Bot et al. "Relaxation tribometry: a generic method to identify the nature of contact forces". *Tribology Letters* 67.2 (2019), p. 53.

[43] Jørgen Kjoshagen Trømborg et al. "Slow slip and the transition from fast to slow fronts in the rupture of frictional interfaces". 111.24 (2014), pp. 8764–8769.

[44] Oleg M Braun and Michel Peyrard. "Seismic quiescence in a frictional earthquake model". *Geophysical Journal International* 213.1 (2018), pp. 676–683.

[45] Gianluca Costagliola, Federico Bosia, and Nicola M Pugno. "A 2-D model for friction of complex anisotropic surfaces". *Journal of the Mechanics and Physics of Solids* 112 (2018), pp. 50–65.

[46] AR Savkoor and GAD Briggs. "The effect of tangential force on the contact of elastic solids in adhesion". *Proceedings of the Royal Society of London. A. Mathematical and Physical Sciences* 356.1684 (1977), pp. 103–114.

[47] John W Hutchinson et al. "Mixed mode fracture mechanics of interfaces". *Metal-ceramic interfaces* 1990 (1990), pp. 295–306.

[48] KL Johnson. "Continuum mechanics modeling of adhesion and friction". *Langmuir* 12.19 (1996), pp. 4510–4513.

[49] Julie F Waters and Pradeep R Guduru. "Mode-mixity-dependent adhesive contact of a sphere on a plane surface". *Proceedings of the Royal Society A: Mathematical, Physical and Engineering Sciences* 466.2117 (2010), pp. 1303–1325.

[50] Valentin L Popov and Andrey V Dimaki. "Friction in an adhesive tangential contact in the Coulomb-Dugdale approximation". *The Journal of Adhesion* 93.14 (2017), pp. 1131–1145.

[51] Michele Ciavarella. "Fracture mechanics simple calculations to explain small reduction of the real contact area under shear". *Facta universitatis, series: mechanical engineering* 16.1 (2018), pp. 87–91.

[52] Antonio Papangelo and Michele Ciavarella. "On mixed-mode fracture mechanics models for contact area reduction under shear load in soft materials". *Journal of the Mechanics and Physics of Solids* 124 (2019), pp. 159–171.

[53] Antonio Papangelo et al. "Shear-induced contact area anisotropy explained by a fracture mechanics model". *Physical Review E* 99.5 (2019), p. 053005.

[54] John W Hutchinson and Zhigang Suo. "Mixed mode cracking in layered materials". *Advances in applied mechanics* 29 (1991), pp. 63–191.

[55] Janine C Mergel et al. "Continuum contact models for coupled adhesion and friction". *The Journal of Adhesion* 95.12 (2019), pp. 1101–1133.

[56] M Khajeh Salehani, N Irani, and L Nicola. "Modeling adhesive contacts under mixed-mode loading". *Journal of the Mechanics and Physics of Solids* 130 (2019), pp. 320–329.

[57] Janine C Mergel, Julien Scheibert, and Roger A Sauer. "Contact with coupled adhesion and friction: Computational framework, applications, and new insights". *Journal of the Mechanics and Physics of Solids* 146 (2020), p. 104194.

[58] RM McMeeking et al. "The interaction of frictional slip and adhesion for a stiff sphere on a compliant substrate". *Journal of Applied Mechanics* 87.3 (2020), p. 031016.

[59] J Wang et al. "Sphere and cylinder contact mechanics during slip". *Journal of the Mechanics and Physics of Solids* 143 (2020), p. 104094.

[60] Jakub Lengiewicz et al. "Finite deformations govern the anisotropic shear-induced area reduction of soft elastic contacts". *Journal of the Mechanics and Physics of Solids* 143 (2020), p. 104056.

[61] Antoine Chateauminois, Christian Fretigny, and Ludovic Olanier. "Friction and shear fracture of an adhesive contact under torsion". *Physical Review E* 81.2 (2010), p. 026106.

[62] Alexis Prevost, Julien Scheibert, and Georges Debregeas. "Probing the micromechanics of a multi-contact interface at the onset of frictional sliding". *The European Physical Journal E* 36.2 (2013), pp. 1–12.

[63] R Sahli et al. "Shear-induced anisotropy in rough elastomer contact". *Physical review letters* 122.21 (2019), p. 214301.

[64] Riad Sahli. "Mise en glissement des interfaces multicontacts élastomères: étude expérimentale par visualisation in situ". PhD thesis. Université de Lyon, 2017.

[65] J Matsuoka et al. "Temperature dependence of refractive index of SiO2 glass". *Journal of non-crystalline solids* 135.1 (1991), pp. 86–89.

[66] The Dow Chemical Company. *SYLGARD 184 Silicone Elastomer Kit Technical Data Sheet*. URL: `https://www.dow.com/en-us/document-viewer.html?ramdomVar=4882862481917761218&docPath=/content/dam/dcc/documents/en-us/productdatasheet/11/11-31/11-3184-sylgard-184-elastomer.pdf` (visited on 11/09/2020).

[67] James Friend and Leslie Yeo. "Fabrication of microfluidic devices using polydimethylsiloxane". *Biomicrofluidics* 4.2 (2010), p. 026502.

[68] Seok Woo Lee and Seung S Lee. "Shrinkage ratio of PDMS and its alignment method for the wafer level process". *Microsystem technologies* 14.2 (2008), pp. 205–208.

[69] J Cooper McDonald et al. "Fabrication of microfluidic systems in poly (dimethylsiloxane)". *Electrophoresis: An International Journal* 21.1 (2000), pp. 27–40.

[70] Khalid Anwar, Taeheon Han, and Sun Min Kim. "Reversible sealing techniques for microdevice applications". *Sensors and Actuators B: Chemical* 153.2 (2011), pp. 301–311.

[71] Rafael C Gonzales and Richard E Woods. *Digital image processing*. Prentice hall New Jersey, 2002.

[72] N Otsu. "Threshold Selection Method from Gray-level Histograms". *IEEE Transactions on Systems, Man, and Cybernetics* 9.1 (1979), pp. 62–66.

[73] Katherine Vorvolakos and Manoj K Chaudhury. "The effects of molecular weight and temperature on the kinetic friction of silicone rubbers". *Langmuir* 19.17 (2003), pp. 6778–6787.

[74] A Galliano, S Bistac, and J Schultz. "The role of free chains in adhesion and friction of poly (dimethylsiloxane)(PDMS) networks". *The Journal of Adhesion* 79.10 (2003), pp. 973–991.

[75] Tamara Elzein, Anthony Galliano, and Sophie Bistac. "Chains anisotropy in PDMS networks due to friction on gold surfaces". *Journal of Polymer Science Part B: Polymer Physics* 42.12 (2004), pp. 2348–2353.

[76] E Kroner, R Maboudian, and E Arzt. "Effect of repeated contact on adhesion measurements involving polydimethylsiloxane structural material". *IOP Conference Series: Materials Science and Engineering*. Vol. 5. 1. 2009, p. 012004.

[77] B Weber et al. "Frictional weakening of slip interfaces". *Science advances* 5.4 (2019), eaav7603.

[78] M Barquins and R Courtel. "Rubber friction and the rheology of viscoelastic contact". *Wear* 32.2 (1975), pp. 133–150.

[79] M Barquins. "Sliding friction of rubber and Schallamach waves—a review". *Materials Science and Engineering* 73 (1985), pp. 45–63.

[80] Atsuyuki Okabe, Barry Boots, and Kokichi Sugihara. *Spatial Tessellations: Concepts and Applications of Voronoi Diagrams*. John Wiley & Sons, Inc., 1992.

[81] Franz Aurenhammer, Rolf Klein, and Der-Tsai Lee. *Voronoi diagrams and Delaunay triangulations*. World Scientific Publishing Company, 2013.

[82] James R Barber. *Contact mechanics*. Vol. 250. Springer, 2018.

[83] Gilles Marckmann and Erwan Verron. "Comparison of hyperelastic models for rubber-like materials". *Rubber chemistry and technology* 79.5 (2006), pp. 835–858.

[84] Danh Toan Nguyen et al. "Surface pressure and shear stress fields within a frictional contact on rubber". *The Journal of Adhesion* 87.3 (2011), pp. 235–250.

[85] Siavash Maraghechi et al. "Experimental full-field analysis of size effects in miniaturized cellular elastomeric metamaterials". *Materials & Design* 193 (2020), p. 108684.

[86] Debashish Das and Ioannis Chasiotis. "Sliding of adhesive nanoscale polymer contacts". *Journal of the Mechanics and Physics of Solids* 140 (2020), p. 103931.

[87] K.L. Johnson. "Adhesion and friction between a smooth elastic spherical asperity and a plane surface". *Proceedings of the Royal Society of London A* 453 (1997), pp. 163–179.

[88] Omer Sirin et al. "Fingerpad contact evolution under electrovibration". *Journal of the Royal Society Interface* 16.156 (2019), p. 20190166.

[89] Julien Scheibert, Riad Sahli, and Michel Peyrard. "Onset of sliding of elastomer multicontacts: failure of a model of independent asperities to match experiments". *Frontiers in Mechanical Engineering* 6 (2020), p. 18.

[90] Frank Philip Bowden and David Tabor. *The friction and lubrication of solids. Part 2*. Oxford : Clarendon Press ; New York : Oxford University Press, 1964.

[91] Bo NJ Persson. "On the theory of rubber friction". *Surface Science* 401.3 (1998), pp. 445–454.

[92] A. Papangelo, M. Ciavarella, and J. R. Barber. "Fracture mechanics implications for apparent static friction coefficient in contact problems involving slip-weakening laws". *Proceedings of the Royal Society A: Mathematical, Physical and Engineering Sciences* 471.2180 (2015).

[93] Johana Kuncová-Kallio and Pasi J. Kallio. "PDMS and its suitability for analytical microfluidic devices". *Annual International Conference of the IEEE Engineering in Medicine and Biology - Proceedings* (2006), pp. 2486–2489.

[94] IA Lyashenko and VL Popov. "The effect of contact duration and indentation depth on adhesion strength: experiment and numerical simulation". *Technical Physics* 65.10 (2020), pp. 1695–1707.

[95] A. Tiwari et al. "Rubber adhesion and friction: role of surface energy and contamination films" (2020).

[96] Danh Toan Nguyen et al. "Non–Amontons-Coulomb local friction law of randomly rough contact interfaces with rubber". *EPL (Europhysics Letters)* 104.6 (2014), p. 64001.

[97] Bharat Bhushan. "Contact mechanics of rough surfaces in tribology: multiple asperity contact". *Tribology letters* 4.1 (1998), pp. 1–35.

[98] A Schallamach. "How does rubber slide?" *Wear* 17.4 (1971), pp. 301–312.

Titre : Mise en glissement des interfaces élastomères : apports fondamentaux issus d'expériences de contacts modèles sphère/plan

Mots clés : mécanique du contact cisaillé, frottement, adhésion, aire de contact, PDMS, mesure *in-situ*, mesure de champ de déplacement.

Résumé : L'objectif principal de cette thèse était d'obtenir une meilleure compréhension de la mise en glissement des contacts secs en élastomère. Lors de la mise en contact de deux surfaces réelles, généralement rugueuses, l'interface crée est bien souvent constituée d'une myriade de micro-contacts individuels entre des aspérités antagonistes. Ainsi, le comportement macroscopique d'une telle interface multi-contact est la somme complexe des réponses individuelles de tous les micro-contacts. Dans cette étude, nous avons cherché à mieux caractériser le comportement des micro-contacts grâce à une étude systématique basée sur des expériences modèle de cisaillement d'une sphère en PDMS sur une plaque de verre. En plus des mesures de force macroscopique lors des expériences de cisaillement, le travail s'est principalement appuyé sur l'analyse *in-operando* de l'évolution de de l'interface de contact par une méthode optique.

Nous avons d'abord revisité les expériences récentes de la littérature sur la réduction de la zone de contact réelle induite par le cisaillement dans les interfaces élastomériques, dont l'origine a été très débattue. À l'aide d'échantillons d'élastomères ensemencés de particules, d'une technique de suivi des particules et d'analyses de trajectoire originales, nous avons démontré la coexistence de plusieurs mécanismes élémentaires de réduction d'aire réelle de contact agissant simultanément et quantifié leur contribution relative à la réduction d'aire globale. Nous avons identifié le soulèvement comme mécanisme principal et avons également prouvé l'existence d'une zone de glissement de type annulaire qui remplace progressivement la zone centrale initialement collée au sein de l'interface. Par comparaison avec un modèle de mécanique des milieux continus, nous avons montré que, à des charges normales importantes, la réduction de surface provient des grandes déformations mise en jeu et des non-linéarités qui y sont associées, plutôt que des effets adhésifs mis en avant dans la littérature.

La réduction de l'aire réelle de contact induite par le cisaillement avait déjà été étudiée, dans la littérature, principalement pour deux gammes de charges normales distinctes : soit dans le millinewton, soit dans la gamme du Newton. Nous avons ainsi réalisé les premières expériences qui comblent l'écart entre ces deux gammes avec le même échantillon et la même configuration expérimentale. Les résultats indiquent que le comportement observé aux charges normales élevées se maintient jusqu'à environ 0.1 N, en dessous de cette limite les effets adhésifs deviennent vraisemblablement non négligeables. Aux faibles charges normales, nous montrons également que la réduction d'aire se poursuit après le pic en force tangentielle, ce qui remet en question la définition du moment exact de la transition vers le glissement.

La plupart des études de la littérature considèrent des expériences de cisaillement à charge normale constante, alors que, dans une interface glissante rugueuse, les micro-contacts subissent vraisemblablement d'importantes variations de charge normale lors du cisaillement. Pour traiter l'effet de ces variations, nous avons introduit des inclinaisons contrôlées dans notre expérience. Après avoir soigneusement corrigé les mesures de force brutes par l'effet de telles inclinaisons pour extraire la force réellement en jeu à l'interface, nous avons pu proposer la première loi de comportement empirique pour l'évolution de la surface de contact due aux variations simultanées des forces normales et de cisaillement.

Tous ces résultats sur le comportement en frottement des contacts élastomériques modèles fournissent la base nécessaire pour mieux comprendre et/ou concevoir des interfaces multi-aspérités fonctionnelles plus complexes.

Title: Onset of sliding of elastomer interfaces: fundamental insights from model sphere/plane contact experiments

Keywords: sheared contact mechanics, friction, adhesion, contact area, PDMS, *in-situ* measurement, full-field displacement measurement.

Abstract: The main objective of this thesis has been to obtain a better understanding of the onset of sliding of dry elastomer contacts. Because real surfaces are rough, contact interfaces are usually multi-contacts made up of a myriad of individual micro-contacts between antagonist asperities. The macroscopic behavior of such interfaces is thus a complex sum of the individual responses of all micro-contacts. Here, we aimed at better characterizing the micro-contact behavior through a systematic study of model PDMS sphere/glass plate shearing experiments. In addition to macroscopic force measurements during shearing experiments, the work mainly relied on the analysis of *in-operando* images of the contact interface.

We first revisited recent literature experiments about shear-induced real contact area reduction in elastomeric interfaces, the origin of which was highly debated. Using particle-seeded elastomer samples, a particle tracking technique and original trajectory analyses, we demonstrated the coexistence of several area reduction elementary mechanisms acting simultaneously and quantified their relative contribution to the global reduction. We identified contact lifting as the main mechanism and also proved the existence of an annular-like slipping zone that progressively replaces the central stuck area. Through comparison with a continuum mechanics model, we showed that, at large normal loads, area reduction originates from large strains and the related non-linearities, rather than from the adhesive effects put forward in the literature.

Shear-induced contact area reduction had previously been studied in two separate and distinct normal load ranges in the literature: either in the millinewton or in the newton ranges. We thus performed the first experiments bridging the gap between those two ranges with the very same sample and experimental setup. The results indicate that the large normal load behavior holds down to about 0.1 N, below which adhesive effects presumably become non-negligible. At low normal loads, we also show that area reduction continues after the tangential peak force, which calls into question the definition of the exact moment of the transition to sliding.

Most of the literature studies consider shearing experiments at a constant normal load, while micro-contacts in a sliding rough-rough interface undergo important normal load variations with time. To address the effect of those variations, we introduced controlled tilts in the experiment. After carefully correcting the force measurements by the effect of such tilts to extract the real force at play at the interface from the raw measurements, we could propose the first empirical behavior law for contact area evolution due to simultaneous normal and shear force variations.

All those results on the friction behavior of single elastomer contacts provide the necessary basis to understand and/or design more complex functional multi-asperity interfaces.